Aus dem Institut für Molekulare Kardiologie

der Heinrich-Heine-Universität Düsseldorf

Prof. Dr. Jürgen Schrader

Moderne Magnetresonanzmethoden zur kardiovaskulären Phänotypisierung von Mäusen

Habilitationsschrift

für das Fach Experimentelle Medizin

vorgelegt von

Dr. rer. nat. Ulrich Flögel

Düsseldorf

2012

Inhaltsverzeichnis

Abkürzungsverzeichnis

ATP	Adenosintriphosphat
carbox.	Carboxylisches Kohlenstoffatom
ceMRI	*Contrast-Enhanced MRI*
CK_{cyto}	Cytosolische Creatinkinase
CO	Kohlenmonoxid
CSI	*Chemical Shift Imaging*
CT	Computertomographie
CW	*Continuous Wave*
D	Dublett
DPG	2,3-Diphosphoglycerat
EDV	Enddiastolisches Volumen
EF	Ejektionsfraktion
EKG	Elektrokardiogramm
eNOS	Endotheliale NO-Synthase
EPI	*Echo Planar Imaging*
ESV	Endsystolisches Volumen
FA	*Fatty Acid*
FDG-PET	^{18}Fluordeoxyglucose-PET
FLASH	*Fast Low-Angle Shot*
FOV	*Field of View*
HF	Herzfrequenz
HZV	Herzzeitvolumen
ID	Innendurchmesser
iNOS	Induzierbare NO-Synthase
IR	Ischämie/Reperfusion
J	Kopplungskonstante
KHB	*Krebs Henseleit Buffer*
LCFA	*Long-Chain Fatty Acid*
LCT	*Long-Chain Triglyceride*
LPS	Lipopolysaccharid
LVDP	*Left Ventricular Developed Pressure*
M_r	Relative Molmasse
Mb	Myoglobin
MbO_2	Oxygeniertes Myoglobin
MCFA	*Medium-Chain Fatty Acid*

MCT	*Medium-Chain Triglyceride*
metMb	Metmyoglobin (Fe^{III})
MPIO	*Micron-sized Paramagnetic Iron Oxide Particle*
MR	Magnetresonanz
MRA	Magnetresonanzangiographie
MRI	*Magnetic Resonance Imaging*
MRS	Magnetresonanzspektroskopie
MRT	Magnetresonanztomographie
MUFA	*Monounsaturated Fatty Acid*
$myo^{-/-}$	Myoglobin-defizient
NMR	*Nuclear Magnetic Resonance*
NO	Stickstoffmonoxid
NOS	NO-Synthase
P_i	Anorganisches Phosphat
PCr	Phosphocreatin
PET	Positronenemissionstomographie
PFC	Perfluorcarbon
PFOB	Perfluoroctylbromid
PO_2	Sauerstoffpartialdruck
PUFA	*Polyunsaturated Fatty Acid*
Q	Quartett
RARE	*Rapid Acquisition with Relaxation Enhancement*
RF	Respirationsfrequenz
ROS	*Reactive Oxygen Species*
S	Singulett
SFA	*Saturated Fatty Acid*
SNR	*Signal-to-Noise Ratio*
SPIO	*Superparamagnetic Iron Oxide Particle*
SV	Schlagvolumen
T	Tesla
$tg\text{-}iNOS^{+}$	iNOS-überexprimierend
$tg\text{-}iNOS^{+}/myo^{-/-}$	iNOS-überexprimierend und Myoglobin-defizient
USPIO	*Ultrasmall Superparamagnetic Iron Oxide Particle*
VLCAD	*Very Long-Chain Acyl-CoA Dehydrogenase*
$VLCAD^{-/-}$	VLCAD-defizient
VO_2	Sauerstoffverbrauch
WT	Wildtyp

I

Einleitung

1

Magnetische Kernresonanz

1.1 Spektroskopie

1.1.1 Entdeckung und Entwicklung

Magnetische Kernresonanz (NMR = *Nuclear Magnetic Resonance*) wurde 1938 erstmals als eine Technik beschrieben, um magnetische Momente in einem Atomstrahl zu bestimmen [1]. Acht Jahre später wurde über die ersten erfolgreichen Kernresonanzexperimente in kondensierter Materie berichtet – auch hier wurde die Resonanz im angelegten Magnetfeld als eine Methode zur exakten Bestimmung kernmagnetischer Momente verwendet [2, 3]. Kurz darauf zeigte sich, daß in einem NMR-Spektrum für denselben Kern in verschiedenen chemischen Verbindungen unterschiedliche NMR-Frequenzen beobachtet werden können [4]. So ist es zum Beispiel möglich, in einem ^{14}N-NMR-Spektrum einer NH_4NO_3-Lösung für die Stickstoffkerne der beiden Ionen NH_4^+ und NO_3^- zwei separate Signale zu detektieren [5]. Da zudem gleiche Kerne an unterschiedlichen Positionen eines Moleküls getrennte Signale liefern [6] und deren Intensität der Konzentration der detektierten Kerne proportional ist, wurde bald deutlich, welches große analytische Potential die NMR-Technik in sich barg.

Im Laufe der 70er Jahre wurden die bis dahin zur Erzeugung des benötigten Magnetfeldes verwendeten Elektromagnete von supraleitenden Magneten mit wesentlich höherer Feldstärke verdrängt, was nicht nur zu einer höheren spektralen Auflösung, sondern auch zu einer erheblichen Steigerung des Signal/Rausch-Verhältnisses führte. Zu derselben Zeit gelang es dank der Entwicklung leistungsfähiger Computer die konventionelle CW-Aufnahmetechnik (CW = *Continuous Wave*), bei der durch Variation der Frequenz oder des Feldes die Resonanzen nacheinander angeregt wurden, durch die mathematisch aufwendige aber erheblich schnellere Puls-Fourier-Transformtechnik zu ersetzen [7,8]. Diese Weiterentwicklungen machten es möglich, die NMR-Spektroskopie auf zahlreiche biologische Probleme anzuwenden. Die verbesserte Empfindlichkeit und Auflösung erlaubten Untersuchungen an Molekülen wachsender Komplexität wie größeren Kohlenhydraten und kleinen Proteinen sowie Nucleinsäuren.

1.1.2 Anwendung auf biomedizinische Fragestellungen

Obwohl die erste biologische NMR-Untersuchung an roten Blutkörperchen bereits 1955 beschrieben wurde [9], konnte sich die NMR-Technik als Methode zur Untersuchung physiologischer Prozes-

se erst 20 Jahre später durchsetzen, als gezeigt wurde, daß es mittels ^{31}P-NMR-Spektroskopie möglich ist, wichtige Stoffwechselprodukte wie Adenosintriphosphat (ATP) und Phosphocreatin (PCr) im Organismus zu detektieren, ohne ihn zu zerstören [10, 11]. Da aus dem Gehalt dieser energiereichen Phosphate Rückschlüsse auf den aktuellen Energiezustand des untersuchten biologischen Systems gezogen werden können, steht mit der ^{31}P-NMR-Spektroskopie ein Instrument zu Verfügung, den Energiehaushalt eines Organismus *in vivo* und nichtinvasiv zu untersuchen. Die pH-Abhängigkeit des Signals für anorganisches Phosphat (P_i) erlaubt zudem die gleichzeitige Bestimmung des aktuellen intrazellulären pH-Werts [10], so daß die kontinuierliche Aufnahme von *in vivo* ^{31}P-NMR-Spektren die Möglichkeit eröffnet, Veränderungen im Energiestatus und pH-Wert unter verschiedenen Bedingungen zu dokumentieren.

Weitere biochemisch relevante Informationen können im Prinzip durch Spektroskopie jedes Kerns mit einer Kernspinquantenzahl > 0 erhalten werden. Dabei findet die NMR-spektroskopische Untersuchung von Kernen mit einer Isotopenhäufigkeit von nahezu 100%, wie ^{1}H, ^{19}F, ^{23}Na und ^{31}P, besonderes Interesse, da sie eine Spektrenaufnahme mit großer Empfindlichkeit und damit auch hoher Zeitauflösung ermöglichen. Hierunter zeichnet den ^{19}F-Kern eine gewisse Sonderstellung aus: Wie aus dem gyromagnetischen Verhältnis γ ersichtlich (Tabelle 1.1) weist er eine vergleichbare Sensitivität wie der ^{1}H-Kern auf, doch aufgrund seiner vernachlässigbar geringen physiologischen Häufigkeit ist von ihm in biologischen Proben nahezu kein Hintergrundsignal zu erwarten. Problematischer gestaltet sich die Messung von Kohlenstoff- und Sauerstoff-Kernen, deren NMR-spektroskopisch detektierbaren Isotope ^{13}C und ^{17}O zum einen durch nicht sehr große natürliche Häufigkeiten ($< 1\%$) und zum anderen durch ein vergleichsweise kleines γ charakterisiert sind. Dies erfordert in der Regel lange Akkumulationszeiten bei der Aufnahme der Spektren, um ein vernünftiges Signal/Rausch-Verhältnis zu erhalten. Auf der anderen Seite erlaubt der Einsatz von ^{13}C- oder ^{17}O-angereicherten Verbindungen, das Schicksal (nicht radioaktiv) markierter Substrate in einem Organismus zu verfolgen [12], und damit Einblick in die Regulation und Aktivität einzelner Schritte im Stoffwechsel (wie zum Beispiel Glycolyse oder Gluconeogenese) zu gewinnen.

Tabelle 1.1: NMR-relevante Eigenschaften einiger Kerne

Isotop	**Spin**	**Natürliche Häufigkeit** Isotop [%]	**Gyromagnetisches Verhältnis** γ [10^7·rad·s^{-1}·T^{-1}]	**NMR-Frequenz bei 9.4 Tesla** ν [MHz]	**Physiologische Häufigkeit** Element [rel.][1]
^{1}H	1/2	99.98	26.75	400.13	100.0000
^{13}C	1/2	1.07	6.73	100.16	19.1840
^{14}N	1	99.64	1.94	28.91	1.8501
^{17}O	5/2	0.04	−3.63	54.24	38.7000
^{19}F	1/2	100.00	25.16	376.50	0.0001
^{23}Na	3/2	100.00	7.08	105.84	0.0626
^{31}P	1/2	100.00	10.84	161.98	0.3627
^{87}Rb	3/2	27.83	8.79	130.92	0.0001
⋮	⋮	⋮	⋮	⋮	⋮

Neben der Spektroskopie dieser direkt am Substratstoffwechsel beteiligten Kerne lassen sich zusätzliche Informationen über die Kerne ^{23}Na, ^{87}Rb (als NMR-spektroskopisch detektierbarer Kalium-Ersatz) und ^{19}F gewinnen. Mit Hilfe von ^{23}Na-NMR- und ^{87}Rb-NMR-Spektroskopie sind Aussagen über den Transport von Na^+- und K^+-Ionen an der Zellmembran möglich [13, 14], während ^{19}F unter anderem als indirekter Reporterkern für Ca^{2+}-Ionen dienen kann [15, 16].

[1] relative Einheiten basierend auf Stoffmenge

Trotz vieler Vorteile muß man sich jedoch immer vergegenwärtigen, daß die Anwendung der NMR-Technik wegen ihrer geringen Empfindlichkeit auf Metabolite beschränkt ist, die in relativ hohen Konzentrationen ($\geq$ 0.5 mM) vorliegen. Im Gegensatz zu den klassischen biochemischen Analysemethoden ist es mittels NMR-Spektroskopie jedoch möglich, in biologischen Proben ohne vorherige Auftrennung mehrere Moleküle gleichzeitig zu charakterisieren. Wie soeben beschrieben, sind unter Einbeziehung weiterer Kerne, wie zum Beispiel ^{31}P und ^{23}Na, zusätzliche Daten zum Energie- und Ionenhaushalt erhältlich, so daß die geringe Empfindlichkeit der NMR-Methode durch die Fülle der zugänglichen Informationen aufgewogen wird. Außerdem erlaubt die Nichtinvasivität der NMR-Technik *in vivo* Studien an prinzipiell allen Lebewesen. Dementsprechend hat die NMR-Spektroskopie verstärkt Einsatz bei Untersuchung biologischer und medizinischer Fragestellungen an Menschen, Tieren und Pflanzen gefunden, aber auch bei perfundierten Organen, Zellen, Bakterien und anderen Mikroorganismen [17].

1.2 Bildgebung

Die Magnetresonanztomographie (MRT oder auch MRI = *Magnetic Resonance Imaging,* synonym mit Kernspintomographie) wurde als bildgebende NMR erstmals zu Beginn der 70er Jahre des letzten Jahrhunderts beschrieben. Auffällig ist, daß die zunehmende Verbreitung der NMR-Techniken im medizinischen Bereich zu einer raschen Eliminierung des „*N*"s aus NMR führte (unter anderem auch bei MRS = Magnetresonanzspektroskopie), was vor allem darauf zurückzuführen ist, daß seit den 70er Jahren der Begriff „nuklear" extrem negativ behaftet ist, und dadurch eine eindeutige Abgrenzung zu den nuklearmedizinischen Techniken vorgenommen werden konnte.

Von entscheidender Bedeutung für die Bildgebung auf Grundlage der MR war die Einführung von (i) magnetischen Gradientenfeldern in das konventionelle MR-Experiment, um eine räumliche Zuordnung der MR-Signale in der Probe zu erreichen, und (ii) Verfahren zur Ortskodierung des Untersuchungsobjektes, aus denen anschließend mit Hilfe der aus der Computertomographie (CT) bekannten Rückprojektion ein Abbild des Untersuchungsobjektes errechnet werden konnte [18]. Das erste mit diesen Techniken erhaltene ^{1}H-MR-Bild zeigt eine zweidimensionale Abbildung von zwei mit normalem Wasser (^1H_2O) gefüllten Röhrchen in einer Umgebung aus „schwerem" Wasser (^2H_2O). Von zentraler Relevanz für eine praktische Nutzung dieser Entdeckung war die anschließende Entwicklung von Techniken zur schichtselektiven Anregung sowie von mathematischen Verfahren, um die Signale zügig in Bildinformationen umzuwandeln. Ende der 70er Jahre wurden bereits die ersten MR-Bilder vom Menschen veröffentlicht. Während zu dieser Zeit eine einzelne Aufnahme noch mehr als fünf Minuten Meßzeit benötigte, konnte dies bis Mitte der 80er Jahre auf fünf Sekunden verkürzt werden. Dies lag zum einen − ähnlich wie bereits weiter oben für die Spektroskopie erwähnt − an der Ablösung der Elektromagnete durch supraleitende Magnete höherer Feldstärke sowie der Entwicklung leistungsfähigerer Gradientensysteme, und zum anderen an der Etablierung neuer schneller Bildgebungspulssequenzen wie EPI = *Echo Planar Imaging* [19], RARE = *Rapid Acquisition with Relaxation Enhancement* [20] und FLASH = *Fast Low-Angle Shot* [21]. Insbesondere die letztgenannte Sequenz eröffnete durch dynamische Aufnahmen der Herzaktion sowie dreidimensionale Gefäßdarstellungen mittels MR-Angiographie (MRA) der zunächst sehr „hirnlastigen" MRI völlig neue Anwendungsfelder. Damit war ab Mitte der 1980er Jahre der Weg frei für eine breite Anwendung der MRI in der medizinischen Diagnostik.

1.3 Kardiovaskuläre MR

1.3.1 Bildgebung von Herz und Gefäßen

Da MRI aufgrund der − im Vergleich zu Ultraschall − recht geringen Empfindlichkeit nur schlecht in Echtzeit betrieben werden kann, ist Bewegung der natürliche Feind der MR-Messung. Daraus ergibt sich auch, warum geraume Zeit die Vielzahl aller MR-Anwendungen auf das Gehirn beschränkt war: dieses Organ ist groß, sehr homogen und läßt sich leicht ruhig halten, so daß hier recht einfach qualitativ hochwertige MR-Bilder zu erhalten sind. Demgegenüber war der Einsatz

der MR-Techniken auf Fragestellungen hinsichtlich des Herz- und Kreislaufsystems lange Zeit nur wenig verbreitet, was vor allem auch darin begründet war, daß die Aufnahme aussagekräftiger Daten zur kardialen Pumpfunktion die Mittelung über mehrere Herzzyklen notwendig macht. Zur Vermeidung von Bewegungsartefakten (Verschmieren) in MR-Bildern vom Thorax muß die Datenakquisition daher immer zum gleichen Zeitpunkt im Herz- und Respirationszyklus stattfinden, was in der Regel eine Kopplung (Triggerung) der Datenaufnahme an diese Rhythmen erforderlich macht.

Daher gelang es erst Ende der 80er Jahre mit der Entwicklung schneller EKG-getriggerter Cine-Sequenzen, die Basis für eine exakte Quantifizierung der systolischen und diastolischen Herzfunktion zu legen [22]. Etwa zur selben Zeit wurde durch die Neueinführung der MR-Angiographie [23] auch die Tür zur Untersuchung des vaskulären Systems aufgestoßen. Der Durchbruch für die kardiovaskuläre MRT erfolgte dann im Laufe der 90er Jahre durch den Einsatz verbesserter Gerätetechnik, stärkerer Gradientenfelder sowie schnellerer Untersuchungssequenzen kombiniert mit neu entwickelten Kontrastmitteln (ceMRI = *Contrast-Enhanced MRI*). Neben der Bestimmung der globalen und regionalen kardialen Pumpfunktion können inzwischen Informationen über Flußgeschwindigkeiten und transvalvuläre Flußprofile sowie die Myokardperfusion in Ruhe und unter Belastung gewonnen werden, und es lassen sich zumindest auch die größeren Koronararterien mit Wand und Lumen darstellen [24, 25].

1.3.2 Über die Anatomie und Funktion hinaus ...

Zelltracking

In den letzten Jahren hat sich für die MR-Bildgebung ein völlig neues Feld in Form des „Zelltracking" ergeben, welches insbesondere durch die Befunde stimuliert wurde, daß nicht nur Stammzellen sondern auch andere Zellen (so zum Beispiel auch Endothelzellen und deren Vorläuferzellen) in der Lage sind, zu anderen Zelltypen zu transdifferenzieren. Insofern besteht nach wie vor die Hoffnung, daß eine Zelltransplantation ins Zielorgan eine neue therapeutische Option darstellt, um irreparabel geschädigtes Gewebe durch Zellen mit organspezifischen Funktionen zu ersetzen. Um nun zu beweisen, daß die transplantierten Zellen tatsächlich transdifferenzieren und anschließend zur Aufrechterhaltung beziehungsweise Reparatur der Organfunktion beitragen, wäre ein kontinuierliches Monitoring „magnetisch markierter" Zellen die Methode der Wahl.

Für die Beladung der zu transplantierenden Zellen wurden insbesondere kleine Eisenoxidpartikel (zum Beispiel SPIOs = *Superparamagnetic Iron Oxide Particles*) verwendet, die von den meisten Zelltypen gut aufgenommen werden und an der Stelle, an der sich die Zellen anschließend ansiedeln, zu einer Signalauslöschung führen [26]. Darüber hinaus weisen superparamagnetische Eisenoxidpartikel eine hohe Affinität für das Monocyten/Makrophagen-System auf. Daher kann zum Beispiel die Akkumulation von SPIOs durch Phagozytose in Makrophagen aortaler Plaques genutzt werden, um mittels nichtinvasiver MRI den Nachweis inflammatorischer Plaqueaktivität mit erhöhter Endothelpermeabilität und Makrophageninfiltration zu führen [27]. Eine klare Limitation liegt jedoch in der geringen Spezifität dieses Ansatzes: Da die Partikel nicht direkt detektiert werden, sondern anhand der am Depositionsort induzierten Magnetfeldinhomogenitäten und der damit verbundenen Schwärzung im MR-Bild, sind die erhaltenen Daten oft nicht einfach zu deuten, da nicht immer sicher ist, ob der Signalverlust durch die Ablagerung der Partikel oder durch unspezifische Artefakte verursacht wird.

X-Kerne und Spektroskopie am Herzen

Auch bei der Kardio-MRT steht aufgrund des hohen Wassergehalts im Körper ($\approx 75\%$ H_2O) bei den meisten Anwendungen vor allem die Detektion des Wasserstoff-(^{1}H)-Kerns im Mittelpunkt des Interesses. Wie jedoch bereits in Abschnitt 1.1.2 angedeutet, sollte nicht außer acht gelassen werden, daß auch über die etwas exotisch anmutenden X-Kerne (wie ^{13}C, ^{19}F, ^{23}Na und ^{31}P) Einblicke gewonnen werden können, die auf anderem Wege nur schwer zugänglich sind. So liefert die normale ^{1}H-MR-Bildgebung zwar detaillierten Einblick in Anatomie und Funktion des Herzens, gibt jedoch wenig Aufschluß über den metabolischen Zustand des Gewebes.

Da insbesondere für das schlagende Herz eine zuverlässige Regulation des Energiehaushalts unabdingbar ist, wurde schon früh versucht, die energiereichen Phosphate ATP und PCr im Myokard über den ^{31}P-Kern *in vivo* zu detektieren. Dementsprechend wurden bereits 1977 die ersten ^{31}P-MR-Spektren am perfundierten Rattenherzen erhalten [28]. Danach fand diese Technik zunächst in einer Fülle von Tierstudien Anwendung − in erster Linie auf Veränderungen des kardialen Energiestatus' bei Unterbrechung der Blutversorgung durch plötzlichen Verschluß der Koronargefäße (wie bei einem Herzinfarkt). Obgleich die ^{31}P-MR-Spektroskopie bislang noch keinen Einzug in die klinische Routinediagnostik gefunden hat, sind inzwischen jedoch auch am Menschen zahlreiche Untersuchungen zur Rolle veränderter energetischer Parameter bei der Entwicklung von Herzinsuffizienzen durchgeführt worden [29].

Weitere Informationen zum myokardialen Stoffwechsel lassen sich mithilfe des ^{13}C-Kerns erlangen. Da dieser eine natürliche Häufigkeit von nur $\approx 1\%$ aufweist (vergleiche Tabelle 1.1), kann nach Gabe von ^{13}C-markierten Substraten (zum Beispiel [1-^{13}C]-Glucose) deren Weg durch die verschiedenen Stoffwechselpfade gezielt verfolgt werden [12]. Damit können krankheitsbedingte Veränderungen im Substratmetabolismus, Aktivitäten von Schlüsselenzymen sowie der Substratflux in bestimmte Stoffwechselzweige, wie β-Oxidation oder Citratzyklus, bestimmt werden [30]. Enorme Belebung hat dieses Feld der MR-Spektroskopie in den letzten Jahren durch die gestiegene Verfügbarkeit hyperpolarisierter ^{13}C-Verbindungen erfahren, die eine Steigerung der Meßempfindlichkeit um einen Faktor von mehr als 10^5 möglich macht [31] und damit die Tür für eine Echtzeitbildgebung metabolischer Flüsse geöffnet hat [32, 33].

Gegenüber ^{31}P und ^{13}C hat die Spektroskopie aller anderen Kerne im Kardio-MR-Bereich bislang einen untergeordneten Stellenwert. Über den ^{23}Na-Kern lassen sich zwar prinzipiell Veränderungen in der Ionenhomöostase bei Herzerkrankungen und Verschiebungen zwischen intra- und extrazellulären Na^+-Pools nachweisen, doch einer „echten" *in vivo* Anwendung steht der hierfür unabdingbare Einsatz von Lanthanoidenshiftreagenzien [34] entgegen, die eine erhebliche Toxizität aufweisen und nur in Studien mit isoliert perfundierten Organen eingesetzt werden können [35]. Auch die ^{1}H-MRS-Techniken − welche vor allem im neurologischen Bereich zur *in vivo* Quantifizierung von Aminosäuren, Zuckern und anderen Metaboliten immer stärkere Verbreitung finden, für die aber aufgrund des extrem schmalen spektralen Bereichs (< 10 ppm) und der Vielfalt der darin auftretenden Metabolitensignale eine sehr gute spektrale Auflösung und ein guter *Shim* Grundvoraussetzung sind − haben angesichts der miserablen magnetischen Feldhomogenität im Thorax für das Herz kaum Bedeutung (→ Suszeptibilitätssprünge Herz/Lunge, → Blutfluß, → kardiale und respiratorische Bewegung). Von diesen Einschränkungen bleibt der ^{19}F-Kern infolge der großen spektralen Breite (≈ 400 ppm) zwar verschont, doch haben sich bisher kaum Anwendungen im kardiovaskulären Bereich ergeben. Lediglich einige ältere Arbeiten haben sich zunutze gemacht, daß die Relaxationszeiten biochemisch inerter Perfluorcarbone stark abhängig vom lokalen Sauerstoffgehalt sind, um über ^{19}F-MR die O_2-Partialdrücke von Lunge, Leber, Milz [36] beziehungsweise im isoliert perfundierten Herz [37] zu bestimmen.

1.3.3 Analyse transgener Mausmodelle

Die Erzeugung transgener Tiermodelle zur Erforschung von Herz-Kreislauf-Erkrankungen hat bereits zum Ende der 1990er Jahre exponentiell zugenommen. Eine wichtige Erkenntnis, die sich hieraus ergeben hat, ist die Tatsache, daß die erzeugten transgenen Mäuse sehr häufig keinen offensichtlichen Phänotyp aufweisen. Daraus ist oft der falsche Schluß gezogen worden, daß das entsprechende Gen funktionell unwichtig ist. Es mehren sich aber die Befunde, denen zufolge es bei offenbar unverändertem Phänotyp häufig zu drastischen Adaptationen auf struktureller und biochemischer Ebene kommt, die durch die Aktivierung von alternativen genetischen Programmen und/oder durch posttranslationale Veränderungen einen Gendefekt ausgleichen können.

Zur Analyse der ausgelösten Kompensationsmechanismen ist daher eine exakte Phänotypisierung von zentraler Bedeutung. Aus der Größe dieser Tierspezies erwuchs zunächst das Problem, daß die gängigen physiologischen Techniken miniaturisiert werden mußten, um den kardialen Phänotyp adäquat charakterisieren zu können. Eine ausgewachsene Maus wiegt typischerweise 25-30 g, das Mäuseherz circa 100-150 mg, bei einer *in vivo* Herzfrequenz von bis zu 600 Schlägen/min und

einer Druckanstiegsgeschwindigkeit (dP/dt) von über 15000 mmHg/s. Mit entsprechend verfeinerten Methoden war es bereits frühzeitig möglich, im akuten Versuch hämodynamische Daten mit Millar Mikro-Tip Manometern zu erheben [38], den Blutdruck kontinuierlich telemetrisch zu bestimmen [39, 40] oder auch detaillierte elektrophysiologische Messungen durchzuführen [41]. Die Möglichkeiten und Schwierigkeiten, hämodynamische Daten an der Maus *in vivo* zu erheben, wurden in einigen Übersichtsartikeln zu dieser Zeit ausführlich dargestellt [42–44].

Um Aussagen über die Herzmorphologie zu machen und daraus abgeleitete funktionelle Parameter zu erhalten, gibt es auch für die Maus im Wesentlichen zwei nichtinvasive Verfahren: Echokardiographie und MRI. Unter Verwendung der am 2D-Bild ausgerichteten M-mode Echokardiographie können Bilder des Herzens erzeugt werden, mit denen Wandstärke und Lumendurchmesser des linken Ventrikels in Systole und Diastole bestimmt werden können. Hieraus werden die fraktionelle Verkürzung, die zirkumferente Kontraktionsgeschwindigkeit und die Ejektionsfraktion sowie linksventrikuläre Volumina und Massen abgeleitet [45]. Das Verfahren ist sensitiv genug, um auch Veränderungen der Pumpleistung des Herzens während der Embryonalentwicklung zu bestimmen [46]. Wichtige Limitation dieser echokardiographischen Volumenquantifizierung ist allerdings, daß die Berechnungsmodelle auf geometrischen Annahmen (ellipsoidale Form des linken Ventrikels) beruhen, die im Fall einer Herzschädigung mit Formänderung des Ventrikels (asymmetrische Dilatation, *Remodeling* nach Myokardinfarkt etc.) nicht länger zutreffen.

MRI als intrinsisch dreidimensional-tomographisches Verfahren bietet die Möglichkeit, Volumenquantifizierungen unabhängig von geometrischen Vorbedingungen durchzuführen. Für die Bestimmung von Wanddicke, Form des Herzens, ventrikulären Volumina und Myokardmasse bewies die Kardio-MRT hohe Meßgenauigkeit und Reproduzierbarkeit sowohl in Tierstudien [47] als auch am Menschen [48] und ist als Goldstandard zur Volumenquantifizierung etabliert. Siri et al. waren 1997 die ersten Autoren, die mit Hilfe von EKG-getriggerter MRI bei 9.4 Tesla (T) quantitative Daten über die Dimensionen des linken Ventrikels der Maus unter Kontroll- und Hypertrophiebedingungen veröffentlicht und diese mit gravimetrischen Messungen validiert haben [49]. Unabhängig davon haben Kubota [50] und Bryant [51] unter Verwendung von Magneten niedrigerer Feldstärke die Validität von MRI für die Bestimmung von Ventrikelvolumina, Wandstärke und Ejektionsfraktion an Mäusen bestätigt, die den Tumor-Nekrose-Factor-α herzspezifisch überexprimierten. Die Anwendung von MRI zur genauen Erfassung von muriner Herzgeometrie und Auswurfleistung wurde in verschiedenen transgenen Modellen mit Herzhypertrophie bestätigt [52, 53].

Die zeitliche und räumliche Auflösung der Kleintier-MRI konnte durch Entwicklung optimierter Pulsfrequenzen und Hardware mit kürzestmöglicher Echozeit und Repetitionszeiten von < 5 ms noch einmal erheblich gesteigert werden [54]. Da bereits Mäuse mit einem Körpergewicht von 2 g untersucht werden können, ist es mit dieser Methode möglich, die Entwicklung des Herzens kontinuierlich vom juvenilen bis zum adulten Tier zu verfolgen [55]. Des Weiteren gelang es auch die großen Koronargefäße im Mäuseherzen in ausgezeichneter Auflösung darzustellen [56] sowie parallel zur Bildgebung mittels volumen-selektiver ^{31}P-MR-Spektroskopie *in vivo* Daten über den Gehalt der energiereichen Phosphormetabolite im Herz der Maus zu erhalten [57, 58]. Im letzten Jahrzehnt sind hier weitere, große Fortschritte gemacht worden − vor einiger Zeit wurde sogar eine Sonderausgabe von *NMR in Biomedicine* der Analyse transgener Mausmodelle gewidmet [59].

1.4 Zielsetzung

Ziel der Arbeiten in den letzten Jahren war es, (i) die zum Teil bereits an größeren Tiermodellen beziehungsweise am Menschen beschriebenen MR-Methoden für eine möglichst vollständige Erfassung des kardiovaskulären Phänotyps bereits vorhandener und neu zu erzeugender transgener Mausmodelle am Institut für Herz- und Kreislaufphysiologie / Molekulare Kardiologie verfügbar zu machen und (ii) diese zur Untersuchung spezieller Fragestellungen um neue, maßgeschneiderte Verfahren zu bereichern. Dabei standen zunächst spektroskopische Arbeiten am Langendorff-Modell zur kardialen Energetik, Sauerstoffversorgung und zum Substratstoffwechsel im Vordergrund des Interesses. Die Etablierung der einzelnen MR-Methoden war insbesondere von der Generierung und Analyse verschiedener Myoglobin-defizienter Mausmutanten in unserem Institut getriggert [60]. Im

Weiteren werden daher die verschiedenen MR-Techniken hauptsächlich am Beispiel dieser Tiermodelle vorgestellt, und es wird gezeigt, wie diese Methoden dazu genutzt werden konnten, um eine Reihe bisher verborgener Eigenschaften von Myoglobin ans Tageslicht zu bringen.

In der Folge wurden dann an dem bis dahin ausschließlich zu MR-spektroskopischen Untersuchungen am isolierten Herzen verwendeten Vertikalmagneten die Parameter für die MR-Bildgebung an der Maus optimiert und Standardprotokolle etabliert, die möglichst schnelle Messungen von hoher Qualität erlauben. Zu Beginn stand hierbei für die kardiale Phänotypisierung der Mutanten *in vivo* vornehmlich die genaue Darstellung der Ventrikelgeometrie mittels ^{1}H-MRI sowie die Bestimmung von Wandstärken und funktionellen Größen wie die Auswurfleistung des Herzens im Mittelpunkt. In jüngster Zeit ist es dann gelungen, die Qualität und Aussagekraft der MR-Analysen nochmals substantiell zu erweitern. Dies beinhaltete die Implementierung angiographischer Methoden zur vaskulären Analyse (auf die in dieser Arbeit nicht eingegangen wird) sowie die Etablierung volumenselektiver Spektroskopie zur umfassenden Bewertung von kardiovaskulärer Funktion und lokalem Stoffwechsel. Darüber hinaus wurde ein völlig neues Verfahren zum *in vivo* Monitoring von Entzündungszellen eingeführt, das es ermöglicht über eine *in situ* Beladung von Monocyten/Makrophagen inflammatorische Prozesse mit einem „positiven Kontrast" darzustellen.

II

Methodische Aspekte

2

Vorgehensweise

2.1 Untersuchungen am perfundierten Mäuseherzen

Untersuchungen an isoliert-perfundierten Organen haben den Vorteil, daß man hier nahezu vollständige Kontrolle über alle experimentelle Bedingungen hat. So können zum Beispiel Pharmaka unter gut definierten Bedingungen direkt über das Koronarsystem appliziert werden, ohne daß es zu störenden Interaktionen mit dem Blutkreislauf oder anderen Organen kommt.

Das Herz eignet sich für solche Untersuchungen besonders gut, da es auch außerhalb des Körpers sofort wieder zu schlagen beginnt, wenn es nur ausreichend mit Sauerstoff und Substraten wie Glucose oder Fettsäuren sowie essentiellen Ionen wie Ca^{2+}, K^+ und Na^+ versorgt wird. Allerdings erfordert die Präparation und das „Aufhängen" des kleinen Mäuseherzens an der Perfusionskanüle etwas experimentelles Geschick (vergleiche Abbildung 2.1; zum Größenvergleich ganz rechts ein normales Streichholz). Links neben dem Herz ist ein wassergefüllter Ballon zu erkennen, der zur Erfassung der Kontraktionskraft in die linke Herzkammer eingeführt wird. Die Perfusion und die

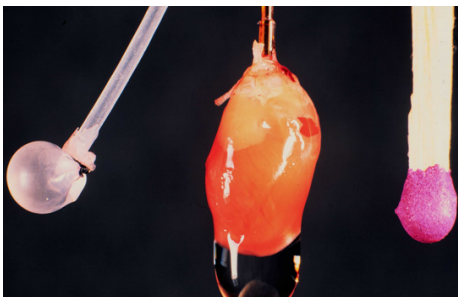

Abbildung 2.1: Perfundiertes Mäuseherz.

adäquate Versorgung des Herzens erfolgt retrograd über die Aorta (vergleiche Abbildungen 2.1 und 2.2) mit einer Pufferlösung (KHB = *Krebs Henseleit Buffer*; oxygeniert mit Carbogen[1]) bei einem physiologischen Druck von 100 mmHg. Nach der Präparation wird das schlagende Herz in ein 10-mm NMR-Röhrchen überführt und anschließend im sensitiven Volumen des Magneten (siehe

[1] 95% O_2/5% CO_2

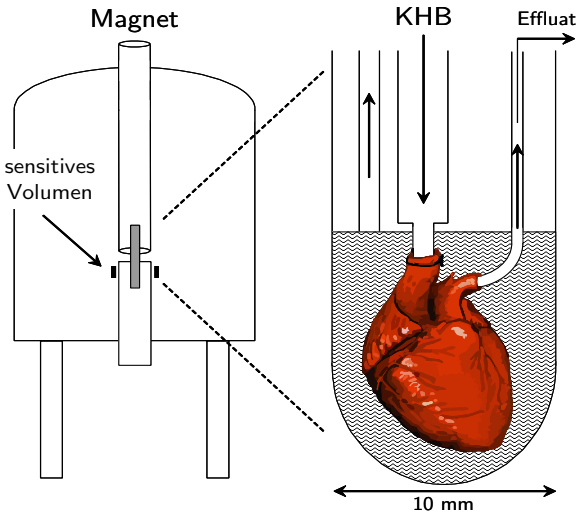

Abbildung 2.2: Perfusion des Mäuseherzens im Magneten.

Abbildung 2.2) bei 37 °C platziert. Die Registrierung der funktionellen Parameter, wie linksventrikuläre Druckentwicklung (LVDP = *Left Ventricular Developed Pressure*) und Herzfrequenz, wird über einen an den Ballon gekoppelten Druckaufnehmer vorgenommen. Außerdem wird der koronare Fluß mithilfe einer Ultraschallsonde sowie der Sauerstoffverbrauch durch Messung von arteriellem und venösem Sauerstoffpartialdruck (PO_2) mittels implantierbarer optischer Mikrosensoren erfaßt.

Die wesentliche Herausforderung bei diesem Versuchsaufbau war die Auswahl geeigneter, MR-kompatibler Materialien zur Gewährleistung physiologischer Bedingungen für das Mäuseherz innerhalb des Magneten (Feldstärke: 9.4 Tesla). Entscheidend für die Funktion und Langzeitstabilität (1-2 Stunden) eines salin-perfundierten Herzens ist vor allem ein ausreichend hohes arterielles Sauerstoffangebot ($PO_2 \geq 600$ mmHg), was in Anbetracht der langen Schlauchwege sowie des geringen Koronarflußes und der damit verbundenen langen Transitzeit des Perfusionsmediums vom begasten Reservoir in den Magneten nur durch die Verwendung von extrem gasdichtem Schlauchmaterial (Viton) sichergestellt werden kann. Die Kanülierung des Herzens erfolgt mit speziellen *Fused Silica* Kapillaren, die bei geringer Wandstärke (0.1 mm) und großem Innendurchmesser (0.5 mm) eine ähnliche Stabilität wie Edelstahlkanülen aufweisen, aber zu keinen Störungen im Magnetfeld führen.

Wie in Abbildung 2.2 zu erkennen ist, „schwimmt" das Herz während der Messung im venösen Effluat – erst oberhalb des Herzens wird der Perfusionspuffer aus dem NMR-Röhrchen abgepumpt. Dies hat insbesondere den Vorteil, daß die Suszeptibilitätssprünge um das Herz reduziert werden und dadurch die Homogenität im Probenvolumen wesentlich höher ist als bei einem Herzen, das mit Luft umgeben ist. Dies erleichtert wiederum das *Shimmen* der Probe und führt zur schmaleren Linienbreiten der Signale, was sowohl Auflösung als auch Empfindlichkeit der Spektren verbessert. Außerdem ermöglicht das Auffangen des Effluats die Bestimmung von freigesetzten Metaboliten beziehungsweise Botenstoffen.

Die Messungen am perfundierten Mäuseherzen, bei denen keine Ortsauflösung notwendig ist, geschieht in 10-mm Probenköpfen, mit denen die entsprechenden Kerne selektiv detektiert werden können (zum Beispiel ^{1}H, ^{13}C, ^{19}F, ^{23}Na, ^{31}P). Diese Probenköpfe sind sowohl für hochaufgelöste Spektroskopie an Gewebeextrakten als auch für physiologische Untersuchungen am isolierten Organ geeignet.

2.2 *In vivo* Messungen an der Maus

Ausgehend von dem oben beschriebenen Versuchsaufbau sind einige entscheidende Modifikationen notwendig, um ortsaufgelöste Messungen am Ganztier durchführen zu können. Hierzu muß

zunächst ein Gradientensystem integriert werden (Abbildung 2.3), welches Magnetfeldgradienten variabler Größe in x-, y-, und z-Richtung erzeugen kann, um eine Ortskodierung des MR-Signals gewährleisten zu können. In dieses Gradientensystem werden anschließend die Bildgebungsprobenköpfe mit den jeweiligen Resonatoren (beziehungsweise Spulen) inklusive des interessierenden Objekts eingeführt.

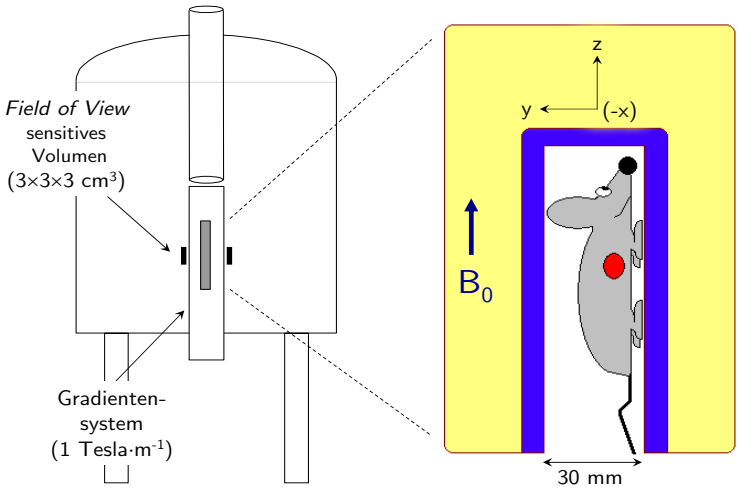

Abbildung 2.3: Gradientensystem und Bildgebungsobjekt im vertikalen Magneten.

Für die im Folgenden beschriebenen *in vivo* Untersuchungen wurden zwei verschiedene wassergekühlte Microimagingsysteme mit aktiv abgeschirmten Gradienten verwendet, die sich hinsichtlich Innendurchmesser (ID) und Gradientenstärke unterscheiden (Micro2.5: ID 40 mm, 1 Tesla/m; Mini0.5: ID 57 mm, 0.2 Tesla/m). In Abhängigkeit von der Größe des Versuchstiers wurden die Messungen mit Resonatoren von 10, 25, 30 beziehungsweise 38 mm ID durchgeführt.

Zur Durchführung der Experimente muß die Maus im Bereich des sensitiven Volumens platziert werden (Abbildung 2.3) und darf für die Dauer der Messungen ihre Position im Magneten nicht verändern. Hierfür ist im Tierexperiment eine Narkose unabdinglich. Wie aus Abbildung 2.4 ersichtlich wird diese mittels einer Atemmaske vorgenommen, über die das Inhalationsnarkotikum Isofluran (1.5% in 20% O_2/80% N_2) appliziert wird. Um die geringen Flüsse, die für die Anästhesie der Maus notwendig sind ($\approx$ 50 ml/min), akkurat einstellen zu können, wurde ein klinischer Isoflu-

Abbildung 2.4: Platzierung der Maus im Resonator.

ranverdampfer über geeignete Adapter mit adäquaten Schwebekörper-Durchflußmessern für O_2 und N_2 verbunden. Eine Injektionsnarkose (zum Beispiel Hypnorm/Diazepam) erwies sich sowohl aufgrund der schlechten Steuerbarkeit der Narkose als auch wegen der kardio- und atemdepressiven Nebenwirkungen dieser Pharmaka als nachteilig. Demgegenüber lassen sich mit der beschriebenen Isofluran-Inhalationsnarkose physiologische Werte von $\approx$ 600 min^{-1} für die Herz- beziehungsweise

$\approx 100\ \mathrm{min}^{-1}$ für die Atemfrequenz über einen Zeitraum von mehr als einer Stunde aufrechterhalten. Isofluran wird auch im humanen Bereich eingesetzt und von Mäusen und Ratten gut toleriert. Etwa 1-2 Minuten nach Beendigung der MR-Untersuchungen wachen die Tiere bereits wieder aus der Narkose auf.

Nach Einleiten der Narkose wird das Versuchstier vorsichtig in das Halterungssystems des Probenkopfs eingebracht (siehe Abbildung 2.4) und dort sorgfältig fixiert, damit es während der Messungen nicht verrutschen kann. Anschließend wird der gesamte Aufbau in den Magneten überführt. Dort werden die vitalen Funktionen (EKG, Atmung) des Tieres mittels im Probenkopf angebrachter EKG-Elektroden und druckempfindlicher Sensoren überwacht. Außerdem wird während der Messung die Körpertemperatur der Maus über ein rektal eingeführtes Thermoelement kontrolliert und über die Temperiereinheit des Gradientensystems auf 37 °C gehalten.

Um auszuschließen, daß die vertikale Lage der Maus innerhalb des Magneten einen Effekt auf die physiologischen Meßparameter hat, haben wir unter Verwendung eines Kipptisches die hämodynamischen und kontraktilen Parameter in vertikaler und horizontaler Lage mit Hilfe eines Millar-Tip-Katheters verglichen (unter Isofluran-Narkose und Temperierung bei 37 °C). Dabei zeigten sich in Übereinstimmung mit publizierten Daten [61] keine wesentlichen Veränderungen, womit sichergestellt ist, daß die senkrechte Positionierung der Maus die erhaltenen Ergebnisse nicht beeinflußt [62].

3

Bildgebung und Spektroskopie

3.1 Herzfunktion – Kardio-MRT an der Maus

Um Aussagen über die Herzmorphologie transgener Tiermodelle zu machen und daraus abgeleitete funktionelle Parameter zu erhalten, wurde an dem zunächst ausschließlich für spektroskopischen Untersuchungen am isolierten Herzen (vergleiche Abschnitt 2.1) verwendeten vertikalen MR-System ein Standardprotokoll etabliert, das möglichst schnelle Messungen von hoher Qualität erlaubt (siehe Abbildung 3.1). Die wichtigsten Aspekte bei der Datenaufnahme und -analyse werden im Folgenden kurz erläutert.

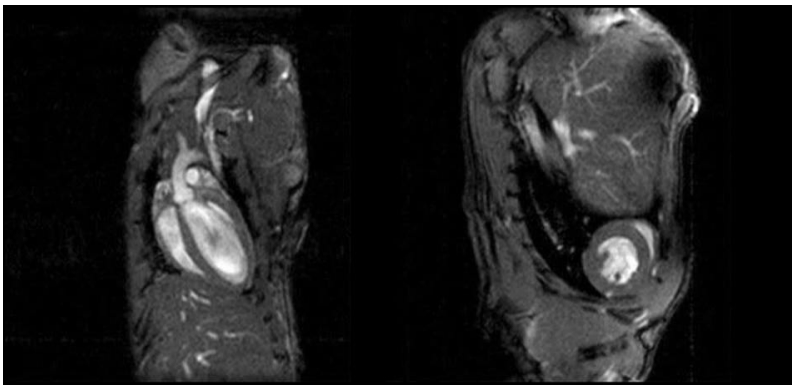

Abbildung 3.1: ^{1}H-MR-Bilder eines Mäuseherzens in der Enddiastole (links, coronal; rechts, axial) aufgenommen mit einer Respirations- und EKG-getriggerten Cine-FLASH-Sequenz über ein *Field of View* von 3×3 cm^2.

Zur Aufnahme von MR-Bildern an definierten Zeitpunkten des Herzzyklus' ist eine Triggerung der Bildgebungssequenz an das EKG unverzichtbar. Hierfür wird das EKG der Maus über die Vorder- und Hinterpfoten abgeleitet. Zusätzlich wird über einen Drucksensor die Respiration der Maus erfaßt, um Artefakte durch die Bewegung des Brustkorbs zu reduzieren. Beide Signale werden über ein speziell zur Erfassung von Respirations- und EKG-Signalen geeignetes Gerät (*Small Animal Monitoring and Gating Unit*, SA Instruments) verarbeitet, das die Datenakquisition auf den

QRS-Komplex sowie auf die Ausatmungsphase triggert. Innerhalb eines Herzzyklus' können bis zu 20 Bilder aufgenommen werden, so daß bei einer Herzfrequenz von ≈ 600 min^{-1} eine Zeitauflösung von 5 ms resultiert. Bei Verwendung einer Schichtdicke von 1 mm, einem *Field of View* (FOV) von 3×3 cm^2 und einer Matrixgröße von 256×256 ergibt sich eine „*in plane*" Auflösung von 117×117 μm^2. Diese zeitliche beziehungsweise räumliche Auflösung ist zur routinemäßigen Ermittlung der Herzfunktion vollkommen ausreichend.

Für die Bestimmung der funktionellen Herzparameter sind insbesondere enddiastolisches und endsystolisches Volumen von Interesse, aus denen sich fast alle anderen Größen berechnen lassen. Hierfür werden senkrecht zur longitudinalen Herzachse aneinandergrenzende Kurzachsenbilder während Enddiastole und -systole aufgenommen. Anschließend werden die endo- und epikardialen Grenzen segmentiert. Nach Multiplikation der ermittelten Flächen mit der Schichtdicke erfolgt die Bestimmung des Kammer- und Myokardvolumens durch Summation der Teilvolumina über alle gemessenen Schichten. Aus den enddiastolischen und -systolischen Volumina können dann Schlagvolumen und Ejektionsfraktion sowie das Herzzeitvolumen (Herzfrequenz $\leftarrow\!\!\prec$ EKG) ermittelt werden. Das Herzgewicht errechnet sich aus dem Volumen innerhalb der epikardialen Grenzen minus des Kammervolumens multipliziert mit der spezifischen Dichte des Myokards (≈ 1.05 g/cm^3). Des Weiteren lassen sich aus den Bildern noch Daten für die Wand- und Septumdicke entnehmen. In der untenstehenden Tabelle 3.1 sind die wichtigsten funktionellen Größen, die bei den MR-Messungen am Mäuseherzen erhoben werden, zusammengefaßt.

Tabelle 3.1: Funktionelle Parameter des Mäuseherzens

Parameter	**Abkürzung**	**typische Werte**
Herzfrequenz	HF	500-600 min^{-1}
Atemfrequenz	RF	100-120 min^{-1}
Enddiastolisches Volumen	EDV	50-60 μl
Endsystolisches Volumen	ESV	15-20 μl
Schlagvolumen	SV	35-40 μl
Ejektionsfraktion	EF	65-70 %
Herzzeitvolumen	HZV	15-20 ml·min^{-1}
Linksventrikuläre Myokardmasse	M_{myo}	80-100 mg
M_{myo}/Körpergewicht	rel. M_{myo}	2.5-3.5 mg·g^{-1}
Myokardiale Septumdicke	d_{sept}	0.8-1.0 mm
Mittlere Wanddicke	d_{mitt}	0.8-1.0 mm

Die typischen Werte, die in der rechten Spalte angegeben sind, beziehen sich auf Wildtyp-Mäuse des C57BL/6-Stammes. Inzwischen ist es möglich, sämtliche Messungen, die zur Ermittlung dieser Parameter für eine Maus notwendig sind, in weniger als 45 Minuten durchzuführen. Die entwickelten MR-Protokolle wurden im Laufe der letzten Jahre in einer Vielzahl von internen Projekten sowie Kooperationen mit externen Arbeitsgruppen eingesetzt.

3.2 Energetik – ^{31}P-MR-Spektroskopie

3.2.1 Perfundiertes Mäuseherz

Damit das Herz regelmäßig schlagen kann, muß sein Energiehaushalt zuverlässig reguliert sein. Der wichtigste Energieträger im Körper und auch für das Herz ist das ATP, dessen Strukturformel in Abbildung 3.2 wiedergegeben ist. Dieses Molekül ist mittels ^{31}P-MR-Spektroskopie ausgezeichnet zu detektieren – wie klar zu erkennen, liefert jedes der drei Phosphoratome ein separates Signal.

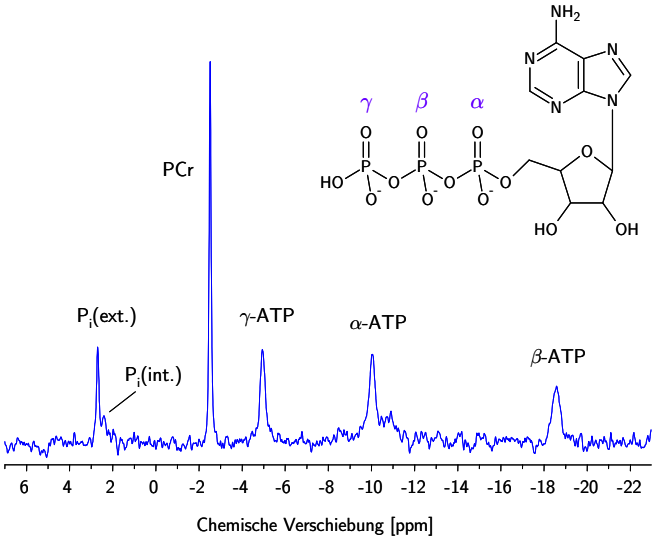

Abbildung 3.2: ^{31}P-MR-Spektrum des perfundierten Mäuseherzens.

Zusätzlich lassen sich im Spektrum des isoliert perfundierten Mäuseherzens noch Signale für PCr sowie für das intra- und extrazelluläre anorganische Phosphat (markiert mit P_i(int.) beziehungsweise P_i(ext.)) zuordnen. Speziell die Lage der letzten beiden Signale im Spektrum ist extrem stark vom pH-Wert der Umgebung abhängig, was genutzt werden kann, um sowohl den extra- als auch den intrazellulären pH (pH_e beziehungsweise pH_i) zu berechnen.

Unter Verwendung der folgenden Beziehung ergibt sich der pH-Wert aus der Differenz der chemischen Verschiebung für das PCr- und das P_i-Signal im ^{31}P-MR-Spektrum (δ in ppm).

$$pH = 6.78 + \log \frac{\delta - 3.29}{5.68 - \delta}$$

Lange Zeit glaubte man, daß nur die Höhe der ATP-Konzentration entscheidend für den Antrieb der energieverbrauchenden zellulären Prozesse sei. Mittlerweile ist jedoch gesichert, daß nicht alleine die ATP-Menge sondern vor allem das Verhältnis von ATP zu seinen Abbauprodukten ADP und P_i maßgebend für die aus der ATP-Hydrolyse (ATP $\leftrightarrow$ ADP + P_i) gewonnenen Energie ist. Die intrazelluläre ADP-Konzentration läßt sich aus dem ^{31}P-MR-Spektrum des Herzens über das Creatinkinase-Gleichgewicht (PCr + ADP $\leftrightarrow$ ATP + Cr) ermitteln.

$$[ADP] = \frac{[ATP] \cdot [Cr]}{[PCr] \cdot [H^+] \cdot K_{obs}}$$

K_{obs} ist die unter Standardbedingungen (37 °C, $[Mg^{2+}] = 1$ mM) beobachtete Gleichgewichtskonstante für die Creatinkinase mit $log\ K_{obs} = 0.87 \cdot pH + 8.31$. Die zur Berechnung benötigte Creatinkonzentration ergibt sich aus dem Gesamtcreatinpool wie folgt $[Cr] = [Cr]_{total} - [PCr]$. Unter Normalbedingungen sind die ADP-Spiegel etwa zwei Größenordnungen niedriger als der ATP-Gehalt ($\approx 30\ \mu$M ADP gegenüber ≈ 6 mM ATP). Setzt man die so ermittelten Werte für pH und $[ADP]$ in folgende Gleichung ein, so erhält man die freie Energie der ATP-Hydrolyse ΔG_{ATP}.

$$\Delta G_{ATP} = \Delta G^0_{ATP(obs)} + R \cdot T \cdot \ln \frac{[ADP] \cdot [P_i]}{[ATP]}$$

$\Delta G^0_{ATP(obs)}$ entspricht der freien Energie der ATP-Hydrolyse unter Standardbedingungen und beträgt $-30.5\ kJ/mol$; T ist die Temperatur in Kelvin und R die allgemeine Gaskonstante (8.314 $J \cdot mol^{-1} \cdot K^{-1}$). Somit ist mit Hilfe der ^{31}P-MR-Spektroskopie die kontinuierliche und nichtinvasive Messung aller Größen, die zur Beurteilung der dem Herzen zu Verfügung stehenden Energie notwendig sind, möglich.

3.2.2 Herzenergetik *in vivo*

Wie im vorigen Abschnitt beschrieben, wurden ^{31}P-MRS-Untersuchungen zur Herzenergetik lange Zeit ausschließlich *ex vivo* an isoliert perfundierten Mäuseherzen durchgeführt (vergleiche ebenso [63, 64]). Diese Untersuchungen haben den offensichtlichen Nachteil, daß sie zum einen nicht unter absolut physiologischen Bedingungen durchgeführt werden und zum anderen *per se* auf Endpunktstudien beschränkt sind. Somit sind keine wiederholten Messungen am selben Objekt möglich, wie sie vor allem wünschenswert wären, um Veränderungen im Energiestatus während eines Krankheitsverlaufs beziehungsweise einer eingeleiteten Behandlung zu verfolgen.

Die Hauptschwierigkeit gegenüber der *ex vivo* Methode, bei der die ^{31}P-MR-Spektren über das gesamte sensitive Volumen aufgenommen werden, besteht darin, eine exakte Lokalisation der Spektren im Herzen zu gewährleisten und eine Kontamination von Signalen aus benachbartem Gewebe zu vermeiden, was insbesondere an dem extrem kleinen und schnell schlagenden Herzen der Maus eine große Herausforderung darstellt. Daher konnte diese Technik zur Untersuchung des Mäuseherzens bisher weltweit nur an zwei Laboratorien unter Zuhilfenahme von ^{31}P-Oberflächenspulen etabliert werden [57,58]. Aufgrund der relativ kleinen Feldstärke der verwendeten Magneten erhielten diese Gruppen allerdings lediglich Spektren mit einer geringen räumlichen Auflösung (Omerovic: 2.35 T, ganzes Herz [58]; Chacko: 4.7 T, Profil der Vorderwand [57]), was Messungen der energiereichen Phosphate in unterschiedlichen Arealen des Herzens unmöglich machte.

Im Unterschied zu den bislang beschriebenen Verfahren bot sich bei unserer Hardware (9.4 T sowie ^{1}H/^{13}P-Resonatoren) die Etablierung einer „echten" zweidimensionalen Methode mittels ^{31}P *Chemical Shift Imaging* (2D-^{31}P-CSI) an. Hierfür „überzieht" man den Brustkorb der Maus mit einem spektroskopischen Gitter, das exakt mit dem anatomischen ^{1}H-MR-Bild korreliert. Abbildung 3.3 zeigt exemplarisch die Überlagerung eines solchen 2D-^{31}P-CSI-Datensatzes und des entsprechenden Protonenbildes. Trotz der geringen Auflösung der Abbildung läßt sich klar erkennen, daß nur da, wo sich Gewebe befindet, ^{31}P-Signale detektiert werden können. Besonders intensive Signale finden sich in der Skelettmuskulatur des Rückens (im oberen Bereich der Abbildung) und in der Herzgegend, während im Bereich der Lungen aufgrund der geringen Dichte dieses Gewebes erwartungsgemäß nur wenig Signal detektiert wird.

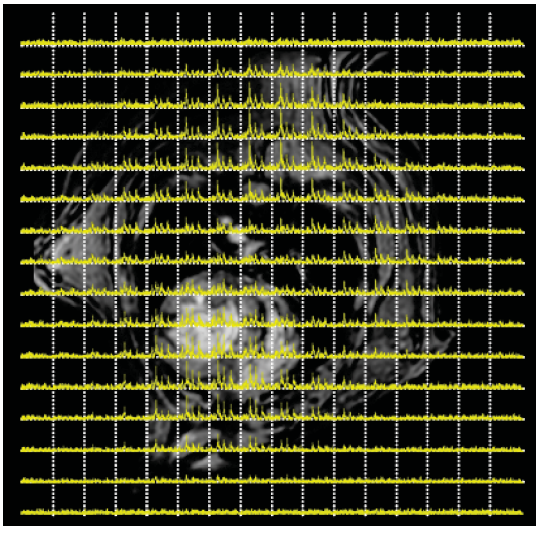

Abbildung 3.3: Überlagerung von ^{1}H-MR-Bild und ^{31}P-MR-Spektren (gelb). Für jedes Voxel aus der 16×16-Matrix (weiß gepunktet) erhält man ein individuelles Spektrum.

Dies läßt sich anhand einer detaillierteren Darstellung noch besser nachvollziehen. Abbildung 3.4 zeigt einzelne, aus der Matrix des 2D-CSI-Datensatzes extrahierte ^{31}P-MR-Spektren in Korrelation zum anatomischen ^{1}H-MR-Bild. Die ortsaufgelösten Spektren der freien, linksventrikulären Wand (#1 → Hinterwand, #2 + #3 → Seitenwand, #4 + #5 → Vorderwand) ähneln stark dem

^{31}P-MR-Spektrum des isoliert perfundierten Herzens (vergleiche Abbildung 3.2). Demgegenüber zeigen die Spektren aus dem Bereich des Septums (#6) in der Regel starke Kontaminationen mit ^{31}P-Signalen aus dem Blut, was sich nicht nur in Form des zusätzlichen Signals von 2,3-Diphosphoglycerat (DPG) bemerkbar macht, sondern auch in einer scheinbaren Reduktion des PCr/ATP-Verhältnisses. Im Spektrum aus der Skelettmuskulatur des Rückens (#8) läßt sich deutlich der im Vergleich zum Herzen höhere PCr-Gehalt erkennen, während man von der Lunge (#7) kaum Signal erhält.

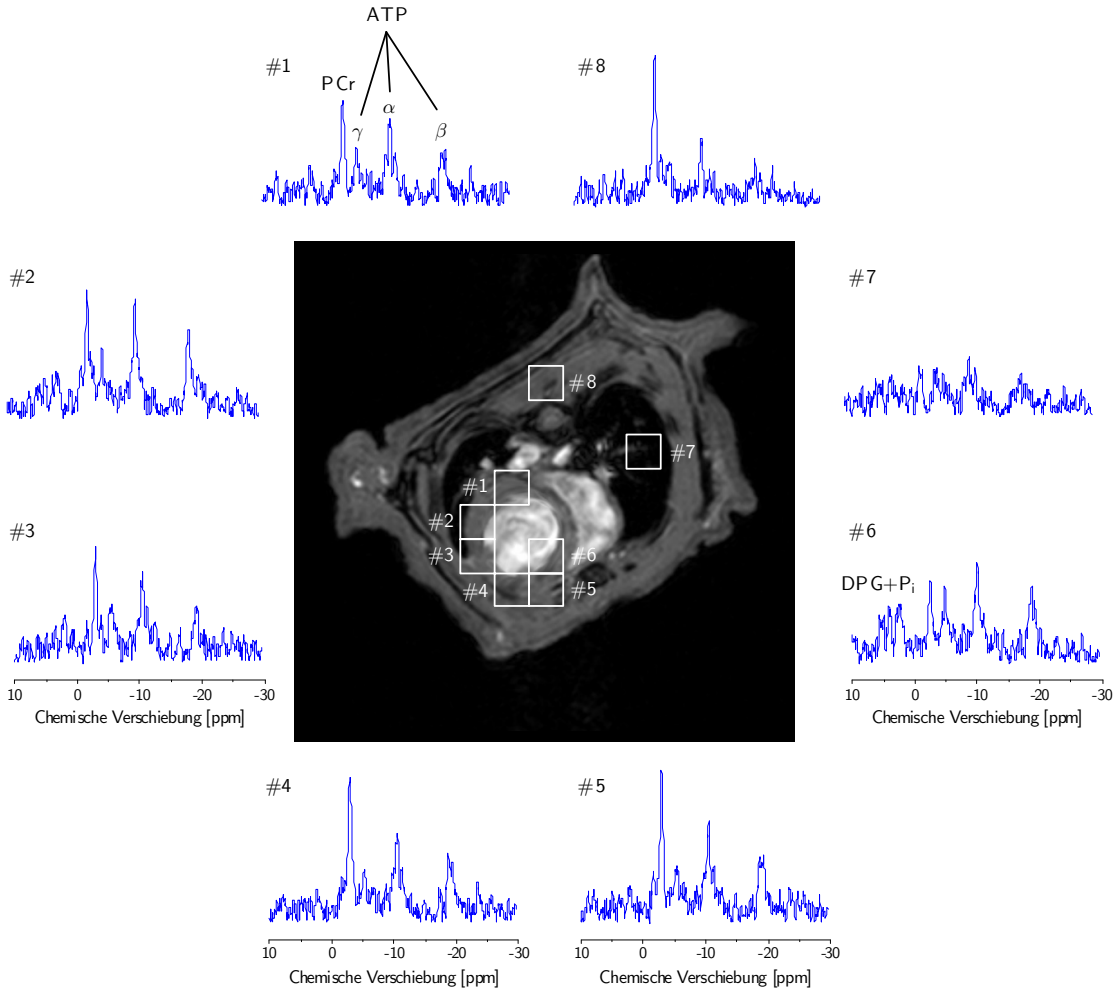

Abbildung 3.4: Repräsentative ^{31}P-MR-Spektren von ausgewählten Voxeln aus dem Mäusethorax in Bezug zum anatomischen ^{1}H-MR-Bild (DPG, 2,3-Diphosphoglycerat).

3.3 Substratmetabolismus – ^{13}C-MR-Spektroskopie

Zur Bereitstellung der für die regelmäßige Herzarbeit notwendigen Energie ist eine ständige Neusynthese des verbrauchten ATPs notwendig. Hierzu werden hauptsächlich Zucker und Fettsäuren verbrannt, wobei ein gesundes Herz normalerweise etwa zu einem Drittel Glucose und zu zwei Dritteln Fettsäuren zur Energieproduktion nutzt. Allerdings kommt es bei einigen Herzerkrankungen – insbesondere bei einer Hypertrophie infolge von dauerhaft erhöher Belastung – zu einer Verschiebung dieses Verhältnisses und zu einer verstärkten Verstoffwechselung von Glucose. Ob solche Veränderungen im Substratstoffwechsel vorliegen, läßt sich experimentell sehr elegant durch

eine Isotopomerenanalyse mittels ^{13}C-MR-Spektroskopie ermitteln, wobei man sich die Kopplungsmuster benachbarter ^{13}C-Atome zunutze macht. Das Prinzip dieser Methode ist in Abbildung 3.5 schematisch dargestellt und soll nachfolgend kurz erläutert werden.

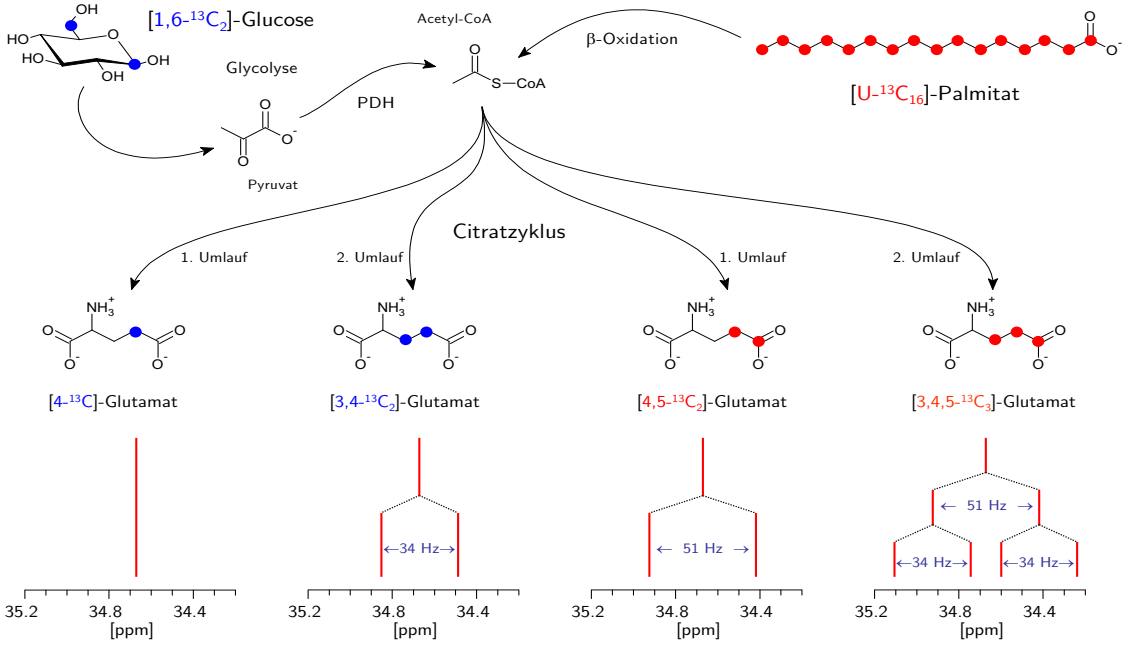

Abbildung 3.5: Substratstoffwechsel und daraus resultierende Glutamat-C4-Kopplungsmuster im ^{13}C-MR-Spektrum: Monomarkierung ergibt ein Singulett (S), Doppelmarkierung ein Dublett (D) und eine Tripelmarkierung ein Dublett von Dublett beziehungsweise ein Quartett (Q). Die unterschiedlichen Kopplungskonstanten J lassen eine Unterscheidung der Doppelmarkierungen an den Kohlenstoffen C3+C4 (J_{34}=34 Hz) beziehungsweise an C4+C5 (J_{45}=51 Hz) zu.

Zur Analyse der Stoffwechselflüsse führt man dem Herzen Substrate zur Verbrennung zu, bei denen an geeigneten Stellen im Molekül das normale Kohlenstoffisotop ^{12}C durch das natürlich nur zu etwa 1% vorkommende Isotop ^{13}C (vergleiche auch Tabelle 1.1) ersetzt ist. Im Gegensatz zu ^{14}C ist ^{13}C ein stabiles Isotop und daher nicht radioaktiv. In Abbildung 3.5 sind die ausgetauschten Atome für Glucose blau beziehungsweise für Palmitat rot gekennzeichnet. Durchlaufen diese Substrate die normalen Stoffwechselwege (erst die Glycolyse beziehungsweise β-Oxidation, dann den Citratzyklus) landet die Markierung schließlich – in Abhängigkeit vom Ausgangssubstrat und der Zahl der Umläufe im Citratzyklus – an unterschiedlichen Positionen im Kohlenstoffgerüst des aus dem Citratzyklus ausgeschleusten Glutamats. Da Glutamat (oder alternativ Glutamin) in nahezu jedem Zelltyp in relativ hohen Konzentrationen ($\approx$ 2-4 mM) im Cytosol vorliegt, ist es im Gegensatz zu den gering konzentrierten Zwischenprodukten des Citratzyklus das ideale Reportermolekül für Veränderungen im Substratstoffwechsel.

Die unterschiedlichen Nachbarschaftsverhältnisse der ^{13}C-Kerne am Kohlenstoffatom C4 der entstandenen Glutamatisotopomeren spiegeln sich in eindeutigen Kopplungsmustern im ^{13}C-MR-Spektrum wider (vergleiche Abbildung 3.5): Eine Monomarkierung ergibt ein Singulett (S), eine Doppelmarkierung ein Dublett (D) und eine Tripelmarkierung ein Dublett von Dublett beziehungsweise ein Quartett (Q). Bemerkenswert ist, daß man aufgrund der unterschiedlichen Kopplungskonstanten (abgekürzt mit J) sogar unterscheiden kann, ob die Doppelmarkierung an C3+C4 (J_{34}=34 Hz) oder an C4+C5 (J_{45}=51 Hz) des Glutamats vorliegt.

Damit läßt sich zweifelsfrei feststellen, aus welchem Ausgangssubstrat die einzelnen Isotopomere gebildet worden sind, und eine mögliche Verschiebung im Substratstoffwechsel nachvollziehen. Die Verwendung von [1,6-^{13}C$_2$]-Glucose und [U-^{13}C$_{16}$]-Palmitat gewährleistet daher nicht nur eine ma-

ximale Anreicherung von ^{13}C-Markierung in der Probe sondern auch, daß das in den MR-Spektren beobachtete Kopplungsmuster eine eindeutige Aussage über die Herkunft der ^{13}C-Markierung erlaubt.

Bezieht man in die Auswertung nicht nur die Kopplungsverhältnisse am C4 sondern auch die Gesamtintensitäten der ^{13}C-MR-Signale für C3 und C4 des Glutamats mit ein, so kann über die drei einfachen Zusammenhänge

$$F_{Glucose} = D_{34[C4]} \cdot \frac{C3}{C4} \qquad F_{Palmitat} = Q_{[C4]} \cdot \frac{C3}{C4} \qquad F_{Endogen} = 1 - F_{Glucose} - F_{Palmitat}$$

der Anteil von Glucose ($F_{Glucose}$), Palmitat ($F_{Palmitat}$) sowie von endogenen Substraten wie Aminosäuren oder auch Glycogen ($F_{Endogen}$) am Gesamtsubstratfluß durch den Citratzyklus berechnet werden [65].

III

Ergebnisse und Diskussion

4

Myoglobin

4.1 Allgemeines

Myoglobin (Mb) ist ein kleines, globuläres Hämoprotein (Abbildung 4.1, links) aus 153 Aminosäuren ($M_r \approx 17000$ Da), das bis zu einer Konzentration von 0.5 mM im Cytosol der Skelett- (Typ I und IIa) sowie der Herzmuskulatur vorkommt. Myoglobinhaltige Muskeln sind rot, wie in Abbildung 4.1 (rechts) am Beispiel eines normalen Mäuseherzens (WT = Wildtyp) gezeigt; ist der Myoglobingehalt reduziert, zum Beispiel im Geflügelfleisch, oder fehlt das Myoglobin aufgrund einer genetischen Manipulation vollständig (myo$^{-/-}$, Abbildung 4.1, rechts), erscheinen die Muskelfasern erheblich blasser.

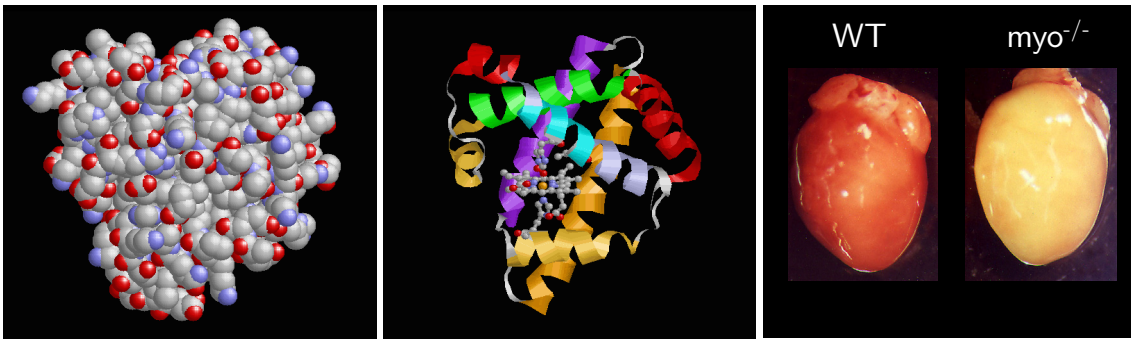

Abbildung 4.1: Myoglobin; (links) globuläre Form, (Mitte) Hämgruppe im Zentrum des Proteins, (rechts) Herzen einer normalen (WT) und einer Myoglobin-defizienten Maus (myo$^{-/-}$).

Ähnlich wie das verwandte Hämoglobin, das den O_2-Transport von der Lunge zu den Zellen bewerkstelligt, bindet das Myoglobin reversibel O_2 – allerdings mit einer sechsfach höheren Affinität als das im Blutkreislauf zirkulierende Hämoglobin. Dadurch kann es den vom Hämoglobin in der Kapillare bereitgestellten O_2 leicht übernehmen (siehe Abbildung 4.2). O_2 bindet an das zentrale Eisenatom der Hämgruppe (in Abbildung 4.1, Mitte, orange markiert; vergleiche auch den nächsten

Abschnitt 4.2). Für das nun gebildete Oxymyoglobin (MbO_2) wurden lange Zeit drei verschiedene Funktionen diskutiert [66]:

- Speicherung von O_2 als Notfallreserve
- Erleichterte O_2-Diffusion – das heißt, daß parallel zu der Diffusion von physikalisch gelöstem O_2 ein Transport von Myoglobin-gebundenem O_2 von der Kapillare zu den Mitochondrien erfolgt (vergleiche Abbildung 4.2)
- Myoglobin-vermittelte oxidative Phosphorylierung

Während die Funktion von Myoglobin als O_2-Reservoir allgemein akzeptiert ist – was insbesondere durch den bis zu zehnfach höheren Myoglobingehalt in Muskeln von tauchenden Säugetieren wie Delphinen und Walen gestützt wird – waren die beiden anderen Funktionen aufgrund der widersprüchlichen Datenlage lange umstritten. Dies lag insbesondere an der Tatsache, daß aus pharmakologischer Sicht nur ein einziger halbwegs spezifischer Inhibitor zur Untersuchung der Funktion von Myoglobin zu Verfügung stand: das extrem giftige Kohlenmonoxid (CO).

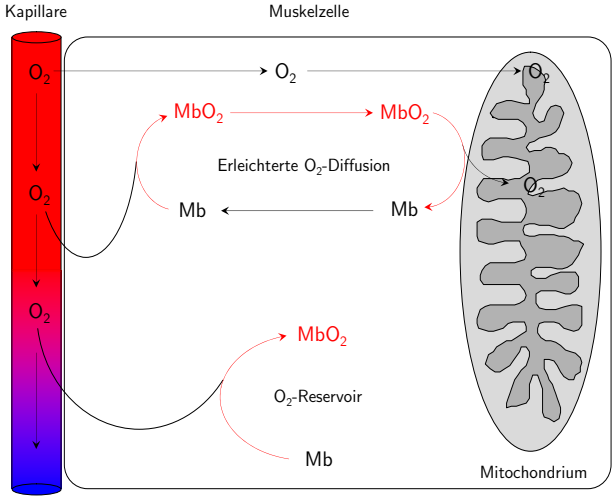

Abbildung 4.2: Funktionen von Myoglobin in der Muskelzelle.

Eine enorme Belebung erfuhr das gesamte Myoglobin-Forschungsgebiet aufgrund der unabhängigen Erzeugung der bereits erwähnten Myoglobinverlustmutanten durch eine amerikanische Arbeitsgruppe [67] und unser Institut [60], da es nun erstmalig möglich war

- die Rolle von Myoglobin ohne pharmakologische Intervention zu untersuchen beziehungsweise
- bei Experimenten mit akuter Inaktivierung von Myoglobin durch CO Mb-defiziente Herzen als adäquate Kontrollen zu verwenden.

Vor allem letztere Option versetzte uns in die Lage, durch vergleichende Experimente mit Myoglobin-defizienten und normalen Wildtyptieren zu zeigen, daß Myoglobin in der Tat eine wichtige Rolle bei der erleichterten O_2-Diffusion im Herzen zukommt, und daß demgegenüber die Myoglobin-vermittelte oxidative Phosphorylierung – wenn überhaupt – nur eine untergeordnete Bedeutung besitzt. Darüber hinaus konnten wir überraschenderweise zwei wichtige neue Funktionen von Myoglobin im Stoffwechsel des Muskels entdecken: Die Sauerstoff-abhängige Modulation der myokardialen NO-Spiegel als auch der effektive Abbau von freien Sauerstoffradikalen (ROS = *Reactive Oxygen Species).*

Die Darstellung der MR-Schlüsselexperimente zu den einzelnen Aspekten und ihre Einordnung in den entsprechenden biologischen Kontext erfolgt in den nächsten Kapiteln. An dieser

Stelle sei bereits vorweggenommen, daß für alle diese Untersuchungen die nichtinvasive ^{1}H-MR-spektroskopische Messung des Myoglobins im Herzen von entscheidender Bedeutung war, so daß zunächst auf diese wenig verbreitete Technik eingegangen werden soll.

4.2 Myoglobinoxygenierung und Valin 68

Die untenstehende Abbildung 4.3 zeigt nochmals im Detail die strukturellen Verhältnisse an der Hämgruppe des Myoglobins. Das zentrale Eisenatom (orange) ist in der Ebene des Porphyrinrings von vier Stickstoffatomen (blau) umgeben. Die untere Koordinationsstelle wird von einem weiteren Stickstoff (des „proximalen" Histidins, His 93 oder F8) besetzt, während die O_2-Bindung oberhalb der Ringebene erfolgt. Die Bindung des O_2 (rot) wird durch eine Wasserstoffbrückenbindung zum „distalen" Histidin (His 64 oder E7) zusätzlich stabilisiert. In unmittelbarer Nachbarschaft dazu erkennt man die beiden Methylgruppen des Valin 68 (oder E11, siehe Pfeil), deren Protonen als Reporterkerne für die aktuelle Situation am Häm genutzt werden können [68, 69].

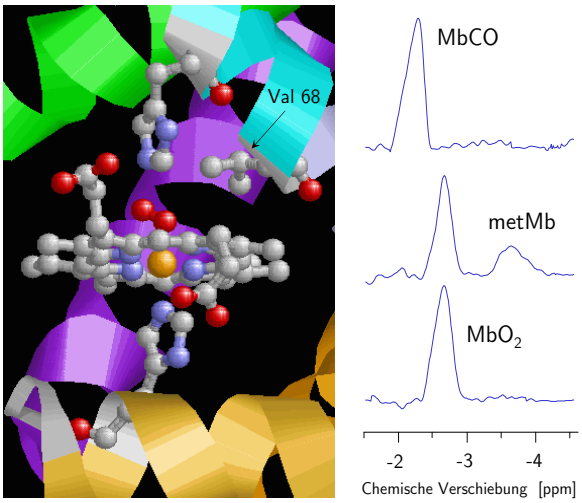

Abbildung 4.3: O_2-Bindung am Häm und ^{1}H-MR-Spektren verschiedener Mb-Spezies.

Bei adäquater O_2-Versorgung des Herzgewebes liegt das Myoglobin infolge seiner hohen O_2-Affinität vollständig oxygeniert vor (MbO_2, siehe auch den vorherigen Abschnitt). In dieser Form erhält man für die Protonen des Valins im ^{1}H-MR-Spektrum des Herzens ein Signal bei -2.7 ppm (untere Spur auf der rechten Seite von Abbildung 4.3).

Das Hauptproblem bei der Detektion dieser Protonen im perfundierten Herzen liegt darin, daß bei der Spektrenakquisition aufgrund der enorm schnellen Relaxation von in Makromolekülen gebundenen Protonen sehr kurze Repetitionszeiten wünschenswert sind, zugleich aber eine effiziente Unterdrückung des Wassersignals notwendig ist, damit dieses nicht die erheblich schwächeren Myoglobinsignale überdeckt ($[H_2O] \approx 50$ M, $[Mb] \approx 0.5$ mM). Da im vorliegenden Fall nur die Signale im Bereich von -2 bis -4 ppm interessieren, kann auf eine zeitraubende Wasserunterdrückung verzichtet werden und stattdessen eine selektive Anregung dieses Areals mittels einer modifizierten $1\bar{3}3\bar{1}$-Sequenz durchgeführt werden, die eine Repetitionszeit von weniger als 50 ms erlaubt (vergleiche OA1 und [70] für experimentelle Details). Wie aus Abbildung 4.3 hervorgeht, ließen sich hiermit die ersten MbO_2-Spektren vom Mäuseherzen in ausgezeichneter Qualität gewinnen.

Wie bereits erwähnt, ist Myoglobin unter normalen Bedingungen vollständig oxygeniert. Nur bei einem Ungleichgewicht zwischen O_2-Angebot und Verbrauch kommt es zu einer Deoxygenierung des Myoglobins und somit zu einer Abnahme in der Intensität des MbO_2-Signals. Insofern läßt sich aus der Stärke (dem Integral) dieses Signals auf den aktuellen Stand der myokardialen O_2-Versorgung schließen. Über einen einfachen mathematischen Zusammenhang (siehe nächsten Abschnitt) kann

man daraus auch den intrazellulären O_2-Partialdruck (PO_2) der Herzmuskelzellen berechnen – eine Größe, die mit anderen Methoden nur sehr schwer zugänglich ist.

Der Oxygenierungsgrad ist jedoch nicht der einzige Parameter, der das Signal für die Protonen des Valins im ^{1}H-MR-Spektrum beeinflußt. Ganz allgemein führen Veränderungen an der chemischen beziehungsweise elektronischen Situation am Häm zu Änderungen von Intensität und Lage dieses Signals. Verdrängt zum Beispiel das giftige CO aufgrund seiner höheren Affinität zum Eisen den gebundenen O_2, so spiegelt sich das entstehende MbCO im Spektrum durch eine Verschiebung des Signal hin zu -2.3 ppm wider (Abbildung 4.3, obere Spur). Neben einem Ligandenaustausch beeinflußt auch der Oxidationsstatus des Eisens das Protonensignal des Valins: Verliert das Eisen im Myoglobin beispielsweise ein Elektron und geht vom normalerweise zweiwertigen in den dreiwertigen Zustand – üblicherweise als Metmyoglobin (metMb) bezeichnet – über, so läßt sich der Anteil des gebildeten metMb anhand seines Signals bei -3.8 ppm [71, 72] eindeutig bestimmen (Abbildung 4.3, mittlere Spur; vergleiche auch Abschnitt 4.4 über Myoglobin und Stickstoffmonoxid).

Insgesamt lassen sich also über die ^{1}H-MR-spektroskopisch detektierbaren Reporterprotonen des Valins vielfältige Informationen über die Situation an der Hämgruppe des Myoglobins gewinnen (Oxygenierung, Ligandenbindung, Redoxstatus), die wiederum den aktuellen metabolischen Zustand des Herzens reflektieren.

4.3 Dissoziationskurve von MbO_2 im Mäuseherzen

Voraussetzung für die in Abschnitt 4.1 beschriebene erleichterte O_2-Diffusion durch Mb ist eine zumindest teilweise O_2-Entsättigung. Während im menschlichen Skelettmuskel eine Myoglobin-Entsättigung bei Arbeit eindeutig mittels ^{1}H-MRS nachgewiesen wurde [73], ist die Situation am Herzen mit seiner ausgeprägten Kapillarisierung jedoch weniger klar. Ein Sättigungsgrad des Myoglobins von 92 % [74] weist jedoch darauf hin, daß auch am Herzen O_2-Gradienten bestehen, die eine Beteiligung der erleichterten Diffusion an der Gesamt-O_2-Versorgung des Myokards erfordern.

Um nun im isolierten Herzen die entsprechenden Bedingungen nachzustellen, die der O_2-Entsättigung von Myoglobin in der *in vivo* Situation möglichst nahe kommen, wurde das Sauerstoffangebot im Perfusionsmedium sukzessive gesenkt und gleichzeitig der Oxygenierungsgrad des Myoglobins mittels ^{1}H-MR-Spektroskopie gemessen. Durch Äquilibrierung des Perfusionsmediums mit Gasgemischen, die einen O_2-Gehalt von 95-12% aufwiesen, wurde hierfür ein definierter arterieller PO_2 eingestellt und aus dem Dissoziationsgleichgewicht von MbO_2 der entsprechende PO_2 im Herzmuskel berechnet:

$$MbO_2 \rightleftharpoons Mb + O_2 \quad \Longrightarrow \quad PO_2 = \frac{[MbO_2]}{[Mb]_{total} - [MbO_2]} \cdot P_{50}$$

Hierbei entspricht P_{50} dem PO_2, bei dem ein Protein zu 50% mit Sauerstoff gesättigt ist; zur Berechnung der unten dargestellten Ergebnisse wurde für Myoglobin der Literaturwert von 2 mmHg zugrunde gelegt [75]. Aus diesen Messungen konnte dann die Dissoziationskurve für das cytosolische MbO_2 sowie der intrazelluläre PO_2 im schlagenden Mäuseherzen in Abhängigkeit vom O_2-Gehalt des Perfusionspuffers abgeleitet werden.

Wie aus Abbildung 4.4 hervorgeht, beginnt die O_2-Entsättigung des Myoglobin in dem von uns untersuchten Modell bei einem arteriellen O_2-Gehalt von 65%. Dabei entspricht der Betrag der Entsättigung (circa 10%) in etwa der Größenordnung, die auch *in vivo* beobachtet wurde (siehe oben). Bei diesen Bedingungen ergibt sich ein intrazellulärer PO_2 von $\approx$ 16 mmHg, der erwartungsgemäß steil abfällt, wenn der O_2-Gehalt im Perfusionspuffer weiter gesenkt wird.

Nachdem aus diesen Experimenten definiert werden konnte, wann die Entsättigung des MbO_2 im Mäuseherzen einsetzt, wurden bei genau diesen Bedingungen (65% O_2 im Puffer) die Auswirkungen einer akuten und vollständigen Hemmung der O_2-Bindungseigenschaften von Myoglobin durch CO untersucht (vergleiche die Abbildungen 4.3 und 4.4). Als Kontrollen wurden hierbei Myoglobin-defiziente ($myo^{-/-}$) Herzen eingesetzt, um sicherzustellen, daß bei den gewählten Bedingungen die Anwesenheit von 20% CO im Perfusionspuffer keinen Einfluß auf die Atmungskette

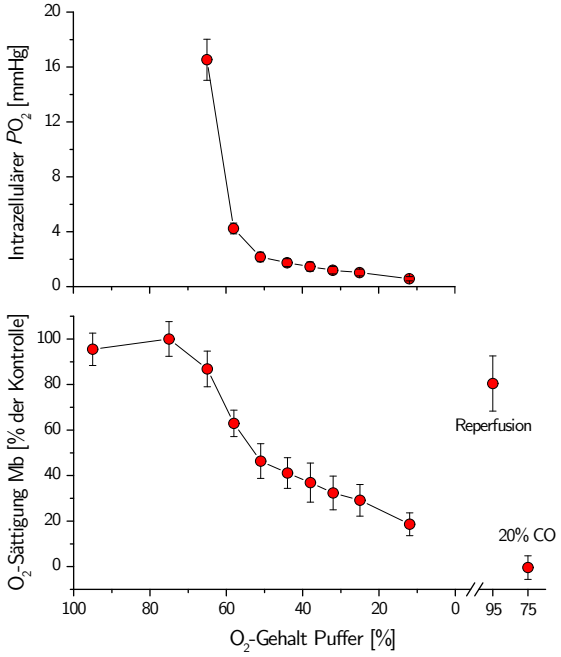

Abbildung 4.4: O_2-Sättigung von Mb im Mäuseherz in Abhängigkeit vom O_2-Angebot.

und kardiale Funktion besitzt. Im Gegensatz zu dieser negativ-Kontrolle kam es in Wildtypherzen mit normalem Myoglobingehalt zu einer signifikanten Einschränkung von O_2-Verbrauch und linksventrikulärer Pumpfunktion [70].

In derselben Arbeit wurde auch die PO_2-Abhängigkeit des Sauerstoffverbrauchs (VO_2) isolierter Kardiomyozyten aus myo$^{-/-}$-Mäusen untersucht. Es zeigte sich, daß der VO_2 Myoglobin-freier Kardiomyozyten bei einem PO_2 kleiner als 15 mmHg ($\rightarrow$ einsetzende MbO_2-Entsättigung, siehe Abbildung 4.4) immer niedriger war als in Wildtyp-Kontrollen. Zusammengenommen belegen diese Daten, daß Myoglobin wesentlich zum O_2-Transport, höchstwahrscheinlich durch erleichterte Diffusion, beiträgt.

4.4 Interaktion von Myoglobin und NO im Herzen

Über die O_2-bindenden Eigenschaften von Myoglobin hinaus war auch schon lange bekannt, daß MbO_2 – ganz ähnlich wie die oxygenierte Form von Hämoglobin – die Fähigkeit besitzt, das biologisch wichtige Signalmolekül Stickstoffmonoxid (NO) zu Nitrat zu inaktivieren [76], und wurde aus diesem Grund in vielen biochemischen und physiologischen Experimenten als NO-Fänger eingesetzt [77]. Bereits in der 80er Jahren konnte im Reagenzglas gezeigt werden [78], daß die Reaktion

$$MbO_2 + NO \rightarrow metMb + NO_3^- \qquad\qquad K = 3.7 \cdot 10^7\ M^{-1} \cdot s^{-1}$$

enorm schnell und effizient abläuft. Unklar blieb jedoch, inwieweit diese *in vitro* Befunde auf die *in vivo* Situation übertragbar sind und ob diese Reaktion für die NO-Homöostase im Herzen physiologische Relevanz besitzt.

Durch die Etablierung der unter 4.2 beschriebenen Meßtechnik war nun erstmals die Gelegenheit gegeben, diese Reaktion im schlagenden Herzen zu verfolgen und durch Vergleich mit Myoglobin-defizienten Herzen als negativ-Kontrolle auf ihre biologische Bedeutsamkeit zu untersuchen. Hierfür wurde zunächst die endogene NO-Freisetzung im Herzen durch intrakoronare Infusion des potenten Vasodilatators Bradykinin maximal stimuliert und gleichzeitig die Veränderungen im ^{1}H-MR-Spektrum beobachtet.

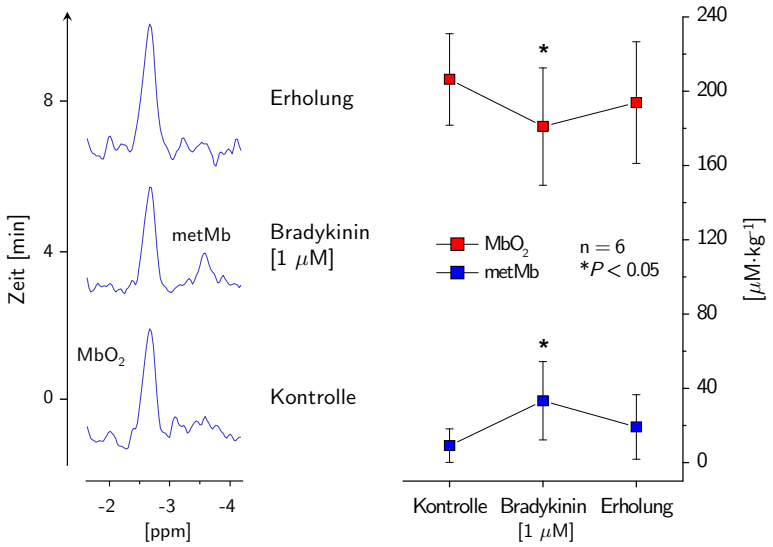

Abbildung 4.5: NO-Freisetzung durch Bradykinin führt zur reversiblen Bildung von metMb.

Wie aus den Spektren auf der linken Seite von Abbildung 4.5 zu entnehmen ist, führte die Stimulation mit Bradykinin zu einer deutlich erkennbaren metMb-Bildung bei gleichzeitiger Abnahme des MbO_2-Signals (mittlere Spur). Dieser Effekt war nach Beendigung der Bradykinin-Infusion rasch umkehrbar (obere Spur). Beim Vergleich der funktionellen Effekte von Bradykinin zeigte sich, daß Herzen ohne Myoglobin erheblich empfindlicher auf die gleiche Bradikinindosis als normale Herzen reagieren: In myo$^{-/-}$-Herzen war zum einen eine stärkere Vasodilatation als in WT-Herzen zu verzeichnen und zum anderen auch eine merkbare Einschränkung der linksventrikulären Druckentwicklung, die im Wildtyp nicht zu beobachten war [OA1].

Zusammengefaßt geben diese ersten Beobachtungen bereits klare Hinweise darauf, daß es bei endogen stimulierter NO-Bildung in der Tat zu einer Umsetzung von NO und MbO_2 unter Bildung von metMb kommt und daß beim Fehlen dieser Reaktion eine gesteigerte NO-Freisetzung kardiodepressive Auswirkungen nach sich ziehen kann. Zur Erhärtung dieses Anfangsverdachts wurden in weiteren Experimenten authentische NO-Lösungen infundiert, um die Interaktion von NO und Mb unter genau definierten Bedingungen untersuchen zu können. Da bekannt ist, daß NO mit O_2 um die Bindungsstellen an den Cytochromen der Atmungskette konkurrieren kann [79], lag es nahe, bei diesen Versuchen neben den Veränderungen am Myoglobin und der Herzfunktion zusätzlich die Auswirkungen auf die kardiale Energetik zu erfassen, um Einblick in die den beobachteten Effekten zugrunde liegenden Mechanismen zu erhalten.

4.5 MbO_2 und NO: Auswirkungen auf den Energiestatus

Wie oben angedeutet, sollten zur weiterführenden Untersuchung der Interaktion von NO und Mb authentische NO-Lösungen infundiert werden, um unter exakt vorgegebenen Bedingungen die Auswirkungen auf kardiale Energetik und Myoglobinstoffwechsel zu dokumentieren. Angesichts der Instabilität der frisch hergestellten NO-Lösungen lag die Hauptherausforderung bei diesen Experimenten darin, die Kontaktzeit der Lösungen mit dem oxygenierten Perfusionspuffer zu minimieren und sie möglichst direkt ins Koronarsystem des im Magneten befindlichen Herzens zu infundieren. Hierfür wurden definiert konzentrierte NO-Lösungen über luftdichte *Fused Silica* Kapillaren (⌀ 0.2 mm) innerhalb des normalen Perfusionssystems (⌀ 1 mm) bis direkt vor die Aorta des Versuchsherzens herangeführt.

Abbildung 4.6 zeigt charakteristische ^{1}H- und ^{31}P-MR-Spektren eines Wildtyp-Herzens, dem schrittweise immer größere Konzentrationen von NO über die Koronargefäße appliziert wurden. Aus den unteren beiden Spuren ist ersichtlich, daß NO-Mengen bis zu 1 μM keinerlei Auswirkungen

auf die Oxygenierung des Myoglobins beziehungsweise auf den Energiestatus des Herzens haben. Steigert man jedoch die infundierte NO-Menge, kommt es ≥ 2.5 μM zu einem Abfall des MbO_2-Signals bei -2.7 ppm. Gleichzeitig läßt sich ein zusätzliches Signal bei -3.8 ppm detektieren, daß zweifelsfrei metMb zugeordnet werden kann (siehe auch Kapitel 4.2 und 4.4).

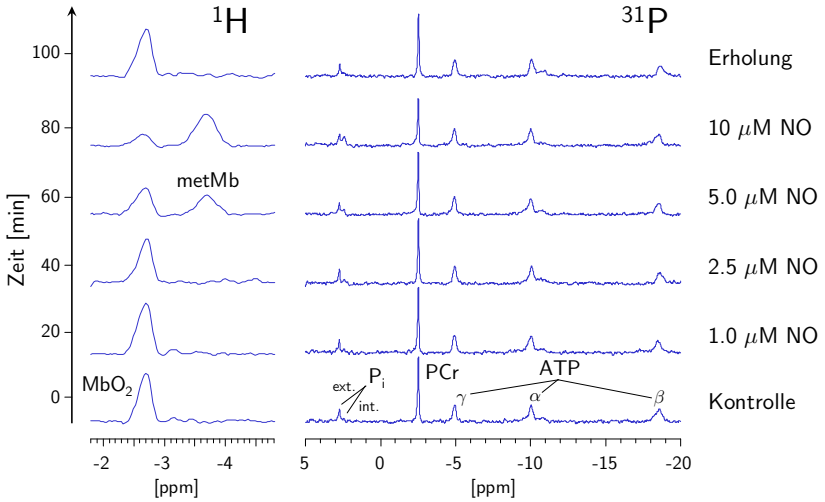

Abbildung 4.6: Auswirkungen steigender NO-Spiegel auf Myoglobin und Energiestatus.

Erhöht man die NO-Konzentration noch weiter, wird das MbO_2 nahezu vollständig in metMb überführt. Diese Reaktion ist jedoch nach Beendigung der NO-Infusion reversibel (oberste Spur), was die rasche Regenerierung des MbO_2 durch die metMb-Reduktase widerspiegelt (siehe nächsten Abschnitt). Bemerkenswert ist, daß die Umwandlung von MbO_2 in metMb bereits bei NO-Mengen nachweisbar ist, bei denen in den ^{31}P-MR-Spektren noch keinerlei Anzeichen für eine Beeinträchtigung des Energiestatus bemerkbar sind.

Vergleicht man in einem weiteren Experiment die dosisabhängigen Effekte von NO auf die Funktion und Energetik von WT- beziehungsweise Myoglobin-defizienten Herzen, so erkennt man, daß genau in dem Konzentrationsbereich, in dem im WT die Umwandlung von MbO_2 in metMb erfolgt, myo$^{-/-}$-Herzen empfindlicher auf gleiche Mengen infundierten NOs reagieren [OA1]. Dies spiegelt sich sowohl in einer stärkeren Einschränkung der linksventrikulären Druckentwicklung als auch des Energiestatus (verminderte PCr- und erhöhte ADP-Spiegel) wider [OA1].

Wie bereits im vorherigen Abschnitt beschrieben, führt das Fehlen des Myoglobins nicht nur zu einer erhöhten Sensitivität des Herzens auf die exogene Gabe von NO sondern auch auf die endogene Stimulation der endothelialen NO-Synthase (eNOS) mittels Bradykinin. Zusammengenommen legen diese am isolierten Herzen erhaltenen Befunde bereits den Schluß nahe, daß es in Gegenwart von Myoglobin offenbar zu einer substantiellen Inaktivierung freigesetzten NOs kommt.

4.6 Schutz vor erhöhter iNOS-Aktivität durch MbO_2

In weiteren *in vitro* Experimenten konnten wir zeigen, daß die Gegenwart von Myoglobin dem Herzen selbst gegen permanent erhöhte NO-Spiegel aufgrund einer massiven Überexpression der induzierbaren NO-Synthase (iNOS) ausgezeichneten Schutz bietet. Erst unter pharmakologischer Inhibition des Myoglobins mit CO hatte die gesteigerte iNOS-Aktivität eine eingeschränkte Herzfunktion und -energetik zur Folge [80]. Da die Myoglobin-Hemmung mittels CO notwendigerweise auf akute Untersuchungen am perfundierten Herzen beschränkt war, blieb zunächst unklar, welche Langzeitauswirkungen *in vivo* dies mit sich führt. Die offen gebliebenen Fragen konnten schließlich mithilfe eines genetischen Ansatzes beantwortet werden: Die Überexpression der iNOS in einen Myoglobin-freien Hintergrund (tg-iNOS$^+ \infty$ myo$^{-/-}$).

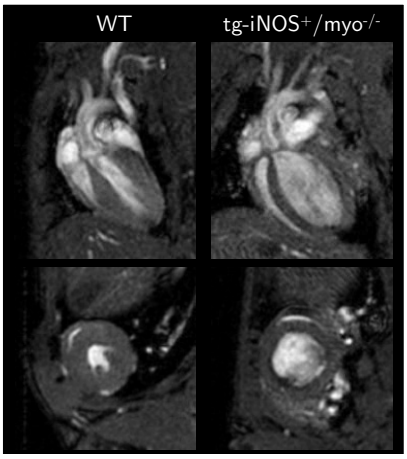

Abbildung 4.7: Endsystolische Bilder einer normalen und einer doppelt-transgenen Maus mit kardiospezifischer iNOS-Überexpression (tg-iNOS^{+}) und gleichzeitiger Myoglobindefizienz.

Abbildung 4.7 zeigt die fatalen Auswirkungen dieses Kreuzungsexperiments anhand endsystolischer ^{1}H-MR-Bilder. Im Vergleich zu normalen WT-Tieren (links) zeigen die Herzen der doppelttransgenen Tiere (rechts) ein massiv erhöhtes endsystolisches Volumen, was eine stark reduzierte Ejektionsfraktion zur Folge hat. Gleichzeitig läßt sich in den coronalen (oben) wie auch in den axialen Schnitten (unten) eine drastisch verringerte systolische Wandverdickung und ein „Ausleiern" des linken Ventrikels erkennen, was alles Anzeichen einer beginnenden Herzinsuffizienz sind. Die detaillierte funktionelle Analyse zeigte, daß die Doppelmutante (tg-iNOS^{+}/myo$^{-/-}$) in der Tat durch das Auftreten einer schweren linksventrikulären Hypertrophie mit anschließender Dilatation gekennzeichnet ist [81].

Dies ist auch nochmals aus den anatomischen Referenzbildern zur energetischen Untersuchung mittels 2D-^{31}P-CSI ersichtlich (Abbildung 4.8), in denen das enddiastolische Volumen der transgenen Maus (rechts) erheblich größer als in der Kontrollmaus (links) ist. Die parallel aufgenommenen ^{31}P-MR-Spektren machen deutlich, daß die kardiale Dysfunktion in der Mutante mit beträchtlich niedrigeren PCr-Spiegeln im Vergleich zum WT einhergeht, was eine limitierte Verfügbarkeit dieses „energetischen Puffers" widerspiegelt (vergleiche Abschnitt 3.2) Dies ist in Abbildung 4.8 anhand repräsentativer Spektren vom Septum (#1) und der Vorderwand (#2) dargestellt. Selbst aus den

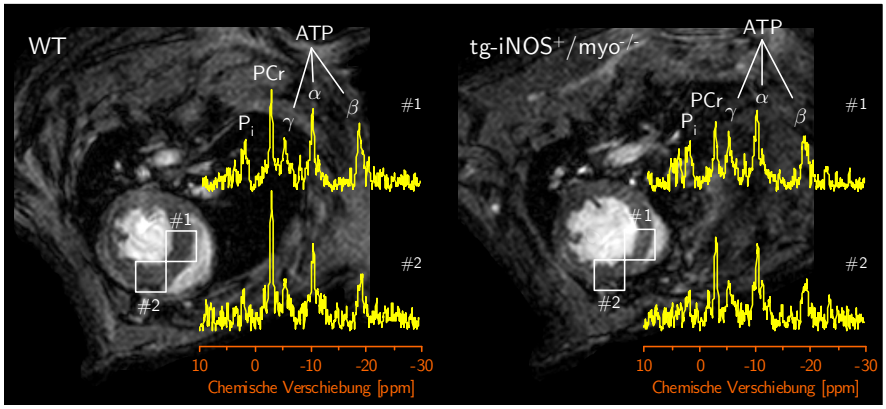

Abbildung 4.8: ^{31}P-MR-Spektren aus Herzseptum (1) und -vorderwand (2) einer Wildtyp- (links) beziehungsweise einer tg-iNOS^{+}/myo$^{-/-}$-Maus.

im Septum gelegenen Voxeln läßt sich trotz der Kontamination mit Signalen aus dem Kammerblut (↬ DPG; vergleiche Abbildung 3.4, #6) eindeutig der reduzierte PCr-Gehalt im Fall der tg-iNOS$^+$/myo$^{-/-}$-Maus erkennen. Eine Überprüfung der am lebenden Tier erhobenen Daten zum Energiestatus anhand hochaufgelöster ^{31}P-MR-Spektroskopie an Gewebextrakten nach Organentnahme lieferte eine ausgezeichnete Übereinstimmung mit den zuvor erhaltenen Ergebnissen (vergleiche OA4).

Diese Daten untermauern nochmals die Bedeutung und die Effizienz von Myoglobin beim Schutz von überschüssigem NO. Zudem liefern sie erstmals einen Beleg am Ganztier dafür, daß beim Fehlen eines wirkungsvollen „NO-Staubsaugers" (siehe unten) von der iNOS gebildetes NO tatsächlich in kritischer Weise mit der Atmungskette interferieren kann, was über die Reduktion des Phosphorylierungspotentials letztlich zu einer Beeinträchtigung der kardialen Energiehomöostase führt [82]. Dieser Effekt ist spezifisch für die doppelt-transgene tg-iNOS$^+$/myo$^{-/-}$-Maus, da frühere Untersuchungen an tg-iNOS$^+$-, myo$^{-/-}$- oder heterocygoten tg-iNOS$^+$/myo$^{+/-}$ -Mäusen keinerlei Anhaltspunkte für eine eingeschränkte Herzfunktion ergeben haben [80, 81, 83]. Der Herzinsuffizienz-Phänotyp der Doppelmutante kann daher eindeutig auf das (vollständige) Fehlen von Myoglobin zurückgeführt werden und ist vermutlich die direkte Konsequenz eines chronisch gestörten Energiestatus'. An dieser Stelle ist bemerkenswert, daß das Ausmaß der hier beobachteten Beeinträchtigung des Energiehaushalts in der gleichen Größenordnung liegt wie die Veränderungen, die beim Menschen während der Entwicklung einer Herzinsuffizienz nachgewiesen wurden [84, 85]. Dies kann daher als weiterer Beleg für die Hypothese dienen, daß Beeinträchtigungen in der kardialen Energieproduktion ausschlaggebende Faktoren bei der Progression von Herzerkrankungen darstellen [86].

Der kardioprotektive Effekt des Myoglobins läßt sich zwanglos mit den bereits lange bekannten chemischen Reaktionen von MbO_2 und NO in Einklang bringen (siehe Abbildung 4.9), die zwar *in vitro* schon ausführlich untersucht worden sind, von denen aber bei weitem nicht klar war, daß sie von physiologischer Relevanz sind. Offensichtlich ist die Reaktion MbO_2 + NO → metMb + Nitrat ein „chemischer Staubsauger", der dafür sorgt, daß selbst bei erhöhter NOS-Aktivität die cytosolischen NO-Spiegel extrem niedrig gehalten und so schädigende Einflüsse der NO-Radikale auf die Atmungskette vermieden werden können.

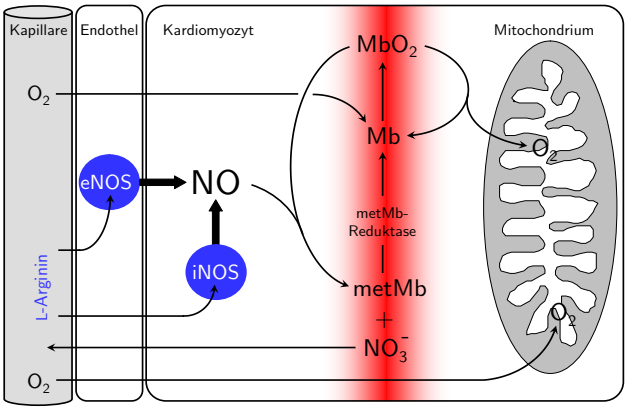

Abbildung 4.9: Inaktivierung von NO durch Myoglobin.

Von entscheidender Bedeutung für die Wirksamkeit dieses Staubsaugers ist die Aktivität der metMb-Reduktase, die dafür sorgt, daß gebildetes metMb wieder in MbO_2 überführt wird und für einen neuen Zyklus zur Verfügung steht (Abbildung 4.9). Diese molekulare *Firewall* arbeitet offenbar so effizient, daß selbst eine massiv gesteigerte NO-Produktion durch eine Überexpression der induzierbaren NO-Synthase neutralisiert werden kann [81, 83].

Erst wenn man parallel dazu durch pharmakologische oder genetische Intervention das Myoglobin ausschaltet, zeigt sich der negative Einfluß permanent erhöhter NO-Mengen, der sich in einer eingeschränkten Funktion und Energetik manifestiert und letztendlich in einer Herzinsuffi-

zienz münden kann [80, 81]. Zusammenfassend läßt sich aus diesen Experimenten ableiten, daß Myoglobin eine zentrale Rolle bei der Inaktivierung von NO zukommt und eine effektive Barriere zum Schutz des Herzens vor nitrosativem Stress bildet. Dies stellt – neben den weiter oben beschriebenen Funktionen wie O_2-Speicher und -Transport – eine neue, bislang im Verborgenen gebliebene physiologische Funktion dieses altbekannten Proteins dar.

4.7 O_2-abhängige NO-Modulation durch Myoglobin

Über die oxidative Inaktivierung hinaus existieren auch noch andere Möglichkeiten, wie Hämoproteine in den NO-Stoffwechsel eingreifen können. Vor einiger Zeit wurde gezeigt, daß deoxygeniertes Hämoglobin auf nichtenzymatischem Wege NO aus Nitrit freisetzen kann [87]. Dieser Prozeß ist allosterisch durch den Umgebungs-PO_2 reguliert und weist beim P_{50} des Hämoglobins maximale Aktivität auf. Da Hämo- und Myoglobin in vielerlei Hinsicht ähnliche chemische Eigenschaften aufweisen und der Gesamtkörpergehalt der beiden Moleküle vergleichbar ist [82], lag es nahe, die Rolle von Myoglobin im Gesamtstoffwechsel von Nitrit zu untersuchen.

In einem ersten Schritt wurde zunächst von der Arbeitsgruppe von Malte Kelm an der RWTH Aachen (jetzt Universitätsklinikum Düsseldorf) gezeigt, daß Myoglobin *in vitro* unter hypoxischen Bedingungen tatsächlich eine relevante Quelle von NO darstellen kann (vergleiche OA5). Anschließend sollte geklärt werden, welche funktionellen Konsequenzen das so gebildete NO auf Muskelkontraktilität und Energiemetabolismus hat. Hierfür wurden die experimentellen Bedingungen anhand der ^{1}H-MR-spektroskopisch erhaltenen O_2-Sättigungskurve (siehe Abschnitt 4.3 sowie Abbildung 4.4) so gewählt, daß – analog zu dem für Hämoglobin beschriebenen Optimum – eine 50%ige O_2-Entsättigung des Myoglobins im perfundierten Herzen gewährleistet war.

Unter diesen Voraussetzungen wurde nun das extrazelluläre Nitritangebot schrittweise erhöht und die Auswirkungen auf hämodynamischer und metabolischer Ebene analysiert, wobei wiederum myo$^{-/-}$-Herzen als adäquate Kontrolle verwendet wurden. Dabei zeigte sich, daß die Gabe von Nitrit ≥ 10 μM nur im WT-Herzen zu einer dosisabhängigen Reduktion der O_2-Extraktion und damit des VO_2 führt (Abbildung 4.10, links). In parallel aufgenommenen ^{31}P-MR-Spektren war zugleich eine Zunahme der myokardialen P_i- und ein Abfall der PCr-Spiegel im Wildtyp erkennbar (Abbildung 4.10, Mitte), was wiederum eine Abnahme der frei verfügbaren Energie ΔG_{ATP} zur Folge hat (vergleiche Abschnitt 3.2.1). Diese Beeinträchtigung des Energiehaushalts wurde im Wildtyp von einer Einschränkung der linksventrikulären Druckentwicklung begleitet – demgegenüber wurden in Myoglobin-defizienten Herzen unter denselben Bedingungen keinerlei Veränderungen in O_2-Verbrauch und Energetik (Abbildung 4.10, rechts) sowie Funktion beobachtet (siehe OA5).

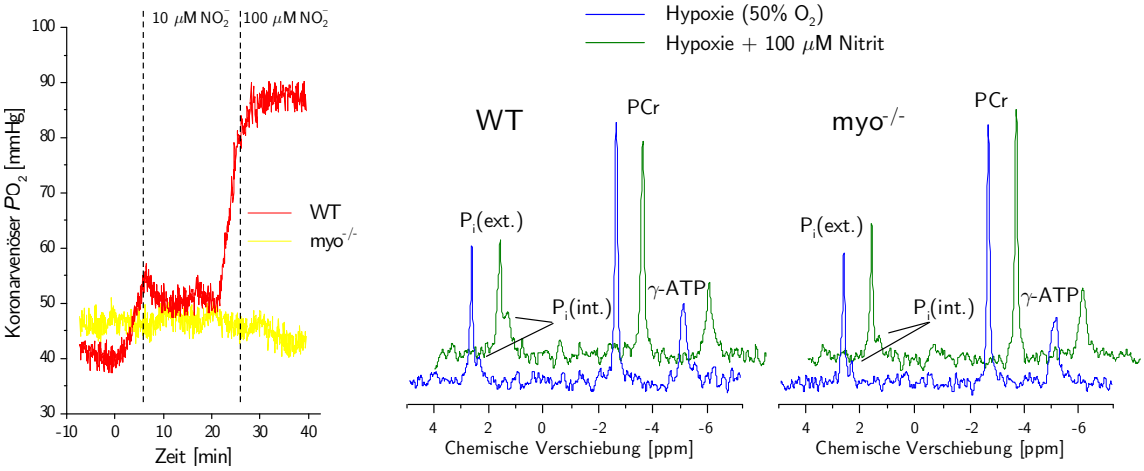

Abbildung 4.10: Einfluß von Nitrit auf Sauerstoffextraktion (links) und Energiestatus in WT- (Mitte) und Myoglobin-defizienten (rechts) Herzen.

Zusammengefaßt belegen diese Ergebnisse, daß Myoglobin unter O_2-Mangel von einem NO-Inaktivator zu einem NO-Produzenten transformieren kann. Das auf diese Weise freigesetzte NO moduliert durch reversible Interaktion mit myocytären Cytochromen den kardialen Energiehaushalt und trägt zu einer Reduktion des VO_2 sowie der Kontraktilität bei.

Dieses Szenario, welches hier im WT-Herzen nach einer Nitritinfusion beobachtet wird, ähnelt auf frappierende Weise dem Phänomen des *Short-term Hibernation* als Folge einer kritischen Einschränkung des koronaren Flusses [88]. Es ist daher denkbar, daß die PO_2-abhängige, nichtenzymatische Bildung von NO durch Reaktion von Mb mit Nitrit hierbei eine wichtige Rolle einnimmt, in dem ein *Mismatch* zwischen O_2-Angebot und -Verbrauch anhand einer fraktionellen Zunahme von deoxygeniertem Mb und der damit verbundenen gesteigerten Nitritreduktase-Aktivität abgelesen wird. Somit könnte Myoglobin als O_2-Sensor fungieren, der über die Freisetzung von NO Muskelenergetik und -funktion an ein limitiertes O_2-Angebot anpaßt (vergleiche [89] für eine ausführliche Diskussion).

4.8 Kardioprotektion durch Myoglobin als Antioxidans

Neben der ausgeprägten Homologie zum Hämoglobin zeigt ein Strukturvergleich von Myoglobin mit anderen Proteinen Ähnlichkeiten zu hämhaltigen Peroxidasen, die vor allem den Bereich der O_2-Bindungstasche betreffen. Bereits Mitte des letzten Jahrhunderts wurde gezeigt, daß Myoglobin rasch mit H_2O_2 reagiert und enzymatische Aktivität als Peroxidase besitzt [90, 91]. Aus einer Vielzahl von weiteren *in vitro* Untersuchungen geht hervor, daß bei der Reaktion von Myoglobin mit Sauerstoffradikalen oder Peroxiden die Hämgruppe des Proteins zwischen verschiedenen Oxidationsstufen oszillieren kann − auch als *Redoxcycling* von Myoglobin bezeichnet [92]. Dabei kann das zentrale Eisenatom vom normalen zweiwertigen Zustand (Fe^{II}) über Fe^{III} (metMb) bis zum Fe^{IV} oxidiert werden, was in der untenstehenden Abbildung 4.11 mit Mb^{2+}, Mb^{3+} und Mb^{4+} dargestellt ist.

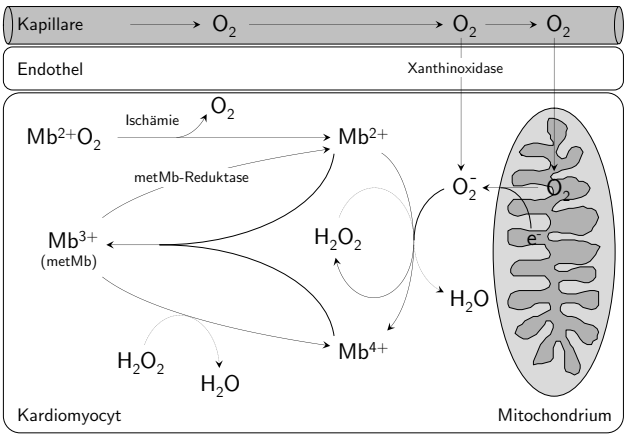

Abbildung 4.11: Interaktion von Myoglobin und reaktiven Sauerstoffspezies.

Trotz zahlreicher Arbeiten zu diesem Thema blieb lange Zeit umstritten, ob diese Redoxreaktionen im intakten Muskel zu einem Nettoabbau von reaktiven Sauerstoffspezies (ROS = *Reactive Oxygen Species*) beitragen oder im Gegenteil über das stark oxidierend wirkende Ferrylderivat (Fe^{IV}) des Myoglobins zur Auslösung abträglicher Kettenreaktionen und zu einer gesteigerten Radikalfreisetzung führen [93]. Auch hier lag der Schlüssel zur Klärung der Frage, welchem der beiden Reaktionspfade im Herzen die größere Bedeutung und damit ob der Interaktion von Myoglobin mit Sauerstoffradikalen eher eine schützende oder schädliche Rolle zukommt, in Experimenten, die auf Myoglobin-defizienten Herzen als negativ-Kontrolle beruhten.

In einer ersten Serie von Untersuchungen zeigte sich, daß Herzen von $myo^{-/-}$-Mäusen deutlich empfindlicher auf die intrakoronare Gabe von ROS (sowohl H_2O_2 als auch Superoxid) reagierten,

dergestalt daß eine erheblich stärkere Beeinträchtigung der Pumpfunktion in der Mutante als im WT zu verzeichnen war [OA2]. Um zu überprüfen, ob dieser Effekt von funktioneller Relevanz ist, wurde zusätzlich ein Ischämie/Reperfusions-Protokoll angewandt, das in der frühen Reperfusionsphase zu einer schlagartigen Freisetzung großer Mengen von ROS führt − und anschließend eine massive Störung der Herzfunktion zur Folge hat [94, 95].

Um hierbei den Effekt von Myoglobin auf den in der Reperfusionsphase hervorgerufenen oxidativen Stress dokumentieren zu können, wurden bei diesen Experimenten neben den bereits beschriebenen funktionellen und energetischen Parametern zudem die ROS-Freisetzung erfaßt. Hierfür wurden die Herzen − ganz ähnlich wie in Kapitel 2.1 für die MR-Messungen beschrieben − im Innern eines Luminometers über einen lichtdichten Adapter in einer 10-mm Küvette perfundiert [OA2] und die Chemilumineszenz in Gegenwart von 5 μM Lucigenin gemessen [96].

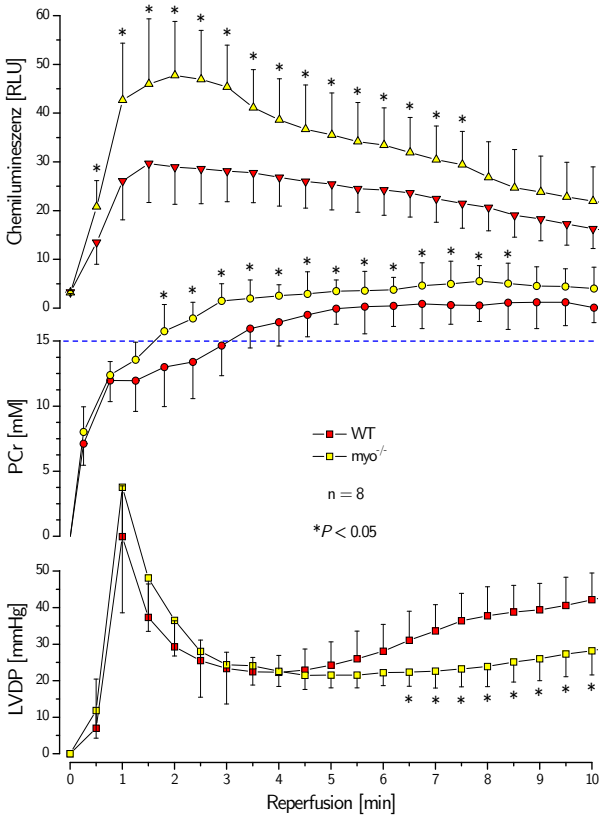

Abbildung 4.12: Reperfusionsphase nach akuter Ischämie: Einfluß von Myoglobin auf die Freisetzung reaktiver Sauerstoffspezies (oben), kardiale Energetik (Mitte) und Kontraktilität (unten); LVDP = *Left Ventricular Developed Pressure*. Die gestrichelte blaue Linie zeigt die initialen PCr-Spiegel vor Auslösen der Ischämie an.

Wie aus Abbildung 4.12, oben, klar hervorgeht, kommt es unmittelbar nach Reperfusionsbeginn in myo$^{-/-}$-Herzen zu einer deutlich gesteigerten Bildung von Sauerstoffradikalen im Vergleich zum WT. Durch Reduktion der Akquisitionszeit für die ^{31}P-MR-Spektren auf 30 Sekunden war es möglich in diesem Zeitfenster nicht nur eine aussagekräftige Korrelation der veränderten ROS-Freisetzung mit funktionellen sondern auch mit energetischen Parametern zu erhalten. Dabei konnte im Anschluß an die erhöhte ROS-Bildung in Mb-defizienten Herzen zunächst ein ausgeprägterer PCr *Overshoot* detektiert werden, was anschließend von einer deutlich stärkeren Einschränkung der Pumpfunktion in der Mutante begleitet wurde (Abbildung 4.12).

Die auf den ersten Blick paradoxe Beobachtung von scheinbar verbesserten energetischen Parametern (PCr$\nearrow$) und schlechterer kontraktiler Funktion (LVDP$\searrow$) wurde bereits vielfach nach kardialer Ischämie und Reperfusion (IR) beschrieben [97, 98]. Das „Überschießen" der PCr-Spiegel

nach IR ist auf eine Inaktivierung der cytosolischen Creatinkinase (CK_{cyto}) aufgrund der Oxidation methioningebundener Sulfhydrylgruppen durch H_2O_2 zurückzuführen [99,100]: Die eingeschränkte CK_{cyto}-Aktivität führt zu einer Hemmung der cytoplasmatischen Umwandlung von PCr zu ATP (vergleiche Abschnitt 3.2), was eine ineffiziente Übertragung von Energieeinheiten zur Verbraucherseite und damit einhergehend eine Depression der kardialen Kontraktilität zur Folge hat. Die beobachteten Geschehnisse in der initialen Reperfusionsphase ergeben insofern auch in der zeitlichen Abfolge ein absolut konsistentes Bild: Die erhöhten ROS-Spiegel nach Reperfusion verursachen eine anhaltende Inhibition der CK_{cyto}, die zu einem stärkeren PCr *Overshoot* führt, was sich aufgrund der eingeschränkten ATP-Bereitstellung in einer verzögerten Erholung der Pumpfunktion in myo$^{-/-}$-Herzen niederschlägt.

Kurzgefaßt belegen diese Daten, daß Myoglobin aufgrund seiner hohen cytosolischen Konzentration (siehe Abschnitt 4.1) auch eine wichtige Rolle in der Metabolisierung reaktiver Sauerstoffspezies zukommt und als molekularer Radikalfänger zum Schutz anderer − niedrig konzentrierterer − Angriffsziele (wie zum Beispiel die Creatinkinase) gegen ein temporäres Ansteigen cytosolischer ROS-Spiegel infolge kurzer Ischämieperioden beitragen kann (vergleiche OA2 für eine ausführliche Diskussion).

Die in den letzten Abschnitten beschriebenen Experimente legen eine grundsätzliche Neubewertung der Rolle von Myoglobin im Herzen nahe [101, 102]. Die anhand von myo$^{-/-}$-Tieren erhaltenen Ergebnisse zeigen, daß Myoglobin neben seiner lange akzeptierten Funktion als O_2-Speicher gleichermaßen eine signifikante Rolle in der NO- und ROS-Homöostase spielt und damit ein Schlüsselmolekül in verschiedenen Redoxgleichgewichten darstellt. Interessanterweise wird die „Entschärfung" von reaktiven Sauerstoffspezies vor allem durch metMb katalysiert (Abbildung 4.11), was als Zwischenprodukt bei der Reaktion mit NO anfällt (siehe Abschnitt 4.4-4.6). Insofern könnte Myoglobin sein kardioprotektives Potential auch bei gleichzeitigem Auftreten von nitrosativem und oxidativem Stress entfalten. Dies ist insbesondere in der Reperfusionsphase nach Myokardinfarkt der Fall, wobei in der Regel die NO- vor der ROS-Freisetzung erfolgt [103, 104], so daß das zunächst bei der NO-Detoxifikation gebildete metMb für den anschließenden Abbau von reaktiven Sauerstoff-spezies zu Verfügung steht. In anschließenden *in vivo* Studien konnte der protektive Effekt von Myoglobin nach Infarkt tatsächlich untermauert werden [105]. Außerdem können die vielfältigen − offenbar auch kooperativen − Effekte, die über das zentrale Eisenatom in der Hämgruppe des Myoglobins vermittelt werden, zum Verständnis kürzlich beschriebener aber mechanistisch unverstandener protektiver Wirkungen von homologen Molekülen wie Neuro- und Cytoglobin bei cerebraler Hypoxie [106] beziehungsweise als Tumorsuppressor [107] beitragen.

4.9 Substratumstellung als O_2-Sparmechanismus

Untersuchungen am roten und weißen Skelettmuskel haben gezeigt, daß diese nicht nur erhebliche Unterschiede im Myoglobingehalt sondern auch im Intermediärstoffwechsel aufweisen, die eng mit ihrer jeweiligen physiologischen Funktion verknüpft sind [108]. Rote Muskeln sind durch eine eher niedrige Zuckungsgeschwindigkeit gekennzeichnet, dafür aber sehr ermüdungsresistent und weisen einen aeroben Fett-, Glucose- und Keton-basierten Metabolismus auf. Demgegenüber sind weiße Muskeln anaerobe, schnell kontrahierende Fasern, die leicht ermatten, weil sie nur wenige respiratorische Pigmente besitzen und Glucose nur wenig effizient bis zum Lactat verstoffwechseln.

Ähnlich zum roten Skelettmuskel hat das Herz einen hohen, andauernden Energiebedarf, der normalerweise zum Großteil durch die Verbrennung von Fettsäuren gedeckt wird [109]. Allerdings wird bei einer Reihe von Herzerkrankungen, wie Hypertrophien sowie ischämischen oder dilatativen Kardiomyopathien, eine reduzierte Oxidation von Fettsäuren und eine erhöhte Verstoffwechselung von Glucose beobachtet [110]. Interessanterweise wurden bei beiden Formen von Kardiomyopathien auch erniedrigte myokardiale Myoglobinspiegel festgestellt [111]. Allerdings wurde nicht überprüft, ob dem mehr als eine lose Korrelation zwischen Muskelmyoglobingehalt und Substratmetabolismus zugrunde liegt.

Um nun die Rolle von Myoglobin bei der Substratselektion des Herzens unter definierten Bedingungen zu untersuchen, wurden WT und Mb-defiziente Herzen gemäß des in Abschnitt 3.3

beschriebenen Ansatzes mit physiologischen Konzentrationen von [1,6-$^{13}C_2$]-Glucose (5 mM) und [U-$^{13}C_{16}$]-Palmitat (0.4 mM) perfundiert und anschließend einer ^{13}C-MR-spektroskopischen Isotopomerenanalyse unterworfen. Abbildung 4.13 zeigt auf der linken Seite charakteristische Ausschnitte aus ^{13}C-MR-Spektren der beiden Spezies im Bereich des Glutamat-C4 (unten WT, oben myo$^{-/-}$). Vergleicht man die Signale in den Spektren mit den in Abbildung 3.5 dargestellten Schemata der Kopplungen, so findet man in beiden Fällen die Muster für die vier denkbaren Isotopomeren des Glutamats wieder. Es fällt jedoch auf, daß sich das Verhältnis der Signale, die von der Verstoffwechselung der beiden verschiedenen Substrate herrühren, deutlich unterscheiden.

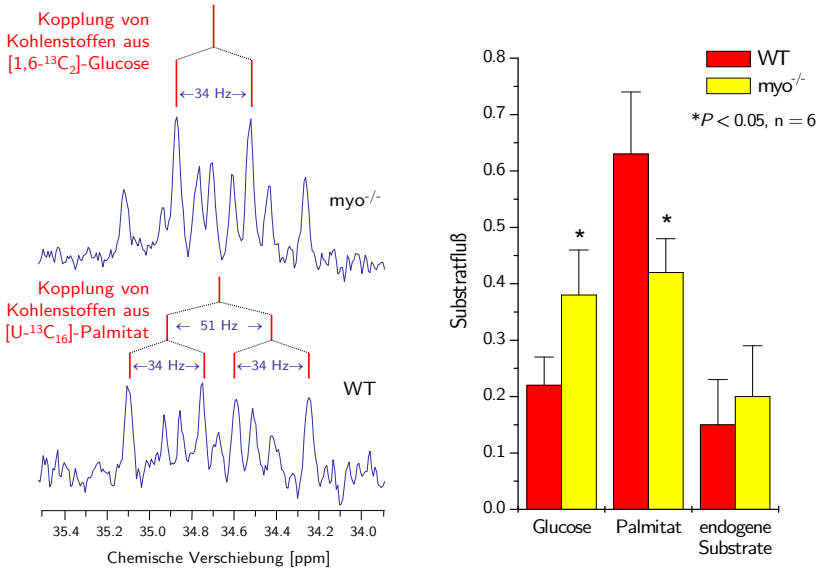

Abbildung 4.13: Substratstoffwechsel in WT- und Myoglobin-defizienten Herzen. Links: Ausschnitte aus ^{13}C-MR-Spektren nach Perfusion mit [1,6-$^{13}C_2$]-Glucose und [U-$^{13}C_{16}$]-Palmitat. Rechts: Quantitative Analyse der Substratflüsse durch den Citratzyklus wie im Abschnitt 3.3 beschrieben.

Während in Abbildung 4.13, links oben, vor allem die Muster, die durch die Verbrennung von Glucose hervorgerufen werden, ins Auge stechen, überwiegen im unteren Spektrum die Signale, die auf die Verwendung von Palmitat schließen lassen. Die Summe der Resonanzen $S + D_{34}$ (vergleiche Abbildung 3.5) gibt die Menge Acetyl-CoA wieder, die aus [1,6-$^{13}C_2$]-Glucose über die Glycolyse als [2-^{13}C]-Acetyl-CoA in den Citrat-Zyklus eintritt, während die Summe $D_{45} + Q$ die Menge Acetyl-CoA widerspiegelt, die aus [U-$^{13}C_{16}$]-Palmitat über die β-Oxidation als [1,2-$^{13}C_2$]-Acetyl-CoA in den Citrat-Zyklus eingeschleust wird. Die quantitative Auswertung (Abbildung 4.13, rechts) zeigt eindeutig, daß das Fehlen des Myoglobins zu einer Verschiebung des normalen Verbrennungsverhältnisses von 1:3 (Glucose:Fettsäure) hin zu einer etwa gleichen Nutzung der beiden Substrate führt – ein Shift, den man auch während der Ausbildung einer Hypertrophie im Menschen beobachtet (siehe oben).

Allerdings zeigen Myoglobin-defiziente Mäuse trotz des Fehlens dieses O_2-Trägerproteins erstaunlicherweise keinerlei Anzeichen einer Herzerkrankung. Dies ist auf die Ausbildung einer ganzen Reihe von Kompensationsmechanismen zurückzuführen, die alle darauf ausgerichtet sind, die Störung in der O_2-Versorgung abzupuffern, wie zum Beispiel Erhöhungen in der Kapillardichte, des koronaren Flusses, der Koronarreserve und des Hämatokrits (siehe [60]). Dadurch wird das O_2-Angebot auf der vaskulären Seite erhöht, der O_2-Gradient von der Kapillare zu den Mitochondrien gesteigert und somit die Diffusion des O_2 vom Gefäß zum Ort der Verbrennung erleichtert.

Parallel dazu wirkt offenbar auf der Verbraucherseite der mittels ^{13}C-MR-Spektroskopie nachgewiesene Substratshift als biochemischer O_2-Sparmechanismus: Es ist bekannt, daß zur Verbrennung von Glucose deutlich weniger Sauerstoff verbraucht wird als bei der Verbrennung von Fettsäuren

– bei Bildung gleicher Mengen von ATP [112, 113]. Somit kompensiert das Myoglobin-defiziente Herz durch vermehrte Verwendung des oxidativ günstigeren Substrates, nämlich von Glucose, den Verlust des O_2-Träger- und -Speicherproteins Myoglobin. Für eine ausführlichere Darstellung und Diskussion der Ergebnisse vergleiche OA3, in der die MR-spektroskopischen Befunde noch auf Proteom- und Transkriptionsebene sowie durch *in vivo* Positronenemissionstomographie von ^{18}F-Deoxyglucose (FDG-PET) untermauert werden.

Bemerkenswerterweise ähneln die Veränderungen im kardialen Substratstoffwechsel bei Myoglobindefizienz den bekannten Unterschieden im metabolischen Muster von rotem und weißem Muskel (siehe oben). Daher legen diese Ergebnisse den Schluß nahe, daß der Myoglobingehalt *per se* bereits ein entscheidender Faktor sein kann, der die Nutzung von Fettsäuren *versus* Glucose bestimmt, was Myoglobin zu einem Schlüsselmolekül im regulatorischen Netzwerk für die Energieproduktion im Herzen macht und die Anregung stützt, Myoglobin als multifunktionelles allosterisches Enzym zu klassifizieren [114].

5

Körperfettanalyse – Stoffwechselerkrankungen

5.1 Analyse des Fettgehalts – ^{1}H-MRI

Wie bereits in der Einleitung erwähnt, beruhen die meisten MR-Anwendungen vor allem auf der Detektion der ^{1}H-Kerne im Wasser (H_2O), das etwa 70-75% der gesamten Körpermasse ausmacht. Von den restlichen Bestandteilen des Organismus' (Proteine $\approx$ 15%, Lipide $\approx$ 10%, Kohlenhydrate $\approx$ 1%, Nucleinsäuren $\approx$ 1%, Mineralstoffe $\approx$ 5%) können vor allem die Lipide einen – in der Regel unerwünschten – Beitrag zum detektierbaren Protonensignal leisten. Die langen CH_2-Ketten, deren Protonen im Wesentlichen die gleiche chemische Verschiebung aufweisen, führen neben dem Wassersignal bei 4.7 ppm zu einem weiteren gut definierten Signal bei 1.3 ppm (siehe auch Abschnitt 5.3), das sich im rekonstruierten Bild als *Chemical Shift* Artefakt niederschlägt. Bei sehr hohem Fettgehalt ist dementsprechend eine Fettunterdrückung mithilfe eines frequenzselektiven Sättigungspulses unerläßlich. Andererseits kann dieses zusätzliche Signal genutzt werden, um zumindest den relativen Körperfettanteil der Mäuse zu bestimmen. In Abbildung 5.1 ist an exemplarischen Bildern vom Kopf einer Maus veranschaulicht, wie sich durch Aufnahme von ^{1}H-MR-Bildern ohne und mit Fettunterdrückung und anschließender Differenzbildung insbesondere die Lipiddeposition im subkutanen Bereich hervorragend darstellen läßt.

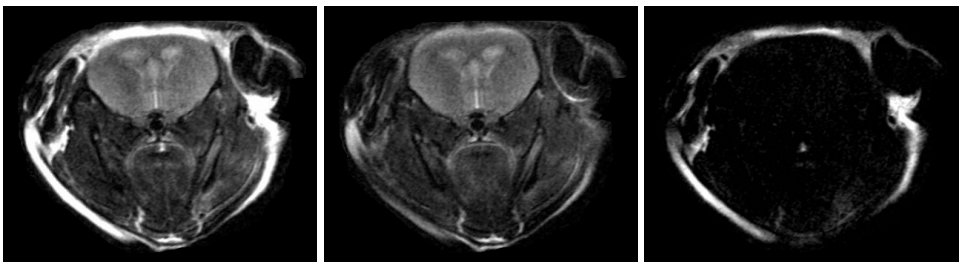

Abbildung 5.1: ^{1}H-MR-Bilder des Kopfes einer Maus ohne (links) und mit Fettunterdrückung (Mitte) sowie das berechnete Differenzbild (rechts).

Diese Technik wurde in einer Kooperation mit der Arbeitsgruppe von Ute Spiekerkötter aus der Kinderklinik dazu genutzt, die Auswirkungen einer bislang als gut verträglich geltenden Diät zur Therapie von angeborenen Fehlern im Stoffwechsel langkettiger Fettsäuren zu untersuchen. Durch einen Defekt in der β-Oxidation (vor allem in der VLCAD = *Very Long-Chain Acyl-CoA Dehydrogenase*) sind diese Patienten nicht in der Lage, Fettsäuren mit einer Kettenlänge von mehr als 16 Kohlenstoffatomen für die Energiegewinnung zu nutzen. Da insbesondere das Herz zur Finanzierung seines permanent hohen Energiebedarfs auf die Verbrennung von Fettsäuren angewiesen ist (siehe auch die Abschnitte 3.3 und 4.9), überrascht es nicht, daß ein solcher genetischer Defekt der Ausbildung einer Kardiomyopathie Vorschub leistet [115]. Um zu vermeiden, daß die betroffenen Patienten metabolisch entgleisen, wird eine Diät mit mittelkettigen Fettsäuren (MCT = *Medium-Chain Triglycerides*) verordnet, die unter Umgehung des „langkettigen Flaschenhalses" unmittelbar für die Energieproduktion in der β-Oxidation genutzt werden können [116]. Diese Therapie hat sich über den bisherigen Beobachtungszeitraum in der Tat als erfolgreich herausgestellt, die Entwicklung von Herz- und auch Skelettmuskelerkrankungen weitgehend einzudämmen [117], doch ist zur Zeit noch völlig unklar, welche Konsequenzen die Langzeitumstellung der Ernährung für den normalen Lipidstoffwechsel nach sich zieht.

Zur Untersuchung dieser Fragestellung wurden transgene Mäuse mit einem der humanen Erkrankung analogen Gendefekt (VLCAD$^{-/-}$) für ein Jahr ausschließlich mit MCT-Futter ernährt und mit gleichaltrigen VLCAD$^{-/-}$-Mäusen, die normales Futter erhielten, sowie mit zwei altersgematchten Wildtyp-Gruppen verglichen, die ebenfalls beiden Diäten für ein Jahr ausgesetzt waren. Anschließend wurde der Effekt dieser Langzeit-MCT-Diät auf die abdominale Fettverteilung der verschiedenen Spezies mithilfe der oben beschriebenen Methode analysiert. Exemplarische Bilder aus dieser Meßreihe sind in Abbildung 5.2 dargestellt. Dabei ist bereits auf den ersten Blick ersicht-

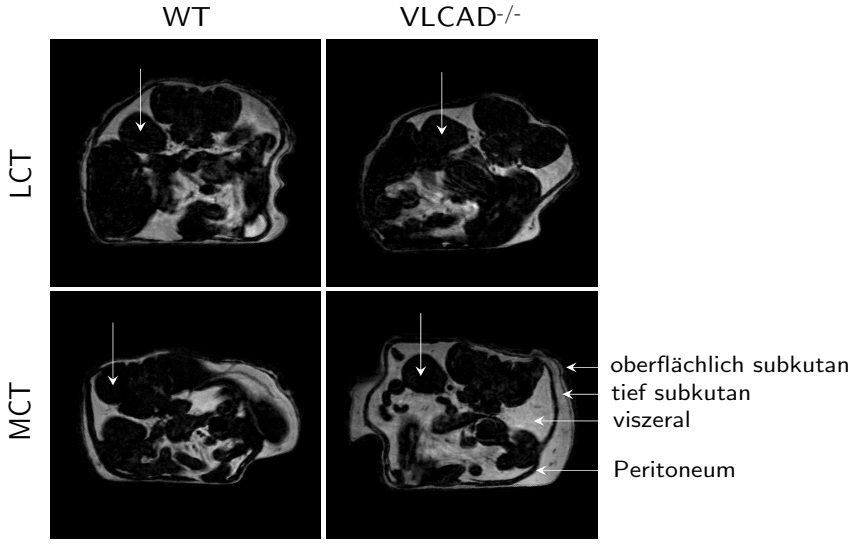

Abbildung 5.2: Abdominale ^{1}H-MR-Fettbilder von WT- und VLCAD$^{-/-}$-Mäusen nach einem Jahr LCT- beziehungsweise MCT-Fütterung (MCT/LCT = *Medium/Long-Chain Triglycerides*). Alle Bilder stammen aus vergleichbaren anatomischen Regionen etwa auf mittlerer Höhe der rechten Niere (senkrechte Pfeile).

lich, daß VLCAD$^{-/-}$-Mäuse unter MCT-Diät einen deutlich höheren Fettgehalt pro Körpervolumen als alle anderen untersuchten Spezies aufweisen (Abbildung 5.2, rechts unten). Die Klassifizierung des abdominalen Fetts in viszerale beziehungsweise tiefe sowie oberflächliche subkutane Segmente anhand der parallel aufgenommenen anatomischen Referenzbilder zeigte, daß dies insbesondere durch eine Zunahme des viszeralen Fetts und nur in untergeordnetem Maße durch Veränderungen im subkutanen Fett bedingt war, wie auch den repräsentativen Beispielen in Abbildung 5.2 zu

entnehmen ist. Dieser überraschende visuelle Befund entpuppte sich nach einer exakten Quantifizierung der Bilder als eine Verdopplung des viszeralen Fetts in der therapierten VLCAD$^{-/-}$-Gruppe, was beträchtliche Zweifel an der Langzeitverträglichkeit der MCT-Diät für Patienten mit Defekten in der β-Oxidation aufwirft.

Zur Beantwortung der Frage, warum ausgerechnet die VLCAD$^{-/-}$-Mäuse die vermeintlich zuträgliche Fütterung mit mittelkettigen Fettsäuren so schlecht tolerieren, waren weitere Experimente mithilfe spektroskopischer Techniken notwendig, die im nächsten Abschnitt beschrieben werden sollen, und mit denen die Auswirkungen der entsprechenden Diät auf den Lipidstoffwechsel geklärt werden konnten.

5.2 *In vivo* ^{13}C-MRS – Triglyceridzusammensetzung

Im Gegensatz zu den in Abschnitt 3.3 beschriebenen Untersuchungen zum Intermediärstoffwechel, wo unter anderem aufgrund der geringen Konzentration der interessierenden Metabolite der Einsatz ^{13}C-angereicherter Substrate unabdingbar ist, läßt sich zur Analyse maßgeblicher Aspekte des Lipidstoffwechsels das in den langen Fettsäureketten in natürlicher Häufigkeit vorkommende ^{13}C nutzen ($\approx 1\%$, vergleiche auch Tabelle 1.1). Mithilfe einer ^{13}C-Oberflächenspule, die zusätzlich in den normalen ^{1}H-Resonator eingefügt wird, erhält man in akzeptabler Meßzeit ($\leq$ 20 min) ^{13}C-MR-Spektren, aus dem zahlreiche Informationen über die Zusammensetzung der im Fettgewebe deponierten Triacylglyceride entnommen werden können. Wie aus Abbildung 5.3 ersichtlich, können

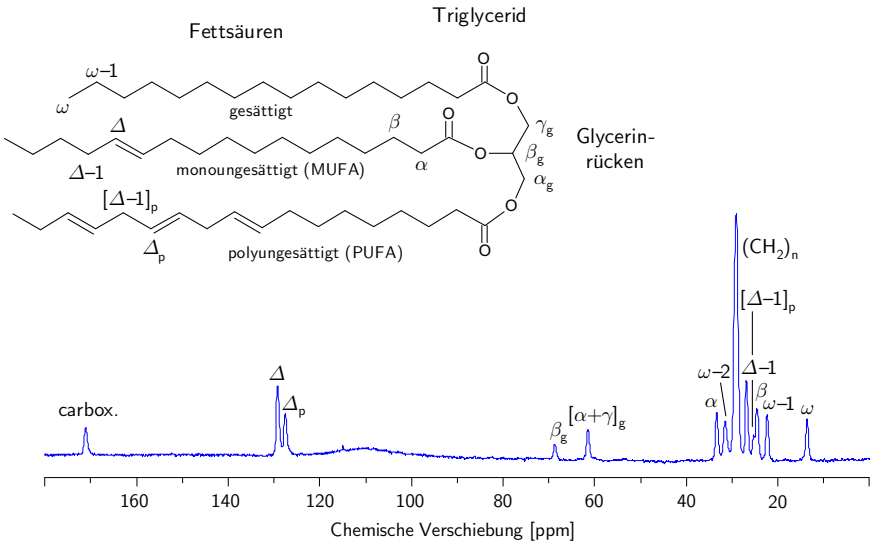

Abbildung 5.3: *In vivo* ^{13}C-MR-Spektrum des murinen Abdomens und Zuordnung der Signale.

insbesondere die Kohlenstoffe der Fettsäuren zu den beiden Kettenenden hin (ω, $\omega-1$, $\omega-2$ beziehungsweise α, carboxylisch) spektral hervorragend aufgelöst werden. Außerdem erkennt man in der Zuckerregion Signale für die Kohlenstoffe des Glycerinrückens ($\alpha_g + \gamma_g$ sowie β_g), wobei $\alpha_g + \gamma_g$ in der Regel nicht getrennt werden können. Darüber hinaus erhält man im olefinischen Bereich diskrete Signale für mono- und polyungesättigte Fettsäuren (Δ und Δ_p). Nach Integration und Korrektur der individuellen Signale für partielle Sättigung (aufgrund der Aufnahme nicht vollständig relaxierter Spektren) können diese zur Berechnung des relativen Anteils gesättigter, mono- und polyungesättigter Fettsäuren (SFA, MUFA, PUFA) in den gespeicherten Triglyceriden genutzt werden [118]:

$$SFA = \frac{\omega - \Delta + carbox.}{\omega + carbox.} \qquad MUFA = \frac{\Delta - \Delta_p}{\omega + carbox.} \qquad PUFA = \frac{\Delta_p}{\omega + carbox.}$$

Außerdem läßt sich aus dem Intensitätsverhältnis der Summe aller zu den terminalen Fettsäurekohlenstoffen die mittlere Kettenlänge (KL) der in die Triglyceride eingebauten Fettsäuren ermitteln [119]:

$$KL = \frac{\sum \left(\omega, \omega-1, \omega-2, (CH_2)_n, \Delta, \Delta_p, \Delta{-}1, [\Delta{-}1]_p, \beta, \alpha, carbox.\right)}{(carbox. + \omega)/2}$$

Da die in den Adipocyten abgelagerten Triglyceride das biochemische Schicksal der aufgenommenen Fettsäuren über einen längeren Zeitraum widerspiegeln und somit im Prinzip eine Art Stoffwechselintegral darstellen, eignet sich diese Technik somit hervorragend, um metabolische Langzeitauswirkungen der Ernährung auf den Lipidstoffwechsel zu untersuchen,

Dementsprechend bot es sich an, mit dieser Methode die metabolischen Konsequenzen der im vorherigen Abschnitt 5.1 beschriebenen MCT-Diät zur Therapie von Stoffwechseldefekten in der β-Oxidation näher zu untersuchen. Parallel zu den oben beschriebenen Bildgebungsexperimenten wurden daher in allen vier Gruppen (WT und VLCAD$^{-/-}$ unter LCT- beziehungsweise MCT-Diät) ^{13}C-MR-Spektren zur Analyse der abdominellen Fettzusammensetzung aufgenommen. Abbildung 5.4 zeigt charakteristische Spektren von VLCAD$^{-/-}$-Mäusen, die ein Jahr nach LCT- beziehungsweise MCT-Fütterung gewonnen wurden, wobei in erster Linie die dramatische Abnahme der Signalintensität für die polyungesättigten Kohlenstoffe (Δ_p, $[\Delta{-}1]_p$) ins Auge fällt. Nach Quan-

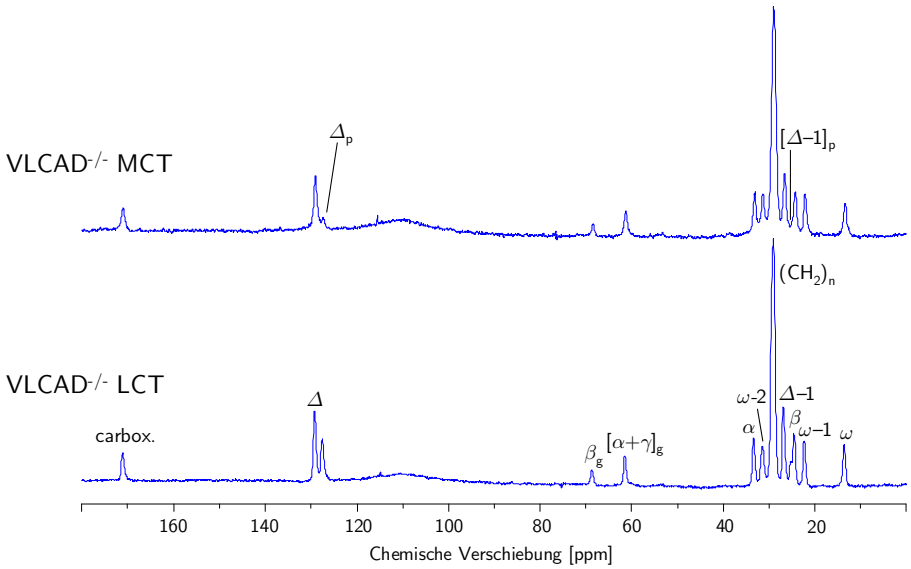

Abbildung 5.4: Auswirkungen einer Langzeit-MCT-Diät auf die Triglyceridzusammensetzung in VLCAD$^{-/-}$-Mäusen. Für die Signalzuordnung vergleiche auch Abbildung 5.3.

tifizierung der Spektren mithilfe der oben dargestellten Beziehungen stellte sich heraus, daß der Anteil der PUFA unter MCT-Diät bis auf etwa 10% im Vergleich zu circa 50% unter Kontrollbedingungen absank. Gleichzeitig war ein massiver Anstieg der MUFA sowie eine moderate Zunahme der gesättigten Fettsäurespiegel zu verzeichnen. Diese Effekte waren allerdings nicht spezifisch für die VLCAD$^{-/-}$-Mäuse, sondern wurden ebenso in WT-Tieren beobachtet. Überraschenderweise hatte die MCT-Fütterung jedoch in beiden Gruppen lediglich einen marginalen Einfluß auf die Kettenlänge der im Abdomen gespeicherten Fettsäuren. Obwohl diese Diät im Wesentlichen C8- und C10-Triacylglyeride beeinhaltet, befand sich die mittlere Fettsäurenlänge der ins abdominale Gewebe inkorporierten Triacylglyceride immer noch im Bereich von 16-17 Kohlenstoffen – selbst nach einer Fütterung mit dieser Diät über ein Jahr (vergleiche OA7 für eine ausführliche Darstellung der Ergebnisse).

Aus diesen Messungen lassen sich zunächst zwei wichtige Schlußfolgerungen ableiten: Zum einen führt die langfristige Einnahme von mittelkettigen Triglyceriden zu einer drastischen Entleerung

der körpereigenen Reserven an PUFA, denen in einer Vielzahl von Studien protektive Eigenschaften zugeschrieben werden [120–123]. Zum anderen werden die mit der Nahrung aufgenommenen mittelkettigen Fettsäuren im Körper offenbar zu langkettigen Fettsäuren umgewandelt – ein Prozeß, der normalerweise vor allem in der Leber stattfindet. Da jedoch die verlängerten Fettsäuren bei VLCAD-Defizienz nur eingeschränkt metabolisiert werden können, sollte dies zu einem verstärkten Rückstau der nicht verwertbaren Lipide in den transgenen Tiere führen. Demnach wurde im letzten Schritt der MR-Fettuntersuchung auch Lipidgehalt und -zusammensetzung der Leber unter den verschiedenen Fütterungsbedingungen in WT- und VLCAD$^{-/-}$-Tieren bestimmt.

5.3 Lokalisierte ^{1}H-MRS – Organselektive Lipidanalyse

Im vorausgegangenen Abschnitt erfolgte die Aufnahme der Spektren zur Untersuchung der Fettzusammensetzung aufgrund der geringen natürlichen Häufigkeit des ^{13}C-Isotops über das gesamte Abdomen – für eine volumenselektive Lipiduntersuchung reicht die Sensitivität dieser Methode jedoch nicht aus; hier bestünde nur bei einer kostenintensiven Langzeitfütterung mit ^{13}C-markierten Substraten Aussicht auf Erfolg.

Alternativ können für eine Charakterisierung von Lipidgehalt und -zusammensetzung auf Organebene auch protonenspektroskopische Methoden eingesetzt werden. Wie aus Abbildung 5.5 ersichtlich, erlaubt die hohe Empfindlichkeit des ^{1}H-Kerns die Spektrenakquisition zur Analyse

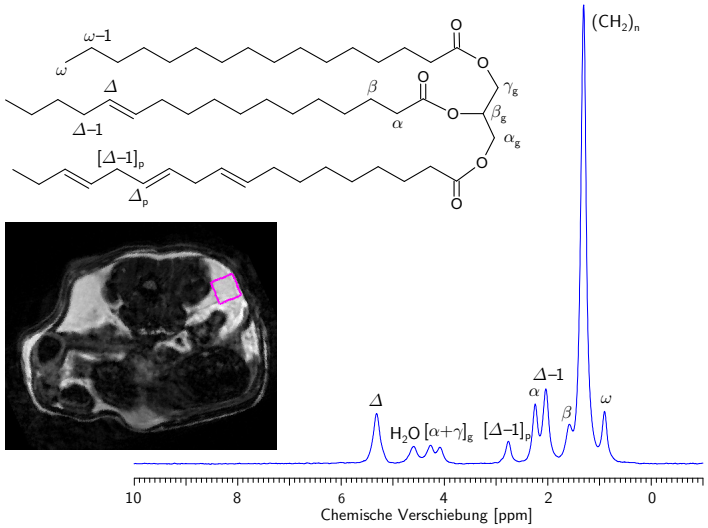

Abbildung 5.5: Volumenselektives ^{1}H-MR-Spektrum aus dem viszeralen Fett.

individueller Fettkompartimente aus vergleichsweise kleinen Volumenelementen. Das dargestellte Spektrum ist mit einer PRESS-Sequenz (PRESS = *Point Resolved Spectroscopy*) ohne Wasserunterdrückung aber mit *Outer Volume Suppression* aus einem im viszeralen Fett platzierten Voxel von 3×3×3 mm^3 (vergleiche violettes Rechteck in Abbildung 5.5) innerhalb von knapp einer Minute aufgenommen worden. Allerdings zeigt sich hier auch gleich der Nachteil dieser Vorgehensweise: Die im Vergleich zu den oben gezeigten ^{13}C-MR-Spektren erheblich geringere spektrale Breite der Protonenspektren (≈ 5 gegenüber fast 200 ppm) führt zu einer deutlich schlechteren Trennung und damit zu einer stärkeren Überlappung der Signale für die einzelnen Triglycerideinheiten. Auf der anderen Seite reicht die Auflösung der ^{1}H-MR-Spektren völlig aus, um anhand des gut separierten doppelallylischen Protonensignals $[\Delta{-}1]_p$ bei 2.8 ppm – als Gradmesser für den PUFA-Anteil – die in Abschnitt 5.2 beschriebenen Auswirkungen der MCT-Diät auf den Sättigungsgrad der im Gewebe deponierten Fettsäuren auch für die Leber nachzuvollziehen. Bei Verzicht auf eine Was-

serunterdrückung während der Spektrenakquisition kann zudem aus dem Verhältnis von Fett- und Wassersignalen gleichzeitig der relative Fettgehalt des Organs ermittelt werden.

In Abbildung 5.6 sind repräsentative ^{1}H-MR-Spektren aus dem rechten Leberlappen (Lokalisation → Rechteck) von VLCAD$^{-/-}$-Mäusen dargestellt, die nach einjähriger LCT- beziehungsweise MCT-Diät aufgenommen wurden. Bereits auf den ersten Blick wird deutlich, daß die MCT-Fütterung in der Mutante fatale Auswirkungen auf die Lipidhomöostase der Leber hat. Aus den Intensitätsveränderungen der Signale für Wasser und Fett ist klar ersichtlich, daß es dort zu einer massiven Lipidakkumulation kommt, während der nahezu vollständiger Verlust des Signals für $[\Delta{-}1]_p$ die starke Verringerung der hepatischen PUFA-Spiegel widerspiegelt, die auch über den

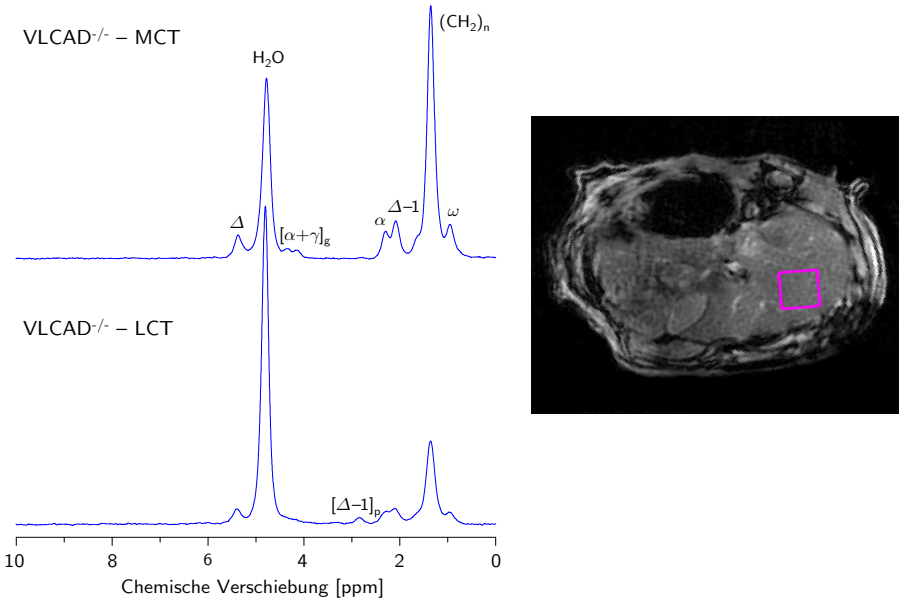

Abbildung 5.6: Lokalisierte ^{1}H-MR-Spektren aus dem rechten Leberlappen (Rechteck) von VLCAD$^{-/-}$-Mäusen nach Langzeitfütterung mit LCT (unten) beziehungsweise MCT (oben).

gesamten abdominalen Bereich beobachtet wurde (vergleiche vorherigen Abschnitt). Die Quantifizierung der Spektren ergab eine Verdopplung des Fettgehalts in der Leber der transgenen Tiere, während in WT-Mäusen unter MCT-Diät lediglich ein Trend zu einer Zunahme des Leberfettgehalts beobachtet wurde, die jedoch nicht das Signifikanzniveau erreichte (siehe OA7 für eine ausführliche Darstellung der Ergebnisse).

Zusammengefaßt zeigen die Ergebnisse aus den kombinierten Bildgebungs- und Spektroskopieexperimenten, daß VLCAD$^{-/-}$-Mäuse nach einem Jahr MCT-Fütterung einen schweren klinischen Phänotyp ähnlich der nichtalkoholischen Fettleber und dem metabolischen Syndrom entwickeln, der mit einer massiven viszeralen und hepatischen Fetteinlagerung einhergeht. Überdies führt die Langzeit-MCT-Diät zu einer drastischen Verschiebung der Triglyceridzusammensetzung im gesamten Abdomen, die einen starken Abfall im Spiegel der physiologisch wichtigen polyungesättigten Fettsäuren zur Folge hat.

Die schwerwiegenden Auswirkungen, die durch die modifizierte Triglyceridkomposition der MCT-Diät hervorgerufen wurden, sind insbesondere überraschend angesichts der Tatsache, daß der Gesamtfettgehalt in beiden Diäten gleich war. Allerdings unterscheidet sich der Stoffwechsel von MCTs in einigen wesentlichen Aspekten von dem der normalen LCTs. MCTs werden deutlich schneller zu freien Fettsäuren hydrolysiert und dementsprechend rasch im gastrointestinalen Trakt absorbiert. Im Gegensatz zu langkettigen werden mittelkettige Fettsäuren (LCFA beziehungsweise MCFA = *Long- or Medium-Chain Fatty Acid*) nur zu einem geringen Teil in Chylomicronen verpackt [124], sondern werden überwiegend unverestert aus den Enterocyten in den Pfortaderkreislauf

entlassen und können daher leicht für die Energiegewinnung im Herz- und Skelettmuskel abgerufen werden. An dieser Stelle ist es wichtig festzuhalten, daß überschüssige MCFAs nicht als MCTs in Adipocyten gespeichert werden: Die ^{13}C-MRS-Analyse der mittleren Fettsäurenkettenlänge im Abdomen zeigte – selbst nach einem Jahr MCT-Fütterung – lediglich eine leichte Verkürzung der Kohlenstoffketten im Vergleich zur LCT-Diät (Abschnitt 5.2). Dies befindet sich im Einklang mit früheren Befunden über eine nur geringe Aufnahme von MCFAs in die Adipocyten [125]. Überschüssige MCFAs werden daher primär zur Leber transportiert [126], wo sie entweder (i) *via* β-Oxidation zu C2-Fragmenten und Ketonkörpern umgewandelt oder (ii) zu LCFAs verlängert und anschließend zu LCTs verestert werden können [127,128]. Wie aus der unter beiden Diäten nahezu unveränderten Kettenlänge der abdominal gespeicherten Fettsäuren hervorgeht, dominiert im vorliegenden Fall eindeutig der letztere Weg. Da die verlängerten Fettsäuren in VLCAD-defizienten Mäusen nicht für die Energieproduktion genutzt werden können, führt dies in der Mutante zu einer massiven Lipidakkumulation, was auf lange Sicht für die Leber aufgrund der permanenten Belastung durch gesteigerte Zufuhr und Prozessierung von MCFAs einen metabolischen Teufelskreis darstellt [129].

Vom klinischen Standpunkt aus gesehen, hat sich die Gabe von MCTs zur Eindämmung von Herz- und Muskelerkrankungen bei Defekten in der Verwertung langkettiger Fettsäuren bewährt, in dem – durch Überbrückung des metabolischen Flaschenhalses in der β-Oxidation – die Organe, die auf Fettsäuren als Hauptenergiequelle angewiesen sind, mit den benötigten Substraten versorgt werden. Bis jetzt wurden dabei keine ernsthaften Nebenwirkungen beobachtet; allerdings sind bislang keine belastbaren Daten aus Langzeituntersuchungen verfügbar. Auf der anderen Seite geht aus einigen Kurzzeitstudien hervor, daß MCT-Diäten aufgrund der eingeschränkten Deposition von MCFAs im Fettgewebe [125] auch erfolgreich zur Adipositas-Behandlung eingesetzt werden könnten [130]. Der gesteigerte Energiebedarf für die oben beobachtete Verlängerung der MCFAs kann in der Tat zu einem kurzfristigen Gewichtsverlust beitragen [131], doch die dauerhaft erhöhte Fettzufuhr in die Leber steigert unweigerlich das Risiko für die Ausbildung einer Steatohepatitis. Es ist daher nicht überraschend, daß in der Literatur über das Auftreten einer Fettleber während ketogener MCT-Diät bei unheilbarer Epilepsie berichtet wird [132].

Bei zusätzlichem Vorliegen eines Defekts im Fettsäurestoffwechsel führt der verstärkte MCFA-Zufluß in die Leber jedoch nicht nur zu einer Steatose, sondern vielmehr zu den klinischen Charakteristiken des metabolischen Syndroms. Da aufgrund der weltweiten Neugeborenen-Screening-Programme zunehmend mehr angeborene Stoffwechselfehler entdeckt werden und neben symptomatischen auch asymptomatische Kinder bereits im neonatalen Alter mit MCTs supplementiert werden, erscheint ein regelmäßiges *Screening* der betroffenen Patienten auf mögliche Lebererkrankungen zwingend angezeigt. Für die nichtinvasive Kontrolle auf Veränderungen von Verteilung und Zusammensetzung des Körperfetts könnten die hier für die Maus beschriebenen MR-Techniken problemlos auf klinische MR-Scanner übertragen werden.

6

Entzündliche Prozesse – ^{19}F-MRI

6.1 Hintergrund

Entzündungen sind mit einer Vielzahl von Erkrankungen wie Atherosklerose, Multiple Sklerose, Arthritis, Glomerulonephritis, Colitis, Transplantatabstoßung, Herz- und Hirninfarkte sowie auch Myokarditis verbunden. Obgleich das medizinische Problem enorm ist, sind zur Zeit die Diagnosemöglichkeiten – insbesondere wenn innere Organe betroffen sind – limitiert und damit die Therapie oft auf die Eindämmung der Symptome beschränkt. Nichtinvasive bildgebende Verfahren wie Ultraschall, PET, CT und MRI liefern zwar detaillierte anatomische Informationen und sind dadurch wertvolle Hilfsmittel zur Beurteilung von Organfunktionen − allerdings ist es bis jetzt mit keinem der genannten Verfahren möglich, entzündliche Vorgänge mit hoher räumlicher Auflösung eindeutig nachzuweisen, da speziell in der initialen Phase der Erkrankung das betroffene Gewebe keine spezifischen physikalischen Eigenschaften aufweist, die zur Kontrasterzeugung zwischen gesunden und entzündeten Arealen genutzt werden können.

Ein erfolgversprechender Ansatz, inflammatorische Regionen vom umgebenden Gewebe abzugrenzen, stellt die Markierung immunkompetenter Zellen mit Kontrastmitteln dar. Zur nichtinvasiven Darstellung infiltrierender Zellen mittels MRI wurden bislang nahezu ausschließlich superparamagnetische Eisenoxidnanopartikel (SPIOs) verwendet, wobei die hohe Affinität dieser Teilchen zum Monocyten/Makrophagen-System genutzt wird [133, 134]. Allerdings werden diese Partikel nicht direkt detektiert, sondern ihre lokale Deposition führt zu regionalen Magnetfeldinhomogenitäten und dadurch zu einer Auslöschung des MR-Signals. Deshalb sind die so gewonnenen MR-Bilder oft schwierig zu interpretieren, da nicht immer klar ist, ob dunkle Areale durch die Ablagerung dieser Nanopartikel hervorgerufen werden oder eher unspezifische Ursachen haben.

6.2 Prinzip

Aus diesem Grund wurde versucht, ein alternatives Verfahren zu entwickeln, um entzündliche Prozesse über einen eindeutig „positiven Kontrast" mittels Fluor-MRI nachzuweisen. Das natürlich vorkommende, stabile Fluorisotop ^{19}F (100% natürliche Häufigkeit) ist MR-aktiv und weist eine ähnliche Empfindlichkeit wie der für die anatomische Bildgebung genutzte ^{1}H-Kern auf (vergleiche Abschnitt 1.1.2). Durch das nahezu vollständige Fehlen eines natürlichen ^{19}F-Hintergrundes im Körper (Tabelle 1.1) sind die detektierten Signale von injizierten ^{19}F-beinhaltenden Substanzen

hochspezifisch. Eine exakte anatomische Lokalisation der ^{19}F-haltigen Verbindungen innerhalb des Organismus läßt sich dann ganz einfach durch Aufnahme morphologisch übereinstimmender ^{1}H- und ^{19}F-MR-Bilder und deren anschließender Überlagerung vornehmen.

Als Kontrastmittel haben wir Nanopartikel verwendet, die Perfluorcarbone (PFCs) enthalten – eine Substanzfamilie, die bekanntermaßen biochemisch inert ist (zum Beispiel Teflon beziehungsweise Goretex). Einige Mitglieder dieser Substanzklasse, wie Perfluordecalin, Perfluortripropylamin, Perfluordichloroctan und Perfluoroctylbromid wurden bereits klinisch als künstliche Blutersatzstoffe eingesetzt. In unseren Untersuchungen haben wir jedoch das PFC Perfluor-15-krone-5-ether (Abbildung 6.1) eingesetzt, in dem alle 20 Fluorkerne chemisch sowie magnetisch äquivalent sind und das dadurch hervorragende Eigenschaften für die Detektion mittels ^{19}F-MRI aufweist. Nach intravenöser Gabe der emulgierten PFCs war ebenso wie oben für die SPIOs beschrieben eine effiziente und selektive Aufnahme des Kontrastmittels durch zirkulierende Zellen des Monocyten/Makrophagen-Sytems zu erwarten (Abbildung 6.1). Die Einwanderung der ^{19}F-beladenen, immunkompetenten Zellen in entzündetes Gewebe sollte dann eine eindeutige Identifikation der betroffenen Areale mittels kombinierter ^{1}H/^{19}F-MRI *in vivo* ermöglichen.

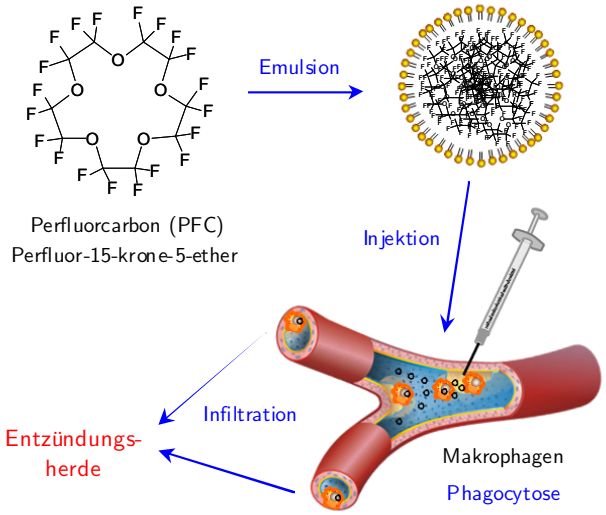

Abbildung 6.1: Schema zur Verwendung von PFCs zur Darstellung entzündlicher Prozesse. Nach Injektion werden die emulgierten Partikel durch phagocytierende Monocyten/Makrophagen aufgenommen und zu den Entzündungsherden transportiert. Aufgrund des Fehlens jeglichen ^{19}F-Hintergrunds sind die detektierten Signale hochspezifisch für infiltrierende, immunkompetente Zellen, die mit PFCs beladen sind.

6.3 Anwendungen

6.3.1 Entzündung nach kardialer Ischämie

Die Machbarkeit des oben vorgestellten Ansatzes wurde zunächst in einem murinen Herzinfarktmodell überprüft. Hierzu wurde die LAD (*Left Anterior Descending Coronary Artery*) legiert – eine Prozedur, von der bekannt ist, daß sie eine akute Entzündungsantwort nach sich zieht. Zwei Stunden nach Induktion des Infarktes wurde die PFC-Emulsion über die Schwanzvene appliziert (Partikelgröße circa 130 nm, ζ-Potential 31.3 ± 1.5 mV, vergleiche OA6 bezüglich Details über Herstellung und Charakterisierung der Emulsion). Hiernach wurde das Geschehen mittels kombinierter ^{1}H/^{19}F-MR-Bildgebung über einen Zeitraum von einer Woche verfolgt. Zunächst wurde die vom Infarkt betroffene Region anhand seiner eingeschränkten Kontraktilität mittels ^{1}H-Cine-Aufnahmen (siehe Abschnitt 3.1) lokalisiert, und die anschließende Akquisition anatomisch gematchter ^{19}F-

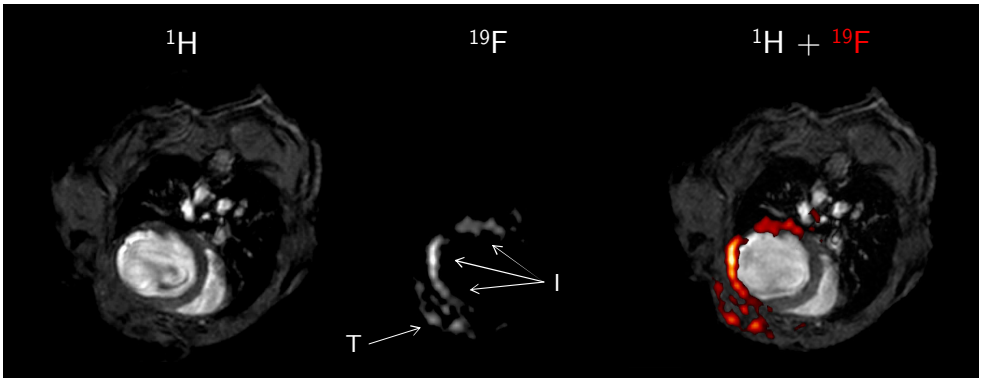

Abbildung 6.2: Infiltration von PFCs nach Myokardinfarkt mittels *in vivo* ^{19}F-MRI. Anatomisch korrespondierende ^{1}H- (links) und ^{19}F-MR-Bilder (Mitte) eines Mäusethorax 4 Tage nach Verschluß der LAD. Die Überlagerung (rechts) zeigt die Akkumulation von ^{19}F-Signalen (rot) in der infarzierten Region (I) sowie an der Stelle der Thorakotomie (T).

Bilder ermöglichte dann ein *Tracking* der injizierten PFCs. Ein typisches Beispiel konsekutiv aufgenommener ^{1}H- und ^{19}F-MR-Bilder vier Tage nach Ligation der LAD ist in Abbildung 6.2 dargestellt. Im enddiastolischen ^{1}H-MR-Bild (links) ist deutlich eine ventrikuläre Dilatation sowie eine Verdünnung der Wand im infarzierten Areal zu erkennen, während sich im korrespondierenden ^{19}F-MR-Bild (Mitte) ein Signalmuster in Form der freien linksventrikulären Wand abzeichnet. Die Überlagerung dieser Bilder (rechts) bestätigt die Lokalisation der PFCs innerhalb der Vorder-, Seiten- und Hinterwand des Herzens. Außerdem zeigt sich eine PFC-Deposition im benachbarten Brustgewebe, wo der Thorax für den experimentellen Eingriff eröffnet wurde. Darüber hinaus ist keinerlei Hintergrundsignal aus anderem Gewebe sichtbar. An dieser Stelle ist es wichtig anzumerken, daß mit der für die Fluorbildgebung verwendeten RARE-Sequenz keine Signale von fließenden Blutpartikeln erfaßt werden. Daher können die detektierten ^{19}F-Signale eindeutig im Gewebe deponierten Nanopartikeln zugeordnet und Kontaminationen durch Signale von zirkulierenden PFCs ausgeschlossen werden.

Repetitive Messungen beginnend an Tag 1 nach Verschluß der LAD dokumentieren eine zeitabhängige Akkumulation von PFCs im Infarktgebiet (Abbildung 6.3). Die enddiastolischen Protonenbilder belegen die zunehmende linksventrikuläre Dilatation als Folge des Infarkts. Die Fusion mit den entsprechenden Fluordaten (rot) demonstriert die fortlaufende PFC-Infiltration in das betroffene Herzareal und ebenso in die aufgrund der Operation verletzte Brustregion. Wie aus den repräsentativen Aufnahmen in Abbildung 6.3 hervorgeht, sind die detektierten ^{19}F-Signale räumlich auf den infarzierten Bereich des Herzens beschränkt − zu keinem Zeitpunkt konnte eine Deposition von PFCs im Septum beobachtet werden. Ebenso wurden in zahlreichen Kontrollversuchen an gesunden Herzen in keinem Fall ^{19}F-Signale im Myokard gefunden. Anschließende immunhistochemische Untersuchungen bestätigten die Infiltration von PFC-beladenen Monocyten/Makrophagen in die entzündeten Regionen (vergleiche OA6).

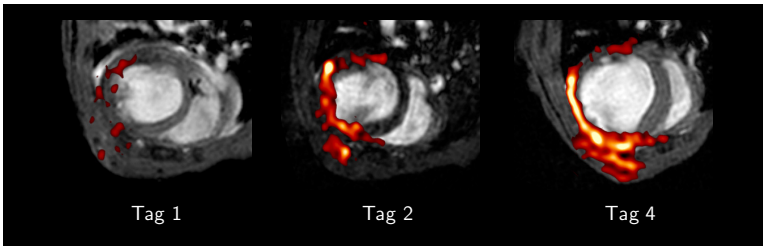

Abbildung 6.3: ^{1}H/^{19}F-MRI an Tag 1, 2 und 4 nach Myokardinfarkt.

Die Empfindlichkeit der Methode wurde sowohl an *in vivo* als auch *in vitro* gewonnenen Proben bestimmt. Die quantitative Analyse der Blutkomponenten nach PFC-Injektion, Blutentnahme, Dichtegradientenzentrifugation und ^{19}F-MRI ergab, daß circa 100 Zellen pro MR-Voxel (hier 0.2 μl) detektiert werden können. Ganz ähnliche Ergebnisse wurden nach PFC-Inkubation einer Makrophagenzelllinie unter *in-vivo*-vergleichbaren Bedingungen und anschließender Quantifizierung der aufgenommenen PFCs erhalten [135].

6.3.2 Lunge – Pneumonie

Veränderungen in der Lunge lassen sich mittels konventioneller MR-Techniken nur extrem schlecht diagnostizieren, da dieses Gewebe aufgrund seiner geringen Protonendichte und der großen Suszeptibilitätsunterschiede zwischen Lungengewebe und umgebender Luft im ^{1}H-MR-Bild in der Regel kein Signal liefert (siehe auch Abbildung 3.1). Daher ist die Etablierung einer alternativen MR-Technik von großem Interesse, und es wurde im nächsten Schritt untersucht, ob sich die oben beschriebene Vorgehensweise auch zur Detektion entzündlicher Prozesse in der Lunge nutzen läßt.

Hierzu wurde eine akute Pneumonie durch intratracheales Einträufeln einer Lösung von Lipopolysacchariden (LPS) in die Mauslunge ausgelöst. Für dieses Entzündungsmodell ist gut dokumentiert, daß es innerhalb von 24 Stunden zu einer signifikanten Infiltration von Monozyten ins Lungengewebe kommt [136, 137]. Die Gabe der PFC-Emulsion erfolgte in diesem Fall sechs Stunden nach LPS-Applikation, und die Tiere wurden anschließend zu verschiedenen Zeitpunkten der Bildgebung unterworfen. Eine erste Untersuchung nach 24 Stunden zeigte keinerlei Auffälligkeiten im Protonenbild – wie für die Lunge zu erwarten, wurden lediglich einige Signale in der Nähe des Herzens registriert (Abbildung 6.4, links oben), die vom Blutfluß durch die Pulmonalgefäße herrühren und auch unter Kontrollbedigungen sichtbar sind (siehe Abbildung 3.4). Demgegenüber läßt das korrespondierende Fluorbild zur selben Zeit eindeutig eine Akkumulation von PFCs in beiden Lungenlappen erkennen (Abbildung 6.4, links Mitte). Erst 48 Stunden nach LPS-Gabe konnten an einigen, anatomisch entsprechenden Stellen – in erster Linie im linken Lungenlappen – ebenfalls Veränderungen mittels ^{1}H-MRI beobachtet werden (Abbildung 6.4, oben Mitte), die vor allem auf die mit der Enzündungsreaktion einhergehende Ödembildung zurückzuführen sind. Weitere zwei

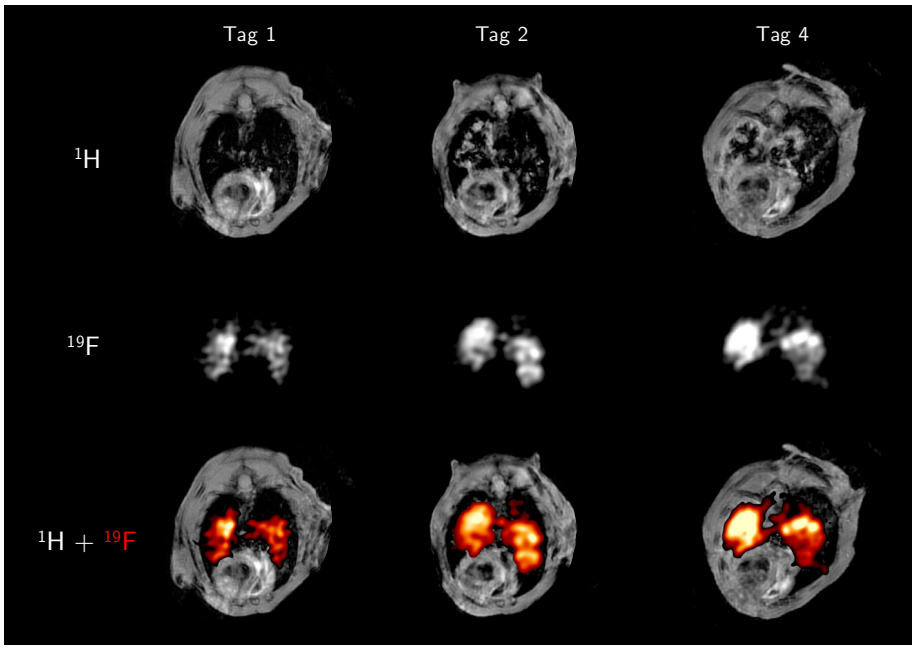

Abbildung 6.4: Visualisierung inflammatorischer Prozesse in der Lunge. (Oben) Respirationsgetriggerte ^{1}H-, (Mitte) anatomisch gematchte ^{19}F-MR-Bilder und deren Überlagerung (unten).

Tage später wird dann auch im Protonenbild deutlich, daß ebenso der rechte Teil der Lunge stark betroffen ist (Abbildung 6.4, oben rechts). Offensichtlich erscheinen die Signale im ^{19}F-MR-Bild bereits einen Tag nach Induktion der Pneumonie genau an den Stellen, die im ^{1}H-MR-Bild erst beträchtlich später auffällig werden. Ohne LPS wurden im übrigen zu keiner Zeit ^{19}F-Signale in der Lunge detektiert (siehe auch Abbildung 6.2).

Ähnlich wie im vorigen Abschnitt, belegten histologische Untersuchungen, daß die beobachteten Fluorsignale im LPS-gereizten Pulmonalgewebe gut mit dem Muster der eingewanderten Phagocyten korrelieren [138]. Um weiteren Einblick in den Mechanismus zu gewinnen, der für die Deposition der PFCs im entzündeten Bereich verantwortlich ist, wurden nach Verdau der entnommenen Lunge und anschließendem Sortieren der aus dem Gewebe herausgelösten Zellen die erhaltenen Subpopulationen mittels *in vitro* ^{19}F-MRI hinsichtlich ihres PFC-Gehalts untersucht. Dabei wurde der Hauptanteil (90%) des ^{19}F-Signals in Monocyten wiedergefunden. Interessanterweise zeigte sich bei diesen Messungen, daß auch Neutrophile in der Lage sind, die PFCs aufzunehmen – wenn auch in einem deutlich geringeren Ausmaß. Separate Experimente mit schrittweise erhöhter LPS-Dosis beziehungsweise mit antiinflammatorischer Behandlung demonstrierten darüber hinaus, daß der Schweregrad der induzierten Pneumonie direkt mit der Signalintensität im ^{19}F-MR-Bild korreliert, was diesen Ansatz auch zur Beurteilung von Therapieerfolgen nutzbar macht [138].

6.3.3 Organabstoßung nach Herztransplantation

Innerhalb der letzten Jahrzehnte hat sich die Herztransplantation als letztes Mittel zur Behandlung einer anderweitig unheilbaren Herzinsuffizienz erfolgreich etablieren können. Die Überlebensrate konnte aufgrund enormer Fortschritte in der Organkonservierung sowie in der immunsuppressiven Therapie beträchtlich gesteigert werden. Allerdings bleibt die Abstoßung des körperfremden Organs nach wie vor eine der Hauptkomplikationen nach der Operation. Den Goldstandard für die Überwachung der Organabstoßung stellt noch immer die Entnahme von Biopsien dar – ein Verfahren, das nicht nur invasiv, sondern aufgrund seines Stichprobencharakters extrem anfällig für Zufallsfehler ist. Da der Beginn der Abstoßungsreaktion mit einer Infiltration von Immunzellen in das betroffene Gewebe einhergeht [139,140], bot es sich an zu untersuchen, ob die ^{19}F-MR-Methode auch zur nichtinvasiven Diagnose des Abstoßungsprozesses geeignet ist.

Hierfür wurde in Zusammenarbeit mit der Arbeitsgruppe von Oliver Witzke im Universitätsklinikum Essen ein heterotopes Herztransplantationsmodell eingesetzt, in dem die Aorta des Transplantats an die abdominale Aorta der Empfängermaus und der Ausflußtrakt vom rechten Vorhof des Spenderherzens an die *Vena cava inferior* des Empfängers angeschlossen wird (Abbildung 6.5,

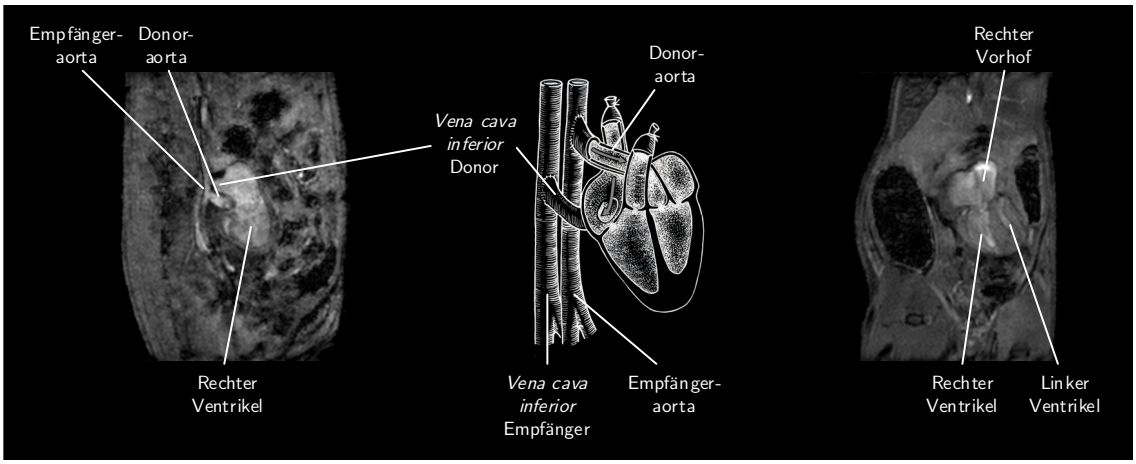

Abbildung 6.5: Schema des heterotopen Herztransplantationsmodells (Mitte) sowie sagittale (links) und coronale (rechts) ^{1}H-MR-Bilder, die die Lokalisation des Spenderherzens im Abdomen sowie die Anastomosen zum Gefäßsystem des Empfängers veranschaulichen.

Mitte). Damit wird ein retrograder Blutfluß durch die Koronargefäße des Transplantats gewährleistet, wodurch dieses einen regulären Herzschlag aufnimmt, ohne jedoch zur vitalen Funktion des Empfängers beizutragen. Um die mit der Abstoßung verbundene Immunreaktion zeitlich gut von der durch die Operation verursachten inflammatorischen Prozesse abgrenzen zu können, wurde ein Transplantationsregime benutzt, bei dem die Abstoßung erst beginnt, wenn die Folgen der Operation bereits weitgehend abgeklungen sind. Als Empfänger wurden „normale" C57BL/6-Mäuse (H-2^b) verwendet, denen Spenderherzen von C57B10.A-Mäusen (H-2^a) implantiert wurden. Diese unterlaufen anschließend einen kontinuierlichen Abstoßungsprozeß, der zu einem vorhersagbaren Transplantatversagen nach etwa zwei Wochen führt [141, 142].

Ein kritischer Punkt bei der Bildgebung war das Triggern der Imagingsequenzen an die Herzaktion des Transplantats zur Vermeidung von Bewegungsartefakten. Eine selektive Ableitung des Spenderherz-EKGs ohne Kontamination mit Signalen aus dem „eigentlichen" Herzen des Empfängers im Thorax gelang überraschend einfach durch Anbringen der EKG-Elektroden an den beiden Hinterpfoten. Abbildung 6.5 illustriert die Lokalisation des transplantierten Herzens im Abdomen des Empfängers anhand coronaler und sagittaler Beispielschnitte.

Ganz analog zu der in den beiden vorherigen Abschnitten beschriebenen Vorgehensweise erfolgte nach Aufnahme der ^{1}H-MR-Scans die Akquisition der anatomisch gematchten ^{19}F-MR-Bilder. In der oberen Hälfte von Abbildung 6.6 ist ein repräsentatives ^{1}H/^{19}F-MR-Bildpaar dargestellt, das 6 Tage nach Allotransplantation erhalten wurde – die PFC-Emulsion wurde hier 24 Stunden vor der MR-Untersuchung appliziert. Das ^{1}H-MR-Referenzbild zeigt das Spenderherz aus axialer Sicht und im korrespondierenden ^{19}F-MR-Bild ist ein Muster zu erkennen, das die Konturen der ventrikulären Wände widerspiegelt. Die anschließende Bildfusion (Abbildung 6.6, oben rechts) bestätigt die Deposition der PFCs im Myokard der rechten und linken Kammer. Wie bereits oben erwähnt, führt die RARE-Sequenz, die für die ^{19}F-MR-Bildgebung eingesetzt wurde, zu einem

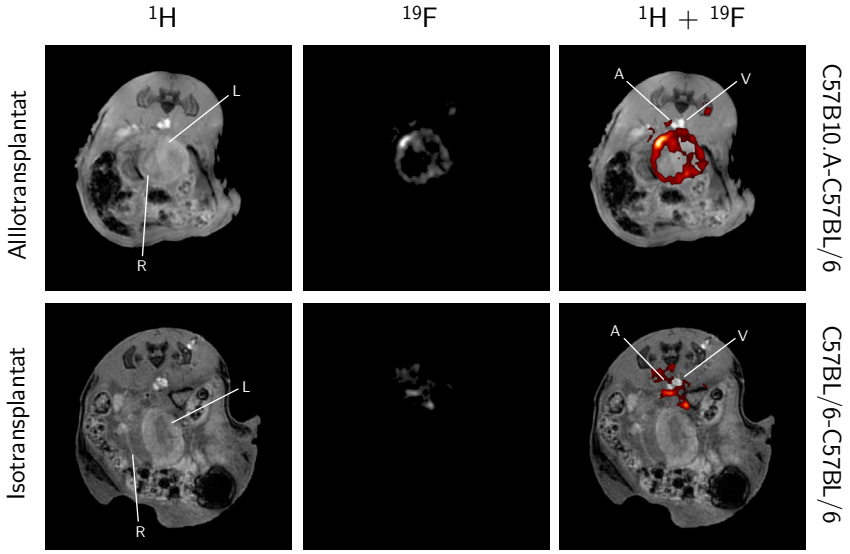

Abbildung 6.6: Abdominale ^{1}H- und ^{19}F-MRIs sowie deren Überlagerung 6 Tage nach Allo- (oben) beziehungsweise Isotransplantation (unten). L/R, linker/rechter Ventrikel des Transplantats; A/V, Abdominale Aorta/ *Vena cava inferior* des Empfängers.

Signalverlust für fließende Spins, so daß Signale von zirkulierenden PFCs unterdrückt und die detektierten ^{19}F-Signale eindeutig im Gewebe akkumulierenden PFCs zugeordnet werden können. In Kontrollexperimenten mit Isotransplantaten, bei denen keine Abstoßungsreaktion hervorgerufen wird (Spender und Empfänger: C57BL/6), wurden zum gleichen Zeitpunkt ^{19}F-Signale in erster Linie an den Anastomosestellen und lediglich in einem ganz geringen Ausmaß im Myokard registriert (Abbildung 6.6, unten), die vermutlich auf das operationsbedingte Gewebetrauma beziehungswei-

se den Ischämie/Reperfusions-Schaden während der Transplantationsphase zurückzuführen sind. Auch hier untermauerte die anschließende Histologie, daß die Intensität der detektierten Fluorsignale tatsächlich mit dem Ausmaß der Immunzellinvasion ins transplantierte Gewebe korreliert (siehe OA8), und bestätigte, daß im Allotransplantat in dieser Zeitspanne – 6 Tage nach Operation – bereits eine massive Zellinfiltration stattgefunden hatte, während im Isotransplantat nur eine geringfügige Akkumulation von Immunzellen festzustellen war.

In weiteren Experimenten wurde der Zeitverlauf der Abstoßung ab Tag 3 nach Transplantation verfolgt. Frühere Untersuchungszeitpunkte wurden unterlassen, damit sich die Tiere von der komplizierten Operation erholen konnten. Wie aus Abbildung 6.7 ersichtlich, war schon beim ersten Meßpunkt eine signifikant erhöhte PFC-Deposition im Allotransplantat erfaßbar, während weder im normalen Protonenscan noch im konventionell verwendeten Palpationsscore Anhaltspunkte für eine beginnende Abstoßung zu verzeichnen waren. Im weiteren Zeitverlauf steigt das ^{19}F-Signal in allotransplantierten Spenderherzen stark an – interessanterweise ist dabei eine progressive Ausbreitung des Fluorsignals von den epi- und endokardialen Grenzen zum Zentrum des Myokards zu beobachten (vergleiche OA8). Demgegenüber führt die Kaltischämie in Isotransplantaten lediglich zu einer moderaten PFC-Deposition mit nahezu unveränderter Signalintensität über den gesamten Untersuchungszeitraum (Abbildung 6.7, links).

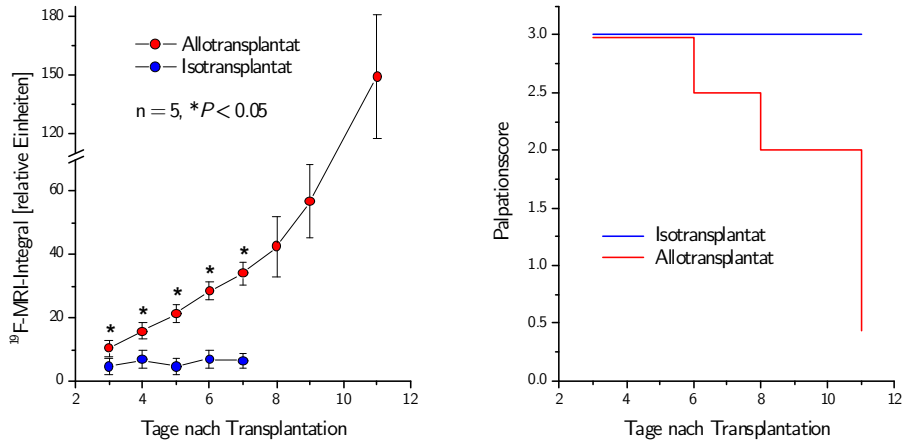

Abbildung 6.7: Zeitverlauf der ^{19}F-MR-Signale (links) beziehungsweise des Palpationsscores (rechts) in Allo- (rot) und Isotransplantaten (blau).

Abschließend konnte noch gezeigt werden, daß es mit dieser Methode auch möglich ist, die Wirksamkeit einer immunosuppressiven Therapie zu beurteilen. Während Rapamycin-behandelte Tiere nach Allotransplantation mehr oder weniger einen „Isotransplantat-Phänotyp" aufwiesen, ergab sich in den unbehandelten Tieren wiederum der bereits oben beschriebene charakteristische Verlauf der PFC-Verteilung beginnend vom Randbereich hin zum Innern der Ventrikelwände (vergleiche OA8 für eine ausführliche Darstellung und Diskussion der Ergebnisse).

6.4 Perspektiven und Limitationen

Die in den letzten drei Abschnitten vorgestellten Ergebnisse zeigen, daß die kombinierte ^{1}H/^{19}F-MR-Bildgebung in Verbindung mit der Gabe inerter PFCs als Kontrastmittel bei einer Vielzahl von Erkrankungen ein hervorragendes Instrument zur selektiven und spezifischen Darstellung inflammatorischer Prozesse verkörpert. Mit den verwendeten Akquisitionsparametern läßt sich in den ^{19}F-MR-Bildern innerhalb einer akzeptablen Meßzeit (20 min) ein gutes Signal-zu-Rausch-Verhältnis (SNR $\approx$ 20) mit einer Auflösung erreichen, die nahe an das anatomische ^{1}H-MR-Bild herankommt (Voxelgröße 0.2 μl). Durch das Bereitstellen eines „positiven Kontrasts" kann dieser

Ansatz – im Unterschied zu der verwandten Vorgehensweise mit SPIOs – auch in Szenarien eingesetzt werden kann, in denen eine Signalauslöschung nur schwerlich hilfreich ist (⇒ Lunge). Dies verleiht der ^{19}F-Methode auch in heterogenen Körperarealen (⇒ Thorax, Abdomen) eine deutlich größere Spezifität, da hier die großen Suszeptibilitätssprünge im Grenzbereich zu „spontanen" Signalverlusten im Protonenbild führen können, die die Bildinterpretation und -quantifikation erheblich erschweren. Darüber hinaus belegen die Daten zur Pneumonie und zur Organabstoßung, daß über die Gabe der PFCs – zumindest im Tierversuch – eine erheblich frühere und sensitivere Diagnose als mit konventionellen Methoden möglich ist.

Aus den Ergebnissen können die Mechanismen, die zur Kontrasterzeugung im Fluorbild beitragen, eindeutig nachvollzogen werden: Kombinierte Experimente zur Blutanalyse mittels Dichtegradientenzentrifugation, Durchflußcytometrie und ^{1}H/^{19}F-MRI bestätigten die initiale Arbeitshypothese, daß intravenös applizierte PFCs vor allem von Zellen des Monocyten/Makrophagen-Systems aufgenommen und danach in die Entzündungsherde transportiert werden. Die Beladung der zirkulierenden Zellen scheint diese in ihren Funktionen nicht zu beeinträchtigen, da die Infiltrationskinetik und das Verteilungsmuster der PFC-markierten Zellen, die mittels ^{19}F-MRI in den verschiedenen Entzündungsmodellen beobachtet wurde, sich in ausgezeichneter Übereinstimmung mit publizierten Daten befindet (vergleiche OA6 und OA8 sowie [138] für eine ausführliche Diskussion). Darüber hinaus haben andere Arbeitsgruppen in detaillierten Untersuchungen gezeigt, daß die Aufnahme der PFCs keine Auswirkungen auf Proliferation, Funktion oder Reifung von Makrophagen, Monocyten, T- und B-Zellen sowie dendritischen Zellen hat [143]. Dieser physiologisch inerte Charakter der PFCs ist zum einen auf die Stärke der C-F-Bindung, die von keinem endogenen Enzym gespalten werden kann, und zum anderen auf die dichte und abweisende Elektronenhülle, die die C-F-Ketten überzieht und nur extrem schwache intermolekulare Wechselwirkungen zuläßt, zurückzuführen [144].

In weiteren Untersuchungen konnten wir inzwischen zeigen, daß PFCs auch in vielen anderen Organen zum Nachweis inflammatorischer Prozeße genutzt werden können, wie zum Beispiel im Gehirn (nach cerebraler Ischämie), im Gefäßsystem (in einem Restenosemodell), im Gelenk (zur Früherkennung von rheumatoider Arthritis) sowie in der Niere (nach Autoimmunnephritis). Insbesondere im letztgenannten Fall ist für eine exakte Diagnose – ähnlich wie bei Transplantaten – immer noch die histologische Untersuchung einer Gewebeprobe aus der Niere unerläßlich. Auch hier ist eine Biopsie aufgrund ihres invasiven Charakters mit Risiken verbunden, und es können dabei leicht falsch-positive Ergebnisse erhalten werden. Dies wird auch nochmals durch das heterogene Fluormuster in der Transplantationsstudie (Abschnitt 6.3.3) unterstrichen, wo eine progressive PFC-Deposition vom Epi- und Endokard hin zum Zentrum des Myokards registriert wurde. Diese Heterogenität befindet sich im Einklang mit früheren Beobachtungen [145] und führt nochmals nachdrücklich die Probleme vor Augen, die mit der stichprobenartigen Entnahme kleiner Gewebeproben verbunden sind. Da die Bildgebung infiltrierender Immunzellen mittels ^{1}H/^{19}F-MRI nicht nur nichtinvasiv ist, sondern darüberhinaus eine tomographische Darstellung des gesamten Organs erlaubt, könnte dieser Ansatz insbesondere als Alternative zur Entnahme von Biopsien Anwendung im klinischen Bereich finden.

Von der apparativen Seite her sollte dies kein größeres Problem darstellen, da die klinischen MR-Geräte lediglich mit zusätzlichen Fluorspulen ausgerüstet werden müßten. Auch die geringere Feldstärke der klinischen Scanner (1.5 oder 3 T) gegenüber den 9.4 T unseres Kleintiergerätes sollte keinen entscheidend limitierenden Faktor darstellen, da die Voxelgröße in der diagnostischen Kardio-MRT mit 2 bis 30 μl – gemessen an den 0.2 bis 0.4 μl in unseren Studien an der Maus – vergleichsweise groß ist und den Verlust im SNR aufgrund der geringeren Magnetfeldstärke zumindest wettmachen sollte. Erfreulicherweise haben inzwischen initiale Messungen bei 1.5 T am Schwein die prinzipielle Umsetzbarkeit der Methode unter klinischen Bedingungen dokumentiert.

Allerdings zeigte sich in allen bisherigen Versuchen, daß der von uns verwendete Perfluor-15-krone-5-ether nicht nur von zirkulierenden Monocyten/Makrophagen sondern auch von Lymphknoten, Leber sowie Milz aufgenommen wird und dort eine Halbwertszeit von mehreren Monaten aufweist, ohne selbst toxisch zu sein. Für tierexperimentelle Studien ist diese lange Retentionszeit sehr vorteilhaft: Sind die Monocyten/Makrophagen einmal markiert, kann ihr Schicksal im Körper in longitudinalen Studien verfolgt werden. Um jedoch einen Einsatz im humanen Bereich zu

ermöglichen, müßten andere PFCs eingesetzt werden, die eine biologische Halbwertszeit von nur wenigen Tagen haben, gleichermaßen nicht toxisch sind und sich durch eine selektivere Anreicherung in entzündetem Gewebe im Vergleich zu Leber und Milz auszeichnen. Alternative Substanzen, die hierfür in Frage kommen und auch bereits in klinischen Studien als Blutersatzstoffe eingesetzt wurden, sind in Abbildung 6.8 dargestellt. Der bekannteste Vertreter ist hierbei sicherlich das Perfluoroctylbromid (PFOB), für das auch die Bezeichnungen Perflubron und Oxygent geläufig sind. Das terminal eingeführte Brom sorgt dafür, daß sich der lipophile Charakter der Verbindung erhöht und dadurch dessen Membrangängigkeit verbessert wird. Hiermit wird gewährleistet,

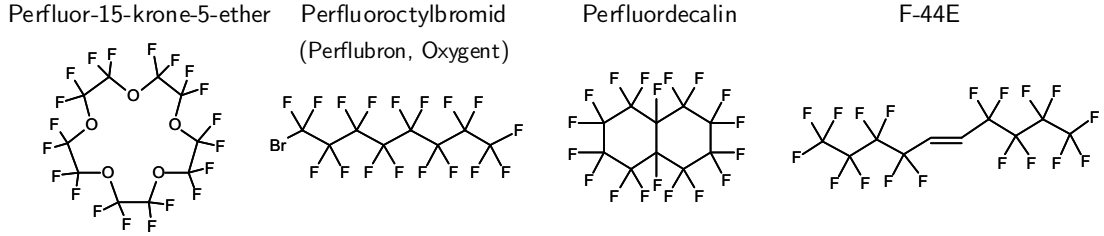

Abbildung 6.8: Strukturformeln verschiedener Perfluorcarbone (PFCs).

daß die Substanz schneller über die Lunge abgeatmet und innerhalb von etwa einer Woche aus dem Körper ausgeschleust werden kann [146]. Auch das Perfluordecalin sowie das F-44E weisen ähnliche Retentionszeiten wie das PFOB auf. Wie aus Abbildung 6.8 hervorgeht, enthalten diese drei Verbindungen eine dem Kronenether vergleichbare Anzahl von Fluoratomen im Molekül – im Unterschied zum Kronenether sind diese dort jedoch nicht alle äquivalent, was zu verschiedenen Signalen im ^{19}F-MR-Spektrum und bei konventioneller Bildgebung zu *Chemical Shift* Artefakten führt (vergleiche auch Abschnitt 5.1).

Um zu zeigen, daß eine artefaktfreie und sensitive Detektion von PFCs mit komplexen Spektren möglich ist, haben wir die – bereits für die *in vivo* ^{31}P-MR-Spektroskopie verwendete [147] – 2D-CSI-Methode (siehe Abschnitt 3.2.2) modifiziert und für den breiten spektralen Bereich der PFCs optimiert. Bei ähnlicher Meßzeit (16 min) konnte hier die gleiche Auflösung wie in den Kronenether-Experimenten mit der RARE-Sequenz erreicht und nach entsprechender Anpassung der Akquisitions- und Rekonstruktionsparameter zur artefaktfreien Bildgebung von Perfluoroctylbromid, Perfluordecalin und F-44E eingesetzt werden. Mittels eines selbstentwickelten Softwaremoduls können dabei alle Signale zur Bildrekonstruktion genutzt werden. Von dieser Methode haben wir Gebrauch gemacht, um die Verweilzeit einiger dieser Verbindungen in den Organen bevorzugter PFC-Akkumulation (insbesondere Leber und Milz) zu bestimmen. Aus diesen Vorversuchen läßt sich klar erkennen, daß die ausgewählten PFCs tatsächlich eine deutlich kürzere Retentionszeit als der Kronenether aufweisen und somit für eine potentielle klinische Anwendung in Frage kommen.

7

Zusammenfassung

Die Erzeugung transgener Mauslinien bietet vielfältige Möglichkeiten zur Beantwortung basaler kardiovaskulärer Fragestellungen und hat daher in den letzten zwei Jahrzehnten stetig zugenommen. Um den Phänotyp der Mutanten möglichst vollständig und nichtinvasiv charakterisieren zu können, wurde im Institut für Herz- und Kreislaufphysiologie / Molekulare Kardiologie in den letzten Jahren ein umfangreiches Arsenal an spektroskopischen und bildgebenden Magnetresonanztechniken (MRS, MRI) etabliert.

Hierfür wurde zunächst das isolierte Mäuseherz für die Spektroskopie nutzbar gemacht, um über den ^{31}P-Kern parallel zur Erfassung der kontraktilen Funktion zentrale Größen des kardialen Energiehaushalts zu ermitteln. Außerdem gelang es mittels ^{1}H-MRS die myokardiale Oxygenierung am intakten Herzen zu bestimmen, was ein entscheidender Faktor war, um weiteren Einblick in die Sauerstofftransportfunktionen von Myoglobin zu gewinnen. Unter Zuhilfenahme dieser Techniken konnten außerdem Schlüsselexperimente zur Interaktion von Myoglobin mit Stickstoffmonoxid (NO) und reaktiven Sauerstoffspezies (ROS) durchgeführt werden. Diese belegten, daß dem Myoglobin neben seiner Trägerfunktion für Sauerstoff eine wichtige Entgiftungsfunktion im Herzstoffwechsel zukommt und führten letztlich zu einer völligen Neubewertung der Rolle von Myoglobin im Herzen. Über ^{13}C-Tracer-Analysen konnten zusätzlich wichtige biochemische Kompensationsmechanismen im Substratstoffwechsel der Myoglobinverlustmutante nachgewiesen werden.

Weiterhin wurden für die kardiale Phänotypisierung der Mutanten *in vivo* dynamische Bildgebungsmethoden zur Analyse des Mäuseherzens verfügbar gemacht, mit denen die genaue Ventrikelgeometrie dargestellt, Wandstärken bestimmt und funktionelle Größen wie die Auswurfleistung des Herzens quantifiziert werden können. Über die Kardio-MR hinaus erfolgte anschließend die Implementierung angiographischer Methoden (MRA) zur vaskulären Analyse mit isotropen Voxelgrößen bis zu 1 nl [148] und die Etablierung volumenselektiver Spektroskopie zur parallelen Bewertung von kardiovaskulärer Funktion und lokalem Stoffwechsel. Neben den Experimenten zur Interaktion von Myoglobin und NO zeigen dabei insbesondere die Untersuchungen zu den metabolischen Konsequenzen des Defektes in der β-Oxidation, daß die Verknüpfung spektroskopischer und bildgebender MR-Verfahren ein mächtiges Werkzeug für die nichtinvasive Analyse der kardiovaskulären Langzeitfolgen von Störungen in basalen Stoffwechselwegen darstellt.

Durch den kombinierten Einsatz biochemisch inerter Perfluorcarbone (PFCs) und ^{19}F-MRI konnte eine alternative Bildgebungsplattform zur Darstellung entzündlicher Prozesse in den inneren Organen aufgebaut werden. Die intravenös verabreichten PFCs werden in erster Linie von Monocyten/Makrophagen aufgenommen und anschließend in Entzündungsherde transportiert, die

sich in ^{19}F-MR-Bildern anhand der progressiven Infiltration PFC-beladener Zellen identifizieren lassen. Aufgrund eines fehlenden natürlichen ^{19}F-Hintergrundes im Körper sind die beobachteten Signale extrem robust und durch eine exzellente Spezifität gekennzeichnet. Daher hat dieser Ansatz das Potential, auch in der Klinik als neues diagnostisches Verfahren zur Früherkennung von akuten und chronischen Entzündungen bei einer Vielzahl von Erkrankungen zu dienen.

IV

Anhang

Literaturverzeichnis

[1] Rabi II, Zacharias JR, Millman S & Kusch P: A new method of measuring nuclear magnetic moment. *Phys Rev.* 53: 318, 1938.

[2] Purcell EM, Torrey HC & Pound RV: Resonance absorption by nuclear magnetic moments in a solid. *Phys Rev.* 69: 37–38, 1946.

[3] Bloch F, Hansen WW & Packard M: Nuclear induction. *Phys Rev.* 69: 127, 1946.

[4] Knight WD: Nuclear magnetic resonance shift in metals. *Phys Rev.* 76: 1259–1260, 1949.

[5] Proctor WG & Yu FC: The dependence of a nuclear magnetic resonance frequency upon chemical compound. *Phys Rev.* 77: 717, 1950.

[6] Arnold JT, Dharmatti SS & Packard ME: Chemical effects on nuclear induction signals from organic compounds. *J Chem Phys.* 19: 507–507, 1951.

[7] Lowe IJ & Norberg RE: Free-induction decays in solids. *Phys Rev.* 107: 46–61, 1957.

[8] Ernst R & Anderson W: Application of fourier transform spectroscopy to magnetic resonance. *Rev Sci Instrum.* 37: 93–102, 1966.

[9] Odeblad E, Bhar BN & Lindström G: Proton magnetic resonance of human red blood cells in heavy-water exchange experiments. *Arch Biochem Biophys.* 63: 221–225, 1956.

[10] Moon RB & Richards JH: Determination of intracellular pH by ^{31}P magnetic resonance. *J Biol Chem.* 248: 7276–7278, 1973.

[11] Hoult DI, Busby SJ, Gadian DG, Radda GK, Richards RE & Seeley PJ: Observation of tissue metabolites using ^{31}P nuclear magnetic resonance. *Nature.* 252: 285–287, 1974.

[12] Shulman RG, Brown TR, Ugurbil K, Ogawa S, Cohen SM & den Hollander JA: Cellular applications of ^{31}P and ^{13}C nuclear magnetic resonance. *Science.* 205: 160–166, 1979.

[13] Gupta RK: *NMR Spectrosopy of Cells and Organisms - vol. II,* chap. ^{23}Na-NMR spectroscopy of intact cells and tissue, pp. 1–32 CRC Press, Boca Raton, 1987.

[14] Allis JL, Snaith CD, Seymour AM & Radda GK: ^{87}Rb NMR studies of the perfused rat heart. *FEBS Lett.* 242: 215–217, 1989.

[15] Gupta RK & Gillies RJ: *NMR Spectrosopy of Cells and Organisms - vol. II,* chap. ^{19}F-NMR measurement of intracellular free calcium ions in intact cells, pp. 45–54 CRC Press, Boca Raton, 1987.

[16] Benters J, Flögel U, Schäfer T, Leibfritz D, Hechtenberg S & Beyersmann D: Study of the interactions of cadmium and zinc ions with cellular calcium homoeostasis using ^{19}F-NMR spectroscopy. *Biochem J.* 322: 793–799, 1997.

[17] Certaines JD & Bovee WMMJ: *Magnetic Resonance Spectroscopy in Biology and Medicine: Functional and Pathological Tissue Characterization - An Introduction.* Pergamon Press, Oxford, 1992.

[18] Lauterbur PC: Image formation by induced local interactions: Examples employing nuclear magnetic resonance. *Nature.* 242: 190–191, 1973.

[19] Mansfield P & Maudsley AA: Medical imaging by NMR. *Br J Radiol.* 50: 188–194, 1977.

[20] Hennig J, Nauerth A & Friedburg H: RARE imaging: a fast imaging method for clinical MR. *Magn Reson Med.* 3: 823–833, 1986.

[21] Frahm J, Haase A & Matthaei D: Rapid NMR imaging of dynamic processes using the FLASH technique. *Magn Reson Med.* 3: 321–327, 1986.

[22] Sechtem U, Pflugfelder PW, White RD, Gould RG, Holt W, Lipton MJ & Higgins CB: Cine MR imaging: potential for the evaluation of cardiovascular function. *Am J Roentgenol.* 148: 239–246, 1987.

[23] Dumoulin CL & Hart HR: Magnetic resonance angiography. *Radiology.* 161: 717–720, 1986.

[24] Manning WJ & Pennell DJ: *Cardiovascular Magnetic Resonance.* Churchill Livingstone, Philadephia, 2002.

[25] Lardo AC, Fayad ZA, Chronos NA & Fuster V: *Cardiovascular Magnetic Resonance: Established and Emerging Applications.* Informa Healthcare, Martin Dunitz, London, 2003.

[26] Hoehn M, Küstermann E, Blunk J, Wiedermann D, Trapp T, Wecker S, Föcking M, Arnold H, Hescheler J, Fleischmann BK, Schwindt W & Bührle C: Monitoring of implanted stem cell migration in vivo: a highly resolved in vivo magnetic resonance imaging investigation of experimental stroke in rat. *Proc Natl Acad Sci USA.* 99: 16267–16272, 2002.

[27] Schmitz SA, Taupitz M, Wagner S, Coupland SE, Gust R, Nikolova A & Wolf KJ: Iron-oxide-enhanced magnetic resonance imaging of atherosclerotic plaques: postmortem analysis of accuracy, inter-observer agreement, and pitfalls. *Invest Radiol.* 37: 405–411, 2002.

[28] Garlick PB, Radda GK & Seeley PJ: Phosphorus NMR studies on perfused heart. *Biochem Biophys Res Commun.* 74: 1256–1262, 1977.

[29] Neubauer S: The failing heart - an engine out of fuel. *N Engl J Med.* 356: 1140–1151, 2007.

[30] Malloy CR, Sherry AD & Jeffrey FM: Evaluation of carbon flux and substrate selection through alternate pathways involving the citric acid cycle of the heart by ^{13}C NMR spectroscopy. *J Biol Chem.* 263: 6964–6971, 1988.

[31] Ardenkjaer-Larsen JH, Fridlund B, Gram A, Hansson G, Hansson L, Lerche MH, Servin R, Thaning M & Golman K: Increase in signal-to-noise ratio of $>$ 10,000 times in liquid-state NMR. *Proc Natl Acad Sci USA.* 100: 10158–10163, 2003.

[32] Golman K, in 't Zandt R & Thaning M: Real-time metabolic imaging. *Proc Natl Acad Sci USA.* 103: 11270–11275, 2006.

[33] Schroeder MA, Atherton HJ, Ball DR, Cole MA, Heather LC, Griffin JL, Clarke K, Radda GK & Tyler DJ: Real-time assessment of Krebs cycle metabolism using hyperpolarized ^{13}C magnetic resonance spectroscopy. *FASEB J*, 2009.

[34] Springer CS, Pike MM, Balschi JA, Chu SC, Frazier JC, Ingwall JS & Smith TW: Use of shift reagents for nuclear magnetic resonance studies of the kinetics of ion transfer in cells and perfused hearts. *Circulation.* 72: IV89–IV93, 1985.

[35] Buster DC, Castro MM, Geraldes CF, Malloy CR, Sherry AD & Siemers TC: $Tm(DOTP)^{5-}$: a $^{23}Na^{+}$ shift agent for perfused rat hearts. *Magn Reson Med.* 15: 25–32, 1990.

[36] Fishman JE, Joseph PM, Floyd TF, Mukherji B & Sloviter HA: Oxygen-sensitive ^{19}F NMR imaging of the vascular system in vivo. *Magn Reson Imaging.* 5: 279–285, 1987.

[37] Mason RP, Jeffrey FM, Malloy CR, Babcock EE & Antich PP: A noninvasive assessment of myocardial oxygen tension: ^{19}F NMR spectroscopy of sequestered perfluorocarbon emulsion. *Magn Reson Med.* 27: 310–317, 1992.

[38] Lorenz JN & Robbins J: Measurement of intraventricular pressure and cardiac performance in the intact closed-chest anesthetized mouse. *Am J Physiol.* 272: H1137–H1146, 1997.

[39] Kramer K, van Acker SA, Voss HP, Grimbergen JA, van der Vijgh WJ & Bast A: Use of telemetry to record electrocardiogram and heart rate in freely moving mice. *J Pharmacol Toxicol Methods.* 30: 209–215, 1993.

[40] Mansier P, Médigue C, Charlotte N, Vermeiren C, Coraboeuf E, Deroubai E, Ratner E, Chevalier B, Clairambault J, Carré F, Dahkli T, Bertin B, Briand P, Strosberg D & Swynghedauw B: Decreased heart rate variability in transgenic mice overexpressing atrial β_1-adrenoceptors. *Am J Physiol.* 271: H1465–H1472, 1996.

[41] Berul CI, Aronovitz MJ, Wang PJ & Mendelsohn ME: In vivo cardiac electrophysiology studies in the mouse. *Circulation.* 94: 2641–2648, 1996.

[42] James JF, Hewett TE & Robbins J: Cardiac physiology in transgenic mice. *Circ Res.* 82: 407–415, 1998.

[43] Kass DA, Hare JM & Georgakopoulos D: Murine cardiac function: a cautionary tail. *Circ Res.* 82: 519–522, 1998.

[44] Hoit BD: New approaches to phenotypic analysis in adult mice. *J Mol Cell Cardiol.* 33: 27–35, 2001.

[45] Iwase M, Uechi M, Vatner DE, Asai K, Shannon RP, Kudej RK, Wagner TE, Wight DC, Patrick TA, Ishikawa Y, Homcy CJ & Vatner SF: Cardiomyopathy induced by cardiac $G_s\alpha$ overexpression. *Am J Physiol.* 272: H585–H589, 1997.

[46] Gui YH, Linask KK, Khowsathit P & Huhta JC: Doppler echocardiography of normal and abnormal embryonic mouse heart. *Pediatr Res.* 40: 633–642, 1996.

[47] Florentine MS, Grosskreutz CL, Chang W, Hartnett JA, Dunn VD, Ehrhardt JC, Fleagle SR, Collins SM, Marcus ML & Skorton DJ: Measurement of left ventricular mass in vivo using gated nuclear magnetic resonance imaging. *J Am Coll Cardiol.* 8: 107–112, 1986.

[48] Cranney GB, Lotan CS, Dean L, Baxley W, Bouchard A & Pohost GM: Left ventricular volume measurement using cardiac axis nuclear magnetic resonance imaging. validation by calibrated ventricular angiography. *Circulation.* 82: 154–163, 1990.

[49] Siri FM, Jelicks LA, Leinwand LA & Gardin JM: Gated magnetic resonance imaging of normal and hypertrophied murine hearts. *Am J Physiol.* 272: H2394–H2402, 1997.

[50] Kubota T, McTiernan CF, Frye CS, Slawson SE, Lemster BH, Koretsky AP, Demetris AJ & Feldman AM: Dilated cardiomyopathy in transgenic mice with cardiac-specific overexpression of tumor necrosis factor α. *Circ Res.* 81: 627–635, 1997.

[51] Bryant D, Becker L, Richardson J, Shelton J, Franco F, Peshock R, Thompson M & Giroir B: Cardiac failure in transgenic mice with myocardial expression of tumor necrosis factor α. *Circulation.* 97: 1375–1381, 1998.

[52] Franco F, Dubois SK, Peshock RM & Shohet RV: Magnetic resonance imaging accurately estimates LV mass in a transgenic mouse model of cardiac hypertrophy. *Am J Physiol.* 274: H679–H683, 1998.

[53] Slawson SE, Roman BB, Williams DS & Koretsky AP: Cardiac MRI of the normal and hypertrophied mouse heart. *Magn Reson Med.* 39: 980–987, 1998.

[54] Ruff J, Wiesmann F, Hiller KH, Voll S, von Kienlin M, Bauer WR, Rommel E, Neubauer S & Haase A: Magnetic resonance microimaging for noninvasive quantification of myocardial function and mass in the mouse. *Magn Reson Med.* 40: 43–48, 1998.

[55] Wiesmann F, Ruff J, Hiller KH, Rommel E, Haase A & Neubauer S: Developmental changes of cardiac function and mass assessed with MRI in neonatal, juvenile, and adult mice. *Am J Physiol Heart Circ Physiol.* 278: H652–H657, 2000.

[56] Ruff J, Wiesmann F, Lanz T & Haase A: Magnetic resonance imaging of coronary arteries and heart valves in a living mouse: techniques and preliminary results. *J Magn Reson.* 146: 290–296, 2000.

[57] Chacko VP, Aresta F, Chacko SM & Weiss RG: MRI/MRS assessment of in vivo murine cardiac metabolism, morphology, and function at physiological heart rates. *Am J Physiol Heart Circ Physiol.* 279: H2218–H2224, 2000.

[58] Omerovic E, Basetti M, Bollano E, Bohlooly-Y M, Bohlooly M, Törnell J, Isgaard J, Hjalmarson A, Soussi B & Waagstein F: In vivo metabolic imaging of cardiac bioenergetics in transgenic mice. *Biochem Biophys Res Commun.* 271: 222–228, 2000.

[59] Wadghiri YZ & Helpern JA: MR of transgenic mice. *NMR Biomed.* 20: 151–153, 2007.

[60] Gödecke A, Flögel U, Zanger K, Ding Z, Hirchenhain J, Decking UK & Schrader J: Disruption of myoglobin in mice induces multiple compensatory mechanisms. *Proc Natl Acad Sci USA.* 96: 10495–10500, 1999.

[61] Wiesmann F, Neubauer S, Haase A & Hein L: Can we use vertical bore magnetic resonance scanners for murine cardiovascular phenotype characterization? Influence of upright body position on left ventricular hemodynamics in mice. *J Cardiovasc Magn Reson.* 3: 311–315, 2001.

[62] Jacoby C, Molojavyi A, Flögel U, Merx MW, Ding Z & Schrader J: Direct comparison of magnetic resonance imaging and conductance microcatheter in the evaluation of left ventricular function in mice. *Basic Res Cardiol.* 101: 87–95, 2006.

[63] Saupe KW, Spindler M, Tian R & Ingwall JS: Impaired cardiac energetics in mice lacking muscle-specific isoenzymes of creatine kinase. *Circ Res.* 82: 898–907, 1998.

[64] Flögel U, Decking UK, Gödecke A & Schrader J: Contribution of NO to ischemia-reperfusion injury in the saline-perfused heart: A study in endothelial NO synthase knockout mice. *J Mol Cell Cardiol.* 31: 827–836, 1999.

[65] Malloy CR, Thompson JR, Jeffrey FM & Sherry AD: Contribution of exogenous substrates to acetyl coenzyme A: measurement by ^{13}C NMR under non-steady-state conditions. *Biochemistry.* 29: 6756–6761, 1990.

[66] Wittenberg BA & Wittenberg JB: Transport of oxygen in muscle. *Annu Rev Physiol.* 51: 857–878, 1989.

[67] Garry DJ, Ordway GA, Lorenz JN, Radford NB, Chin ER, Grange RW, Bassel-Duby R & Williams RS: Mice without myoglobin. *Nature.* 395: 905–908, 1998.

[68] Patel DJ, Kampa L, Shulman RG, Yamane T & Wyluda BJ: Proton nuclear magnetic resonance studies of myoglobin in H_2O. *Proc Natl Acad Sci USA.* 67: 1109–1115, 1970.

[69] Kreutzer U, Wang DS & Jue T: Observing the ^1H NMR signal of the myoglobin Val-E11 in myocardium: an index of cellular oxygenation. *Proc Natl Acad Sci USA.* 89: 4731–4733, 1992.

[70] Merx MW, Flögel U, Stumpe T, Gödecke A, Decking UK & Schrader J: Myoglobin facilitates oxygen diffusion. *FASEB J.* 15: 1077–1079, 2001.

[71] La Mar GN, Budd DL, Smith KM & Langry KC: Nuclear magnetic resonance of high-spin ferric hemoproteins. assignment of proton resonances in met-aquo myoglobins using deuterium-labeled hemes. *J Am Chem Soc.* 102: 1822–1827, 1980.

[72] Chung Y, Xu D & Jue T: Nitrite oxidation of myoglobin in perfused myocardium: implications for energy coupling in respiration. *Am J Physiol.* 271: H1166–H1173, 1996.

[73] Richardson RS, Noyszewski EA, Kendrick KF, Leigh JS & Wagner PD: Myoglobin O_2 desaturation during exercise. Evidence of limited O_2 transport. *J Clin Invest.* 96: 1916–1926, 1995.

[74] Arai AE, Kasserra CE, Territo PR, Gandjbakhche AH & Balaban RS: Myocardial oxygenation in vivo: optical spectroscopy of cytoplasmic myoglobin and mitochondrial cytochromes. *Am J Physiol.* 277: H683–H697, 1999.

[75] Schenkman KA, Marble DR, Burns DH & Feigl EO: Myoglobin oxygen dissociation by multiwavelength spectroscopy. *J Appl Physiol.* 82: 86–92, 1997.

[76] Ignarro LJ, Fukuto JM, Griscavage JM, Rogers NE & Byrns RE: Oxidation of nitric oxide in aqueous solution to nitrite but not nitrate: comparison with enzymatically formed nitric oxide from L-arginine. *Proc Natl Acad Sci USA.* 90: 8103–8107, 1993.

[77] Ignarro LJ, Buga GM, Wood KS, Byrns RE & Chaudhuri G: Endothelium-derived relaxing factor produced and released from artery and vein is nitric oxide. *Proc Natl Acad Sci USA.* 84: 9265–9269, 1987.

[78] Doyle MP & Hoekstra JW: Oxidation of nitrogen oxides by bound dioxygen in hemoproteins. *J Inorg Biochem.* 14: 351–358, 1981.

[79] Giuffrè A, Sarti P, D'Itri E, Buse G, Soulimane T & Brunori M: On the mechanism of inhibition of cytochrome c oxidase by nitric oxide. *J Biol Chem.* 271: 33404–33408, 1996.

[80] Wunderlich C, Flögel U, Gödecke A, Heger J & Schrader J: Acute inhibition of myoglobin impairs contractility and energy state of iNOS-overexpressing hearts. *Circ Res.* 92: 1352–1358, 2003.

[81] Gödecke A, Molojavyi A, Heger J, Flögel U, Ding Z, Jacoby C & Schrader J: Myoglobin protects the heart from inducible nitric-oxide synthase (iNOS)-mediated nitrosative stress. *J Biol Chem.* 278: 21761–21766, 2003.

[82] Flögel U, Merx MW, Gödecke A, Decking UK & Schrader J: Myoglobin: A scavenger of bioactive NO. *Proc Natl Acad Sci USA*. 98: 735–740, 2001.

[83] Heger J, Gödecke A, Flögel U, Merx MW, Molojavyi A, Kühn-Velten WN & Schrader J: Cardiac-specific overexpression of inducible nitric oxide synthase does not result in severe cardiac dysfunction. *Circ Res*. 90: 93–99, 2002.

[84] Neubauer S, Krahe T, Schindler R, Horn M, Hillenbrand H, Entzeroth C, Mader H, Kromer EP, Riegger GA & Lackner K: ^{31}P magnetic resonance spectroscopy in dilated cardiomyopathy and coronary artery disease. Altered cardiac high-energy phosphate metabolism in heart failure. *Circulation*. 86: 1810–1818, 1992.

[85] Conway MA, Bottomley PA, Ouwerkerk R, Radda GK & Rajagopalan B: Mitral regurgitation: impaired systolic function, eccentric hypertrophy, and increased severity are linked to lower phosphocreatine/ATP ratios in humans. *Circulation*. 97: 1716–1723, 1998.

[86] Ingwall JS & Weiss RG: Is the failing heart energy starved? On using chemical energy to support cardiac function. *Circ Res*. 95: 135–145, 2004.

[87] Cosby K, Partovi KS, Crawford JH, Patel RP, Reiter CD, Martyr S, Yang BK, Waclawiw MA, Zalos G, Xu X, Huang KT, Shields H, Kim-Shapiro DB, Schechter AN, Cannon RO & Gladwin MT: Nitrite reduction to nitric oxide by deoxyhemoglobin vasodilates the human circulation. *Nat Med*. 9: 1498–1505, 2003.

[88] Ross J: Myocardial perfusion-contraction matching. implications for coronary heart disease and hibernation. *Circulation*. 83: 1076–1083, 1991.

[89] Flögel U, Fago A & Rassaf T: Keeping the heart in balance: the functional interactions of myoglobin with nitrogen oxides. *J Exp Biol*. 213: 2726–2733, 2010.

[90] George P & Irvine DH: Reaction of metmyoglobin with hydrogen peroxide. *Nature*. 168: 164–165, 1951.

[91] Keilin D & Hartree EF: Catalase, peroxidase and metmyoglobin as catalysts of coupled peroxidatic reactions. *Biochem J*. 60: 310–325, 1955.

[92] Patel RP, Svistunenko DA, Darley-Usmar VM, Symons MC & Wilson MT: Redox cycling of human methaemoglobin by H_2O_2 yields persistent ferryl iron and protein based radicals. *Free Radic Res*. 25: 117–123, 1996.

[93] Arduini A & Hochstein P: *Oxidative Damage and Repair* chap. Myoglobin, a double-edged sword in myocardial infarction., pp. 406–414 Pergamon, Oxford, 1991.

[94] McCord JM: Oxygen-derived free radicals in postischemic tissue injury. *N Engl J Med*. 312: 159–163, 1985.

[95] Flaherty JT & Weisfeldt ML: Reperfusion injury. *Free Radic Biol Med*. 5: 409–419, 1988.

[96] Li Y, Zhu H, Kuppusamy P, Roubaud V, Zweier JL & Trush MA: Validation of lucigenin (bis-N-methylacridinium) as a chemilumigenic probe for detecting superoxide anion radical production by enzymatic and cellular systems. *J Biol Chem*. 273: 2015–2023, 1998.

[97] Ichihara K & Abiko Y: Rebound recovery of myocardial creatine phosphate with reperfusion after ischemia. *Am Heart J*. 108: 1594–1597, 1984.

[98] Flaherty JT, Weisfeldt ML, Bulkley BH, Gardner TJ, Gott VL & Jacobus WE: Mechanisms of ischemic myocardial cell damage assessed by phosphorus-31 nuclear magnetic resonance. *Circulation*. 65: 561–570, 1982.

[99] Banerjee A, Grosso MA, Brown JM, Rogers KB & Whitman GJ: Oxygen metabolite effects on creatine kinase and cardiac energetics after reperfusion. *Am J Physiol.* 261: H590–H597, 1991.

[100] Kaplan LJ, Blum H, Bellows CF, Banerjee A & Whitman GJ: Reversible injury: creatinine kinase recovery restores bioenergetics and function. *J Surg Res.* 62: 103–108, 1996.

[101] Wittenberg JB & Wittenberg BA: Myoglobin function reassessed. *J Exp Biol.* 206: 2011–2020, 2003.

[102] Cossins A & Berenbrink M: Physiology: Myoglobin's new clothes. *Nature.* 454: 416–417, 2008.

[103] Garlick PB, Davies MJ, Hearse DJ & Slater TF: Direct detection of free radicals in the reperfused rat heart using electron spin resonance spectroscopy. *Circ Res.* 61: 757–760, 1987.

[104] Wang P & Zweier JL: Measurement of nitric oxide and peroxynitrite generation in the postischemic heart. evidence for peroxynitrite-mediated reperfusion injury. *J Biol Chem.* 271: 29223–29230, 1996.

[105] Hendgen-Cotta UB, Merx MW, Shiva S, Schmitz J, Becher S, Klare JP, Steinhoff HJ, Goedecke A, Schrader J, Gladwin MT, Kelm M & Rassaf T: Nitrite reductase activity of myoglobin regulates respiration and cellular viability in myocardial ischemia-reperfusion injury. *Proc Natl Acad Sci USA.* 105: 10256–10261, 2008.

[106] Sun Y, Jin K, Mao XO, Zhu Y & Greenberg DA: Neuroglobin is up-regulated by and protects neurons from hypoxic-ischemic injury. *Proc Natl Acad Sci USA.* 98: 15306–15311, 2001.

[107] Shivapurkar N, Stastny V, Okumura N, Girard L, Xie Y, Prinsen C, Thunnissen FB, Wistuba II, Czerniak B, Frenkel E, Roth JA, Liloglou T, Xinarianos G, Field JK, Minna JD & Gazdar AF: Cytoglobin, the newest member of the globin family, functions as a tumor suppressor gene. *Cancer Res.* 68: 7448–7456, 2008.

[108] Hoppeler H: Skeletal muscle substrate metabolism. *Int J Obes Relat Metab Disord.* 23 Suppl 3: S7–10, 1999.

[109] Lopaschuk GD, Belke DD, Gamble J, Itoi T & Schönekess BO: Regulation of fatty acid oxidation in the mammalian heart in health and disease. *Biochim Biophys Acta.* 1213: 263–276, 1994.

[110] Sambandam N, Lopaschuk GD, Brownsey RW & Allard MF: Energy metabolism in the hypertrophied heart. *Heart Fail Rev.* 7: 161–173, 2002.

[111] O'Brien PJ & Gwathmey JK: Myocardial Ca^{2+}- and ATP-cycling imbalances in end-stage dilated and ischemic cardiomyopathies. *Cardiovasc Res.* 30: 394–404, 1995.

[112] Suga H: Ventricular energetics. *Physiol Rev.* 70: 247–277, 1990.

[113] Korvald C, Elvenes OP & Myrmel T: Myocardial substrate metabolism influences left ventricular energetics in vivo. *Am J Physiol Heart Circ Physiol.* 278: H1345–H1351, 2000.

[114] Frauenfelder H, McMahon BH, Austin RH, Chu K & Groves JT: The role of structure, energy landscape, dynamics, and allostery in the enzymatic function of myoglobin. *Proc Natl Acad Sci USA.* 98: 2370–2374, 2001.

[115] Ørngreen MC, Nørgaard MG, Sacchetti M, van Engelen BGM & Vissing J: Fuel utilization in patients with very long-chain acyl-CoA dehydrogenase deficiency. *Ann Neurol.* 56: 279–283, 2004.

[116] Spiekerkoetter U, Lindner M, Santer R, Grotzke M, Baumgartner MR, Boehles H, Das A, Haase C, Hennermann JB, Karall D, de Klerk H, Knerr I, Koch HG, Plecko B, Röschinger W, Schwab KO, Scheible D, Wijburg FA, Zschocke J, Mayatepek E & Wendel U: Management and outcome in 75 individuals with long-chain fatty acid oxidation defects: results from a workshop. *J Inherit Metab Dis.* 32: 488–497, 2009.

[117] Roe CR, Sweetman L, Roe DS, David F & Brunengraber H: Treatment of cardiomyopathy and rhabdomyolysis in long-chain fat oxidation disorders using an anaplerotic odd-chain triglyceride. *J Clin Invest.* 110: 259–269, 2002.

[118] Moonen CT, Dimand RJ & Cox KL: The noninvasive determination of linoleic acid content of human adipose tissue by natural abundance carbon-13 nuclear magnetic resonance. *Magn Reson Med.* 6: 140–157, 1988.

[119] Künnecke B, Verry P, Bénardeau A & von Kienlin M: Quantitative body composition analysis in awake mice and rats by magnetic resonance relaxometry. *Obes Res.* 12: 1604–1615, 2004.

[120] Calder PC: n-3 polyunsaturated fatty acids, inflammation, and inflammatory diseases. *Am J Clin Nutr.* 83: 1505S–1519S, 2006.

[121] Harris WS, Miller M, Tighe AP, Davidson MH & Schaefer EJ: Omega-3 fatty acids and coronary heart disease risk: clinical and mechanistic perspectives. *Atherosclerosis.* 197: 12–24, 2008.

[122] Massaro M, Scoditti E, Carluccio MA & Caterina RD: Basic mechanisms behind the effects of n-3 fatty acids on cardiovascular disease. *Prostaglandins Leukot Essent Fatty Acids.* 79: 109–115, 2008.

[123] Mori TA & Beilin LJ: Omega-3 fatty acids and inflammation. *Curr Atheroscler Rep.* 6: 461–467, 2004.

[124] Swift LL, Hill JO, Peters JC & Greene HL: Medium-chain fatty acids: evidence for incorporation into chylomicron triglycerides in humans. *Am J Clin Nutr.* 52: 834–836, 1990.

[125] Guo W, Xie W & Han J: Modulation of adipocyte lipogenesis by octanoate: involvement of reactive oxygen species. *Nutr Metab (Lond).* 3: 30, 2006.

[126] Guillot E, Vaugelade P, Lemarchal P & Rérat A: Intestinal absorption and liver uptake of medium-chain fatty acids in non-anaesthetized pigs. *Br J Nutr.* 69: 431–442, 1993.

[127] Tucci S, Primassin S, Veld FT & Spiekerkoetter U: Medium-chain triglycerides impair lipid metabolism and induce hepatic steatosis in very long-chain acyl-CoA dehydrogenase (VLCAD)-deficient mice. *Mol Genet Metab.* 101: 40–47, 2010.

[128] Turner N, Hariharan K, TidAng J, Frangioudakis G, Beale SM, Wright LE, Zeng XY, Leslie SJ, Li JY, Kraegen EW, Cooney GJ & Ye JM: Enhancement of muscle mitochondrial oxidative capacity and alterations in insulin action are lipid species dependent: potent tissue-specific effects of medium-chain fatty acids. *Diabetes.* 58: 2547–2554, 2009.

[129] Tucci S, Flögel U, Sturm M, Borsch E & Spiekerkoetter U: Disrupted fat distribution and composition due to medium-chain triglycerides in mice with a β-oxidation defect. *Am J Clin Nutr.* 94: 311–322, 2011.

[130] Nagao K & Yanagita T: Medium-chain fatty acids: functional lipids for the prevention and treatment of the metabolic syndrome. *Pharmacol Res.* 61: 208–212, 2010.

[131] Hill JO, Peters JC, Swift LL, Yang D, Sharp T, Abumrad N & Greene HL: Changes in blood lipids during six days of overfeeding with medium or long chain triglycerides. *J Lipid Res.* 31: 407–416, 1990.

[132] Beverley D & Arthur R: Fatty liver and medium chain triglyceride (MCT) diet. *Arch Dis Child.* 63: 840–842, 1988.

[133] Weissleder R, Elizondo G, Wittenberg J, Rabito CA, Bengele HH & Josephson L: Ultrasmall superparamagnetic iron oxide: characterization of a new class of contrast agents for MR imaging. *Radiology.* 175: 489–493, 1990.

[134] Jander S, Schroeter M & Saleh A: Imaging inflammation in acute brain ischemia. *Stroke.* 38: 642–645, 2007.

[135] Flögel U, Ding Z, Hardung H, Jander S, Reichmann G, Jacoby C, Schubert R & Schrader J: In vivo monitoring of inflammation after cardiac and cerebral ischemia by fluorine magnetic resonance imaging. *Circulation.* 118: 140–148, 2008.

[136] Li XC, Miyasaka M & Issekutz TB: Blood monocyte migration to acute lung inflammation involves both CD11/CD18 and very late activation antigen-4-dependent and independent pathways. *J Immunol.* 161: 6258–6264, 1998.

[137] Reutershan J, Basit A, Galkina EV & Ley K: Sequential recruitment of neutrophils into lung and bronchoalveolar lavage fluid in LPS-induced acute lung injury. *Am J Physiol Lung Cell Mol Physiol.* 289: L807–L815, 2005.

[138] Ebner B, Behm P, Jacoby C, Burghoff S, French BA, Schrader J & Flögel U: Early assessment of pulmonary inflammation by ^{19}F MRI in vivo. *Circ Cardiovasc Imaging.* 3: 202–210, 2010.

[139] Wyburn KR, Jose MD, Wu H, Atkins RC & Chadban SJ: The role of macrophages in allograft rejection. *Transplantation.* 80: 1641–1647, 2005.

[140] Russell ME, Hancock WW, Wallace AF, Wyner LR & Karnovsky MJ: Modulation of inflammatory activation pathways in the Lewis-to-F-344 rat chronic cardiac rejection model. *Transplant Proc.* 27: 2100–2104, 1995.

[141] Wasowska BA, Qian Z, Cangello DL, Behrens E, Tran KV, Layton J, Sanfilippo F & Baldwin WM: Passive transfer of alloantibodies restores acute cardiac rejection in IgKO mice. *Transplantation.* 71: 727–736, 2001.

[142] Hasegawa T, Bouïs D, Liao H, Visovatti SH & Pinsky DJ: Ecto-5' nucleotidase (CD73)-mediated adenosine generation and signaling in murine cardiac allograft vasculopathy. *Circ Res.* 103: 1410–1421, 2008.

[143] Ahrens ET, Flores R, Xu H & Morel PA: In vivo imaging platform for tracking immunotherapeutic cells. *Nat Biotechnol.* 23: 983–987, 2005.

[144] Krafft MP & Riess JG: Chemistry, physical chemistry, and uses of molecular fluorocarbon − hydrocarbon diblocks, triblocks, and related compounds − unique „apolar" components for self-assembled colloid and interface engineering. *Chem Rev.* 109: 1714–1792, 2009.

[145] Wu YL, Ye Q, Foley LM, Hitchens TK, Sato K, Williams JB & Ho C: In situ labeling of immune cells with iron oxide particles: an approach to detect organ rejection by cellular MRI. *Proc Natl Acad Sci USA.* 103: 1852–1857, 2006.

[146] Spahn DR: Blood substitutes. Artificial oxygen carriers: perfluorocarbon emulsions. *Crit Care.* 3: R93–R97, 1999.

[147] Flögel U, Jacoby C, Gödecke A & Schrader J: In vivo 2D mapping of impaired murine cardiac energetics in NO-induced heart failure. *Magn Reson Med.* 57: 50–58, 2007.

[148] Jacoby C, Böring YC, Beck A, Zernecke A, Aurich V, Weber C, Schrader J & Flögel U: Dynamic changes in murine vessel geometry assessed by high-resolution magnetic resonance angiography: a 9.4T study. *J Magn Reson Imaging.* 28: 637–645, 2008.

Danksagung

Mein herzlicher Dank gilt

- Professor Dr. Jürgen Schrader für seine stete Förderung meiner wissenschaftlichen Arbeit, die Vielzahl von Anregungen und wertvollen Diskussionen sowie die exzellenten Arbeitsbedingungen im Institut für Herz- und Kreislaufphysiologie und später im Institut für Molekulare Kardiologie,
- Dr. Christoph Jacoby für seine Hilfe und Geduld bei den vielen Experimenten, Programmierarbeiten und Nachsitzungen,
- Prof. Dr. Axel Gödecke für die hervorragende Zusammenarbeit in zahlreichen Projekten und viele stimulierende Diskussionen,
- Prof. Dr. Ulrich Decking, der mir insbesondere in der Anfangszeit mit viel Geduld half, mich an die medizinische Welt zu gewöhnen,
- Dr. Zhaoping Ding, ohne dessen mikrochirurgisches Geschick vieler der *in vivo* Experimente undurchführbar gewesen wären,
- Dr. Nadine Abanador, Dr. Yang Chul Böring, Patrick Behm, Inga Kreideweiß und Lisa Galbarz, die ich im Rahmen Ihrer Doktorarbeiten betreut habe, und deren Mitarbeit wesentlich zur Erhebung einer Vielzahl von Daten für diese Arbeit beigetragen hat,
- allen aktuellen und ehemaligen Mitarbeitern des Instituts für Herz- und Kreislaufphysiologie sowie des Instituts für Molekulare Kardiologie für Ihre Hilfsbereitschaft, Kooperation und die angenehme Arbeitsatmosphäre,
- den Mitarbeitern der Glasbläser- und der mechanischen Werkstatt, insbesondere Herrn Stefan Schätz, für die Erfüllung (fast) aller Sonderwünsche,
- allen externen Kooperationspartnern, ohne die viele interessante Projekte überhaupt nicht zustande gekommen wären: insbesondere den Arbeitsgruppen von Prof. Dr. Rolf Schubert in Freiburg für ihre Hilfe bei der Erstellung der PFC-Emulsionen, von Prof. Dr. Oliver Witzke aus Essen für die Zusammenarbeit bei dem Herztransplantationsprojekt sowie von Prof. Dr. Ute Spiekerkötter für die gute Kooperation bei dem VLCAD-Projekt.

Ausgewählte Originalarbeiten

1. Flögel U, Merx MW, Gödecke A, Decking UK & Schrader J: Myoglobin: A scavenger of bioactive NO. *Proc Natl Acad Sci USA.* 98: 735–740, 2001.

2. Flögel U, Gödecke A, Klotz LO & Schrader J: Role of myoglobin in the antioxidant defense of the heart. *FASEB J.* 18: 1156–1158, 2004.

3. Flögel U*, Laussmann T*, Gödecke A, Abanador N, Schäfers M, Fingas CD, Metzger S, Levkau B, Jacoby C & Schrader J: Lack of myoglobin causes a switch in cardiac substrate selection. *Circ Res.* 96: e68–e75, 2005.

4. Flögel U, Jacoby C, Gödecke A & Schrader J: In vivo 2D mapping of impaired murine cardiac energetics in NO-induced heart failure. *Magn Reson Med.* 57: 50–58, 2007.

5. Rassaf T*, Flögel U*, Drexhage C, Hendgen-Cotta U, Kelm M & Schrader J: Nitrite reductase function of deoxymyoglobin: oxygen sensor and regulator of cardiac energetics and function. *Circ Res.* 100: 1749–1754, 2007.

6. Flögel U, Ding Z, Hardung H, Jander S, Reichmann G, Jacoby C, Schubert R & Schrader J: In vivo monitoring of inflammation after cardiac and cerebral ischemia by fluorine magnetic resonance imaging. *Circulation.* 118: 140–148, 2008.

7. Tucci S*, Flögel U*, Sturm M, Borsch E & Spiekerkoetter U: Disrupted fat distribution and composition due to medium-chain triglycerides in mice with a β-oxidation defect. *Am J Clin Nutr.* 94: 439-449, 2011.

8. Flögel U, Su S, Kreideweiss I, Ding Z, Galbarz L, Fu J, Jacoby C, Witzke O & Schrader J: Non-invasive detection of graft rejection by in vivo ^{19}F MRI in the early stage. *Am J Transplant.* 11: 235–244, 2011.

*Both authors contributed equally to this study.

Myoglobin: A scavenger of bioactive NO

Ulrich Flögel, Marc W. Merx, Axel Gödecke, Ulrich K. M. Decking, and Jürgen Schrader*

Institute for Cardiovascular Physiology, Heinrich-Heine-University, 40225 Düsseldorf, Germany

Edited by Louis J. Ignarro, University of California, Los Angeles, CA, and approved November 9, 2000 (received for review September 27, 2000)

The present study explored the role of myoglobin (Mb) in cardiac NO homeostasis and its functional relevance by employing isolated hearts of wild-type (WT) and myoglobin knockout mice. ^{1}H NMR spectroscopy was used to measure directly the conversion of oxygenated Mb (MbO_2) to metmyoglobin (metMb) by reaction with NO. NO was applied intracoronarily (5 nM to 25 μM), or its endogenous production was stimulated with bradykinin (Bk; 10 nM to 2 μM). We found that infusion of authentic NO solutions dose-dependently ($\geq$ 2.5 μM NO) increased metMb formation in WT hearts that was rapidly reversible on cessation of NO infusion. Likewise, Bk-induced release of NO was associated with significant metMb formation in the WT ($\geq$1 μM Bk). Hearts lacking Mb reacted more sensitively to infused NO in that vasodilatation and the cardiodepressant actions of NO were more pronounced. Similar results were obtained with Bk. The lower sensitivity of WT hearts to changes in NO concentration fits well with the hypothesis that in the presence of Mb, a continuous degradation of NO takes place by reaction of MbO_2 + NO to metMb + NO_3^-, thereby effectively reducing cytosolic NO concentration. This breakdown protects myocytic cytochromes against transient rises in cytosolic NO. Regeneration of metMb by metMb reductase to Mb and subsequent association with O_2 leads to reformation of MbO_2 available for another NO degradation cycle. Our data indicate that this cycle is crucial in the breakdown of NO and substantially determines the dose–response curve of the NO effects on coronary blood flow and cardiac contractility.

Myoglobin (Mb) is an important intracellular O_2-binding hemoprotein found in the cytoplasm of vertebrate type I and IIa skeletal and cardiac muscle tissue (1). As a major breakthrough in understanding globular protein structure, its tertiary structure was derived from x-ray diffraction studies by John Kendrew and his colleagues as early as the 1950s (2). Mb is a relatively small (M_r 16,700) and densely packed protein consisting of a single polypeptide chain of 153 amino acid residues. It contains an iron-porphyrin heme group identical to that of hemoglobin (Hb), and like Hb is capable of reversible oxygenation and deoxygenation. In mammals, half O_2 saturation of Mb is achieved at an intracellular O_2 partial pressure as low as 2.4 mmHg (1 mmHg = 133 Pa; ref. 3), suggesting a predominance of oxygenated Mb (MbO_2) under basal conditions.

Mb's function as an oxygen store is well accepted. Mb serves as a short-term O_2 reservoir in exercising skeletal muscle and in the beating heart, tiding the muscle over from one contraction to the next (4). In diving mammals, the concentrations of Mb exceed those of terrestrial mammals up to 10-fold, and Mb most likely serves for the extension of diving time when pulmonary ventilation ceases (5). Similarly, in mammals and humans adapted to high altitudes, Mb is expressed in high concentrations in skeletal muscle (6).

It has been proposed that Mb facilitates intracellular delivery of O_2, in that Mb adjacent to the cell membrane picks up oxygen, traverses the cytosol by translational diffusion to unload O_2 in the vicinity of mitochondria, and finally diffuses back to the cell membrane in the deoxygenated state (7). This circuit, termed "facilitated O_2 diffusion," may be a critical link between capillary O_2 supply and O_2-consuming cytochromes within mitochondria in the steady state. Facilitated O_2 diffusion has been unambiguously demonstrated in concentrated Mb solutions (8), but experiments carried out in isolated cells, papillary muscle, and at the whole organ level have yielded conflicting results (9–11). Likewise, model calculations have both refuted and supported the contribution of Mb-bound O_2 to total O_2 flux (11, 12).

The recent generation of transgenic mice lacking Mb has shed new light on the role of Mb in the intracellular delivery of O_2 (13, 14). Loss of Mb led to a surprisingly benign phenotype, with exercise and reproductive capacity, as well as cardiac and skeletal function, largely unaltered (13). Maintenance of function was accomplished by the activation of numerous compensatory mechanisms (14). However, direct evidence for an important role of Mb in facilitating O_2 diffusion was only recently produced by experiments employing CO to acutely inactivate Mb in the isolated wild-type (WT) heart by using hearts of Mb knockout ($myo^{-/-}$) mice as appropriate controls (15). Additionally, supportive evidence is derived from observations on single isolated cardiomyocytes (15, 16).

Mb is a molecular relative of Hb and together these hemoproteins play vital roles in one of the most important aspects of animal metabolism: the acquisition and utilization of O_2. With the advent of NO research there is now also abundant literature about the interaction of Hb with NO. It is generally accepted that Hb is crucial for oxidative inactivation of NO by reaction to nitrate and methemoglobin (17). However, the role of Hb, through *S*-nitrosothiol formation, in providing a protected route for delivery of bioactive NO is a matter of intense debate (18, 19). A comparison of the kinetic and thermodynamic properties of NO interactions with Mb and Hb (derived from *in vitro* investigations) reveals similar data for NO association and dissociation as well as for chemical reactions for both proteins (for review, see ref. 20), suggesting similar biological functions in NO homeostasis. However, there are at present no studies on the role of Mb in the *in vivo* metabolism of NO. Likewise, it is not known whether the presence of Mb alters the biological response to NO, whether exogenously supplied or endogenously formed.

The aim of the present study was to explore the role of Mb in cardiac NO homeostasis by using isolated hearts of WT and $myo^{-/-}$ mice, recently generated in our laboratory (14), as models. We were able to directly measure the NO-induced conversion of MbO_2 to metmyoglobin (metMb) in the WT heart with ^{1}H NMR spectroscopy. Furthermore, we found that Mb is important in the inactivation of NO and substantially determines the dose–response curve of the NO effects on coronary blood flow and cardiac contractility.

PHYSIOLOGY

This paper was submitted directly (Track II) to the PNAS office.

Abbreviations: Mb, myoglobin; Bk, bradykinin; ETU, *S*-ethylisothiourea; $myo^{-/-}$, myoglobin knockout mice; L-NMMA, N^G-monomethyl-L-arginine methyl ester; LVDP, left ventricular developed pressure; MbO_2, oxygenated myoglobin; metMb, metmyoglobin; PCr, phosphocreatine; WT, wild type.

*To whom reprint requests should be addressed at: Institut für Herz-und Kreislaufphysiologie, Heinrich-Heine-Universität Düsseldorf, Universitätsstrasse 1, 40225 Düsseldorf, Germany. E-mail: schrader@uni-duesseldorf.de.

The publication costs of this article were defrayed in part by page charge payment. This article must therefore be hereby marked "*advertisement*" in accordance with 18 U.S.C. §1734 solely to indicate this fact.

Article published online before print: *Proc. Natl. Acad. Sci. USA*, 10.1073/pnas.011460298. Article and publication date are at www.pnas.org/cgi/doi/10.1073/pnas.011460298

Materials and Methods

Animals. Myo$^{-/-}$ mice were generated by deletion of the essential exon-2 via homologous recombination in embryonic stem cells, as described (14). Body weight ranged from 27 to 38 g and heart weight ranged from 170 to 250 mg, with no significant differences between the two groups.

Langendorff Experimental Setup for NMR Measurements. The preparation of murine hearts and retrograde perfusion at constant pressure of 100 mmHg with modified Krebs–Henseleit buffer—gassed at 95% O_2/5% CO_2 (carbogen), resulting in a pH of 7.4—were performed essentially as described (21). In brief, mice were injected with 250 units of heparin i.p. and anesthetized with urethane (1.5 g/kg) i.p. Hearts were rapidly excised and the aortas were cannulated. Nonrecirculating perfusion at 100 mmHg was initiated. Each heart was placed inside a 10-mm NMR tube and transferred into a heated (37°C) 10-mm probe inside a Bruker AMX 400-MHz WB NMR spectrometer. Perfusion pressure, coronary flow, and left ventricular developed pressure (LVDP) were measured continuously, the latter via a home-made fluid-filled balloon inserted into the left ventricle. Signals were recorded by using a PC with dedicated software (EMKA Technologies, Paris). After hearts stabilized inside the magnet, cardiac pacing (500 beats per min) was initiated and continued throughout. Left ventricular end-diastolic pressure was set to 5 mmHg. After the onset of cardiac pacing (30 min), the coronary perfusion rate was fixed to the steady flow already established and was maintained constant. After the switch to constant flow, baseline spectra were recorded. Subsequently, solutions with increasing concentrations of NO (5 nM to 25 μM), Bk (10 nM to 2 μM), adenosine (5–500 nM), N^G-monomethyl-L-arginine methyl ester (L-NMMA; 100 μM), or *S*-ethylisothiourea (ETU; 50 μM) were infused stepwise, and hemodynamic data as well as NMR spectra were acquired. After application of the highest respective concentration, infusion was stopped, hearts were allowed to recover for 10 min, and data/spectra were collected once more.

Infusion of NO Solutions. Aqueous solutions of NO were prepared essentially as described (22). Briefly, argon (quality = 5.0, >99.99%; Linde, Unterschleissheim, Germany) was passed through a closed all-glass system, composed of two scrubbing bottles, one containing an alkaline pyrogallol solution (5%, wt/vol) to remove traces of oxygen, and the other one containing potassium hydroxide (10%, wt/vol) to scavenge higher oxides of nitrogen. The bottles were connected in series with a three-necked beaker containing saline (0.9% NaCl) to dissolve NO. After flushing with argon for 30 min, the gas flow was switched to NO (quality = 3.0, >99.9%; AGA Gas, Hamburg, Germany) and maintained for an additional 45 min. Aliquots were transferred to air-tight syringes through a septum. The system was kept under positive pressure with NO to avoid changes in NO concentration because of re-equilibration between the aqueous and gas phases. Concentrations ranged between 1.6 and 1.9 mM NO, depending on the ambient pressure and temperature.

Dilutions were made in deoxygenated and argon-flushed saline, and concentrations were determined immediately before application by injecting 200 μl of the samples into a NO chemiluminescence analyzer (Sievers Instruments, Boulder, CO). Infusion of the NO solutions was performed by using air-tight fused-silica capillaries (inside diameter 0.2 mm; Supelco, Deisenhofen, Germany), the ends of which were positioned right in front of the aorta to minimize the contact time of NO solution and oxygenated buffer.

NMR Spectroscopy. Spectra were recorded by a Bruker AMX 400 WB NMR spectrometer, operating at frequencies of 400 MHz for ^{1}H and 161.97 MHz for ^{31}P. Shimming was done on the free-induction decay of the water signal. A line width at half height of 15 Hz could be routinely obtained.

^{1}H NMR. For selective excitation of the MbO_2 and metMb resonances at −2 to −4 ppm (23, 24), the standard $1\bar{3}3\bar{1}$ pulse sequence of the Bruker library was used. The delay for binomial H_2O suppression was set to 166 μs, resulting in maximal excitation of the region of interest. A 45° pulse (12.5 μs, estimated from the H_2O signal) was used; 16K transients were averaged for a typical ^{1}H NMR spectrum requiring 15 min of signal accumulation (acquisition time, 42 ms; sweep width, 12,195 Hz; data size, 1K; zero filling to 2K; exponential weighting resulting in a 40-Hz line broadening; chemical shifts were referenced to the H_2O resonance at 4.8 ppm). For Bk experiments 4K transients (≈4 min accumulation time) were averaged. Excitation with the $1\bar{3}3\bar{1}$ sequence led to large phase dispersion resulting in positive lipid signals and negative signals for the MbO_2 and metMb resonances (compare to ref. 15; for a theoretical explanation, see ref. 25). For a better presentation, these signals were inverted in Fig. 1 and Fig. 5. Relative peak areas were obtained by integration after baseline correction.

^{31}P NMR. Transients (n = 240) were accumulated with a 75° flip angle, a repetition time of 1 s, a spectral width of 5,882 Hz, a data size of 4K, zero filling to 8K, and exponential weighting resulting in a 10-Hz line broadening (≈4 min of signal accumulation). Chemical shifts were referenced to the phosphocreatine (PCr) resonance at −2.52 ppm. Relative peak areas were obtained by integration. These areas were scaled according to saturation factors of the respective phosphorus compounds determined from fully relaxed ^{31}P NMR spectra in control experiments for each strain.

After equilibration of the hearts within the magnet, NMR spectra were continuously recorded. For absolute quantification, baseline spectra of each experiment were related to the respective HPLC and SDS/PAGE data for ATP and Mb (14), respectively (assuming 100% NMR visibility of the particular compounds). Peak areas were converted to concentrations as described before (21). PCr and metMb concentrations were determined from the PCr/ATP and MbO_2/metMb ratios, respectively, measured by NMR spectroscopy. Cytosolic free ADP concentration was determined from the creatine kinase equilibrium as described before (21). Because ^{1}H NMR spectra during NO infusion were acquired in 15 min, a maximum of five different NO concentrations were applied within one experiment to avoid exceeding 2 h of total protocol time.

Materials. All compounds used in this study were either analytical grade or of the highest purity available. Bk, ETU, L-NMMA, and Mb were obtained from Sigma. All other reagents were obtained from Merck.

Statistical Analysis. All results are expressed as means ± SD. For multiple comparisons, ANOVA was applied, followed by the Bonferroni correction. A P value of <0.05 was considered significant.

Results

Functional and Metabolic Effects of Authentic NO Solutions. Fig. 1 shows a representative experiment on the effects of intracoronary infusion of NO on the Mb and high-energy phosphate levels as measured with ^{1}H and ^{31}P NMR spectroscopy. In WT hearts, the MbO_2 signal at −2.7 ppm (26) remained unchanged up to [NO] = 1 μM. At [NO] ≥ 2.5 μM, spectra showed a decrease of the MbO_2 signal and concomitantly a new signal at −3.8 ppm became detectable. This signal could be unequivocally assigned to metMb by both control measurements of commercially available Mb and comparison with literature data (24, 27). At [NO] = 5 μM, approximately 50% of the MbO_2 was converted to

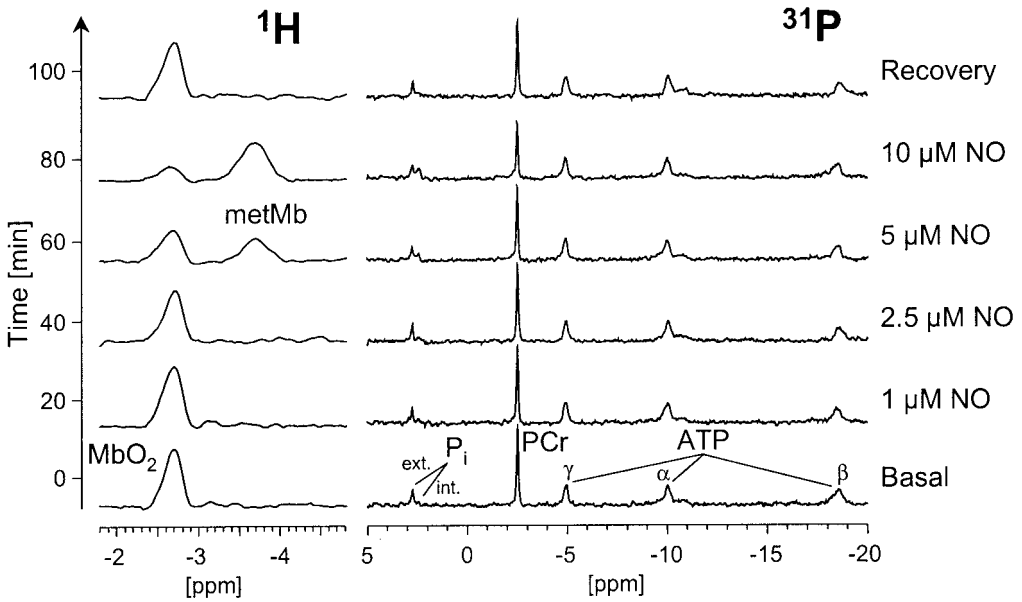

Fig. 1. ^{1}H (*Left*) and ^{31}P NMR (*Right*) spectra of WT hearts showing the effect of increasing NO concentration on cardiac Mb and energy status. Assignments: ATP, adenosine triphosphate (γ-, α-, and β-phosphorus); MbO_2, oxygenated myoglobin; metMb, metmyoglobin; PCr, phosphocreatine; P_i (ext.) and (int.), extracellular and intracellular inorganic phosphate, respectively.

metMb, reaching nearly 100% conversion at 25 μM NO (Fig. 2 *Top*). This reaction was reversible after cessation of the NO infusion (Fig. 1), reflecting the rapid regeneration of MbO_2 by metMb reductase activity in the WT (28, 29). It is noteworthy that the conversion of MbO_2 to metMb is already detectable at NO concentrations at which ^{31}P NMR spectra did not yet show any adverse effect on cardiac energy status (Fig. 1, third trace from top).

The dose-dependent effects of NO on Mb, cardiac contractile force, and energetic parameters in WT and Mb-deficient hearts are summarized in Fig. 2. As can be seen, cardiac contractility progressively decreased at [NO] $>$ 100 nM, resulting in a 50% reduction of LVDP at the maximal [NO] applied. In the NO dose range of 1–5 μM, a significantly greater decrease in LVDP was observed in myo$^{-/-}$ as compared with WT hearts, with most pronounced differences at 5 μM NO (62.4 $\pm$ 6.4 vs. 74.0 $\pm$ 3.9% of control, $n = 8$ each, $P < 0.01$; Fig. 2 *Middle*). Cardiodepression was accompanied by a severe deterioration of energy status, which was indicated by a reduction of the myocardial PCr content by more than 50% of the respective control level at [NO] = 25 μM (Fig. 1, bottom). At [NO] = 5 μM, impairment of energy homeostasis again was greater in the myo$^{-/-}$ group, as reflected by significantly increased myocardial ADP in myo$^{-/-}$ compared with WT hearts (42.3 $\pm$ 9.5 vs. 30.5 $\pm$ 8.4 μM, $n = 8$ each, $P < 0.05$; Fig. 1, bottom; calculated from ^{31}P NMR data). It should be noted that the differences in contractility and energetics between WT and myo$^{-/-}$ hearts became significant only in the NO concentration range that caused the formation of metMb (shaded area in Fig. 2). When [NO] $>$ 10 μM was applied, the differences with regard to LVDP and energetic parameters were blurred.

At [NO] lower than 1 μM we observed a significant enhancement of NO-induced vasodilatation corresponding to a left shift of the NO dose–response curve in myo$^{-/-}$ compared with WT hearts (data not shown). In this concentration range cardiac function and energy status were not substantially affected in both groups. Control experiments with the NO-independent vasodilator adenosine (5–500 nM) revealed no differences between WT and myo$^{-/-}$ hearts ($n = 8$ each, data not shown) for all parameters measured; even at maximal vasodilatation no changes in energy status or MbO_2 concentration were observed.

Role of Endogenous NO Synthesis. To assess whether endogenously synthesized NO contributes differently to the setting of basal vascular tone in WT and myo$^{-/-}$ hearts, experiments with the NO synthase inhibitors L-NMMA and ETU were undertaken. As shown in Fig. 3, there was no difference in coronary perfusion pressure under basal conditions; however, both inhibitors induced a significantly stronger vasoconstriction in the myo$^{-/-}$ as compared with the WT group, resulting in an increase of perfusion pressure from 100 mmHg to approximately 150 and 125 mmHg ($n = 6$ each, $P < 0.01$), respectively. Cardiac function and energy status remained unchanged in both groups and no effect on MbO_2 concentration could be detected in WT hearts (data not shown).

To increase endogenous NO release, hearts were stimulated by application of Bk. We found that the Mb-deficient group displayed a more sensitive response (Fig. 4), that was similar to previous results. The Bk-induced vasodilatation was more pronounced in myo$^{-/-}$ than in WT hearts, resulting in a drop of coronary perfusion pressure from 100 mmHg to 46.7 $\pm$ 5.1 and 64.1 $\pm$ 9.6 mmHg, respectively ($n = 8$ each, $P < 0.01$, at maximal [Bk]). Furthermore, at [Bk] $>$ 1 μM there was a perceptible LVDP decrease in myo$^{-/-}$ hearts only (78.3 $\pm$ 7.6% vs. 90.1 $\pm$ 4.9% of control, $n = 8$, $P < 0.01$; Fig. 4 *Lower*). ^{31}P NMR spectra did not reveal any changes in energy status (data not shown). However, we found significant differences in ^{1}H NMR spectra of WT hearts acquired within 4 min before, during, and after 1 μM Bk stimulation (Fig. 5). There was a small but significant decrease in the MbO_2 signal with the concomitant appearance of the metMb signal. This effect was rapidly reversed after the cessation of Bk infusion.

Discussion

This study reports a previously undescribed function of Mb: the reaction of MbO_2 with NO to metMb and nitrate as a major mechanism of attenuating intracellular NO bioactivity in cardiac muscle. This mechanism is physiologically relevant, because not only did NO infusion result in enhanced formation of metMb,

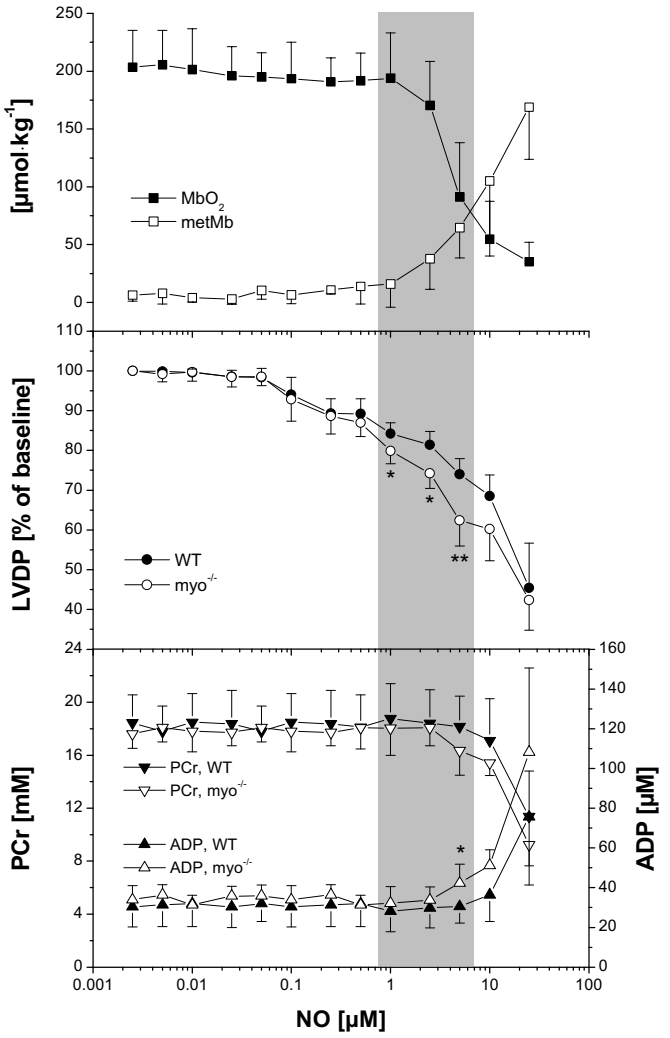

Fig. 2. Analysis of cardiac Mb (*Top*), function (*Middle*), and energetics (*Bottom*) of isolated perfused hearts with increasing NO concentration. Symbols show means ± SD for $n = 8$ hearts; * = $P < 0.05$; ** = $P < 0.01$; For abbreviations see Fig. 1. The shaded area emphasizes the association of metMb formation in WT hearts and the more pronounced impairment of cardiac function and energy status in Mb-deficient as compared with WT hearts.

but stimulation of endogenous NO release by Bk did also. Hearts from Mb-deficient ($myo^{-/-}$) mice were consistently more sensitive to endogenously formed and exogenously applied NO; the vasodilatory response and the depression of contractile as well as energetic parameters were more pronounced when compared with WT hearts.

^{1}H NMR spectroscopy enabled us to directly monitor the NO-induced formation of metMb from MbO_2 in the beating heart. Although this very fast reaction ($K = 3.7 \times 10^7\ M^{-1}{\cdot}s^{-1}$) is well known to occur *in vitro* (30), no conclusive experimental evidence existed until now that this reaction has functional relevance in cardiac NO homeostasis *in vivo*. After cessation of NO infusion or Bk stimulation, we found MbO_2 is rapidly regenerated, reflecting the presence of cardiac metMb reductase (28, 29). Obviously, the metMb signal becomes detectable only when metMb production from MbO_2 and NO exceeds the capacity of metMb reductase to reconvert metMb into Mb.

As shown in Fig. 6, the formation of metMb can occur via two different reactions: (*i*) directly by the interaction of NO and MbO_2 or (*ii*) by nitrosylation of deoxygenated Mb, yielding

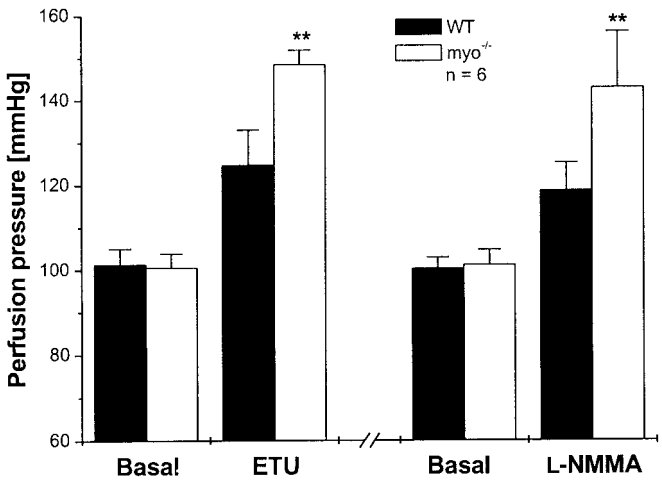

Fig. 3. Effect of the NO synthase inhibitors ETU (50 µM) and L-NMMA (100 µM) on coronary perfusion pressure of constant-flow-perfused hearts of WT and $myo^{-/-}$ mice. Symbols show means ± SD for $n = 6$ hearts; ** = $P < 0.01$.

MbNO as intermediate and its subsequent reaction with O_2. On the basis of our data, it cannot be decided by which of these pathways metMb is primarily formed. The rate of NO binding to deoxygenated Mb ($K = 1.7 \times 10^7\ M^{-1}{\cdot}s^{-1}$; ref. 31) is in the same order of magnitude as the conversion of MbO_2 to metMb by reaction with NO ($K = 3.7 \times 10^7\ M^{-1}{\cdot}s^{-1}$; ref. 30). However, because MbO_2 is the dominant form under fully oxygenated conditions (3), the probability of the encounter of NO and MbO_2 by far exceeds that of NO and deoxygenated Mb. Under *in situ* conditions with partial deoxygenation of MbO_2, the formation of MbNO might be of greater relevance. Especially in the vicinity of the mitochondria, where the concentration of deoxygenated

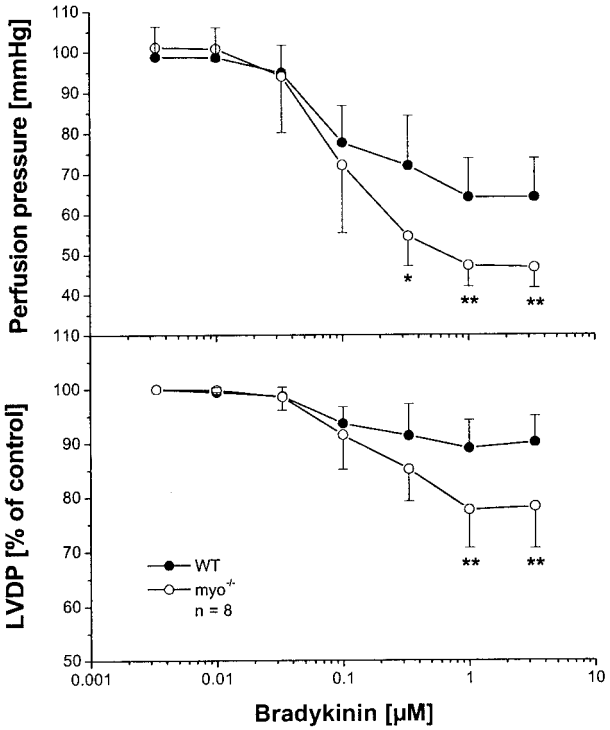

Fig. 4. Analysis of coronary perfusion pressure (*Upper*) and cardiac function (*Lower*) of constant flow perfused hearts under Bk stimulation. Symbols show means ± SD for $n = 8$ hearts; * = $P < 0.05$; ** = $P < 0.01$.

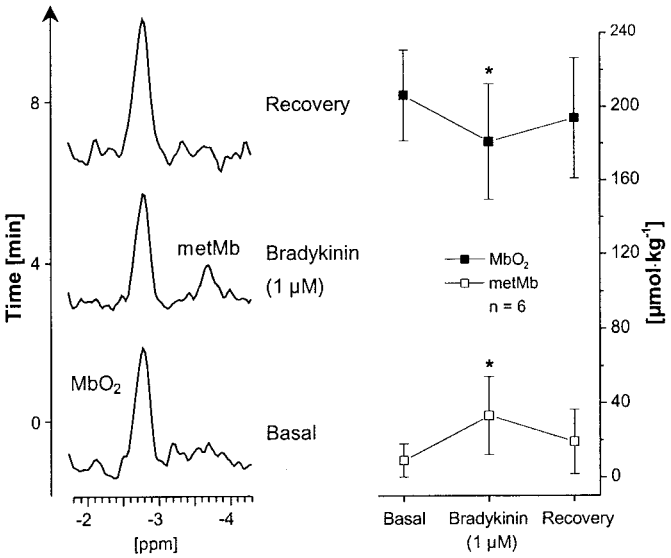

Fig. 5. ^{1}H NMR spectra (*Left*, 4 min accumulation time) of WT hearts showing the effect of Bk stimulation on cardiac Mb. Symbols on the Right show means ± SD for $n = 6$ hearts, $* = P < 0.05$.

Mb should be higher than in proximity to the capillaries, more MbNO is expected to be formed (Fig. 6). In the presence of O_2, MbNO is preferentially converted to metMb ($K = 1 \times 10^{-3}$·s^{-1}; ref. 20) being kinetically favored over the dissociation into Mb + NO ($K = 1 \times 10^{-4}$·s^{-1}; ref. 20), the latter taking place at a rate almost 10^4-fold slower than the corresponding dissociation of MbO_2 ($K = 10$ s^{-1}; ref. 20). Furthermore, it is noteworthy that the reaction of NO with the O_2 bound to the heme group was estimated to be at least 20-fold faster compared with both the rate of NO reaction with free O_2 ($K = 1.6 \times 10^6$ M^{-2}·s^{-1}; ref. 32) and to O_2 displacement by NO (30).

Considering the large amount of Mb in the heart (approx. 200 μmol/kg wet weight; refs. 7 and 14), both pathways—the direct reaction of MbO_2 with NO and the intermediate formation of MbNO—can account for a substantial NO breakdown in cardiomyocytes. Thus, Mb may be regarded as a molecular scavenger protecting the lower concentrated cytochromes (≈30 μmol/kg wet weight; refs. 33 and 34) against transient increases in cytosolic NO brought about by stimulation of NO synthase located in the endothelium, the sarcoplasmatic reticulum, and the mitochondria (35–38). Support for this hypothesis can be derived from comparison of the ^{1}H and ^{31}P NMR spectroscopic data presented in this study, because the conversion of MbO_2 to metMb is already detectable at NO concentrations at which ^{31}P NMR spectra do not indicate any adverse effect on cardiac energy status.

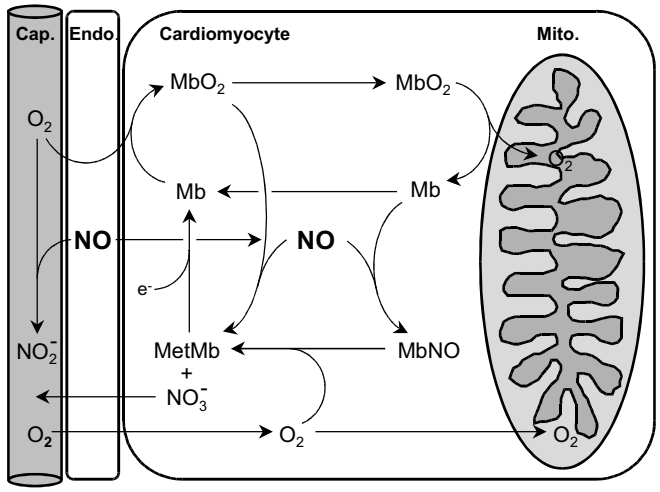

Fig. 6. Schematic drawing summarizing possible interactions of the different Mb compounds with O_2 and NO. For a detailed discussion refer to the text. Cap., capillary; Endo., endothelium; Mito., mitochondrion.

NO scavenging by Mb in cardiac muscle has important functional consequences: in hearts lacking Mb, changes in NO concentration have a much larger impact on the maintenance of vascular tone and cardiac function, as well as on energetic parameters compared with WT hearts. The lower sensitivity of Mb-containing WT hearts to alterations in NO concentration fits well with the assumption that in the presence of Mb, a continuous breakdown of NO takes place by reaction of MbO_2 with NO to metMb + NO_3^-, thereby reducing the effective cytosolic NO concentration. The recovery of MbO_2 and its availability for another NO degradation cycle is ensured by regeneration of metMb by metMb reductase to Mb and subsequent association with O_2 (cf. Fig. 6). Thus, the inhibition of NO synthase caused a more pronounced vasoconstriction in Mb-deficient hearts, which was most likely caused by the increased contribution of NO to the setting of basal vascular tone, in turn caused by the lower rate of NO bioinactivation. Along the same line, maximally stimulated endogenous NO release by Bk resulted in a more pronounced vasodilatation and, additionally, resulted in a more substantial depression of cardiac function in myo$^{-/-}$ compared with WT hearts. Similar effects were achieved by infusion of NO solutions > 1 μM. It should be noted that cardiac function was significantly better maintained in WT than myo$^{-/-}$ hearts in the NO dose range in which metMb becomes detectable (1–5 μM NO). These findings very likely reflect a reduced NO interference with heme enzymes of the mitochondrial electron-transport chain as well as creatine kinase and guanylate cyclase, all of which have been described as contributing to NO-mediated cardiodepression (39–43). However, when concentrations of infused NO exceeded 10 μM, functional and energetic parameters in WT and Mb-deficient hearts converged to similar levels. At such high NO levels, the protective capacity of Mb in WT hearts is exhausted, as indicated by the almost complete conversion of MbO_2 to metMb, resulting in a depression of myocardial energy generation and induction of contractile dysfunction, as observed in the present and other studies (42, 44).

It is difficult to assess the effective NO concentration that cardiomyocytes are exposed to when hearts are perfused with authentic NO solutions. It is well known that a considerable amount of NO will be inactivated by reaction with buffer O_2 or scavenged along its route to the interstitial space (45). We have reported before (46) that during a single passage through the heart, more than 85% of the infused NO is converted to nitrite ions and the NO half-life is as short as 100 ms. In addition, because there is lateral diffusion of NO, there is most likely a steep concentration gradient from the sarcolemma to the mitochondria. Therefore, the given concentrations of the infused NO solutions can only be regarded as an upper estimate of the amount of NO acting on the cardiomyocytes.

Our data indicate that Mb is crucial to the inactivation of NO and substantially determines the dose–response curve of the NO effects on coronary blood flow and cardiac contractility. These results uncover an additional physiological function of Mb besides its known role in oxygen storage and delivery. In this context, Mb's function seems to be limited to NO degradation, whereas its molecular relative Hb interacts with NO homeostasis not only by oxidative inactivation of NO (17), but also through (*i*) binding of NO to deoxygenated heme moieties (47) and (*ii*) formation of *S*-nitrosothiols (18). However, the latter reactions

are rather unlikely for Mb because (*i*) the oxygen binding curve for Mb in comparison to Hb is both shifted to the left and much steeper, resulting in a substantially lower amount of deoxygenated Mb than Hb at the same oxygen partial pressure, and (*ii*) the sulfur-containing amino acid cysteine, the prerequisite for nitrosothiol formation (18), is nonexistent in almost all Mb species characterized to this day.

Considering the large amounts of Mb in red muscle [0.5 mmol/kg (7, 33)], Mb may be important for NO turnover of the entire organism. On this larger scale, the reaction of NO with Hb to metHb and nitrate is generally considered to be the main route of intravascular NO breakdown. However, the recent observation that at physiological NO concentrations the binding of NO to the minor population of Hb's deoxygenated hemes outweighs the inactivation of NO by reaction with oxygenated Hb to metHb (47) challenged this hypothesis, thus raising the question about which other mechanisms might additionally contribute to NO breakdown (48). Estimation of the total body Mb content reveals that the quantities of Mb and Hb are within the same range. Assuming skeletal muscle in humans makes up 40–45% of total body weight (70 kg), and skeletal muscle consists of approximately 2/3 red muscle, the total body content of Mb can be approximated to 200 g (10 mmol), compared to 750 g of Hb (12 mmol). Furthermore, rate constants for NO-mediated conversion of the oxygenated hemoproteins to their respective met-compounds are almost equal for Hb and Mb ($K = 3.4 \times 10^7$ vs. 3.7×10^7 $M^{-1} \cdot s^{-1}$; refs. 30 and 49), suggesting that Mb may indeed contribute to whole body NO homeostasis. We therefore propose that Mb not only is a key element determining the magnitude of the NO response in muscle but also plays an important role in overall NO inactivation *in vivo*.

We dedicate this work to Beatrice and Jonathan Wittenberg, who pioneered the biology of myoglobin. We thank C. Ferfers, D. Haubs, and C. Kirberich for excellent technical assistance. This study was supported by the Biologisch-Medizinisches Forschungszentrum of the Heinrich-Heine-Universität Düsseldorf and the Anton-Betz-Stiftung of the Rheinische Post.

1. Wittenberg, B. A. & Wittenberg, J. B. (1989) *Annu. Rev. Physiol.* **51,** 857–878.
2. Kendrew, J. C. (1961) *Sci. Am.* **205,** 96–111.
3. Schenkman, K. A., Marble, D. R., Burns, D. H. & Feigl, E. O. (1997) *J. Appl. Physiol.* **82,** 86–92.
4. Millikan, G. A. (1937) *Proc. R. Soc. London Ser. B* **123,** 218–241.
5. Guyton, G. P., Stanek, K. S., Schneider, R. C., Hochachka, P. W., Hurford, W. E., Zapol, D. G., Liggins, G. C. & Zapol, W. M. (1995) *J. Appl. Physiol.* **79,** 1148–1155.
6. Terrados, N. (1992) *Int. J. Sports Med.* **13,** Suppl. 1, S206–S209.
7. Wittenberg, J. B. (1970) *Physiol. Rev.* **50,** 559–636.
8. Wittenberg, J. B. (1959) *Biol. Bull.* **117,** 402–403.
9. Wittenberg, B. A. & Wittenberg, J. B. (1985) *J. Biol. Chem.* **260,** 6548–6554.
10. Takahashi, E., Sato, K., Endoh, H., Xu, Z. L. & Doi, K. (1998) *Am. J. Physiol.* **275,** H225–H233.
11. Jones, D. P. & Kennedy, F. G. (1982) *Biochem. Biophys. Res. Commun.* **105,** 419–424.
12. Gardner, J. D. & Schubert, R. W. (1997) *Adv. Exp. Med. Biol.* **411,** 157–169.
13. Garry, D. J., Ordway, G. A., Lorenz, J. N., Radford, N. B., Chin, E. R., Grange, R. W., Bassel-Duby, R. & Williams, R. S. (1998) *Nature (London)* **395,** 905–908.
14. Gödecke, A., Flögel, U., Zanger, K., Ding, Z., Hirchenhain, J., Decking, U. K. & Schrader, J. (1999) *Proc. Natl. Acad. Sci. USA* **96,** 10495–10500.
15. Merx, M. W., Flögel, U., Stumpe, T., Gödecke, A., Decking, U. K. & Schrader, J. (2001) *FASEB J.*, in press.
16. Takahashi, E., Endoh, H. & Doi, K. (2000) *Biophys. J.* **78,** 3252–3259.
17. Ignarro, L. J., Fukuto, J. M., Griscavage, J. M., Rogers, N. E. & Byrns, R. E. (1993) *Proc. Natl. Acad. Sci. USA* **90,** 8103–8107.
18. Stamler, J. S., Jia, L., Eu, J. P., McMahon, T. J., Demchenko, I. T., Bonaventura, J., Gernert, K. & Piantadosi, C. A. (1997) *Science* **276,** 2034–2037.
19. Gladwin, M. T., Ognibene, F. P., Pannell, L. K., Nichols, J. S., Pease-Fye, M. E., Shelhamer, J. H. & Schechter, A. N. (2000) *Proc. Natl. Acad. Sci. USA* **97,** 9943–9948. (First Published August 22, 2000; 10.1073/pnas.180155397)
20. Cooper, C. E. (1999) *Biochim. Biophys. Acta* **1411,** 290–309.
21. Flögel, U., Decking, U. K., Gödecke, A. & Schrader, J. (1999) *J. Mol. Cell. Cardiol.* **31,** 827–836.
22. Kelm, M., Dahmann, R., Wink, D. & Feelisch, M. (1997) *J. Biol. Chem.* **272,** 9922–9932.
23. Kreutzer, U., Wang, D. S. & Jue, T. (1992) *Proc. Natl. Acad. Sci. USA* **89,** 4731–4733.
24. Chung, Y., Xu, D. & Jue, T. (1996) *Am. J. Physiol.* **271,** H1166–H1173.
25. Davis, A. L. & Wimperis, S. (1989) *J. Magn. Reson.* **84,** 620–626.
26. Patel, D. J., Kampa, L., Shulman, R. G., Yamane, T. & Wyluda, B. J. (1970) *Proc. Natl. Acad. Sci. USA* **67,** 1109–1115.
27. La Mar, G. N., Budd, D. L., Smith, K. M. & Langry, K. C. (1980) *J. Am. Chem. Soc.* **102,** 1822–1827.
28. Hagler, L., Coppes, R. I., Jr., & Herman, R. H. (1979) *J. Biol. Chem.* **254,** 6505–6514.
29. Livingston, D. J., McLachlan, S. J., La Mar, G. N. & Brown, W. D. (1985) *J. Biol. Chem.* **260,** 15699–15707.
30. Doyle, M. P. & Hoekstra, J. W. (1981) *J. Inorg. Biochem.* **14,** 351–358.
31. Hoshino, M., Ozawa, K., Seki, H. & Ford, P. C. (1993) *J. Am. Chem. Soc.* **115,** 9568–9575.
32. Wink, D. A., Darbyshire, J. F., Nims, R. W., Saavedra, J. E. & Ford, P. C. (1993) *Chem. Res. Toxicol.* **6,** 23–27.
33. Hickson, R. C. (1981) *J. Appl. Physiol.* **51,** 746–749.
34. Balaban, R. S., Mootha, V. K. & Arai, A. (1996) *Anal. Biochem.* **237,** 274–278.
35. Xu, K. Y., Huso, D. L., Dawson, T. M., Bredt, D. S. & Becker, L. C. (1999) *Proc. Natl. Acad. Sci. USA* **96,** 657–662.
36. Brahmajothi, M. V. & Campbell, D. L. (1999) *Circ. Res.* **85,** 575–587.
37. Bates, T. E., Loesch, A., Burnstock, G. & Clark, J. B. (1996) *Biochem. Biophys. Res. Commun.* **218,** 40–44.
38. Giulivi, C., Poderoso, J. J. & Boveris, A. (1998) *J. Biol. Chem.* **273,** 11038–11043.
39. Poderoso, J. J., Peralta, J. G., Lisdero, C. L., Carreras, M. C., Radisic, M., Schopfer, F., Cadenas, E. & Boveris, A. (1998) *Am. J. Physiol.* **274,** C112–C119.
40. Torres, J., Sharpe, M. A., Rosquist, A., Cooper, C. E. & Wilson, M. T. (2000) *FEBS Lett.* **475,** 263–266.
41. Xie, Y. W., Shen, W., Zhao, G., Xu, X., Wolin, M. S. & Hintze, T. H. (1996) *Circ. Res.* **79,** 381–387.
42. Gross, W. L., Bak, M. I., Ingwall, J. S., Arstall, M. A., Smith, T. W., Balligand, J. L. & Kelly, R. A. (1996) *Proc. Natl. Acad. Sci. USA* **93,** 5604–5609.
43. Brady, A. J., Warren, J. B., Poole, W. P., Williams, T. J. & Harding, S. E. (1993) *Am. J. Physiol.* **265,** H176–H182.
44. Kelm, M., Schäfer, S., Dahmann, R., Dolu, B., Perings, S., Decking, U. K. M., Schrader, J. & Strauer, B. E. (1997) *Cardiovasc. Res.* **36,** 185–194.
45. Lancaster, J. R., Jr. (1994) *Proc. Natl. Acad. Sci. USA* **91,** 8137–8141.
46. Kelm, M. & Schrader, J. (1990) *Circ. Res.* **66,** 1561–1575.
47. Gow, A. J., Luchsinger, B. P., Pawloski, J. R., Singel, D. J. & Stamler, J. S. (1999) *Proc. Natl. Acad. Sci. USA* **96,** 9027–9032.
48. Gross, S. S. & Lane, P. (1999) *Proc. Natl. Acad. Sci. USA* **96,** 9967–9969.
49. Eich, R. F., Li, T., Lemon, D. D., Doherty, D. H., Curry, S. R., Aitken, J. F., Mathews, A. J., Johnson, K. A., Smith, R. D., Phillips, G. N., Jr., *et al.* (1996) *Biochemistry* **35,** 6976–6983.

The FASEB Journal • FJ Express

Role of myoglobin in the antioxidant defense of the heart

ULRICH FLÖGEL,*,[1] AXEL GÖDECKE,* LARS-OLIVER KLOTZ,† AND JÜRGEN SCHRADER*
*Institut für Herz- und Kreislaufphysiologie, †Institut für Biochemie und Molekularbiologie I, Heinrich-Heine-Universität Düsseldorf, Germany

To read the full text of this article, go to http://www.fasebj.org/cgi/doi/10.1096/fj.03-1382fje; doi: 10.1096/fj.03-1382.fje

SPECIFIC AIMS

The aim of the present study was to explore the role of myoglobin (Mb) in cardiac metabolism of reactive oxygen species (ROS). We analyzed the functional and energetic effects of ROS either pharmacologically applied or endogenously generated in beating hearts of Mb-deficient (myo$^{-/-}$) and control mice.

PRINCIPAL FINDINGS

1. Mb attenuates the effect of exogenously induced oxidative stress on cardiac contractile force

Langendorff-perfused hearts were exposed to pharmacologically induced oxidative stress by stepwise increasing the concentrations of intracoronary infused H_2O_2 or 2,3-dimethoxy-1,4-naphtoquinone (DMNQ), a compound continuously releasing superoxide by redox cycling. Left ventricular developed pressure (LVDP) progressively decreased at [DMNQ] >0.3 μM, resulting in a 30% reduction of cardiac contractility at the maximal [DMNQ] applied. In the DMNQ dose range of 1–10 μM, a significantly greater decrease in LVDP was observed in myo$^{-/-}$ than in wild-type (WT) hearts. Comparable differences between the WT and myo$^{-/-}$ groups were detected for dP/dt. Similar to the results with DMNQ, we found the Mb-deficient group was more sensitive to exogenously applied H_2O_2. Up to [H_2O_2] = 10 μM, there was a significant LVDP decrease in myo$^{-/-}$ hearts only (90.4±4.2 vs. 98.1±0.7% of control, n=6, P<0.05). Again, comparable differences were observed for dP/dt between the WT and myo$^{-/-}$ groups in the H_2O_2 dose range of 3–100 μM.

2. Lack of Mb leads to a delayed postischemic recovery of cardiac function paralleled by an enhanced release of ROS during reperfusion

To assess whether the greater sensitivity of Mb-deficient hearts to oxidative stress is of functional significance, we applied an ischemia-reperfusion (IR) protocol to enhance the endogenous release of ROS. Hearts were subjected to a 12 min period of a global no-flow ischemia and subsequently reperfused for 1 h. Cardiac contractility together with ^{31}P NMR spectroscopy was used to monitor function and energy state of the hearts. In parallel experiments, hearts were perfused via a home-built adaptor inside a Berthold LB 500 luminometer (**Fig. 1*A***) under corresponding conditions and cardiac ROS release was continuously monitored by lucigenin-enhanced chemiluminescence (measured as relative light units (RLU; Fig. 1*B*). Cardiac function and energetic parameters of WT and myo$^{-/-}$ hearts were not different under control conditions or during ischemia. In reperfusion, however, WT hearts showed a significantly faster recovery of the postischemic function compared with myo$^{-/-}$ hearts: LVDP was 35.6 ± 7.5 mmHg in WT vs. 22.4 ± 5.3 mmHg in myo$^{-/-}$ after 10 min of reperfusion (P<0.01, n=8). ^{31}P NMR revealed that, concomitantly, a substantially larger overshoot of the phosphocreatine (PCr) signal occurred in myo$^{-/-}$ hearts (125±5% of control in myo$^{-/-}$ vs. 110±7% of control in WT after 10 min of reperfusion, P<0.05, n=8). As shown in Fig. 1*C*, the retarded restoration of functional and metabolic parameters in myo$^{-/-}$ compared with WT hearts was accompanied by increased release of ROS in myo$^{-/-}$ hearts (465±87 RLU in myo$^{-/-}$ vs. 287±73 RLU in WT after 2.5 min of reperfusion, P<0.05, n=8). Additional experiments in presence of the NO synthase inhibitor N^G-monomethyl-L-arginine methyl ester (L-NMMA, 100 μM) confirmed the findings: again, the retarded recovery of cardiac contractility and energetics in Mb-deficient hearts was accompanied by a significantly higher release of ROS in myo$^{-/-}$ than in WT hearts.

3. Oxidative stressors lead to the formation of globin radical intermediates

We further examined whether intermediates of ROS-consuming reactions by Mb could be identified in control hearts. It was recently shown that the reaction

[1] Correspondence: Institut für Herz- und Kreislaufphysiologie, Heinrich-Heine-Universität Düsseldorf, Universitätsstrasse 1, 40225 Düsseldorf, Germany. E-mail: floegel@uni-duesseldorf.de

0892-6638/04/0018-1156 © FASEB

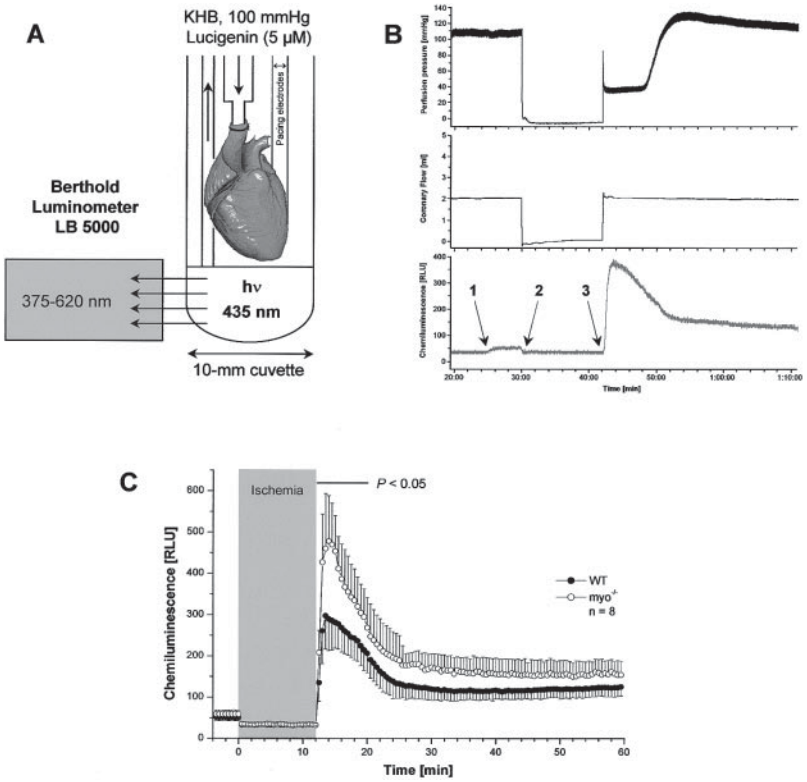

Figure 1. Analysis of cardiac ROS release of isolated perfused hearts. *A)* Langendorff setup for chemiluminescence measurements of ROS release. Mouse hearts were perfused via a home-built adaptor inside the luminometer and paced at 500 bpm. *B)* Typical recording: *1)* start of the lucigenin infusion, *2)* begin ischemia, *3)* reperfusion. Perfusion pressure (top), coronary flow (middle), and lucigenin-enhanced chemiluminescence (bottom) were continuously acquired. *C)* Cardiac ROS release of perfused WT and myo$^{-/-}$ hearts during 12 min of global ischemia and subsequent reperfusion for 1 h. Symbols show means ± SD for $n = 8$ hearts; $P < 0.05$ vs. WT; RLU, relative light units. Shaded area emphasizes the ischemic period.

of Mb with H_2O_2 results in covalent binding of the heme prosthetic group, most likely via formation of a tyrosyl radical at position 103 of the apo-myoglobin chain. Thus, these protein-bound heme adducts are indicators of Mb's peroxidase activity. Heme-Mb adducts retain their redox activity even after SDS-PAGE and electroblotting, and can be detected by the use of enhanced chemiluminescence detection reagents. Extracts from WT hearts perfused with 30 µM H_2O_2, the concentration where the most pronounced differences in cardiac contractility between WT and myo$^{-/-}$ were observed, revealed three major signals, including a band of 17,000 Da. No signal corresponding to Mb was detected in extracts from myo$^{-/-}$ mice or in hearts under basal conditions.

CONCLUSIONS

This study describes a novel in vivo function of Mb: the attenuation of oxidative stress in cardiac muscle. Hearts from myo$^{-/-}$ mice were found to be more sensitive to the infusion of ROS (e.g.,. H_2O_2 and superoxide) in that depression of myocardial contractile force was more pronounced than in WT controls. Mb-deficient hearts released significantly more ROS during IR; this was accompanied by a delayed functional and metabolic recovery after the ischemic insult.

The reaction of H_2O_2 with hemoglobin was described for the first time more than 100 years ago; and in the meantime the interactions of ROS with hemoproteins have been object of numerous in vitro investigations. From these studies it became evident that ROS formed by the endothelial xanthine oxidase or incomplete reduction of O_2 within the mitochondria during IR are likely to interact with Mb, as hypothesized in **Fig. 2**. Reaction of peroxides with both Mb (Fe^{II}) and metMb (Fe^{III}) yields the ferryl derivative (Fe^{IV}) of Mb, characterized by a very high oxidative capacity. Comproportionation of ferryl Mb with Mb leads to formation of metMb; the reduction of metMb by cardiac metMb reductase results in regeneration of Mb (Fe^{II}) available for initiation of another breakdown cycle. Although the individual steps are known to occur in vitro, the present study indicates that together they can

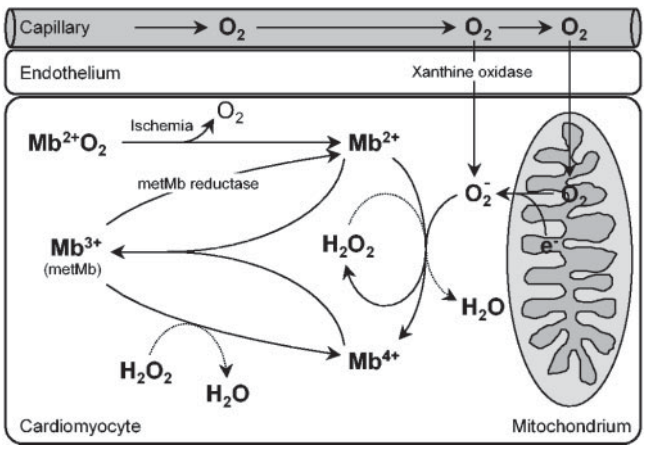

Figure 2. Schematic drawing summarizing possible interactions of the different Mb compounds with reactive oxygen species. Mb^{2+}, Mb^{3+}, and Mb^{4+} stand for Mb with a heme iron in the oxidation state Fe^{II}, Fe^{III}, and Fe^{IV}, respectively. See text for details.

constitute in vivo a metabolic cycle that contributes to the attenuation of oxidative stress in the heart.

Protection against oxidant injury is particularly meaningful during the early reperfusion period after an ischemic insult, which is characterized by the sudden formation of large amounts of ROS. The chemiluminescence approach presented in this study enabled us via intracoronary infusion of low nontoxic lucigenin doses to measure online the kinetics of ROS release into the venous effluent perfusate, yielding similar time courses for the initial oxygen radical burst and the subsequent slow decrement when compared with spin trap and ESR measurements or by determination of peroxide production. The ~60% increased chemiluminescence level in Mb-deficient hearts during early reperfusion indicates that redox cycling of Mb contributes significantly to ROS breakdown under these conditions. Therefore, Mb can be regarded as an additional oxygen radical scavenger among the various enzymatic and nonenzymatic antioxidant defenses including superoxide dismutase (SOD), glutathione peroxidase, catalase, etc. Since the high amounts of cytosolic Mb (~200 μmol/kg wet weight) can account for a substantial ROS breakdown, our results may explain why cytosolic Cu/Zn-SOD knockout mice appeared to be almost normal whereas knockout of mitochondrial Mn-SOD resulted in a dilated cardiomyopathy and lethality.

The functional significance of ROS scavenging by Mb is apparent when comparing the data for cardiac contractility and energetics during IR in WT and myo$^{-/-}$ hearts. The more pronounced PCr overshoot during initial reperfusion in Mb-deficient hearts is consistent with the retarded restoration of cardiac contractility in these hearts, since the degree of PCr overshoot has been related to the extent of mechanical dysfunction during reperfusion. The PCr overshoot in IR has been reported to be caused by an inactivation of cytosolic creatine kinase (CK_{cyto}) due to H_2O_2 oxidation of methionine-bound sulfhydryl groups of this enzyme: The impaired CK_{cyto} activity prevents cytoplasmic conversion of PCr to ATP, impeding the efficient delivery of energy to utilization sites with resultant depression of cardiac contractility. In our experiments it is most likely that sustained inhibition of CK_{cyto} by elevated levels of ROS during reperfusion caused the more pronounced overshoot of PCr in myo$^{-/-}$ hearts. Aside from CK_{cyto} inactivation, ROS may exert further detrimental effects on cardiac function by the initiation of peroxidation of cell membranes, unspecific destruction of enzymes, and cleavage of DNA strands.

Several lines of evidence suggest that during IR there is an enhanced production of NO by endothelial NO synthase that results in a NO burst in the initial phase of reperfusion. Since we have shown that Mb contributes to NO breakdown in the heart, it is conceivable that a diminished NO degradation plays a role in the delayed recovery of myo$^{-/-}$ hearts during IR. However, inhibition of endogenous NO release by L-NMMA did not alter the retarded restoration of functional and metabolic parameters in Mb-deficient hearts, indicating that NO does not account for the differences observed. Comparing the time course of ROS and NO production during reperfusion, it seems likely that the prolonged release of ROS observed in this and other studies outweighs the NO burst, which lasts only 1–2 min. Our findings can explain the recently described (but mechanistically unresolved) protection of neurons from hypoxic-ischemic injury by the homologous neuroglobin, a phenomenon that has been shown to be independent of NO or oxygen storage.

The data of the present study show that lack of Mb leads to increased vulnerability of the heart when challenged by oxidative stress. However, previous investigations by us and others provided no evidence for an unbalanced oxidative status in Mb-deficient mice under basal conditions. Similarly, genomic and proteomic analysis did not reveal the induction of potential regulatory mechanisms to encounter an increased oxidative stress or reprogramming of antioxidant-related genes in myo$^{-/-}$ mice. Deoxygenated Mb has been described to be the species oxidized by H_2O_2 (cf. Fig. 2), so that myocardial PO_2 appears to be a major determinant in this context. It has been shown that the reaction of H_2O_2 with the ferric form of Mb (metMb) is almost 10-fold faster than the rate of H_2O_2 reaction with the ferrous deoxygenated form of Mb. Thus, the reaction of Mb with ROS is likely to be functionally relevant under conditions of reduced oxygen supply associated with enhanced deoxygenation of Mb, and even more so during oxidative stress when increased amounts of metMb are formed, but not in the well-oxygenated heart where MbO_2 dominates. This view is supported by the detection of globin radical intermediates in the presence of oxidative stressors, suggesting a significant contribution of the Mb-peroxidase reaction to H_2O_2 turnover especially during oxidative challenge. This may be particularly important in diving mammals, whose Mb concentrations exceed those of terrestrial mammals by up to 10-fold. Here, the high Mb content is likely not only to extend diving time by O_2 storage when pulmonary ventilation ceases, but also to attenuate cytosolic oxidative stress during reoxygenation after surfacing.

In summary, our data indicate that Mb contributes to the attenuation of increased oxidant stress and substantially determines the dose-dependent effects of ROS on cardiac contractility and energetics. Thus, Mb may be regarded as a molecular radical scavenger protecting other targets (such as creatine kinase) against transient rises of cytosolic ROS brought about after short periods of ischemia, thereby complementing the known muscular antioxidant defense mechanisms. Taking into account Mb's NO scavenging properties, we propose that Mb is not only important in intracellular oxygen supply but also constitutes a key element to influence various redox pathways in the muscle cell, supporting the recent suggestion to classify Mb as a multifunctional allosteric enzyme. FJ

Lack of Myoglobin Causes a Switch in Cardiac Substrate Selection

Ulrich Flögel,* Tim Laussmann,* Axel Gödecke, Nadine Abanador, Michael Schäfers, Christian Dominik Fingas, Sabine Metzger, Bodo Levkau, Christoph Jacoby, Jürgen Schrader

Abstract—Myoglobin is an important intracellular O_2 binding hemoprotein in heart and skeletal muscle. Surprisingly, disruption of myoglobin in mice ($myo^{-/-}$) resulted in no obvious phenotype and normal cardiac function was suggested to be mediated by structural alterations that tend to steepen the oxygen pressure gradient from capillary to mitochondria. Here we report that lack of myoglobin causes a biochemical shift in cardiac substrate utilization from fatty acid to glucose oxidation. Proteome and gene expression analysis uncovered key enzymes of mitochondrial β-oxidation as well as the nuclear receptor PPARα to be downregulated in myoglobin-deficient hearts. Using FDG-PET we showed a substantially increased in vivo cardiac uptake of glucose in $myo^{-/-}$ mice (6.7 ± 2.3 versus 0.8 ± 0.5% of injected dose in wild-type, n=5, $P<0.001$), which was associated with an upregulation of the glucose transporter GLUT4. The metabolic switch was confirmed by ^{13}C NMR spetroscopic isotopomer studies of isolated hearts which revealed that [1,6-$^{13}C_2$]glucose utilization was increased in $myo^{-/-}$ hearts (38 ± 8% versus 22 ± 5% in wild-type, n=6, $P<0.05$), and concomitantly, [U-$^{13}C_{16}$]palmitate utilization was decreased in the myoglobin-deficient group (42 ± 6% versus 63 ± 11% in wild-type, n=6, $P<0.05$). Because of the O_2-sparing effect of glucose utilization, the observed shift in substrate metabolism benefits energy homoeostasis and therefore represents a molecular adaptation process allowing to compensate for lack of the cytosolic oxygen carrier myoglobin. Furthermore, our data suggest that an altered myoglobin level itself may be a critical determinant for substrate selection in the heart. The full text of this article is available online at http://circres.ahajournals.org. **(*Circ Res*. 2005;96:e68-e75.)**

Key Words: metabolism ■ β-oxidation ■ glucose ■ oxygen ■ heart

It is well known that red and white muscle are not only characterized by a largely different content of myoglobin (Mb), but also by significant differences in metabolism closely related to their physiological function.[1,2] Red muscles exhibit slow twitch speed, are fatigue resistant, and have an aerobic fat-, glucose-, and ketone-based metabolism. In contrast, white muscle fibers are fast contracting anaerobic fibers and easily fatigued because they have few respiratory proteins and metabolize glucose only as far as lactate. Similar to the red skeletal muscle, the heart has a high, enduring energy demand, which under normal conditions is primarily met by metabolism of fatty acids (FAs).[3] Nevertheless, in several cardiac diseases, such as ischemic cardiomyopathy, heart failure, hypertrophy, and dilated cardiomyopathy, a reduced oxidation of FAs and an enhanced glucose utilization has been found.[4] Interestingly, dilated and ischemic cardiomyopathies have also been reported to be accompanied by a decreased myocardial Mb content.[5] However, whether there is more then a mere correlation between muscle Mb level and substrate metabolism has not been explored so far.

In mice lacking Mb ($myo^{-/-}$), multiple compensatory mechanisms are induced that tend to steepen the oxygen pressure gradient to the mitochondria.[6–8] These include a higher capillary density, reduction in cell width, elevated hematocrit, increased coronary flow, and coronary flow reserve. However, substrate utilization was reported to be preserved in the absence of Mb, although in vitro, a modest increase in lactate utilization in the Mb mutant heart was noted.[8] To address the role of Mb in substrate selection of the heart in more detail, we utilized positron emission tomography (PET) using [^{18}F]fluorodeoxyglucose (FDG) and ^{13}C nuclear magnetic resonance (NMR) spectroscopy using [1,6-$^{13}C_2$]glucose and [U-$^{13}C_{16}$]palmitate to study cardiac intermediary metabolism in wild-type (WT) and Mb-deficient mice generated in our laboratory.[7] Furthermore, we analyzed the myocardial protein pattern of WT and $myo^{-/-}$ mice by 2-dimensional gel electrophoresis (2D-PAGE) and identified differentially expressed proteins by mass spectrometry. Additionally, we verified whether alterations at the protein level

Original received May 11, 2004; resubmission received March 3, 2005; revised resubmission received March 24, 2005; accepted March 28, 2005.

From the Institut für Herz-und Kreislaufphysiologie (U.F., T.L., A.G., N.A., C.D.F., C.J., J.S.), Heinrich-Heine-Universität Düsseldorf; Klinik und Poliklinik für Nuklearmedizin (M.S.), Universitätsklinikum Münster; Biomedizinisches Forschungszentrum (S.M.), Heinrich-Heine-Universität Düsseldorf; and Institut für Pathophysiologie, Zentrum für Innere Medizin (B.L.), Universitätsklinikum Essen, Germany.

*Both authors contributed equally to this work.

Correspondence to Dr Ulrich Flögel, Heinrich-Heine-Universität Düsseldorf, Universitätsstrasse 1, 40225 Düsseldorf, Germany. E-mail floegel@uni-duesseldorf.de

Circulation Research **is available at http://www.circresaha.org** **DOI: 10.1161/01.RES.0000165481.36288.d2**

are related to a gene regulatory switch. We found that similar to skeletal muscle, lack of Mb causes a switch in cardiac substrate selection from fatty acid to glucose utilization that is accompanied by a downregulation of key enzymes of the β-oxidation pathway.

Materials and Methods

Animals

Myo$^{-/-}$ mice were generated in our laboratory by deletion of the essential exon-2 via homologous recombination in embryonic stem cells as described previously.[7] Animal experiments were performed in accordance with the national guidelines on animal care and were approved by the local government. Before all metabolic experiments mice were fed with a standard chow diet and received tap water ad libitum.

Heart Perfusion for Metabolic Analysis

Preparation of murine hearts and retrograde perfusion at constant pressure of 100 mm Hg was performed essentially as described.[9] After hemodynamic and contractile parameters maintained constant under these conditions, hearts were finally switched to buffer containing 5 mmol/L [1,6-$^{13}C_2$]glucose, 0.5 mmol/L [U-$^{13}C_{16}$]palmitate (the latter bound to 3% essentially fatty acid free albumin; both from Cambridge Isotope Laboratories), and 50 μU insulin. After 25 minutes of perfusion, hearts were freeze-clamped, extracted with perchloric acid (PCA), neutralized, lyophilized, and stored at −20°C. A more detailed description of the heart perfusion protocol is provided in the expanded Materials and Methods section in the online data supplement available at http://circres.ahajournals.org.

Magnetic Resonance Measurements

Data were recorded on a Bruker DRX 9.4 Tesla WB NMR spectrometer operating at frequencies of 400.1 MHz for ^{1}H and 100.6 MHz for ^{13}C measurements.

Spectroscopy

Lyophilized PCA extracts were redissolved in 0.5 mL D_2O. Spectra were recorded from a 5-mm ^{1}H/^{13}C dual probe. Acquisition and processing parameters are given in detail in the online data supplement.

Isotopomer Analysis of Carbon Flow Into the Tricarboxylic Acid Cycle

The relative contributions of palmitate, glucose, and endogenous sources to the total acetyl-CoA pool entering the tricarboxylic acid (TCA) cycle were determined from isotopomer analysis of glutamate carbons C3 and C4. Consult the online data supplement for a detailed description of the analysis of ^{13}C NMR spectra.

Imaging

MRI was performed using a microimaging unit (Mini 0.5, Bruker) as described in the online data supplement.

High-Resolution PET

Myocardial glucose transport was noninvasively assessed in vivo by monitoring the uptake of FDG in intact mice, which before PET analysis had been functionally and morphologically characterized by MRI. Mice were anesthetized with isoflurane (1.5%) and kept at 37°C. Each mouse was injected with 10 MBq FDG in 100 μL 0.9% saline intravenously. After 60 minutes, mice were positioned on the bed of a submillimeter-resolution PET camera (quad-HIDAC, Oxford Positrons Ltd), and a 15-minute acquisition was initiated. Coronal images were then reconstructed (voxel size 0.25 mm^3, 0.7 mm full-width half-maximum). Myocardial FDG uptake was quantified by the ratio between myocardial radioactivity in a region-of-interest encompassing the left ventricular myocardium and the total injected dose (% injected dose, % ID).

Blood Serum

Determination of glucose, lactate, and fatty acids in blood serum was performed by the Central Laboratory of the University Hospital Düsseldorf using clinical routine protocols.

Proteome Analysis

Sample preparation and 2D-PAGE were essentially performed as previously reported[10] and a more detailed description is provided in the online data supplement. SDS-PAGE was performed on an ETTAN-DALT II vertical electrophoresis unit (Amersham Pharmacia Biotech). Equilibrated IPG strips were placed on top of the gel (size of 0.1×25.5×20 cm^3) and fixed in place by agarose sealing solution. Twelve gels were run simultaneously (settings: 30 minutes, 30 W; 4.5 hours, 180 W) and either silver-stained or stained by Coomassie blue R250. The gels were digitized and the obtained images analyzed as described in the online data supplement.

Protein Identification

Coomassie-stained spots were excised from preparative gels and analyzed by nano spray ESI-MS/MS using a SCIEX Q-STAR system (PE Sciex), as previously described.[10]

Expression Analysis

Expression levels were analyzed by real-time PCR using an ABI SDS 5700 real-time PCR analysis system on reverse-transcribed myocardial RNA isolated from 8 WT and myo$^{-/-}$ hearts, respectively. cDNA derived from 100 ng of total RNA was used for each reaction. Signals were amplified using the Taqman based assays on demand (ABI) for PPARα (Mm00440939_m1), short chain enoyl-CoA hydratase (Mm00659670_g1), and short chain acyl-CoA dehydrogenase (Mm00431617_m1) according to the suppliers instructions. Relative expression levels were determined by normalization to transferrin receptor (Mm00441941_m1) and TATA binding protein (Mm00446973_m1) as housekeeping genes.

Cell Fractionation and Western Analysis of GLUT4 Expression

Hearts were isolated from WT and myo$^{-/-}$ mice and separated into membranous and cytosolic fractions according to published procedures.[11] For Western analysis, 10 μg of membrane proteins and the corresponding volume fractions of the 30 000g supernatant were analyzed by Western blotting using a polyclonal rabbit anti-GLUT4 antibody (Abcam Ltd; 1:2500) followed by secondary HRPO-coupled goat anti-rabbit antibody (Sigma Heidelberg; 1:5000). Signals were detected by use of an ECL-kit (Amersham Biosciences).

Statistical Analysis

All results are expressed as mean±SD. For multiple comparisons, ANOVA followed by the Bonferroni correction was applied. A probability value of less than 0.05 was considered significant. The statistical analysis of the raw data from 2D-PAGE experiments was performed by the program "statistical analysis of microarrays, SAM."[12] The parameter "δ value" was adjusted in order to keep the number of false significant protein spots (90%) below 1. In a nonpaired t test, this translates to approximately $P<0.005$ for n=12. Additionally, changes in protein expression below 30% were considered to be of low biological relevance.

Results

^{13}C NMR Isotopomer Analysis

For analysis of the contribution of FA and glucose oxidation to TCA cycle turnover, isolated hearts paced at 500 bpm were perfused for 25 minutes with 5 mmol/L [1,6-$^{13}C_2$]glucose and 0.5 mmol/L [U-$^{13}C_{16}$]palmitate in the presence of 50 μU insulin. Under these conditions, left ventricular developed pressure was equal in both groups (114.4±9.8 mm Hg in WT versus 115.0±10.4 mm Hg in Mb-deficient hearts, n=8).

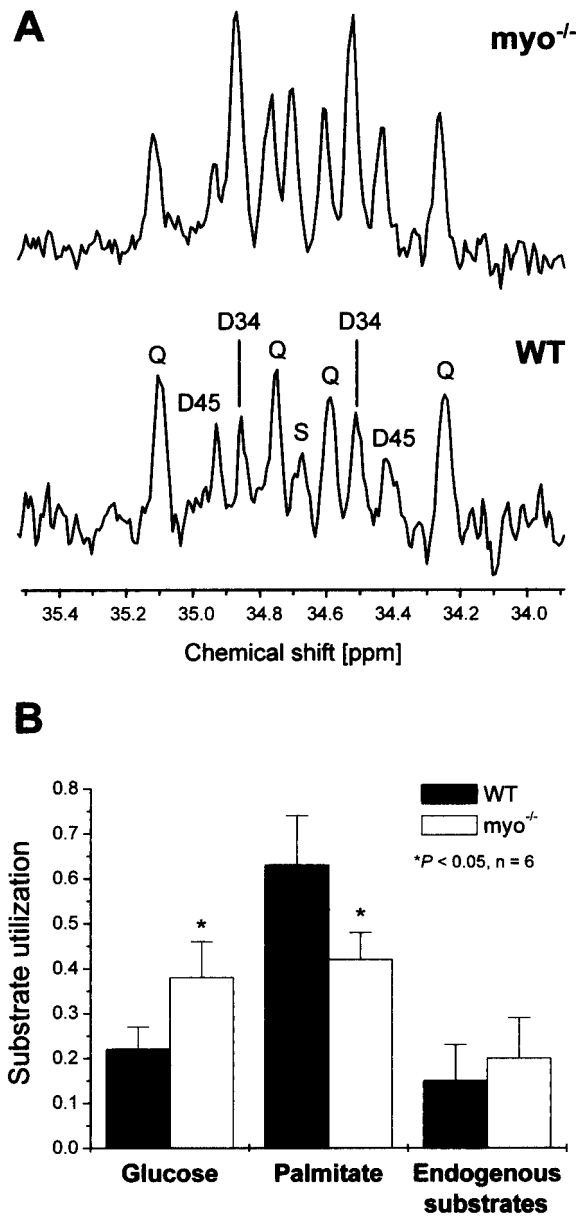

Figure 1. A, Representative sections of ^{13}C NMR spectra showing the glutamate C4 isotopomer pattern for WT and myo$^{-/-}$ PCA heart extracts. Hearts were perfused for 25 minutes with 5 mmol/L [1,6-$^{13}C_2$]glucose and 0.5 mmol/L [U-$^{13}C_{16}$]palmitate in the presence of 50 μU insulin. D34 indicates doublet because of J_{34} coupling (34 Hz); D45, doublet because of J_{45} coupling (51 Hz); Q, quartet (doublet of doublet) because of J_{345} coupling (J_{34} 34 Hz, J_{45} 51 Hz); S, singlet. B, Analysis of carbon flow into the TCA cycle in WT and myo$^{-/-}$ hearts under the conditions given above. Data are mean±SD (n=6, *P<0.05 vs WT). By definition, $F_{Palmitate}+F_{Glucose}+F_{Endogenous}=1$.

However, despite unrestricted cardiac function, we found myocardial oxygen consumption to be reduced by 7.5% in the transgenic group (15.63±1.43 μmol · min^{-1} · g^{-1} in WT versus 14.46±1.37 μmol · min^{-1} · g^{-1} in myo$^{-/-}$, n=8; P=0.09). High-resolution ^{13}C NMR spectra of the respective PCA extracts (Figure 1A) showed pronounced differences in the isotopomer pattern of the glutamate carbon C4 of WT (bottom) and myo$^{-/-}$ (top) hearts. The sum of the resonances (S+D34) reports the amount of acetyl-CoA derived from

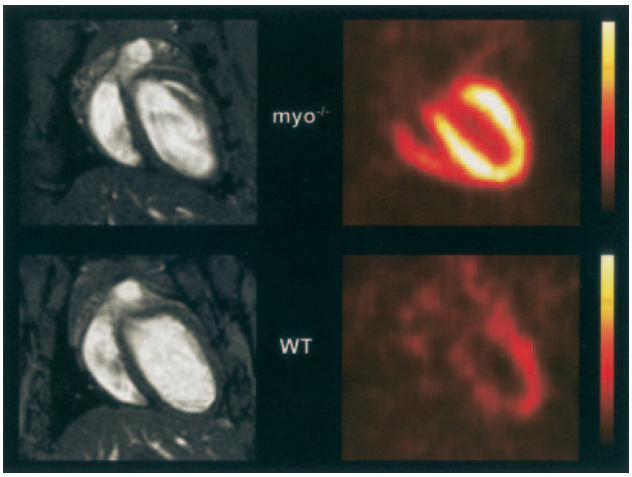

Figure 2. Matched noninvasive functional and metabolic imaging of WT (bottom) and myo$^{-/-}$ (top) mice in vivo. MRI (left panel, coronal slices) shows normal cardiac morphology and function (cf. online Table II) in WT and myo$^{-/-}$, whereas myocardial glucose uptake (right panel, matching coronal slices) measured by FDG-PET is markedly increased in myo$^{-/-}$ as compared with WT.

[1,6-^{13}C]glucose (entry of [2-^{13}C]acetyl-CoA into the TCA cycle), and the sum of (D45+Q) reflects the amount of acetyl-CoA derived from [U-$^{13}C_{16}$]palmitate (entry of [1,2-$^{13}C_2$]acetyl-CoA), irrespective of any cycling intermediate or pool sizes.[13] Thus, in the example shown in Figure 1A, it is obvious that in Mb-deficient hearts, the amount of carbons incorporated into glutamate that originate from glucose were increased whereas carbons originating from palmitate were decreased compared with WT hearts.

Quantitative analysis of the ^{13}C NMR spectra (Figure 1B) revealed that glucose utilization was significantly increased in myo$^{-/-}$ hearts (38±8% versus 22±5% in WT, n=6; P<0.05), and concomitantly, palmitate utilization was significantly decreased in the Mb-deficient group (42±6% versus 63±11% in WT, n=6; P<0.05), whereas the contribution of endogenous substrates (ie, glycogen or unlabeled glucose and FAs) was similar in both groups. Furthermore, no differences were observed in pool sizes of metabolites (cf. Table I in the online data supplement) and fractional enrichments (data not shown) of alanine, glutamate, and lactate between WT and myo$^{-/-}$ hearts.

In Vivo MRI and PET Analysis

In order to verify whether the enhanced glucose metabolization found in isolated perfused hearts of myo$^{-/-}$ mice can also be observed under in vivo conditions, myocardial glucose transport was noninvasively assessed by monitoring the uptake of FDG in intact mice. Before PET analysis, all mice were initially characterized by MRI, which showed similar values for diastolic and systolic volumes as well as cardiac output in both groups (Figure 2, left, and online Table II). Despite being morphologically and functionally undistinguishable, FDG-PET revealed significant differences between WT and myo$^{-/-}$ mice (Figure 2, right) in that myocardial FDG uptake was substantially enhanced in Mb-deficient

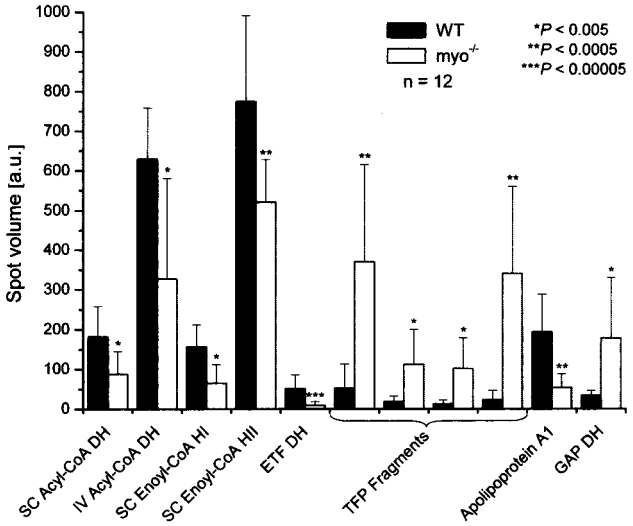

Figure 3. Differentially expressed proteins in WT vs myo$^{-/-}$ mice related to intermediary metabolism. For the complete list of altered proteins, refer to online Table IV. Data are mean±SD (n=12, *P<0.005, **P<0.0005, ***P<0.00005 vs WT). DH indicates dehydrogenase; ETF, electron transferring flavoprotein; GAP, glyceraldehyde 3-phosphate; HI/HII, hydrogenase isoform I/II; IV, isovaleryl; SC; short chain; TFP, trifunctional protein.

mice (6.7±2.3%ID versus 0.8±0.5%ID in WT, n=5; P<0.001).

Analysis of Blood Serum Substrates

Both ^{13}C NMR and PET data indicate a shift to increased glucose and reduced fatty acid utilization in transgenic hearts. To clarify whether these alterations may have been caused by differences in serum substrate concentrations, we determined the amounts of glucose, lactate, and various FAs (16:0, 16:1, 18:0, 18:1, 20:0, 20:1, 20:2, 20:3, and 20:4) in WT and myo$^{-/-}$ mice (n=6). However, there were no significant differences between the 2 groups concerning all parameters analyzed (data are given in online Table III).

Proteome Analysis

To investigate whether the observed alterations in cardiac metabolism are related to changes in myocardial protein expression, proteome patterns of WT and myo$^{-/-}$ mice were analyzed by 2D-PAGE (see Figure II in the online data supplement for representative gels). Aside from Mb, 21 protein species were found to be differentially expressed when comparing myo$^{-/-}$ with WT samples (online Table IV). Noticeably, more than half of the altered proteins are involved in intermediary metabolism (Figure 3), and 9 of these are part of the mammalian mitochondrial β-oxidation pathway,[14] which is illustrated in the schematic drawing of Figure 4. The first step of the β-oxidation spiral is catalyzed by acyl-CoA dehydrogenases (DHs), which lead to the oxidation of acyl-CoA to enoyl-CoA by FAD. Two members of this enzyme family, short-chain and isovaleryl acyl-CoA DH, were reduced in expression by ≈ 50%. The next steps of β-oxidation are mediated by enoyl-CoA hydratases: two forms of the short-chain FA selective soluble enzyme were decreased in expression by 58% and 33% in myo$^{-/-}$ hearts.

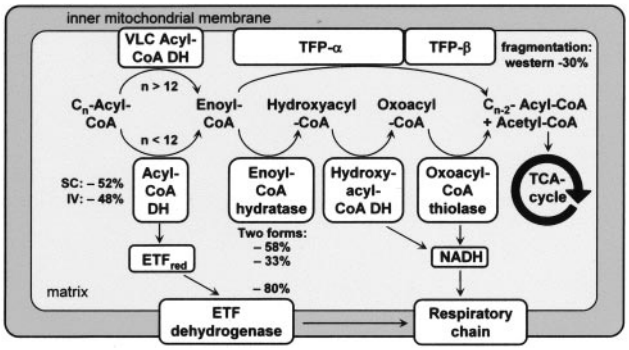

Figure 4. Schematic drawing of key steps of mitochondrial β-oxidation incorporating the observed alterations in protein expression of myo$^{-/-}$ hearts (changes in percent relative to WT hearts). DH indicates dehydrogenase; ETF, electron transferring flavoprotein; IV, isovaleryl; SC; short chain; TFP, trifunctional protein; VLC, very long chain.

The membrane-bound enoyl-CoA hydratase (selective for long-chain FAs) is part of the α-subunit of mitochondrial trifunctional protein (TFP), which combines 3 long-chain (LC) FA selective enzymatic activities: LC enoyl-CoA hydratase and LC 3-hydroxyacyl-CoA DH, both located on the α-subunit, as well as LC 3-ketoacyl-CoA-thiolase, located on the β-subunit.[15] Whereas 2D-PAGE analysis did not reveal a difference in expression of the intact α- and β-subunits of TFP between the groups, 4 cleavage fragments of α-TFP were prominently found on gels of Mb mutant hearts (Figure 3). Similarly, fragments of the β-subunit were clearly visible in myo$^{-/-}$ samples. Western blot analysis using a polyclonal antibody raised against the β-subunit of TFP[16] revealed a downregulation of the intact subunit by 30% (n=9 per group, P<0.05). Furthermore, we found the membrane-bound enzyme electron-transferring flavoprotein DH (ETF DH), which feeds the reduction equivalents into the respiratory chain (Figure 4) to be downregulated by 80% in the knockout (Figure 3). On the other hand, the glycolytic enzyme glyceraldehyde 3-phosphate DH was significantly upregulated (+420%) in myo$^{-/-}$ hearts (Figure 3). For a more detailed description of the proteome data including the other differentially expressed proteins refer to the online data supplement.

Because GLUT4 is the major transport system for uptake of glucose into cardiomyocytes,[17] we further verified whether the enhanced glucose utilization in Mb-deficient hearts is associated with alterations in overall cardiac GLUT4 expression and/or translocation of this transporter from the cytosol to the plasma membrane. Western blot analysis revealed GLUT4 expression to be significantly increased in both the cytosolic and the membranous fraction of myo$^{-/-}$ as compared with WT heart extracts (Figure 5). However, it is noteworthy that the relative raise of the transporter in the plasma membrane (60%) is more pronounced than in the cytosol (20%), which reflects in addition to an increased expression an enhanced translocation of GLUT4 into the membrane.

Gene Expression

We further analyzed whether the altered expression of enzymes of FA oxidation relates to a gene regulatory switch.

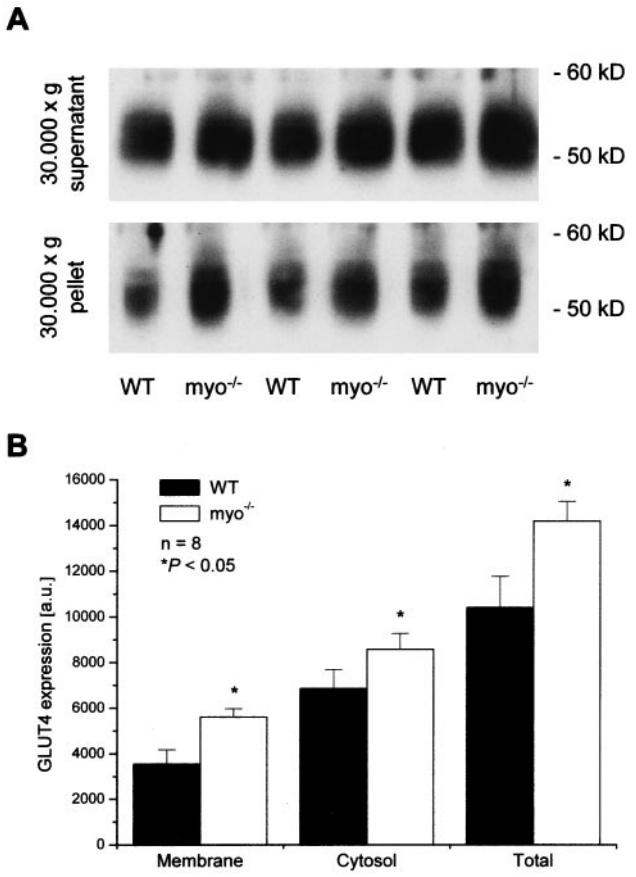

Figure 5. GLUT4 expression in membranous and cytosolic fractions of WT and myo$^{-/-}$ hearts. A, Representative Western blots. B, Densitometric quantification. Data are mean±SD (n=8, *P<0.05 vs WT)

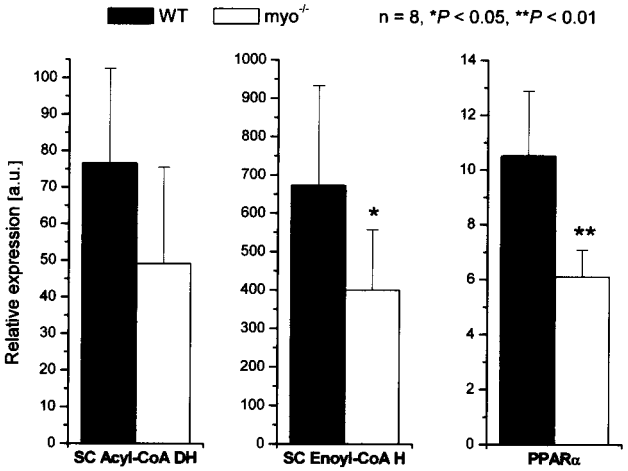

Figure 6. mRNA levels of selected proteins in hearts of WT and myo$^{-/-}$ mice. Data are mean±SD (n=8, *P<0.05, **P<0.01 vs WT). DH indicates dehydrogenase; H, hydrogenase, PPAR, peroxisome proliferator activated receptor; SC; short chain.

For this purpose, we measured mRNA levels of a subset of proteins that were downregulated in Mb-deficient hearts and, additionally, the expression of the nuclear receptor PPARα (peroxisome proliferator activated receptor α), which has been shown to be a key factor in regulation of several genes involved in β-oxidation of fatty acids.[18] Transcripts of short-chain acyl-CoA DH and enoyl-CoA hydratase were found to be reduced in myo$^{-/-}$ hearts by ≈40% to 50% (Figure 6), which fits well to the alterations observed at the translated protein level (Figure 3). Furthermore, expression of PPARα was decreased by a similar extent (≈40%) in the transgenic group (Figure 6, right; WT: 10.5±2.4 AU, myo$^{-/-}$: 6.1±1.0 AU, n=8; P<0.01).

Discussion

The results of the present study show that lack of Mb causes a shift from free FA to glucose oxidation in cardiac energy production. Enhanced glucose uptake in myo$^{-/-}$ hearts was noninvasively visualized by FDG-PET in vivo and the substrate switch was confirmed by ^{13}C NMR isotopomer studies of isolated hearts. Protein and gene expression analysis demonstrated that the most abundant glucose transporter in the heart, GLUT4, is upregulated whereas important enzymes of mitochondrial β-oxidation and the key regulator of genes involved in FA metabolism, PPARα, are downregulated in Mb-deficient hearts. Based on these data and the finding that cardiac structure and function remained fully unchanged in myo$^{-/-}$ hearts, it appears that Mb is a critical determinant of cardiac substrate selection.

Quantitative evaluation of the individual substrate fluxes in WT hearts revealed a utilization of FAs more than glucose in the order of 3:1, which is close to the normal situation in humans.[3] In contrast, myo$^{-/-}$ hearts used approximately equal amounts of FAs and glucose. This shift in substrate utilization in myo$^{-/-}$ hearts resembles the known differences in metabolism of red and white muscle. Early investigations on the enzyme pattern of white (fast) and red (slow) muscles showed that white muscle fibers contain high amounts of glycolytic enzymes, whereas red muscles predominantly express enzymes of the β-oxidation pathway.[1] The analogy to skeletal muscle is further supported by the observed differences in expression level of α-(B)-crystallin in myo$^{-/-}$ and WT hearts (online Table IV), which is also similar to that found between white and red muscle.[19]

The correlation of myocardial Mb content with the capacity of β-oxidation has been described in previous studies under both physiological and pathophysiological conditions. In a recent study of the heterogeneity of cardiac flow and metabolism, we showed that certain areas in the well-perfused dog heart that normally receive <50% of mean myocardial blood flow exhibited reduced Mb levels accompanied by decreased expression of enzymes of the β-oxidation pathway and enhanced expression of glycolytic enzymes.[10] Studies in canine and bovine models of dilated cardiomyopathy also demonstrated a reduced expression of Mb and concomitant upregulation of glycolytic and/or downregulation of β-oxidation enzymes.[20,21] Together with the results of the present work, these data suggest a causal relationship between myocytic Mb content and β-oxidation of fatty acids. As to the molecular mechanisms involved,

several possibilities must be considered by which Mb might directly or indirectly affect muscle substrate selection.

Mb is generally thought not only to provide the O_2 needed for aerobic muscle metabolism and to augment the flow of O_2 to the mitochondria but also to buffer intracellular O_2 concentrations in response to mitochondrial demand.[22] A possible mismatch between O_2 requirement and O_2 supply because of the lack of Mb could be overcome by a shift from FA oxidation to O_2-sparing glucose utilization. It is well known that the complete oxidation of FAs consumes more O_2 per mole energy-rich phosphate than the complete oxidation of glucose. On basis of the respective phosphate-to-oxygen ratios (P:O) myocardial O_2 consumption (MVO_2) can be assumed to increase by ≈10% when FAs are exclusively utilized as compared with glucose.[23] This value, however, may be an underestimation, because it has been recently demonstrated in the in vivo unloaded myocardium that FA usage requires 48% more O_2 when compared with glucose.[24] MVO_2 measurements in the present study have shown an oxygen saving of 7.5% (at a shift of glucose/FA utilization from ≈1:3 to an equal ratio), which supports the notion of the latter study that the benefit of using glucose may be considerably higher as calculated on basis of the P:O ratios. Thus, a shift toward glucose oxidation will improve the O_2 balance in the Mb-deficient heart and may be considered as a molecular adaptation mechanism in the myo$^{-/-}$ heart.

Besides its function in O_2 storage and transport, Mb has also been suggested to support ATP generation by cardiac cells under conditions of fully oxygenated Mb: a phenomenon referred to as Mb-mediated oxidative phosphorylation.[25] As an underlying mechanism, a preferred uptake of Mb-bound O_2 by mitochondria and/or the acceptance of electrons by sarcoplasmic Mb with concomitant reduction of heme iron-ligated O_2 to H_2O were suggested. However, because an enhanced oxidative phosphorylation would support aerobic oxidation of both glucose and FAs, it is rather unlikely that an impaired Mb-mediated oxidative phosphorylation causes the metabolic shift in hearts lacking Mb.

In addition to its function as respiratory pigment, Mb of bovine, chicken, and rat muscle was shown to bind FAs.[26–28] Therefore, Mb has been suggested to function as transport protein for FAs in the cytosol working in concert with the well-known fatty acid binding protein, which is generally assumed to be the major player.[29] Interestingly, FA binding of Mb depends on its oxygenation in that conformational changes induced by O_2 binding favor the interaction of Mb with FAs.[28] Although the functional relevance of FA binding to Mb remains to be explored, the simultaneous delivery of O_2 and FAs to mitochondria would clearly be advantageous for aerobically working muscle. According to this hypothesis, lack of Mb as putative FA carrier would supply less substrate to the mitochondria, thereby triggering the downregulation of β-oxidation to total energy production of myo$^{-/-}$ hearts.[30]

Because we have previously shown that Mb substantially contributes to NO breakdown in the heart,[31] it is conceivable that increased levels of NO as a result of diminished NO degradation may affect cardiac metabolism in Mb-deficient hearts. Indeed, it has been demonstrated that NO is involved in stimulation of glucose uptake and metabolism (eg, via GLUT4 translocation) particularly in skeletal[32] but also in heart muscle.[33,34] Furthermore, it has also been described that endogenous NO reduces O_2 use in excitation-contraction coupling and attenuates cardiac contractility without changing contractile efficiency.[35] This could further contribute to improved O_2 balance in the Mb-deficient heart.

It is becoming increasingly evident that protein-protein interactions within the living cell are important in various cellular signal transduction pathways, and that in vivo, many proteins do not work by themselves but, in most cases, by forming a complex or interacting with other proteins, DNA, RNA, or ligands (interactome).[36] However, little is known about the interactome of Mb, albeit dynamic docking and electron transfer between Mb and cytochrome b5 have lately been discovered.[37] Furthermore, there is recent evidence that the ferric form of neuroglobin, which is homologous to Mb, acts as a heterotrimeric Gα protein guanine nucleotide dissociation inhibitor thereby shutting off signaling pathways linked to Gα effectors and favoring G$\alpha\gamma$ effector pathways leading to protection against neuronal death.[38] Because Mb is present in the cytosol in high concentrations (up to 0.5 mmol/L) it is quite conceivable that multiple interactions with other cellular proteins exist, which—when lacking—may cause metabolic rearrangements.

Taken together the combined effect of Mb's different biological functions is likely to trigger the changes in intermediary metabolism when Mb is lacking. Decreased mitochondrial O_2 availability and increased amounts of bioactive NO may act as complementary players in this process: because lack of Mb results in an enhanced vulnerability to mild or short periods of hypoxic/ischemic conditions,[39] it is conceivable that even the unstressed Mb-deficient heart is characterized by a "microhypoxic" environment promoting the expression of hypoxia-responsive genes,[8] which have been described to mediate inhibition of expression of the nuclear receptor PPARα.[40] The NO-induced stimulation of expression and translocation of GLUT4[34] together with the recently proposed regulatory "crosstalk" between PPARα signaling and GLUT4 gene expression[41] could provide the molecular framework of the observed substrate switch to an increased glucose utilization. Note that, conversely, transgenic mice with cardiac-specific overexpression of PPARα exhibit increased fatty acid uptake and oxidation as well as reciprocal inhibition of glucose uptake and metabolism.[42]

Similar shifts in cardiac substrate selection as described in this study for the myo$^{-/-}$ mouse have been frequently reported to occur during hypertrophy and several other cardiac diseases (see reviews[43,44]). It has been postulated that this rearrangement of cardiac energy production contributes to the compensated state during progression to heart failure.[43,44] Metabolic remodeling has been as yet seen as part of the reactivation of the fetal gene expression program typically observed during development of left ventricular hypertrophy. However, there is no evidence for an upregulation of atrial natriuretic peptide and skeletal muscle actin or other markers of the fetal gene expression program in myo$^{-/-}$ hearts.[45] Furthermore, it should be noted that in this and previous studies we and others found no indication for an impaired cardiac function in Mb-deficient mice under normal condi-

tions.[6,7] Therefore, the Mb knockout mouse clearly illustrates that metabolic remodeling represents an important compensatory mechanism that can be activated independent of the fetal gene expression program. Thus, this model can be used in future studies to determine the potentially protective role of increased glucose utilization in certain pathological states like ischemia and/or diabetes without interference of mechanisms governed by the reactivation of the fetal gene expression program.

In summary, our data show that lack of Mb leads to an enhanced glucose and a decreased FA utilization in the mouse heart. Because equimolar production of ATP from glucose consumes less O_2 than from FAs, this metabolic switch may be viewed as an additional adaptive mechanism in myo$^{-/-}$ hearts. The changes in substrate selection of Mb-deficient hearts resemble the well-known differences in metabolic pattern of red and white muscle. Our data suggest that an altered Mb level by itself is one crucial factor that determines the relative utilization of FAs versus glucose, thus placing Mb in a central stage within the regulatory network that controls cardiac energy production.

Acknowledgments

This study was supported by the Biologisch-Medizinisches Forschungszentrum of the Heinrich-Heine-Universität Düsseldorf, the Sonderforschungsbereich 612 "Molekulare Analyse kardiovaskulärer Funktionen and Funktionsstörungen", Teilprojekt Z2, and in part by the Interdisziplinäres Zentrum für Klinische Forschung (IZKF), Münster, Germany (grant ZPG 4 to M.S.). We thank D. Haubs, S. Küsters, and C. Kirberich for excellent technical assistance, and R. Hoffmann and S. Lauter for their expert help in protein identification by ESI-MS/MS. We thank A. Strauss from the Department of Pediatrics at Vanderbilt University, Nashville, Tenn, for providing us with anti-TFP antibody.

References

1. Bass A, Brdiczka D, Eyer P, Hofer S, Pette D. Metabolic differentiation of distinct muscle types at the level of enzymatic organization. *Eur J Biochem*. 1969;10:198–206.
2. Hoppeler H. Skeletal muscle substrate metabolism. *Int J Obes Relat Metab Disord.* 1999;23:S7–S10.
3. Lopaschuk GD, Belke DD, Gamble J, Itoi T, Schonekess BO. Regulation of fatty acid oxidation in the mammalian heart in health and disease. *Biochim Biophys Acta*. 1994;1213:263–276.
4. Sambandam N, Lopaschuk GD, Brownsey RW, Allard MF. Energy metabolism in the hypertrophied heart. *Heart Fail Rev*. 2002;7:161–173.
5. O'Brien PJ, Gwathmey JK. Myocardial Ca^{2+}- and ATP-cycling imbalances in end-stage dilated and ischemic cardiomyopathies. *Cardiovasc Res*. 1995;30:394–404.
6. Garry DJ, Ordway GA, Lorenz JN, Radford NB, Chin ER, Grange RW, Bassel-Duby R, Williams RS. Mice without myoglobin. *Nature*. 1998; 395:905–908.
7. Gödecke A, Flögel U, Zanger K, Ding Z, Hirchenhain J, Decking UK, Schrader J. Disruption of myoglobin in mice induces multiple compensatory mechanisms. *Proc Natl Acad Sci U S A*. 1999;96:10495–10500.
8. Meeson AP, Radford N, Shelton JM, Mammen PP, DiMaio JM, Hutcheson K, Kong Y, Elterman J, Williams RS, Garry DJ. Adaptive mechanisms that preserve cardiac function in mice without myoglobin. *Circ Res*. 2001;88:713–720.
9. Flögel U, Decking UK, Gödecke A, Schrader J. Contribution of NO to ischemia-reperfusion injury in the saline-perfused heart: a study in endothelial NO synthase knockout mice. *J Mol Cell Cardiol*. 1999;31: 827–836.
10. Laussmann T, Janosi RA, Fingas CD, Schlieper GR, Schlack W, Schrader J, Decking UK. Myocardial proteome analysis reveals reduced NOS inhibition and enhanced glycolytic capacity in areas of low local blood flow. *FASEB J*. 2002;16:628–630.
11. Nürnberg B. Pertussis toxin as a pharmacological tool. In: Aktories K, Just I, eds. *Handbook of Experimental Pharmacology, vol 145: Bacterial Protein Toxins*. Berlin, Heidelberg: Springer Verlag; 2000:187–206.
12. Tusher VG, Tibshirani R, Chu G. Significance analysis of microarrays applied to the ionizing radiation response. *Proc Natl Acad Sci U S A*. 2001;98:5116–5121.
13. Malloy CR, Thompson JR, Jeffrey FM, Sherry AD. Contribution of exogenous substrates to acetyl coenzyme A: measurement by ^{13}C NMR under non-steady-state conditions. *Biochemistry*. 1990;29:6756–6761.
14. Eaton S, Bartlett K, Pourfarzam M. Mammalian mitochondrial β-oxidation. *Biochem J*. 1996;320:345–357.
15. Uchida Y, Izai K, Orii T, Hashimoto T. Novel fatty acid β-oxidation enzymes in rat liver mitochondria. II. Purification and properties of enoyl-coenzyme A (CoA) hydratase/3-hydroxyacyl-CoA dehydrogenase/3-ketoacyl-CoA thiolase trifunctional protein. *J Biol Chem*. 1992;267: 1034–1041.
16. Ibdah JA, Paul H, Zhao Y, Binford S, Salleng K, Cline M, Matern D, Bennett MJ, Rinaldo P, Strauss AW. Lack of mitochondrial trifunctional protein in mice causes neonatal hypoglycemia and sudden death. *J Clin Invest*. 2001;107:1403–1409.
17. Abel ED. Glucose transport in the heart. *Front Biosci*. 2004;9:201–215.
18. Barger PM, Kelly DP. PPAR signaling in the control of cardiac energy metabolism. *Trends Cardiovasc Med*. 2000;10:238–245.
19. Neufer PD, Benjamin IJ. Differential expression of B-crystallin and Hsp27 in skeletal muscle during continuous contractile activity. Relationship to myogenic regulatory factors. *J Biol Chem*. 1996;271: 24089–24095.
20. O'Brien PJ, O'Grady M, McCutcheon LJ, Shen H, Nowack L, Horne RD, Mirsalimi SM, Julian RJ, Grima EA, Moe GW. Myocardial myoglobin deficiency in various animal models of congestive heart failure. *J Mol Cell Cardiol*. 1992;24:721–730.
21. Weil J, Eschenhagen T, Magnussen O, Mittmann C, Orthey E, Scholz H, Schafer H, Scholtysik G. Reduction of myocardial myoglobin in bovine dilated cardiomyopathy. *J Mol Cell Cardiol*. 1997;29:743–751.
22. Wittenberg JB, Wittenberg BA. Myoglobin function reassessed. *J Exp Biol*. 2003;206:2011–2020.
23. Suga H. Ventricular energetics. *Physiol Rev*. 1990;70:247–277.
24. Korvald C, Elvenes OP, Myrmel T. Myocardial substrate metabolism influences left ventricular energetics in vivo. *Am J Physiol Heart Circ Physiol*. 2000;278:H1345–H1351.
25. Wittenberg BA, Wittenberg JB. Myoglobin-mediated oxygen delivery to mitochondria of isolated cardiac myocytes. *Proc Natl Acad Sci U S A*. 1987;84:7503–7507.
26. Gloster J, Harris P. Fatty acid binding to cytoplasmic proteins of myocardium and red and white skeletal muscle in the rat: a possible new role for myoglobin. *Biochem Biophys Res Commun*. 1977;74:506–513.
27. Moore KK, Cameron PJ, Ekeren PA, Smith SB. Fatty acid-binding protein in bovine longissimus dorsi muscle. *Comp Biochem Physiol B*. 1993;104:259–266.
28. Götz FM, Hertel M, Groschel-Stewart U. Fatty acid binding of myoglobin depends on its oxygenation. *Biol Chem Hoppe Seyler*. 1994;375:387–392.
29. van der Vusse GJ, van Bilsen M, Glatz JF. Cardiac fatty acid uptake and transport in health and disease. *Cardiovasc Res*. 2000;45:279–293.
30. Augustus A, Yagyu H, Haemmerle G, Bensadoun A, Vikramadithyan RK, Park SY, Kim JK, Zechner R, Goldberg IJ. Cardiac-specific knock-out of lipoprotein lipase alters plasma lipoprotein triglyceride metabolism and cardiac gene expression. *J Biol Chem*. 2004;279: 25050–25057.
31. Flögel U, Merx MW, Gödecke A, Decking UK, Schrader J. Myoglobin: A scavenger of bioactive NO. *Proc Natl Acad Sci U S A*. 2001;98: 735–740.
32. Young ME, Radda GK, Leighton B. Nitric oxide stimulates glucose transport and metabolism in rat skeletal muscle in vitro. *Biochem J*. 1997;322:223–228.
33. McFalls EO, Hou M, Bache RJ, Best A, Marx D, Sikora J, Ward HB. Activation of p38 MAPK and increased glucose transport in chronic hibernating swine myocardium. *Am J Physiol Heart Circ Physiol*. 2004; 287:H1328–H1334.
34. Li J, Hu X, Selvakumar P, Russell RR III, Cushman SW, Holman GD, Young LH. Role of the nitric oxide pathway in AMPK-mediated glucose uptake and GLUT4 translocation in heart muscle. *Am J Physiol Endocrinol Metab*. 2004;287:E834–E841.
35. Suto N, Mikuniya A, Okubo T, Hanada H, Shinozaki N, Okumura K. Nitric oxide modulates cardiac contractility and oxygen consumption without changing contractile efficiency. *Am J Physiol*. 1998;275:H41–H49.

36. Gerstein M, Lan N, Jansen R. Proteomics: integrating interactomes. *Science*. 2002;295:284–287.
37. Liang ZX, Nocek JM, Huang K, Hayes RT, Kurnikov IV, Beratan DN, Hoffman BM. Dynamic docking and electron transfer between Zn-myoglobin and cytochrome b(5). *J Am Chem Soc*. 2002;124:6849–6859.
38. Wakasugi K, Nakano T, Morishima I. Oxidized human neuroglobin acts as a heterotrimeric Gα protein guanine nucleotide dissociation inhibitor. *J Biol Chem*. 2003;278:36505–36512.
39. Merx MW, Flögel U, Stumpe T, Gödecke A, Decking UK, Schrader J. Myoglobin facilitates oxygen diffusion. *FASEB J*. 2001;15:1077–1079
40. Narravula S, Colgan SP. Hypoxia-inducible factor 1-mediated inhibition of peroxisome proliferator-activated receptor α expression during hypoxia. *J Immunol*. 2001;166:7543–7548.
41. Finck BN, Bernal-Mizrachi C, Ho Han D, Coleman T, Sambandam N, LaRiviere LL, Holloszy JO, Semenkovich F, Kelly DP. A potential link between muscle peroxisome proliferator-activated receptor-α signaling and obesity-related diabetes. *Cell Metab*. 2005;1:133–144.
42. Finck BN, Lehman JJ, Leone TC, Welch MJ, Bennett MJ, Kovacs A, Han X, Gross RW, Kozak R, Lopaschuk GD, Kelly DP. The cardiac phenotype induced by PPARα overexpression mimics that caused by diabetes mellitus. *J Clin Invest*. 2002;109:121–130.
43. van Bilsen M. "Energenetics" of heart failure. *Ann N Y Acad Sci*. 2004; 1015:238–249.
44. Taegtmeyer H, Golfman L, Sharma S, Razeghi P, van Arsdall M. Linking gene expression to function: metabolic flexibility in the normal and diseased heart. *Ann N Y Acad Sci*. 2004;1015:202–213.
45. Gödecke A, Molojavyi A, Heger J, Flögel U, Ding Z, Jacoby C, Schrader J. Myoglobin protects the heart from inducible nitric-oxide synthase (iNOS)-mediated nitrosative stress. *J Biol Chem*. 2003;278:21761–21766.

Magnetic Resonance in Medicine 57:50–58 (2007)

In Vivo 2D Mapping of Impaired Murine Cardiac Energetics in NO-Induced Heart Failure

Ulrich Flögel,* Christoph Jacoby, Axel Gödecke, and Jürgen Schrader

^{31}P MRS studies in humans have shown that an impairment of cardiac energetics is characteristic of heart failure. Although numerous transgenic mouse models with a heart-failure phenotype have been generated, current methods to analyze murine high-energy phosphates (HEPs) in vivo are hampered by limited spatial resolution. Using acquisition-weighted 2D ^{31}P chemical shift imaging (CSI) at 9.4 Tesla, we were able to acquire ^{31}P MR spectra over the entire thorax of the mouse with high spatial resolution in defined regions of the heart (the anterior, lateral, posterior, and septal walls) within a reasonable acquisition time of about 75 min. Analysis of a transgenic cardiomyopathy model (double mutant: cardiospecific inducible nitric oxide synthase (iNOS) overexpression and lack of myoglobin (tg-iNOS^{+}/myo$^{-/-}$) revealed that cardiac dysfunction in the mutant was associated with an impaired energy state (phosphocreatine (PCr)/adenosine triphosphate (ATP) 1.54 ± 0.18) over the entire left ventricle (LV; wild-type (WT): PCr/ATP 2.06 ± 0.22, $N = 5$, $P < 0.05$), indicating that in the absence of efficient cytosolic NO scavenging, iNOS-derived NO critically interferes with the respiratory chain. In vivo data were validated against ^{31}P MR spectra of perchloric acid extracts (PCr/ATP: 1.87 ± 0.21 (WT), 1.39 ± 0.17 (tg-iNOS^{+}/myo$^{-/-}$, $N = 5$, $P < 0.05$). Future applications will substantially benefit studies on the cause-and-effect relationship between cardiac energetics and function in other genetically well-defined models of heart failure. Magn Reson Med 57:50–58, 2007. © 2006 Wiley-Liss, Inc.

Key words: magnetic resonance spectroscopy; magnetic resonance imaging; energy metabolism; heart failure; nitric oxide

High-energy phosphates (HEPs), such as adenosine triphosphate (ATP) and phosphocreatine (PCr), are the chemical currency that pays for almost all of the energy-consuming processes within the body. This holds true in particular for the heart, which consumes more energy per gram than any other organ under resting conditions. The importance of a tightly balanced myocardial energy state is emphasized by the association of disturbed HEP levels and ventricular dysfunction. Several combined magnetic resonance imaging (MRI) and spectroscopy (MRS) studies in humans have demonstrated that the normal cardiac PCr-to-ATP (PCr/ATP) ratio of about 1.8–2.0 (1–5) is reduced in chronic heart failure (3,6,7). These observations have renewed interest in the decade-old hypothesis that the failing heart is energy starved (8,9). However, whether these metabolic changes are the cause or consequence of the disease, or even contribute to the progression of failure is still a matter of debate.

Both clinical (10,11) and experimental (12,13) studies have reported that the development of heart failure is associated with the upregulation of inducible nitric oxide synthase (iNOS) expression and activity, although conflicting results have also been published (14). Therefore, it has been hypothesized that an enhanced cytosolic NO production may account at least in part for the myocardial dysfunction observed in a variety of heart muscle disorders. At the same time, mounting evidence points to NO as a pivotal element in mitochondrial pathophysiology (for review see Ref. 15). Relevant to ischemic conditions is the ability of NO to bind to the oxygen-binding center of cytochrome c oxidase with an affinity similar to that for guanylate cyclase. The interaction of NO with components of the electron-transport chain may therefore represent the crucial link between derangements in mitochondrial ATP generation and heart failure.

With the advent of molecular techniques to produce targeted gene mutations, it has become possible to generate mouse models to study the underlying molecular mechanisms of heart failure. For the functional characterization of these transgenic models in vivo, several imaging techniques have been adapted to the small (~0.1 g) and fast (~600 beats/min or 10 beats/s) mouse heart, including x-ray computed tomography (CT), positron emission tomography (PET), echocardiography (ECG), and MRI. Characterization of cardiac energetics in these models has been mostly performed ex vivo by ^{31}P MRS in isolated, saline-perfused preparations (16,17), which are restricted per se to end-point studies. In vivo ^{31}P MRS of the mouse heart has been employed up to now only in two laboratories using ^{31}P surface coils (18,19). However, due to the relative low field strength of the magnets used, spectroscopic data could be acquired only with sequences that resulted in limited spatial resolution (2.35 T, ISIS → entire heart (18), 4.7 T, 1D CSI → profile of the anterior wall (19)), which precluded measurement of HEP in different areas of the heart.

The present study examined the feasibility of analyzing the murine cardiac energy state with high spatial resolution in vivo by acquisition-weighted 2D ^{31}P CSI at a field strength of 9.4T. In our experiments we used a double-tuned ^{1}H/^{31}P birdcage resonator to record anatomical ^{1}H MR images and the corresponding 2D ^{31}P CSI data set. Additionally, we employed this setting for an integrated energetic and functional characterization of a transgenic mouse model characterized by NO-induced heart failure (20).

Institut für Herz und Kreislaufphysiologie, Universitätsklinikum Düsseldorf, Heinrich Heine Universität, Düsseldorf, Germany.

Grant sponsor: Deutsche Forschungsgemeinshaft (DFG); Grant numbers: Sonderforschungsbereich 612, Teilprojekt Z2; SCHR159/9.

*Correspondence to: Ulrich Flögel, Institut für Herz und Kreislaufphysiologie, Universitätsklinikum Düsseldorf, Heinrich Heine Universität, Postfach 101007, 40001 Düsseldorf, Germany. E-mail: floegel@uni-duesseldorf.de

Received 13 April 2006; revised 7 August 2006; accepted 21 August 2006.
DOI 10.1002/mrm.21101
Published online 30 November 2006 in Wiley InterScience (www.interscience.wiley.com).

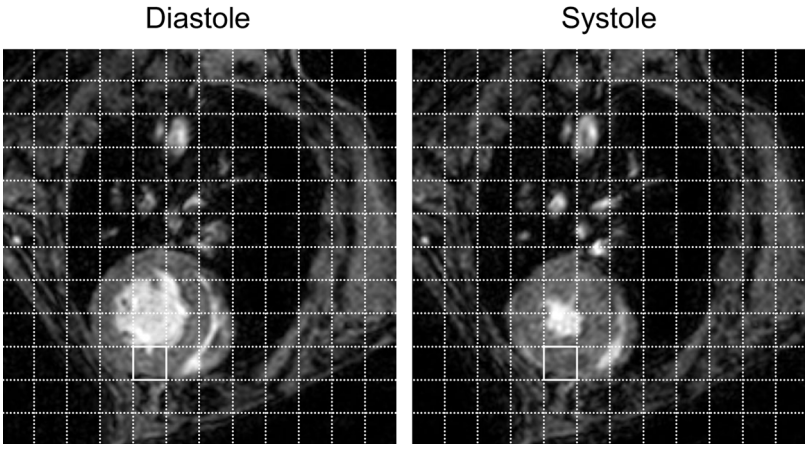

FIG. 1. Sections of end-diastolic (left) and end-systolic (right) MR images from a WT mouse heart superimposed with the corresponding spectroscopic matrix, showing that heart tissue is only slightly displaced within the spectroscopic grid from diastole to systole. Therefore, averaging without cardiac gating introduces only a minor error in voxel assignment to the anterior, lateral, posterior, and septal walls.

MATERIALS AND METHODS

Animals

Animal experiments were performed in accordance with the national guidelines on animal care and were approved by the Bezirksregierung Düsseldorf. The mice used in this study were bred at the Tierversuchsanlage of Heinrich Heine Universität, Düsseldorf, Germany. They were fed with a standard chow diet and received tap water ad libitum. tg-iNOS^{+} (21) mice (FVB strain) and myo$^{-/-}$ (22) mice (NMRI strain) were crossed to obtain heterozygous tg-iNOS^{+}/myo$^{+/-}$ mice. Double heterozygous males and females were intercrossed, and the F2 offspring was used for analysis. This approach allowed us to analyze the phenotype of both mutations independently of the different genetic backgrounds of both parent strains. The genotypes of mice were established by PCR (40 cycles with 94°C 30″, 55°C 1′ and 72°C 1′) using the following primers: detection of iNOS cDNA: iNOS1746F: 5′-TGCTAATGCGAAAGGTCATGG; iNOS–1948R: 5′-CCCAAATGTGCTTGTCACCAC; detection of myoglobin wild-type (WT) allele: mygA: 5′-GTCTGTTTAAGACTCACC, mygB: 5′-TACCTCCAGGTACTTGACC, detection of the disrupted allele: mym1: 5′-TGTTCGCCAGGCTCAAGG, mym2: 5′-GGGGAGAAAGCTAACGGG. Amplified fragments were analyzed on 1.5% agarose gels. The weights of the animals used for MRI analysis ranged from 38 to 44 g, and five male mice from each group were investigated.

MR Measurements

Data were recorded on a Bruker DRX 9.4T wide-bore (89 mm) NMR spectrometer operating at frequencies of 400.13 MHz for ^{1}H and 161.97 MHz for ^{31}P measurements. In vivo experiments (MRI, 2D CSI) were performed using a Bruker microimaging unit (Mini 0.5) equipped with an actively shielded 57-mm gradient set (capable of 200 mT/m maximum gradient strength and 110 μs rise time at 100% gradient switching) and Paravision 3.01 as operating software. Depending on the mouse size, a double-tuned ^{1}H/^{31}P 30- or 38-mm birdcage resonator was used to ensure a geometrical optimal filling of the coil. High-resolution spectra from tissue extracts were recorded with a 10-mm ^{1}H/^{31}P dual probe (operating software, XWinNMR 3.5).

In Vivo Experiments

The mice were anesthetized with 1.5% isoflurane in a water-saturated gas mixture of 20% oxygen in nitrogen applied at a rate of 75 ml/min by manually restraining the animal and placing its head in an in-house-built nose cone. The front paws and the left hind paw were attached to ECG electrodes (Klear-Trace; CAS Medical Systems, Branford). To minimize antenna artifacts, the ECG wires were shielded and arranged in loops within the probe head. Respiration was monitored by means of a pneumatic pillow positioned at the animal's back. Vital functions were acquired by a M1025 system (SA Instruments, Stony Brook, NY, USA) and used to synchronize data acquisition with cardiac and respiratory motion.

The anesthetized mice were carefully fixed within the animal-handling system by small pieces of soft rubber foam, which positioned the heart as close as possible to the center of the system in order to ensure the greatest possible magnetic homogeneity for cardiac MRS measurements. Therefore, the mice were sometimes slightly tilted within the *xy*-plane, and the linear shape of the rubber foam pieces is occasionally reflected in the anatomical images of the mouse thorax. Throughout the experiment the mice were breathing spontaneously at a rate of approximately 100 min^{-1} and were kept at 37°C. For in vivo cardiac MR measurements, a phantom-optimized shim file was used, which routinely resulted in a linewidth at half maximum of 40–80 Hz. Neither additional automatic nor manual localized shimming could considerably improve the quality of the heart spectra in a reasonable time frame. With the use of the phantom-optimized shim file, high-resolution images were obtained in each case, and only one spectroscopic session (out of 11) had to be rejected because of too-large linewidths.

MRI

For functional analysis, high-resolution images of the mouse hearts were acquired using an ECG- and respiratory-triggered fast gradient-echo cine sequence essentially as described previously (23,24). A flip angle of 15°, echo time (TE) of 1.8 ms, and repetition time (TR) of about 4 ms were used. The pixel size after zero-filling was 117 × 117 μm^2 (field of view (FOV) = 30 × 30 mm^2; matrix = 128 × 128;

acquisition time per slice for one cine sequence = 1–2 min). Six to eight contiguous ventricular short-axis slices (slice thickness = 1 mm) were acquired to cover the entire heart. Functional parameters were analyzed as previously described (23,24).

2D ^{31}P Chemical Shift Imaging (CSI)

After orthogonal scout images were acquired, the spectroscopic volume was positioned in the coronal and sagittal planes to cover the entire heart. In the axial plane the grid was placed to obtain at least one voxel of the anterior wall with minimal spatial contamination of blood or chest muscle. No cardiac or respiratory gating was applied. The 2D ^{31}P CSI data set was recorded using a sine-bell acquisition-weighted sequence to improve the spatial response function (25), with flip angle = 45°; TR = 250 ms; FOV = 30 × 30 mm^2; data points in the spectral domain = 1024; spectral width = 6510 Hz; and slice selection with a 500-μs sinc3 pulse. The numbers of acquisitions in the middle row of the symmetrical acquisition matrix were 0, 256, 768, 1024, 1024, 768, 256, and 0 (for a total of 18432 acquisitions within 75 min). An exponential filter of 20 Hz was applied in the spectroscopic direction, and zero-filling by a factor of 2 was applied in each spatial dimension, resulting in a 16 × 16 matrix with a resolution of 1.875 mm in the *x* and *y* directions. The slice thickness depended on the heart size (usually 6–8 mm, yielding a voxel size of 21–28 μL).

After the CSI sequence was terminated, orthogonal scout images were again recorded to ensure that the position of the mouse had not changed during acquisition of the spectroscopic data. The full experimental protocol, including both functional and energetic analyses, took about 2 hr and was well tolerated by all of the mice, which recovered from anesthesia within 1–2 min after the nose cone was removed.

The 2D data sets were analyzed after they were imported into an in-house-developed software module based on the LabVIEW package (National Instruments, Austin). Several display and analysis tools were implemented (including the signal-to-noise ratio (SNR), integration, calibration, full width at half maximum (FWHM), file algebra, data export, and spectra overlay) to allow quantification of spatially localized ^{31}P MR spectra in direct correlation with the morphological ^{1}H MR image. After Fourier transformation and magnitude calculation were performed, the peak areas were obtained by integration. These areas were scaled according to saturation factors determined as described below. ATP peak areas were converted to concentrations on basis of the heart extract data for each individual mouse (see below). Subsequently, PCr concentrations were calculated from the PCr/ATP ratio measured in vivo. Chemical shifts were referenced to the PCr resonance at −2.52 ppm.

Correction factors for partial saturation were derived from unlocalized spectra of the thorax acquired with the same flip angle and TR given above, as well as under fully relaxed conditions (flip angle = 90°; TR = 15 s), assuming that cardiac and chest muscle metabolites have the same T_1 values (26,27). We obtained a saturation correction factor for the PCr/ATP ratio of 1.63 ± 0.13 (N = 6). No differences were found between WT and transgenic mice. Using the T_1 values for ATP and PCr obtained from previous isolated perfused heart experiments (unpublished data; see below) the required saturation correction for a sequence with an excitation angle of 45° and a TR of 250 ms is calculated to be 1.61 ± 0.09 for the PCr/ATP ratio, which is in good agreement with the value determined in vivo.

T_1 values for PCr and ATP were determined from conventional inversion-recovery experiments. The calculated values (PCr: 1.9 ± 0.1 s; ATP: 0.9 ± 0.1 s) were in agreement with published data for rat hearts at 9.4T (28). No differences were found between the strains.

High-Resolution Spectroscopy of Heart PCA Extracts

Tissue extracts were prepared 1 day after the in vivo MR investigation. Mice were anesthetized with urethane (1.5 g/kg i.p.). Immediately after thoracotomy the hearts were arrested with an ice-cold cardioplegic solution and flushed with ice-cold saline. The blood-free hearts were rapidly excised, snap-frozen, and subsequently extracted with 1 mol/L perchloric acid (PCA) as previously described (17). The extracts were neutralized, lyophilized, and stored at −20°C.

Lyophilized PCA extracts were redissolved in 0.5 ml D_2O and transferred into a 5-mm NMR tube. Shimming was done manually on the D_2O lock signal as well as the free induction decay (FID), and a linewidth at half height of <1 Hz was obtained. ^{1}H MR spectra were acquired with a flip angle of 90°, TR of 15 s, low-power water presaturation, 512 scans, spectral width of 5580 Hz, and data size of 16 K zero-filled to 32 K. Chemical shifts were referenced to (trimethylsilyl)-propionic-2,2,3,3d$_4$-acid (TSP) at 0 ppm. For the ^{31}P MR spectra, 20 K scans were accumulated with a flip angle of 75°, TR of 2.5 s, composite pulse decoupling with Waltz16, spectral width of 8090 Hz, data size of 8 K zero-filled to 16 K, and exponential weighting resulting in a 1-Hz line-broadening. Chemical shifts were referenced to the PCr resonance at −2.52 ppm.

The pool size of various metabolites (in particular creatine (Cr) and PCr) was quantified from the fully relaxed high-resolution ^{1}H MR spectra. TSP (1 mM) was used to standardize the concentration, and the results were correlated with the protein content as previously described (17,29). The PCr values determined from the ^{1}H MR spectra were subsequently used as internal standards in the corresponding ^{31}P MR spectra of the PCA extracts to calculate myocardial ATP concentrations. Partial saturation was corrected by factors that were obtained from ^{31}P NMR spectra of model solutions recorded with the same acquisition and processing parameters as the spectra of the heart extracts. The model solutions contained equimolar metabolite mixtures, 140 mmol/L KCl, and 5 mmol/L $MgCl_2$, and were additionally saturated with $KClO_4$ in order to obtain an ionic strength similar to that of the redissolved cell extracts.

Materials

All compounds used in this study were of analytical grade or the highest purity available. TSP and D_2O were ob-

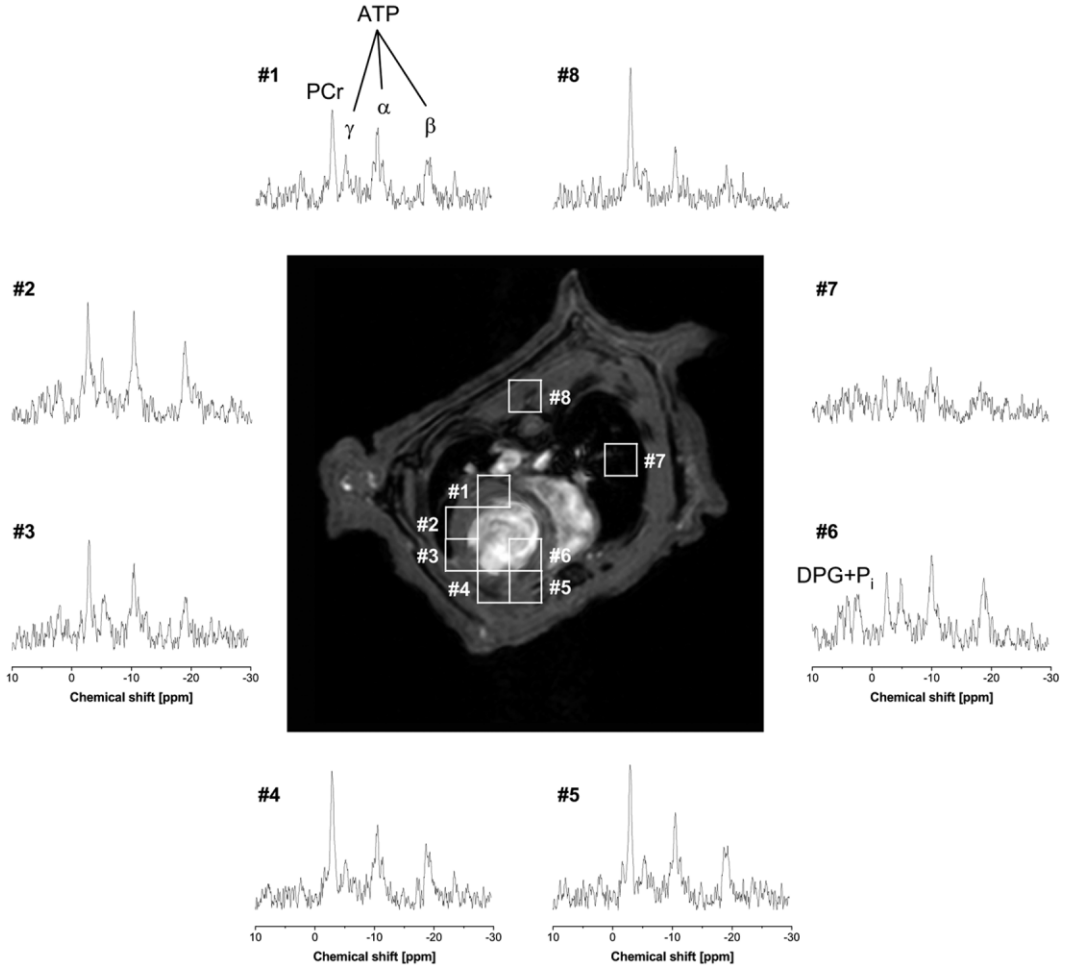

FIG. 2. Representative ^{31}P MR spectra from selected voxels of the mouse thorax superimposed with the anatomical ^{1}H MR image (30 × 30 mm^2) acquired in the same examination without repositioning the animal. Spectra were recorded using an acquisition-weighted 2D ^{31}P CSI sequence with a resolution of 1.875 × 1.875 × 6.5 mm^3 (22.8 μL). Spatially localized spectra of the posterior (#1), lateral (#2 and #3), and anterior (#4 and #5) walls, and the septum (#6) of the heart are displayed. Additionally, spectra from the lungs (#7) and the skeletal muscle of the animal's back (#8) are shown.

tained from Sigma-Aldrich. All other reagents were obtained from Merck.

Statistical Analysis

All results are expressed as the means ± SD. Data were compared by means of Student's unpaired *t*-test, and a *P*-value lower than 0.05 was considered to be significant.

RESULTS

Spectroscopic Imaging of Normal Hearts

The 2D ^{31}P CSI data set was recorded using acquisition weighting without cardiac or respiratory gating in order to save time and to avoid inconsistent saturation effects due to varying repetition rates. Preliminary experiments revealed no significant differences in spectral quality when gating was applied (data not shown). Observing heart movement within the spectroscopic grid during the cardiac cycle demonstrated that myocardial tissue was only slightly displaced within the CSI matrix from end-diastole to end-systole (Fig. 1). Therefore, averaging without cardiac gating introduced only a minor error in voxel assignment to the anterior, lateral, posterior, and septal walls. Since diastole accounts for approximately two-thirds of the cardiac cycle, spectroscopic voxels are related in the following text to the corresponding end-diastolic images.

Characteristic ^{31}P MR spectra extracted from a representative CSI data set are presented in Fig. 2 in correlation with the anatomical ^{1}H MR image. Spectral data of the highlighted voxels located over the posterior (#1), lateral (#2 and #3), and anterior walls (#4 and #5), and the septum (#6) of the heart are displayed. As can be seen, spectra of good quality could be acquired with high spatial resolution (1.875 × 1.875 × 6.5 mm^3, i.e., 22.8 μL) at defined regions of the heart within a reasonable acquisition time of 75 min. For comparison, spectra from the right lung (#7) and the skeletal muscle of the animal's back (#8) are shown. Almost all spectra from voxels covering the free LV wall appear to be exempt from measurable chest wall contamination (voxels #1–5), as can be deduced by the

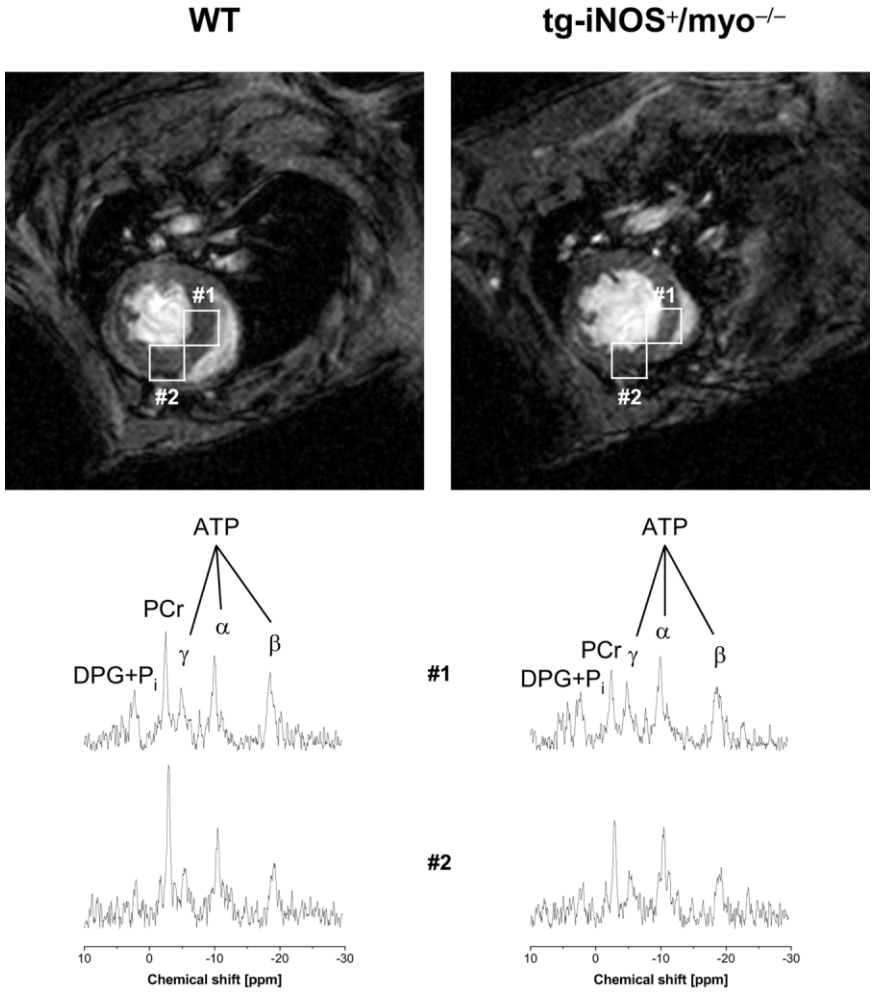

FIG. 3. Axial ^{1}H MR images (FOV = 30 × 30 mm^2) in end-diastole and corresponding cardiac ^{31}P MR spectra of WT (left) and tg-iNOS$^+$/myo$^{-/-}$ (right) mice. Characteristic spectra of the septum (#1) and the anterior wall (#2) show that impaired cardiac function in tg-iNOS$^+$/myo$^{-/-}$ mice is accompanied by a decreased PCr/ATP ratio. Note that the end-diastolic volume is increased and that in both regions of the heart the myocardial PCr/ATP ratio is lower in the mutant mouse compared to the WT mouse.

lack of inorganic phosphate (P_i) signals. Furthermore, the lack of detectable 2,3-diphosphoglycerate (DPG) indicates that blood metabolites do not significantly contaminate these voxels. However, voxels located over the septum contained ^{31}P signals from blood in almost each examination (cf., #6 in Fig. 2 and #1 in Fig. 3). The enhanced contribution of chamber blood to septal voxels results not only in the appearance of the DPG signal, but also in an apparent reduction of the myocardial PCr/ATP ratio in these spectra (#6). As expected, almost no ^{31}P signal was obtained from the lung (voxel #7), whereas in skeletal muscle the high PCr/ATP ratio was evident (voxel #8).

Analysis of Mice Lacking Myoglobin and Overexpressing iNOS (tg-iNOS$^+$/myo$^{-/-}$)

In a separate series we used the integrated MRI/MRS approach developed in this study to investigate cardiac function and energetics of a murine hypertrophy model that was recently generated in our laboratory (20). ^{1}H MRI revealed signs of ventricular dilatation in tg-iNOS$^+$/myo$^{-/-}$ mice as reflected by an increase in both end-diastolic (Fig. 3, top) and end-systolic volumes (EDV and ESV in the mutant: 110 ± 5 and 51 ± 4 μl, respectively; WT: 93 ± 6 and 28 ± 5 μl, respectively; $P < 0.05$, $N = 5$). This was accompanied by a substantial functional depression in double transgenic hearts characterized by a significant reduction of the ejection fraction (tg-iNOS$^+$/myo$^{-/-}$, 53.9% ± 3.8%; WT, 69.7% ± 3.6%) and systolic wall thickening (tg-iNOS$^+$/myo$^{-/-}$, 35.8% ± 7.6%; WT, 64.4% ± 11.9%; $P < 0.05$, $N = 5$) compared to normal hearts (Table 1). 2D ^{31}P CSI demonstrated that cardiac dysfunction in the mutant was associated with a lowered PCr/ATP ratio, as shown in Fig. 3 by means of representative spectra from the septum (#1) and the anterior wall (#2) of both WT (left) and transgenic (right) mice. Note that despite contamination of septal voxels with chamber blood, as reflected by the occurrence of DPG signals in the spectra of both groups, the reduced PCr/ATP ratio in the mutant was still detectable. However, for quantification of HEP levels, only voxels covering the free left ventricle (LV) wall were considered. Analysis of voxels from the posterior, lateral, and anterior walls (Fig. 4) revealed a significantly reduced LV PCr content over the entire LV in tg-iNOS$^+$/myo$^{-/-}$ (8.8 ± 0.8 mmol/L) as compared to WT (12.3 ± 1.1 mmol/L, $N = 5$, $P < 0.05$) mice, whereas ATP levels remained unaltered between the two groups (PCr/ATP-ratio: WT, 2.05 ± 0.22; tg-iNOS$^+$/myo$^{-/-}$ 1.54 ± 0.18, $N = 5$, $P < 0.05$).

The noninvasive spectroscopic measurements were validated against tissue extract data from the same hearts

Table 1
Basal Cardiac Parameters of WT and tg-iNOS^{+}/myo$^{-/-}$ Mice as Assessed by MRI In Vivo

Parameter		WT	tg-iNOS^{+}/myo$^{-/-}$
Animal weight	(g)	41.4 ± 1.7	40.6 ± 1.3
Heart rate	(bpm)	481 ± 23	484 ± 16
Enddiastolic volume (EDV)	(μl)	93 ± 6	110 ± 5**
Endsystolic volume (ESV)	(μl)	28 ± 5	51 ± 4***
Stroke volume (SV)	(μl)	65 ± 4	60 ± 6
Ejection fraction (EF)	(%)	69.7 ± 3.6	53.9 ± 3.8***
Cardiac output (CO)	(ml/min)	31.3 ± 2.4	28.9 ± 3.6
Enddiastolic wall diameter	(mm)	0.97 ± 0.08	1.03 ± 0.11
Endsystolic wall diameter	(mm)	1.60 ± 0.10	1.39 ± 0.13*
Systolic wall thickening	(%)	64.4 ± 11.9	35.8 ± 7.6**
Left ventricular mass	(mg)	126 ± 9	144 ± 16
Heart body index	(mg/g)	3.04 ± 0.20	3.55 ± 0.35*

The values are means ± SD (each group $N = 5$, *$P < 0.05$, **$P < 0.01$, ***$P < 0.001$).

excised 1 day after the in vivo investigation. Figure 5 shows characteristic high-resolution ^{1}H spectra from PCA extracts of snap-frozen WT (bottom) and mutant (top) hearts, with substantially lower PCr and concomitantly higher Cr levels in transgenic than in control myocardium. However, ^{1}H MR data indicated no differences in total creatine content of tg-iNOS^{+}/myo$^{-/-}$ (21.8 ± 2.2 mmol/L) and WT hearts (21.7 ± 2.1 mmol/L, each group $N = 5$). Consistent with the 2D ^{31}P CSI data, the corresponding ^{31}P MR tissue extract spectra (Fig. 6) displayed a lower cardiac PCr/ATP ratio in the double-mutant mice than in WT controls. A comparison of the mean PCr/ATP ratios calculated from in vivo and ex vivo spectra showed an excellent agreement between CSI and tissue extract data (Fig. 7). Furthermore, correlation of the individual data points of in vivo and ex vivo experiments yielded satisfying correlation coefficients for both groups (R^2: WT, 0.972; tg-iNOS^{+}/myo$^{-/-}$, 0.834).

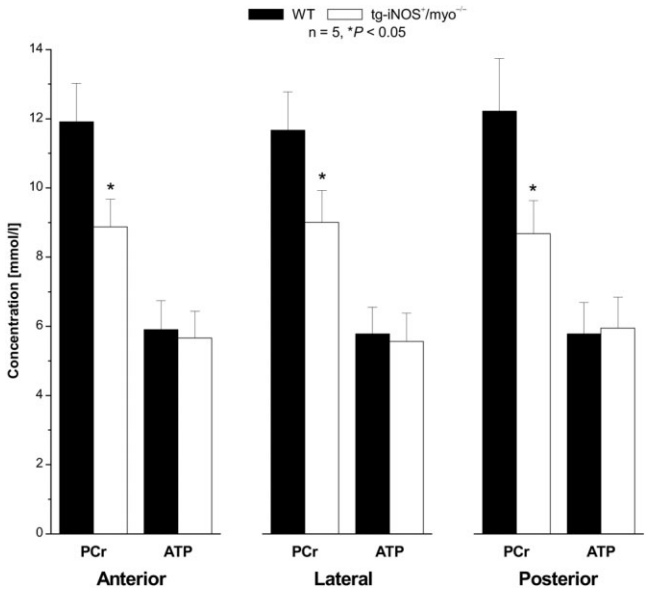

FIG. 4. In vivo LV HEP levels of WT (black bars) and tg-iNOS^{+}/myo$^{-/-}$ (open bars) mice in the posterior, lateral, and anterior walls. The symbols show the means ± SD for five hearts (*$P < 0.05$).

DISCUSSION

In the present study we used high-resolution ^{1}H MRI and acquisition-weighted 2D ^{31}P CSI at a magnetic field strength of 9.4 T to characterize in parallel murine cardiac function and energetics in vivo. Within a reasonable measurement period of 75 min, we obtained ^{31}P MR spectra with high spatial resolution in defined regions of the heart. Spectra from voxels covering the posterior, lateral, anterior, and septal walls were acquired with almost no measurable contribution from ^{31}P compounds of blood or the chest wall. Using this approach we were able to show that in a NO-induced heart failure model, ventricular dilatation and functional depression were accompanied by an impaired cardiac energy homeostasis over the entire LV.

Previously reported volume-selective ^{31}P MR studies of the mouse heart were carried out with the use of surface coils at significantly lower field strengths (2.35 and 4.7T) and were limited to the investigation of the entire heart (18) or a 1D profiling of the anterior wall (19). In this study the magnetic field of 9.4T provided the increased SNR required for the measurement of HEP in different regions

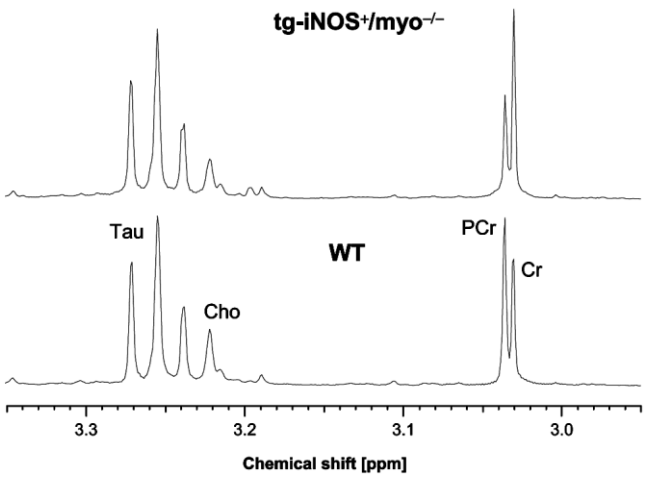

FIG. 5. Characteristic sections of high-resolution ^{1}H MR spectra obtained from heart PCA extracts of WT (bottom) and tg-iNOS^{+}/myo$^{-/-}$ (top) mice used to quantify Cr and PCr levels. Assignments: Cho, cholines; Cr, creatine; PCr, phosphocreatine; Tau, taurine.

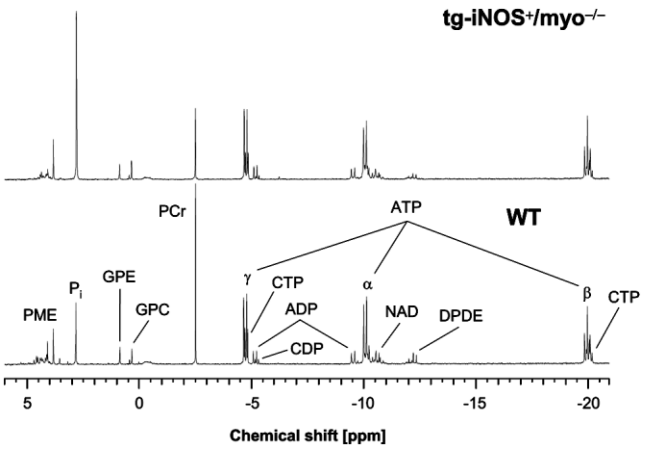

FIG. 6. Representative high-resolution ^{31}P MR spectra of heart PCA extracts from WT (bottom) and tg-iNOS^{+}/myo$^{-/-}$ (top) mice. Assignments: ADP, adenosine diphosphate; ATP, adenosine triphosphate; CDP, cytidine triphosphate; CTP, cytidine triphosphate; DPDE, diphosphodiester; GPC, glycerophosphocholine; GPE, glycerophosphoethanolamine; NAD, nicotinamide adenine dinucleotide; PCr, phosphocreatine; P_i, inorganic phosphate; PME, phosphomonoester.

of the heart. The double-tuned ^{1}H/^{31}P birdcage resonator enabled us to acquire ^{31}P MR spectra over the entire thorax in direct correlation to the morphological ^{1}H MR image independently of the restricted penetration depth of a surface coil, which makes this approach generally applicable to the spectroscopy of any organ or region within the mouse. Moreover, the birdcage resonator allows a defined excitation pulse to be applied over the full FOV, thus avoiding a nonuniform saturation of the metabolites at different locations. Further improvements may be achieved by the use of a volume-transmit/surface receive coil, although the design of this coil in the diameters required may be hampered due to geometrical restrictions, since the outer diameter is limited by the size of the gradient system (57 mm), and the inner diameter is limited by the chest measurements of the mice (30–38 mm). To ameliorate the spatial response function and reduce the signal contamination between adjacent voxels, we used acquisition weighting according to a sine-bell function to record the 2D CSI data set, as introduced by Pohmann and von Kienlin (25).

Since we did not gate the 2D ^{31}P CSI sequence to cardiac and respiratory motion, we were able to acquire data sets with a constant TR, which resulted in considerable time savings. This will become especially relevant for studies of animals in labile hemodynamic conditions, such as infarction or stroke. While in the present study we observed no alterations in vital parameters with time, it cannot automatically be assumed that other transgenic mouse models show a similar long-term stability in the vertical position. The constant repetition also avoids problems due to different saturations of PCr and ATP as a consequence of varying heart and/or respiration rates between individual mice. This should be even more important for the analysis of cardiac energetics in mice with genetic modifications that lead to arrhythmias or changes in heart rate. Additionally, the "smearing" of the data acquisition over the entire cardiac cycle helps to reduce contamination of ^{31}P signals from chamber blood, since the systolic wall thickening diminishes the amount of blood within the voxels covering the myocardium (Fig. 1). Lack of contamination from blood is evidenced by the lack of measurable DPG signals in the spectra attributed to the LV wall. DPG signals, however, are visible in septal voxels (Figs. 2 and 3). Similarly, based on the lack of detectable P_i in voxels of LV tissue, chest wall metabolites are unlikely to contaminate these voxels. On the other hand, averaging without cardiac gating introduces an error in voxel assignment; however, we believe the described advantages outweigh the minor inaccuracy in spatial allocation.

The cardiac PCr/ATP ratios of the anterior, lateral, and posterior walls were found to be close to 2 in normal WT mice, which is consistent with values reported for healthy humans (25,30). Similar ratios were also obtained in the previous studies of murine hearts with lower spatial resolution (18,19). Further validation of the acquired in vivo data was obtained from postmortem analysis of heart extracts by high-resolution ^{31}P MRS. The slightly lower PCr/ATP ratios found in the corresponding tissue extract spectra of both groups may be related to partial hydrolysis of PCr during preparation of the PCA extracts. The ATP concentration determined from these extracts was used as internal standard for absolute quantification of PCr in vivo. This approach implies a homogeneous distribution of ATP over the entire LV, and therefore cannot be applied to models that do not fulfill this assumption (e.g., myocardial infarction). To overcome this limitation of the present study, a direct in vivo quantification would be preferable. For this purpose, an endo- or exogenous concentration standard is required, and the myocardial mass present in each ^{31}P image voxel must be determined to account for partial-volume effects. The latter information is easily available from the corresponding high-resolution anatomical ^{1}H images.

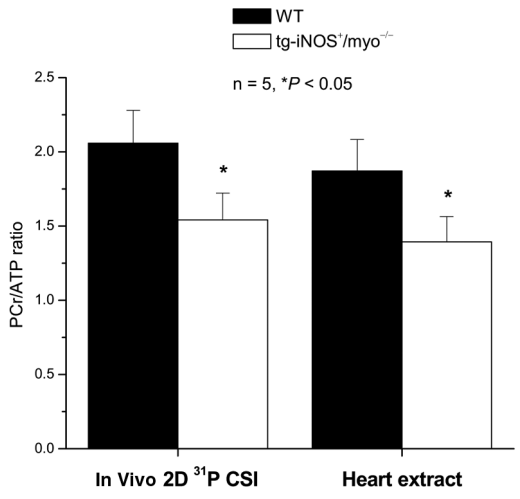

FIG. 7. Comparison of cardiac PCr/ATP ratios of WT (black bars) and tg-iNOS^{+}/myo$^{-/-}$ (open bars) mice determined in vivo by 2D ^{31}P CSI and postmortem by high-resolution ^{31}P MRS of tissue extracts. In vivo data were averaged over the posterior, lateral, and anterior walls. The symbols show the means ± SD for five hearts (*$P < 0.01$).

Using the proposed protocol, we analyzed a transgenic mouse model with cardiac-specific iNOS overexpression and concomitant myoglobin-deficiency (tg-iNOS^{+}/myo$^{-/-}$) that was recently generated in our laboratory (20). Due to enhanced long-term nitrosative stress, these animals develop cardiac hypertrophy, ventricular dilatation, and interstitial fibrosis as demonstrated by histological analysis. Furthermore, we found a reactivation of the fetal gene expression program typical of heart failure, and the upregulation of several biochemical hypertrophy markers (20). In this and a previous study we provided evidence that both chronic and acute inhibition of myoglobin in tg-iNOS^{+} hearts perturbs the cardiac energy state (31). However, we deliberately conducted both investigations in saline-perfused hearts without red blood cells to study the specific role of myoglobin within tg-iNOS^{+} hearts, and to exclude interfering side reactions between NO and hemoglobin. However, in this preparation the lack of hemoglobin, another important player in cardiovascular NO homeostasis, may result in nonphysiologically high NO concentrations. Furthermore, since NO competes with oxygen for binding to cytochrome c oxidase (32), the mitochondrial effect of NO becomes more pronounced when cardiac oxygenation may be borderline, such as in the isolated perfused heart.

Our combined MRI/MRS approach extends and substantiates our previous findings in that NO-induced cardiac dysfunction is now shown to be associated with a severe reduction of cardiac PCr levels over the entire LV in the intact animal. Together with the previously observed reduction of myocardial oxygen consumption in tg-iNOS^{+}/myo$^{-/-}$ mice (20), the results of this study provide first in vivo evidence that in the absence of efficient NO scavenging, iNOS-derived NO can critically interfere with the respiratory chain, leading to a reduction in phosphorylation potential and to a deterioration of the cardiac energy homeostasis (33). This observation is specific for the double mutant, since previous investigations revealed no signs of impaired cardiac function in single transgenic tg-iNOS^{+} (21,31), myo$^{-/-}$ (22,33), or heterozygous tg-iNOS^{+}/myo$^{+/-}$ mice (20). The heart-failure phenotype of tg-iNOS^{+}/myo$^{-/-}$ mice can thus be clearly related to lack of the NO scavenging properties of myoglobin (20,31,33), and it is most likely a consequence of a chronically disturbed energy state. It is noteworthy that the decrease in the PCr/ATP ratio by about 0.5 U in double transgenic hearts is of similar magnitude as the drop in this ratio reported for human cardiomyopathies (7,34,35). This in turn supports the notion that derangements in cardiac energy production are an important determinant of the progression of heart disease (36).

In conclusion, we were able to acquire spatially localized spectra simultaneously from the posterior, lateral, anterior, and septal walls of the mouse heart. This permits the noninvasive, repetitive analysis of transgenic mouse models regarding cardiac anatomy and function together with the regional energy state in one experimental session, and will be of substantial benefit in future studies on the relationship between heart failure and energetics in other genetically well-defined models of heart failure.

ACKNOWLEDGMENTS

We thank Jutta Ziemann and Daniela Haubs for excellent technical assistance.

REFERENCES

1. Weiss RG, Bottomley PA, Hardy CJ, Gerstenblith G. Regional myocardial metabolism of high-energy phosphates during isometric exercise in patients with coronary artery disease. N Engl J Med 1990;323:1593–1600.
2. Menon RS, Hendrich K, Hu X, Ugurbil K. ^{31}P NMR spectroscopy of the human heart at 4 T: detection of substantially uncontaminated cardiac spectra and differentiation of subepicardium and subendocardium. Magn Reson Med 1992;26:368–376.
3. Hetherington HP, Luney DJ, Vaughan JT, Pan JW, Ponder SL, Tschendel O, Twieg DB, Pohost GM. 3D ^{31}P spectroscopic imaging of the human heart at 4.1 T. Magn Reson Med 1995;33:427–431.
4. Neubauer S, Horn M, Cramer M, Harre K, Newell JB, Peters W, Pabst T, Ertl G, Hahn D, Ingwall JS, Kochsiek K. Myocardial phosphocreatine-to-ATP ratio is a predictor of mortality in patients with dilated cardiomyopathy. Circulation 1997;96:2190–2196.
5. Yabe T, Mitsunami K, Okada M, Morikawa S, Inubushi T, Kinoshita M. Detection of myocardial ischemia by ^{31}P magnetic resonance spectroscopy during handgrip exercise. Circulation 1994;89:1709–1716.
6. Hardy CJ, Weiss RG, Bottomley PA, Gerstenblith G. Altered myocardial high-energy phosphate metabolites in patients with dilated cardiomyopathy. Am Heart J 1991;122:795–801.
7. Neubauer S, Krahe T, Schindler R, Horn M, Hillenbrand H, Entzeroth C, Mader H, Kromer EP, Riegger GA, Lackner K. ^{31}P magnetic resonance spectroscopy in dilated cardiomyopathy and coronary artery disease. Altered cardiac high-energy phosphate metabolism in heart failure. Circulation 1992;86:1810–1818.
8. Olson RE, Schwartz WB. Myocardial metabolism in congestive heart failure. Medicine 1951;30:21–41.
9. Olson RE. Myocardial metabolism in congestive heart failure. J Chronic Dis 1959;9:442–464.
10. de Belder AJ, Radomski MW, Why HJ, Richardson PJ, Bucknall CA, Salas E, Martin JF, Moncada S. Nitric oxide synthase activities in human myocardium. Lancet 1993;341:84–85.
11. Haywood GA, Tsao PS, der Leyen HE, Mann MJ, Keeling PJ, Trindade PT, Lewis NP, Byrne CD, Rickenbacher PR, Bishopric NH, Cooke JP, McKenna WJ, Fowler MB. Expression of inducible nitric oxide synthase in human heart failure. Circulation 1996;93:1087–1094.
12. Chen Y, Traverse JH, Du R, Hou M, Bache RJ. Nitric oxide modulates myocardial oxygen consumption in the failing heart. Circulation 2002;106:273–279.
13. Gealekman O, Abassi Z, Rubinstein I, Winaver J, Binah O. Role of myocardial inducible nitric oxide synthase in contractile dysfunction and beta-adrenergic hyporesponsiveness in rats with experimental volume-overload heart failure. Circulation 2002;105:236–243.
14. Stein B, Eschenhagen T, Rüdiger J, Scholz H, Förstermann U, Gath I. Increased expression of constitutive nitric oxide synthase III, but not inducible nitric oxide synthase II, in human heart failure. J Am Coll Cardiol 1998;32:1179–1186.
15. Shiva S, Oh JY, Landar AL, Ulasova E, Venkatraman A, Bailey SM, Darley-Usmar VM. Nitroxia: the pathological consequence of dysfunction in the nitric oxide-cytochrome c oxidase signaling pathway. Free Radic Biol Med 2005;38:297–306.
16. Saupe KW, Spindler M, Tian R, Ingwall JS. Impaired cardiac energetics in mice lacking muscle-specific isoenzymes of creatine kinase. Circ Res 1998;82:898–907.
17. Flögel U, Decking UK, Gödecke A, Schrader J. Contribution of NO to ischemia-reperfusion injury in the saline-perfused heart: a study in endothelial NO synthase knockout mice. J Mol Cell Cardiol 1999;31:827–836.
18. Omerovic E, Basetti M, Bollano E, Bohlooly M, Tornell J, Isgaard J, Hjalmarson A, Soussi B, Waagstein F. In vivo metabolic imaging of cardiac bioenergetics in transgenic mice. Biochem Biophys Res Commun 2000;271:222–228.
19. Chacko VP, Aresta F, Chacko SM, Weiss RG. MRI/MRS assessment of in vivo murine cardiac metabolism, morphology, and function at physiological heart rates. Am J Physiol Heart Circ Physiol 2000;279:H2218–H2224.

20. Gödecke A, Molojavyi A, Heger J, Flögel U, Ding Z, Jacoby C, Schrader J. Myoglobin protects the heart from inducible nitric-oxide synthase (iNOS)-mediated nitrosative stress. J Biol Chem 2003;278:21761–21766.
21. Heger J, Gödecke A, Flögel U, Merx MW, Molojavyi A, Kühn-Velten WN, Schrader J. Cardiac-specific overexpression of inducible nitric oxide synthase does not result in severe cardiac dysfunction. Circ Res 2002;90:93–99.
22. Gödecke A, Flögel U, Zanger K, Ding Z, Hirchenhain J, Decking UK, Schrader J. Disruption of myoglobin in mice induces multiple compensatory mechanisms. Proc Natl Acad Sci U S A 1999;96:10495–10500.
23. Flögel U, Laussmann T, Gödecke A, Abanador N, Schäfers M, Fingas CD, Metzger S, Levkau B, Jacoby C, Schrader J. Lack of myoglobin causes a switch in cardiac substrate selection. Circ Res 2005;96:e68–e75.
24. Jacoby C, Molojavyi A, Flögel U, Merx MW, Ding Z, Schrader J. Direct comparison of magnetic resonance imaging and conductance microcatheter in the evaluation of left ventricular function in mice. Basic Res Cardiol 2006;101:87–95.
25. Pohmann R, von Kienlin M. Accurate phosphorus metabolite images of the human heart by 3D acquisition-weighted CSI. Magn Reson Med 2001;45:817–826.
26. Bottomley PA, Hardy CJ, Roemer PB. Phosphate metabolite imaging and concentration measurements in human heart by nuclear magnetic resonance. Magn Reson Med 1990;14:425–434.
27. Bottomley PA, Hardy CJ, Weiss RG. Correcting human heart ^{31}P NMR spectra for partial saturation. Evidence that saturation factors for PCr/ATP are homogeneous in normal and disease states. J Magn Reson 1991;95:341–355.
28. Friedrich J, Nascimben L, Liao R, Ingwall JS. Phosphocreatine T1 measurements with and without exchange in the heart. Magn Reson Med 1993;30:45–50.
29. Flögel U, Willker W, Leibfritz D. Determination of *de novo* synthesized amino acids in cellular proteins revisited by ^{13}C NMR spectroscopy. NMR Biomed 1997;10:50–58.
30. Yabe T, Mitsunami K, Inubushi T, Kinoshita M. Quantitative measurements of cardiac phosphorus metabolites in coronary artery disease by ^{31}P magnetic resonance spectroscopy. Circulation 1995;92:15–23.
31. Wunderlich C, Flögel U, Gödecke A, Heger J, Schrader J. Acute inhibition of myoglobin impairs contractility and energy state of iNOS-overexpressing hearts. Circ Res 2003;92:1352–1358.
32. Giuffre A, Sarti P, D'Itri E, Buse G, Soulimane T, Brunori M. On the mechanism of inhibition of cytochrome c oxidase by nitric oxide. J Biol Chem 1996;271:33404–33408.
33. Flögel U, Merx MW, Gödecke A, Decking UK, Schrader J. Myoglobin: a scavenger of bioactive NO. Proc Natl Acad Sci USA 2001;98:735–740.
34. Conway MA, Bottomley PA, Ouwerkerk R, Radda GK, Rajagopalan B. Mitral regurgitation: impaired systolic function, eccentric hypertrophy, and increased severity are linked to lower phosphocreatine/ATP ratios in humans. Circulation 1998;97:1716–1723.
35. Jung WI, Sieverding L, Breuer J, Hoess T, Widmaier S, Schmidt O, Bunse M, van Erckelens F, Apitz J, Lutz O, Dietze GJ. ^{31}P NMR spectroscopy detects metabolic abnormalities in asymptomatic patients with hypertrophic cardiomyopathy. Circulation 1998;97:2536–2542.
36. Ingwall JS, Weiss RG. Is the failing heart energy starved? On using chemical energy to support cardiac function. Circ Res 2004;95:135–145.

Nitrite Reductase Function of Deoxymyoglobin

Oxygen Sensor and Regulator of Cardiac Energetics and Function

Tienush Rassaf,* Ulrich Flögel,* Christine Drexhage, Ulrike Hendgen-Cotta, Malte Kelm, Jürgen Schrader

Abstract—Although the primary function of myoglobin (Mb) has been considered to be cellular oxygen storage and supply, recent studies have suggested to classify Mb as a multifunctional allosteric enzyme. In the heart, Mb acts as a potent scavenger of nitric oxide (NO) and contributes to the attenuation of oxidative damage. Here we report that a dynamic cycle exists in which a decrease in tissue oxygen tension drives the conversion of Mb from being an NO scavenger in normoxia to an NO producer in hypoxia. The NO generated by reaction of deoxygenated Mb with nitrite is functionally relevant and leads to a downregulation of cardiac energy status, which was not observed in mice lacking Mb. As a consequence, myocardial oxygen consumption is reduced and cardiac contractility is dampened in wild-type mice. We propose that this pathway represents a novel homeostatic mechanism by which a mismatch between oxygen supply and demand in muscle is translated into the fractional increase of deoxygenated Mb exhibiting enhanced nitrite reductase activity. Thus, Mb may act as an oxygen sensor which through NO can adjust muscle energetics to limited oxygen supply. **(*Circ Res*. 2007;100:1749-1754.)**

Key Words: nitrite ■ hypoxia ■ myoglobin ■ cardiac function

Myoglobin (Mb) is an important intracellular oxygen binding hemeprotein and one of the most widely studied proteins. The first pioneering review on Mb was published as early as 1939, in which Millikan concluded that "muscle hemoglobin" acts primarily as a short term oxygen store, tiding the muscle over from one contraction to the next.[1] In the past decade several additional biological functions were ascribed to Mb[2] and its molecular relative hemoglobin (Hb). Experiments with transgenic mice deficient in Mb have shown that Mb is an important scavenger of nitric oxide (NO) under normoxia[3,4] which also protects the heart against reactive oxygen species.[4] Very recently, it has been reported that Hb participates in NO metabolism not only by oxidative inactivation, but also by the nonenzymatic NO formation from nitrite by deoxyHb.[5] This process is allosterically regulated by ambient oxygen po_2 exhibiting maximal activity at the Hb P_{50}. Despite total body concentration of Mb and Hb are similar,[6] a putative role of Mb in whole body metabolism of nitrite is unknown. Therefore, the aim of the present study was to elucidate (1) whether Mb acting as an NO scavenger under normoxic conditions may function as a relevant source of NO under hypoxia and (2) what functional consequences this Mb-derived NO may have on muscle function and energy metabolism.

Materials and Methods

Reaction of Mb With Nitrite

Horse Mb from Sigma was suspended in phosphate buffer saline (PBS) to a final concentration of 200 μmol/L, according to the myocardial concentration of myoglobin.[7] Mb was deoxygenated by argon and oxygen saturation was measured spectrophotometrically. Nitrite was added to deoxygenated Mb and nitrosylated myoglobin (nitrosylMb) as a "dosimeter of NO formation"[8,9] was measured by gas-phase-chemiluminescence using ferricyanide solution.[10] Further, hearts from mice were homogenated, deoxygenated, spiked with nitrite, and formation of NO was measured directly using gas-phase chemiluminescence. To characterize the impact of xanthine-oxidoreductase and cytochrome on formation of NO, experiments with inhibitors were performed. Xanthine-oxidoreductase was inhibited by incubation of homogenate with 100 μmol/L allopurinol to block the molybdenum-site and 200 μmol/L diphenyliodonium to block the flavin-adenine dinucleotide-(FAD)-site. The electron-transfer from ubiquinol to bc_1-complex in the mitochondrial respiratory chain was blocked by incubation with 300 μmol/L myxothiazol.

NO Analysis of Cardiac Tissue

Tissue nitroso species (the sum of S-nitrosothiols and the mercury-stable NO-adducts N-nitrosamines, iron-nitrosyles[11]) and nitrite were determined applying group-specific reductive denitrosation by triiodine with subsequent detection of the NO liberated by gas-phase-chemiluminescence.[11,12] Nitrate was quantified after enzymatic reduction to nitrite by nitrate reductase using flow-injection analysis based on the Griess reaction.[13,14] NO-heme was determined by parallel injection of replicate aliquots of tissue homogenates into a 0.05 mol/L ferricyanide solution to achieve 1-electron oxidation and quantify the liberated NO using gas-phase-chemiluminescence.[10]

Animals and Langendorff Heart Perfusion

All experiments were approved by the local ethic committee. NO synthase activity was blocked in all animals by pretreatment with

Original received January 19, 2007; resubmission received March 21, 2007; revised resubmission received April 23, 2007; accepted April 30, 2007.

From the University Hospital Aachen, Department of Medicine, Division of Cardiology, Pulmonary and Vascular Diseases (T.R., C.D., U.H.-C., M.K.), Aachen; and the Department of Cardiovascular Physiology (U.F., J.S.), Heinrich-Heine-University Düsseldorf, Germany.

*Both authors contributed equally to this study.

Correspondence Tienush Rassaf, MD, University Hospital Aachen, Department of Medicine, Division of Cardiology, Pulmonary and Vascular Diseases, Pauwelsstr. 30, D-52074 Aachen, Germany. E-mail trassaf@ukaachen.de

Circulation Research **is available at http://circres.ahajournals.org** **DOI: 10.1161/CIRCRESAHA.107.152488**

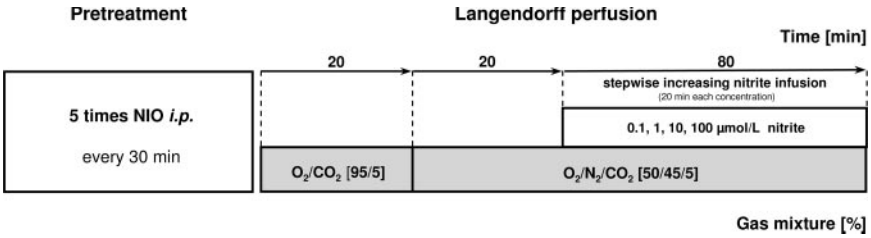

Figure 1. Scheme of the experimental protocol applied to WT and myo$^{-/-}$ hearts. O_2 indicates oxygen; N_2, nitrogen; CO_2, carbon dioxide; and NIO, L-N(5)-(1-iminoethyl)-ornithine.

L-N(5)-(1-iminoethyl)-ornithine (L-NIO).[15] Preparation and perfusion of murine hearts of myo$^{-/-}$[7] and wt animals were performed essentially as described.[16] Until excision of the heart, animals received standard rodent chow. For NMR measurements, hearts were placed inside a 10-mm NMR tube, immersed in perfusion buffer (containing in mmol/L: NaCl 116, KCl 4.6, $MgSO_4$ 1.1, $NaHCO_3$ 24.9, $CaCl_2$ 2.5, KH_2PO_4 1.2, glucose 8.3, and EDTA 0.5), and transferred into a heated (37°C) 10-mm $^1H/^{31}P$ dual probe inside the spectrometer. Perfusion pressure, coronary flow, and left ventricular developed pressure (LVDP) were measured continuously. Signals were recorded with a sampling rate of 1000 Hz using a PC with dedicated software (Chart, AD Instruments). Arterial and venous pO_2 were measured simultaneously with implantable oxygen microsensors based on 140-μm optical silica fiber (Presens) as previously described.[17] All hearts were initially perfused at constant coronary pressure with Krebs-Henseleit buffer equilibrated with 95% O_2/5% CO_2. After heart function had stabilized inside the magnet, cardiac pacing (500 bpm) was initiated and continued throughout. Left ventricular end-diastolic pressure was set to 5 mm Hg. Thirty minutes after the onset of cardiac pacing, coronary perfusion was fixed to the steady flow at which the hearts had stabilized. After the switch to constant flow, baseline data were recorded. Perfusion was then turned to buffer gassed at 50% O_2/45% N_2/5% CO_2 (Figure 1) to induce partial deoxygenation of Mb and a normoxic buffer (95% O_2/ 5% CO_2) as control, respectively. Subsequently, solutions with increasing concentrations of nitrite (0.1; 1; 10; 100 μmol/L) were infused stepwise, and in each section of the protocol hemodynamic data as well as NMR spectra were acquired.

^{31}P NMR Spectroscopy

Spectra were recorded at a Bruker DRX 400 WB NMR spectrometer, operating at frequencies of 400 MHz for ^1H and 161.97 MHz for ^{31}P. Shimming was done on the free induction decay of the water signal. A line width at half height of 15 Hz could be routinely obtained. Transients (n=240) were accumulated with a 75-degree flip angle, a repetition time of 1 second, a spectral width of 5682 Hz, a data size of 4K, zero filling to 8K, and exponential weighting resulting in a 10-Hz line broadening (4 minutes of signal accumulation). Chemical shifts were referenced to the phosphocreatine (PCr) resonance at −2.52 ppm. After baseline correction relative peak areas were obtained by integration and converted to concentrations as described before.[16] Calculated values for the free energy of adenosine-triphosphate (ATP) hydrolysis (ΔG_{ATP}) were derived from established relations.

Results

In a first step we determined whether free NO radicals can be formed from the reaction of nitrite and Mb in vitro. For this purpose nitrite was injected into an aqueous solution of Mb and the formed NO was analyzed by gas-phase-chemiluminescence. At 100% deoxygenated Mb and 10 μmol/L nitrite the rate of NO production was determined to be 1.5±0.2 pmol/L/s. In contrast, in the absence of Mb or when Mb was fully oxygenated there was no detectable formation of NO. Similar to the findings reported for Hb these experiments show that the NO generated can escape from autoscavenging by the remaining heme group.[5] This becomes possible because the reaction with nitrite converts Mb to its ferric form (metMb, $MbFe^{III}$), which exhibits only limited NO scavenging properties.

To characterize the total amount of NO formed by reaction with Mb, consecutive reactions of NO have to be considered. In analogy to what has been reported for Hb, NO released from Mb can be captured by the remaining deoxygenated Mb (deoxyMb; $MbFe^{II}$) as nitrosylated Mb (nitrosyl-Mb; $MbFe^{II}$-NO), which therefore can serve as an index of NO-formation.[9] Using the same gas-phase-chemiluminescence approach described above, but adding ferricyanide to liberate the Mb-bound NO, we found a substantial Mb-mediated formation of NO at physiologically relevant cytosolic levels of pO_2 and nitrite (Figure 2A and 2B). The release of NO into the gas phase increased with the deoxygenation level of Mb and the concentration of nitrite.

We next analyzed the release of NO using murine myocardial tissue homogenates (Figure 2C through 2E). The basal rate of NO formation from deoxygenated tissue homogenates in the presence of 100 μmol/L nitrite was 2.5±0.3 nmol/g/s. In comparison, in homogenates from hearts of Mb-deficient (myo$^{-/-}$) mice the formation of NO was decreased by 60% as compared with wt controls (Figure 2E). Addition of Mb (200 μmol/L final concentration) to myo$^{-/-}$ samples increased the formation of NO to levels of wt mice (Figure 2E). In contrast, inhibition of potential alternative nitrite-dependent NO producers,[18,19] such as xanthine-oxidoreductase and the flavin-adenine dinucleotide-(FAD)-site by allopurinol and diphenyliodonium, respectively, did not reduce NO release (Figure 2D). Similarly, inhibition of the electron-transfer from ubiquinol to the bc_1-complex in the mitochondrial respiratory chain by myxothiazol did not significantly reduce the formation of NO (Figure 2C).

The transport of intracoronarily applied nitrite into the myocardium has not been studied so far. To define the amounts of nitrite needed to increase endogenous levels, in a separate series of experiments we analyzed myocardial tissue content of nitrite. To differentiate between endogenous nitrite formation and the exogenously applied nitrite, NOS activity was inhibited with L-NIO[15] (5 times every 30 minutes before excision of hearts). Isolated perfused mouse hearts were then subjected to mild hypoxia (50% buffer O_2) which increases the fraction of deoxyMb to 50% and is associated with a cellular Po_2 of less than 4 mm Hg.[20] This was followed by replenishment of the nitrite pool during perfusion with increasing nitrite concentrations (0.1, 1, 10, 100 μmol/L). Baseline cardiac nitrite levels were determined to be 2.96±0.42 μmol/L, which were significantly reduced to 1.14±0.06 μmol/L by application of L-NIO (Figure 3A; n=4, $P<0.05$). Perfusion with buffer containing 0.1 μmol/L and 1 μmol/L nitrite did not restore the initial cardiac nitrite levels (1.15±0.13 μmol/L for 0.1 μmol/L nitrite, P=n.s., and 1.59±0.36 μmol/L for 1 μmol/L nitrite, P=n.s.). Replenish-

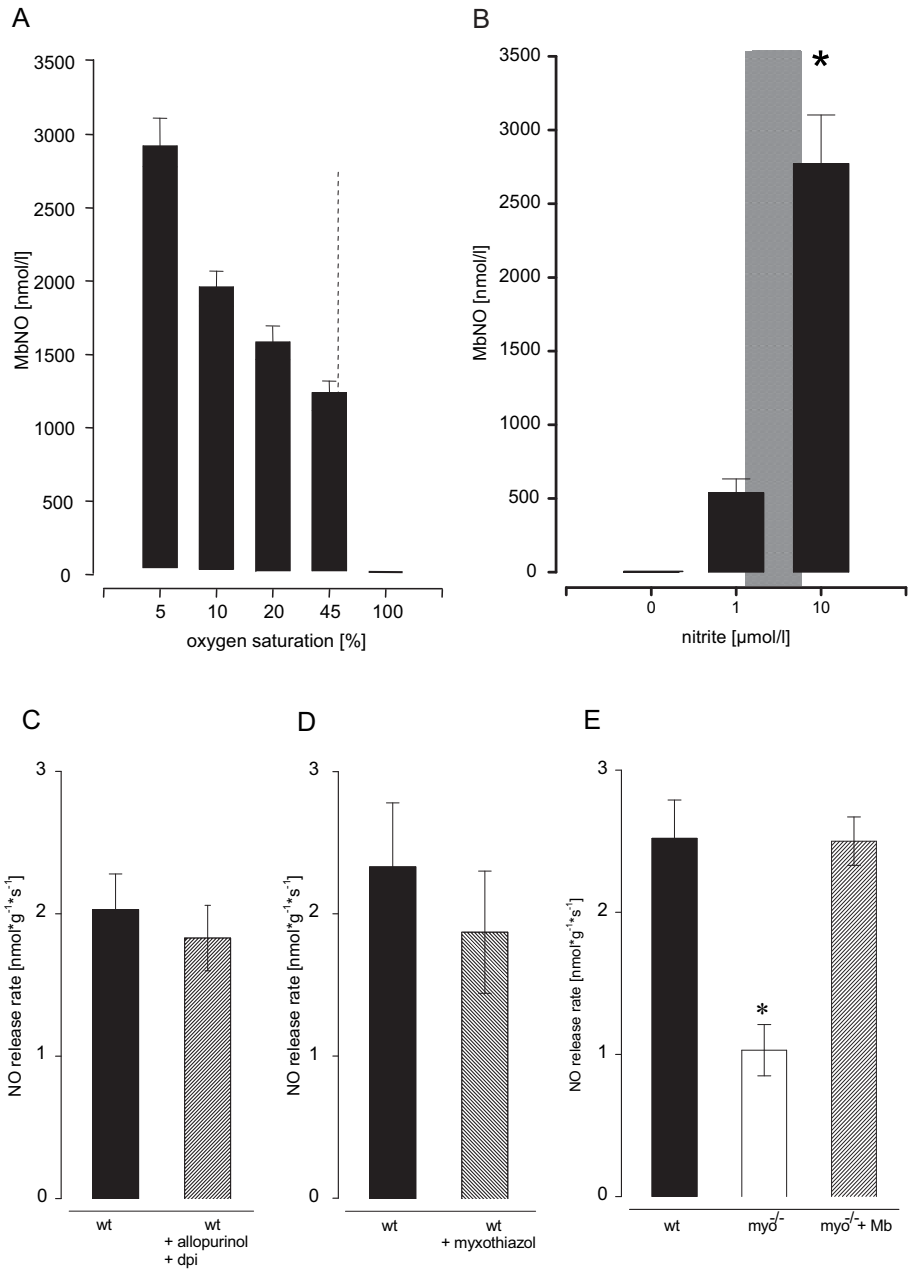

Figure 2. A and B, DeoxyMb converts nitrite to NO leading to the subsequent formation of nitrosyl-Mb. A, Nitrosyl-Mb (M6NO) formation is dependent on oxygen saturation. Deoxygenation of Mb was achieved by purging the solution with argon. Oxygen saturation of Mb was measured spectrophotometrically. Increasing levels of oxygen saturation were obtained by adapting the duration of deoxygenation. The dashed line marks the oxygen saturation of 50% applied in the Langendorff heart studies (Figures 4 and 5). This equals a cellular po_2 of less than 4 mm Hg as shown before.[20] After deoxygenation, nitrite (10 μmol/L) was added. Increasing oxygenation of Mb is associated with decreasing formation of NO and thus nitrosyl-Mb. B, Concentration-dependent formation of nitrosyl-Mb. Nitrite (1 and 10 μmol/L, respectively) was added to deoxygenated Mb solutions. The area shaded emphasizes the concentration range relevant for cardiomyocytes. C through E, Cardiac Mb converts nitrite. Heart-homogenates of wild-type and myo$^{-/-}$ mice (300 μg protein) were added to a solution of deoxygenated nitrite (100 μmol/L at pH 5 and 37°C), and the subsequent formation of NO was measured by gas phase chemiluminescence. Where required, inhibitors were added 30 minutes before addition to nitrite-solution. Inhibition of xanthine-oxidoreductase by incubation of homogenate with 100 μmol/L allopurinol to block the molybdenum-site and 200 μmol/L diphenyliodonium (dpi) to block the flavin-adenine dinucleotide-(FAD)-site (C) and inhibition of the electron-transfer from ubiquinol to bc_1-complex in the mitochondrial respiratory chain by incubation with 300 μmol/L myxothiazol (D) did not influence conversion of nitrite to NO in comparison to untreated wt samples. E, Conversion of nitrite to NO was reduced by 60% in myo$^{-/-}$ as compared with wt mice. Replenishment of Mb in the myo$^{-/-}$ homogenate restored formation of NO to the levels of wt mice. Data represent mean±SED of n=6 with *$P<0.05$.

ment of the depleted tissue nitrite levels was only achieved by perfusion with concentrations ≥10 μmol/L nitrite (Figure 3A). Buffer containing 10 μmol/L nitrite led to cardiac nitrite levels of 2.54±0.75 μmol/L, being close to basal values, whereas 100 μmol/L nitrite increased tissue levels up to 2.5-fold above basal. Additional analysis of cardiac tissue NO content after nitrite application during hypoxia revealed a significant intracellular increase in nitroso-species and NO-heme products only at the level of 10 and 100 μmol/L nitrite, respectively (Figure 3A). No increase in NO-heme and nitroso-species was seen in myo$^{-/-}$ mice (Figure 3B).

Having defined the changes in myocardial tissue nitrite levels we studied the functional consequences of the Mb-mediated NO formation from nitrite (for the full protocol see Figure 1). While stepwise increasing extracellular nitrite concentrations (0.1, 1, 10, 100 μmol/L), hemodynamic analysis combined with ^{31}P NMR spectroscopy was performed in hearts from wt mice with myo$^{-/-}$ mice serving as appropriate controls. No changes were observed in both groups during perfusion with 0.1 and 1 μmol/L nitrite. However, at extracellular concentrations ≥10 μmol/L nitrite dose-dependently increased myocardial inorganic phosphate (P_i) and decreased phosphocreatine (PCr) levels in wt hearts (Figure 4), thereby reducing the free energy of ATP hydrolysis (ΔG_{ATP}). The impairment of the energy status was accompanied by a drop in left ventricular developed pressure and an increase of the coronary venous po_2 in wt mice. Because hearts were perfused in the constant flow mode, an increase in coronary venous po_2 reflects a reduced myocardial oxygen extraction and consumption (Figure 5). Under the same conditions no changes in energetic or functional parameters were observed in hearts of myo$^{-/-}$ mice (Figures 4 and 5)

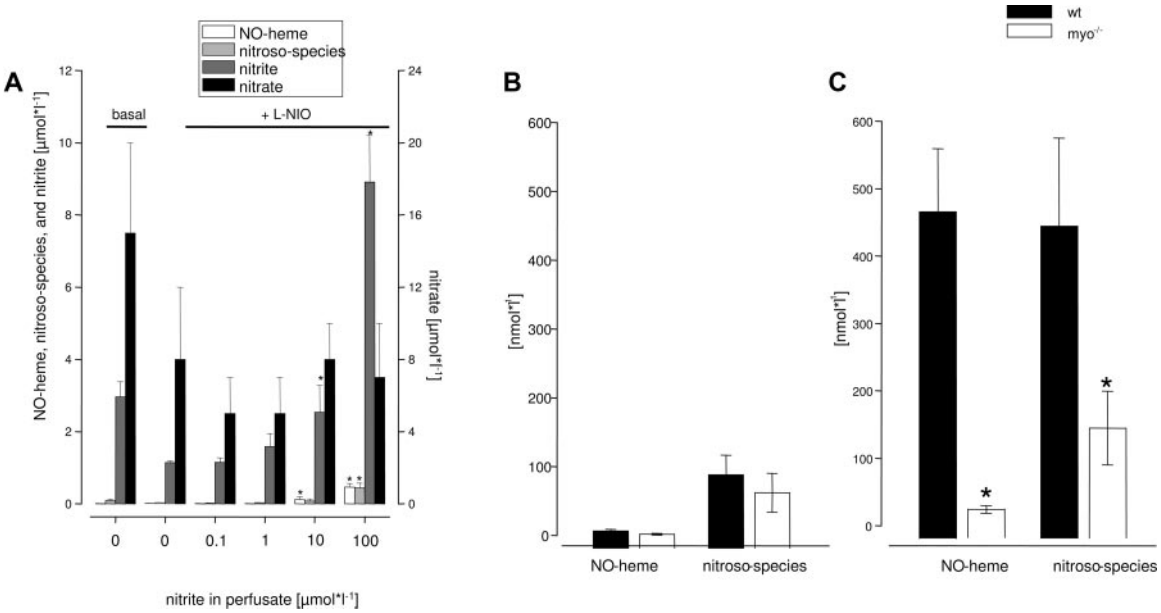

Figure 3. Cardiac tissue levels of NO-heme, nitroso, and nitrite after intracoronary application of nitrite. A, Under hypoxia, baseline cardiac levels of NO-heme, nitroso-species, nitrite, and nitrate of wt-mice are depicted left. Application of L-NIO significantly reduced tissue nitrite content. Perfusion with media containing 0.1, 1, 10, and 100 μmol/L nitrite, respectively, increased intracellular NO-heme, nitroso-species, and nitrite levels. Only 10 and 100 μmol/L nitrite replenished the reduced intracellular levels of nitrite. Data represent mean±SD of n=4 with *$P<0.05$. B, Under basal conditions, cardiac NO-heme and nitroso levels did not differ between wt and myo$^{-/-}$ mice, whereas treatment with nitrite (100 μmol/L) significantly increased NO-heme and nitroso species in wt compared with myo$^{-/-}$-hearts (C). Data represent mean±SD of n=6 with *$P<0.05$.

indicating the observed differences to be specific for deoxyMb. This conclusion is further supported by experiments in which perfusion of wt and myo$^{-/-}$ hearts with normoxic medium (equilibration with 95% O_2) and 100 μmol/L nitrite did not alter cardiac contractility (LVDP: 104±11 versus 103±13 mm Hg for WT and 102±12 versus 104±11 mm Hg for myo$^{-/-}$), oxygen consumption (MVO_2: 12±1 versus 12±1 μmol/min/g for WT and 12±1 versus 12±1 μmol/min/g for myo$^{-/-}$), and cardiac high energy phosphates (ΔG_{ATP}: −61±0.3 versus −61±0.3 kJ/mol for WT and −61±0.2 versus −61±0.2 kJ/mol for myo$^{-/-}$).

Discussion

The results of the present study demonstrate that under hypoxic conditions Mb transforms from an NO scavenger to a potent NO producer. DeoxyMb converts nitrite to NO, which then interacts in a reversible manner with myocytic cytochromes and downregulates cardiac energy status. This leads to a reduction in oxygen consumption and consecutively also of cardiac contractility. The increased inorganic phosphate levels caused by the enhanced breakdown of PCr may furthermore be an additional and important link between energetics and contractility.[21] Together, these reactions may represent a crucial endogenous protecting mechanism for the heart.

It is well known that cardiac contractile function and energy metabolism are actively downregulated, when coronary blood supply is critically reduced and this "perfusion-contraction matching" is a unique feature of the heart.[22] On acute coronary artery inflow reduction, contractile function of the ischemic region is rapidly decreased and is associated with a decrease in oxygen consumption. This dampens the fall in high energy phosphates and over time even can restore myocardial energy balance. The mechanisms underlying this adaptive response, termed short-term hibernation, remained largely unclear until now. On nitrite infusion we observe a scenario which strongly resembles the characteristics described for acute hibernation: a decrease in PCr, a concomitant increase in P_i, and a reduction of the available driving force for all energy-consuming processes (ΔG_{ATP}). Furthermore, we provide evidence for a reduction of ATP utilization (decrease in left ventricular developed pressure) and ATP synthesis (decrease in myocardial oxygen consumption) during nitrite infusion. Obviously, a new steady state for ATP is reached and ATP levels are maintained at lower steady state levels of PCr. Therefore, the po_2-dependent nonenzymatic formation of NO by reaction of Mb with nitrite may represent an important causal factor of short-term hibernation. Although the presented experiments were performed under hypoxic perfusion conditions which cause Mb to be deoxygenated by about 50%, low-flow ischemia certainly can further lower tissue po_2, thereby further augmenting the ability of deoxymyglobin to form NO from nitrite.[23] It is noteworthy that Martin et al[24] recently provided evidence for a NO synthase–independent NO formation during myocardial ischemia, which can be easily explained on the basis of the present work.

Published experimental studies support our findings that under hypoxic conditions myoglobin may react with nitrite to form NO,[25] and that this reaction may play a crucial role in the regulation of physiological functions.[26] Similar to the present work, Shiva et al have most recently demonstrated that in isolated cardiomyocytes the nitrite reductase activity of deoxymyoglobin releases NO in proximity to mitochondria and regulates respiration through cytochrome c oxidase.[27] Furthermore, different groups have shown that the application of low doses of nitrite prevents ischemia/reperfusion-injury in the Langendorff heart model[18] as well as in the liver and heart of mice.[28] The xanthine-oxidoreductase dependent reduction of nitrite to NO[18] and a deoxyhemoglobin- and myoglobin-mediated nitrite reduction to NO[27,28] have been proposed as poten-

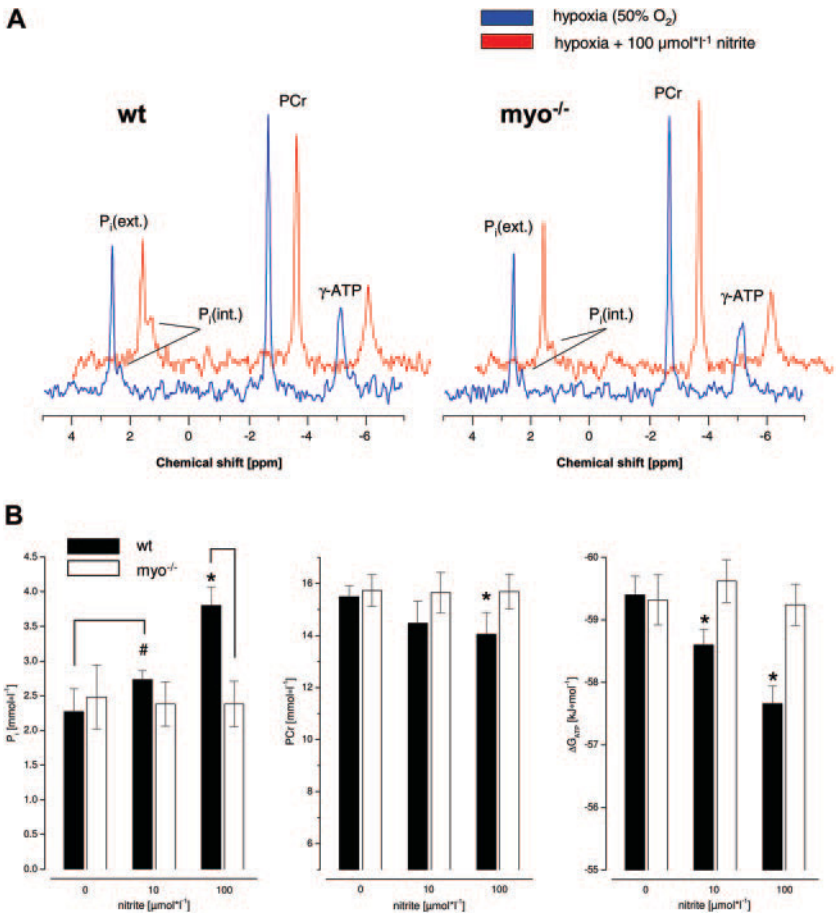

Figure 4. Nitrite downregulates cardiac energy status in wt as compared with myo$^{-/-}$ mice. A, Representative sections from ^{31}P NMR spectra of wt (left) and myo$^{-/-}$ mice (right) showing the effect of nitrite (red traces) on cardiac energy status under hypoxia. Assignments: γ-ATP, adenosine triphosphate (γ-phosphorus); PCr, phosphocreatine; $P_{i\ (ext.)}$ and $P_{i\ (int.)}$, extra- and intracellular inorganic phosphate, respectively. B, In wt, nitrite dose-dependently leads to the accumulation of inorganic phosphate (P_i) and a decay of PCr decreasing the free energy of ATP hydrolysis (ΔG_{ATP}). Data represent mean±SD of n=6 with *P<0.05.

tial mechanisms, but we (Figure 2C and 2D) and others[27] were not able to show a significant role for xanthine-oxidoreductase in reducing nitrite.

Our data may be criticized that rather high extracellular concentrations of nitrite (10 to 100 μmol/L) were required to elicit the biological response. However, it is the intracellular concentration of nitrite which is of critical importance for the reaction with deoxyMb. Pretreatment of animals with the NOS inhibitor NIO decreased cytosolic nitrite by approximately 70%, and perfusion with concentrations ≥10 μmol/L nitrite was required to replenish the myocytic levels to the range of untreated controls. Obviously, comparatively high extracellular nitrite concentrations have to be applied under our experimental conditions to mimic the in vivo conditions with unrestricted activity of NOS and unlimited availability of its substrate arginine which was deliberately not supplemented with the perfusion buffer. Together our data suggest that the effect of nitrite on cardiac function occurred at physiological cytosolic nitrite concentrations.

NO formation by deoxyMb may not only be relevant for the heart, but it also could contribute to hypoxic vasodilation described for the human circulation.[5] As already pointed out above, the total body amounts of Hb and Mb are similar so that the ability of both proteins to act as nitrite-reductase might have been involved in the vasodilation of the exercising muscle previously reported. Using ^{1}H NMR spectroscopy the fraction of deoxyMb in skeletal muscle of healthy humans was found to be 9%.[29] On exercise (50 to 60% of maximum work rate) the deoxyMb signal increases to about 50%, corresponding to an intracellular po_2 lower than 5 mm Hg.[30] This is similar to values obtained in the present study with hypoxic perfusion of the heart. Using quadriceps maximum isometric voluntary torque and measuring PCr and deoxyMb by interleaved ^{1}H and ^{31}P NMR spectroscopy, the fraction of deoxyMb was found to increase up to 70%, whereas PCr reversibly decreased to 20% of control.[31] Given this significant deoxygenation of Mb in human exercising muscle, this most likely has profoundly increased the Mb-mediated formation of NO (Figure 2). Because of the low diffusion distances between Mb and mitochondria, this NO may be critically involved in the observed inhibition of oxidative phosphorylation, which is known to be extremely NO sensitive.[32] This mechanism may therefore play an important role in limiting muscle oxygen consumption and thus the exercise capacity of skeletal muscle.

In summary this study describes a novel homeostatic mechanism by which a mismatch between oxygen supply and demand is translated into the fractional increase of deoxyMb exhibiting enhanced nitrite reductase activity. DeoxyMb may act as an important oxygen sensor through which NO can regulate muscle energetics and function. This appears to be functionally important in the infarcted heart, during acute myocardial hibernation, and intense muscle exercise.

Sources of Funding

This work was supported by grants from the DFG: RA 969/4-1 (to T.R.); SFB 612 (to U.F. and J.S.); and GRK 1089 project 3 (to T.R., C.D., M.K.).

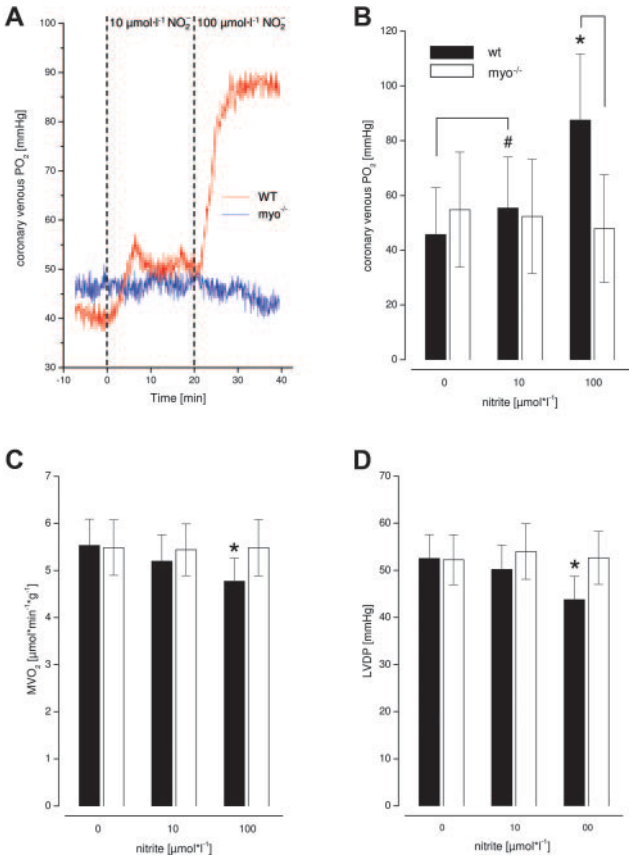

Figure 5. Nitrite dampens myocardial function during hypoxia through Mb. Hypoxia was achieved by equilibrating the perfusion buffer with a gas mixture of 50%O_2/45% N_2/5% CO_2. A, Representative registration of coronary venous pO_2 during application of increasing concentrations of nitrite to perfused wt (red) and myo$^{-/-}$ (blue) hearts. B, Quantitative analysis of coronary venous pO_2 shows a dose-dependent increase in wt hearts, whereas no changes were observed in myo$^{-/-}$. Nitrite dose-dependently reduced myocardial oxygen consumption (C) and LVDP (D) under hypoxia in wt mice (black bars) compared with myo$^{-/-}$ mice (white bars). No such effects of nitrite were seen under normoxic conditions. Data represent mean±SD of n=6 with *P<0.05.

Disclosures

None.

References

1. Millikan GA. Muscle hemoglobin. *Physiol Rev*. 1939;19:503–523.
2. Wittenberg JB, Wittenberg BA. Myoglobin function reassessed. *J Exp Biol*. 2006;206:2011–2020.
3. Brunori M. Nitric oxide moves myoglobin centre stage. *Trends Biochem Sci*. 2001;26:209–210.
4. Flögel U, Gödecke A, Klotz LO, Schrader J. Role of myoglobin in the antioxidant defense of the heart. *FASEB J*. 2004;18:1156–1158.
5. Cosby K, Partovi KS, Crawford JH, Patel RP, Reiter CD, Martyr S, Yang BK, Waclawiw MA, Zalos G, Xu X, Huang KT, Shields H, Kim-Shapiro DB, Schechter AN, Cannon III RO, Gladwin MT. Nitrite reduction to nitric oxide by deoxyhemoglobin vasodilates the human circulation. *Nat Med*. 2003;9:1498–1505.
6. Flögel U, Merx MW, Gödecke A, Decking UKM, Schrader J. Myoglobin: a scavenger of biocative NO. *Proc Natl Acad Sci U S A*. 2001;98:735–740.
7. Gödecke A, Flögel U, Zanger K, Ding Z, Kirchenhain J, Decking UK. Disruption of myoglobin in mice induces multiple compensatory mechanisms. *Proc Natl Acad Sci U S A*. 1999;96:10495–10500.
8. Gladwin MT, Schechter AN, Kim-Shapiro DB, Patel RP, Hogg N, Shiva S, Cannon RO, III, Kelm M, Wink DA, Espey MG, Oldfield EH, Pluta RM, Freeman BA, Lancaster JR, Jr., Feelisch M, Lundberg JO. The emerging biology of the nitrite anion. *Nat Chem Biol*. 2005;1:308–314.
9. Nakamura M, Nakamura S. conversion of metmyoglobin to NO myoglobin in the presence of nitrite and reductants. *Biochim Biophys Acta*. 1996;1289:329–335.
10. Bryan NS, Rassaf T, Maloney RE, Rodriguez CM, Saijo F, Rodriguez JR, Feelisch M. Cellular targets and mechanisms of nitros(yl)ation: An insight into their nature and kinetics *in vivo*. *Proc Natl Acad Sci U S A*. 2004;101:4308–4313.
11. Feelisch M, Rassaf T, Mnaimneh S, Singh N, Bryan NS, Jourd'heuil D, Kelm M. Concomitant S-, N-, and heme-nitros(yl)ation in biological tissues and fluids: implications for the fate of NO in vivo. *FASEB J*. 2002;16:1775–1785.
12. Rassaf T, Bryan NS, Maloney RE, Specian V, Kelm M, Kalyanaraman B, Rodriguez J, Feelisch M. NO adducts in mammalian red blood cells: too much or too little? *Nat Med*. 2003;9:481–482.
13. Rassaf T, Bryan NS, Kelm M, Feelisch M. Concomitant presence of N-nitroso and S-nitroso proteins in human plasma. *Free Radic Biol Med*. 2002;33:1590–1596.
14. Rassaf T, Feelisch M, Kelm M. Circulating NO pool: Assessment of nitrite and nitroso species in blood and tissues. *Free Radic Biol Med*. 2004;36:413–422.
15. Bryan NS, Fernandez BO, Bauer SM, Garcia-Saura MF, Milsom AB, Rassaf T, Maloney RE, Bharti A, Rodriguez J, Feelisch M. Nitrite is a signaling molecule and regulator of gene expression in mammalian tissues. *Nat Chem Biol*. 2005;1:290–297.
16. Flögel U, Decking UKM, Gödecke A, Schrader J. Contribution of NO to ischemia-reperfusion injury in the saline-perfused heart: a study in endothelial NO synthase knockout mice. *J Mol Cell Cardiol*. 1999;31:827–836.
17. Flögel U, Laussmann T, Gödecke A, Abanador N, Schäfer M, Fingas CD, Metzger S, Levkau B, Jacoby C, Schrader J. Lack of myoglobin causes a switch in cardiac substrate selection. *Circ Res*. 2005;96:e68–e75.
18. Webb A, Bond R, McLean P, Uppal R, Benjamin N, Ahluwalia A. Reduction of nitrite to nitric oxide during ischemia protects against myocardial ischemia-reperfusion damage. *Proc Natl Acad Sci U S A*. 2004;101:13683–13688.
19. Zweier JL, Wang P, Samouilov A, Kuppusamy P. Enzyme-independent formation of nitric oxide in biological tissues. *Nat Med*. 1995;1:804–809.
20. Merx MW, Flogel U, Stumpe T, Gödecke A, Decking UK, Schrader J. Myoglobin facilitates oxygen diffusion. *FASEB J*. 2001;15:1077–1079.
21. Nosek TM, Fender KY, Godt RE. It is diprotonated inorganic phospate that depresses force in skinned skeletal muscle fibers. *Science*. 1987;236:191–193.
22. Ross jr J. Myocardial perfusion-contraction matching. Implications for coronary heart disease and hibernation. *Circulation*. 1991;83:1076–1083.
23. Heusch G, Schulz R, Rahimtoola SH. Myocardial hibernation: a delicate balance. *Am J Physiol Heart Circ Physiol*. 2005;288:H984–H999.
24. Martin C, Schulz R, Post H, Boengler K, Kelm M, Kleinbongard P, Gres P, Skyschally A, Konietzka I, Heusch G. Microdialysis-based analysis of interstitial NO in situ: NO synthase-independent NO formation during myocardial ischemia. *Cardiovasc Res*. 2007;74:46–55.
25. Tomoda A, Murakami E, Shibuya T. Changes in nitric oxide generated by the oxidation of oxymyoglobin by nitrite. *Tohoku J Exp Med*. 1997;182:61–67.
26. Reutov V, Sorokina E, Kaiushin L. The nitric oxide cycle in mammals and nitrite reducing activity of heme-containing proteins. *Vopr Med Khim*. 1994;40:31–35.
27. Shiva S, Huang Z, Grubina R, Sun J, Ringwood LA, Macarthur PH, Xu X, Murphy E, Darley-Usmar VM, Gladwin MT. Deoxymyoglobin is a nitrite reductase that generates nitric oxide and regulates mitochondrial respiration. *Circ Res*. 2007.
28. Duranski MR, Greer JJ, Dejam A, Jaganmohan S, Hogg N, Langston W, Patel RP, Yet SF, Wang X, Kevil CG, Gladwin MT, Lefer DJ. Cytoprotective effects of nitrite during in vivo ischemia-reperfusion of the heart and liver. *J Clin Invest*. 2005;115:1232–1240.
29. Richardson RS, Duteil S, Wary C, Wray DW, Hoff J, Carlier PG. Human skeletal muscle intracellular oxygenation: the impact of ambient oxygen availability. *J Physiol (Lond)*. 2006;571:415–424.
30. Richardson RS, Newcomer SC, Noyszewski EA. Sceletal muscle intracellular pO2 assessed by myoglobin desaturation: response to graded exercise. *J Appl Physiol*. 2001;91:2679–2685.
31. Vanderthommen M, Duteil S, Wary C, Raynaud JS, Leroy-Willing A, Crielaard JM, Carlier PG. A comparison of voluntary and electrically induced contractions by interleaved ^{1}H- and ^{31}P-NMRS in humans. *J Appl Physiol*. 2003;94:1012–1024.
32. Xu W, Charles IG, Moncada S. Nitric oxide: orchestrating hypoxia regulation through mitochondrial respiration and the endoplasmic reticulum stress response. *Cell Res*. 2005;15:63–65.

In Vivo Monitoring of Inflammation After Cardiac and Cerebral Ischemia by Fluorine Magnetic Resonance Imaging

Ulrich Flögel, PhD; Zhaoping Ding, MD; Hendrik Hardung, PhG; Sebastian Jander, MD; Gaby Reichmann, PhD; Christoph Jacoby, PhD; Rolf Schubert, PhD; Jürgen Schrader, MD

Background—In this study, we developed and validated a new approach for in vivo visualization of inflammatory processes by magnetic resonance imaging using biochemically inert nanoemulsions of perfluorocarbons (PFCs).

Methods and Results—Local inflammation was provoked in 2 separate murine models of acute cardiac and cerebral ischemia, followed by intravenous injection of PFCs. Simultaneous acquisition of morphologically matching proton (^{1}H) and fluorine (^{19}F) images enabled an exact anatomic localization of PFCs after application. Repetitive ^{1}H/^{19}F magnetic resonance imaging at 9.4 T revealed a time-dependent infiltration of injected PFCs into the border zone of infarcted areas in both injury models, and histology demonstrated a colocalization of PFCs with cells of the monocyte/macrophage system. We regularly found the accumulation of PFCs in lymph nodes. Using rhodamine-labeled PFCs, we identified circulating monocytes/macrophages as the main cell fraction taking up injected nanoparticles.

Conclusions—PFCs can serve as a "positive" contrast agent for the detection of inflammation by magnetic resonance imaging, permitting a spatial resolution close to the anatomic ^{1}H image and an excellent degree of specificity resulting from the lack of any ^{19}F background. Because PFCs are nontoxic, this approach may have a broad application in the imaging and diagnosis of numerous inflammatory disease states. (***Circulation*. 2008;118:140-148.**)

Key Words: inflammation ■ ischemia ■ magnetic resonance imaging ■ monocytes ■ macrophages ■ perfluorocarbons

Inflammation is associated with a large number of human diseases such as atherosclerosis, glomerulonephritis, inflammatory bowel disease, transplant rejection, neurodegenerative brain diseases, brain and spinal cord trauma, myocarditis, and ischemic heart disease. Thus, the medical problem is vast and an exact diagnosis is often difficult. Accordingly, therapy frequently is limited to symptomatic treatment and the success of the prescribed therapy is difficult to assess. Although recent advances involve various imaging modalities such as positron emission tomography, computed tomography, magnetic resonance imaging (MRI), optical imaging, and ultrasound imaging,[1–3] the visualization of inflammatory processes still poses a serious challenge, especially because in the initial phase the affected tissue does not exhibit specific physical properties that can be used to create contrast between inflamed and healthy regions.

Editorial p 109
Clinical Perspective p 148

Among the different noninvasive imaging modalities capable of whole-body imaging such as positron emission tomography and single-photon emission computed tomography, MRI provides superior resolution and the potential to generate the required contrast to noninflamed areas by gadolinium enhancement. However, this attempt relies on the transient accumulation of intravascularly applied gadolinium contrast agent in the interstitial space because of enhanced endothelial permeability,[4,5] which is a rather nonspecific phenomenon found to be associated with a variety of diseases. A more defined approach to delineate inflammatory areas from surrounding tissue is the tagging of infiltrating, immunocompetent cells with contrast agents.[6,7] Noninvasive visualization of immigrating cells by MRI has so far used predominantly superparamagnetic iron oxide particles, taking advantage of the high affinity of these species for the monocyte/macrophage system.[8,9] Despite its excellent sensitivity, this attempt has the disadvantage that the particles are not detected directly. Local deposition results in regional magnetic field inhomogeneities and thus depletion of the MR signal. Consequently, anatomic proton (^{1}H) MRIs often are difficult to interpret because it is not always clear whether dark areas are caused by these nanoparticles or by other inhomogeneities. At

Received September 4, 2007; accepted April 28, 2008.

From the Institut für Herz- und Kreislaufphysiologie (U.F., Z.D., C.J., J.S.) and Institut für Medizinische Mikrobiologie und Krankenhaushygiene (G.R.), Heinrich-Heine-Universität, Düsseldorf; Lehrstuhl für Pharmazeutische Technologie und Biopharmazie, Albert-Ludwigs-Universität Freiburg, Freiburg (H.H., R.S.); and Neurologische Klinik, Universitätsklinikum Düsseldorf, Düsseldorf (S.J.), Germany.

The online-only Data Supplement, which consists of Methods, tables, and figures, can be found with this article at http://circ.ahajournals.org/cgi/content/full/CIRCULATIONAHA.107.737890/DC1.

Correspondence to Ulrich Flögel, PhD, Institut für Herz- und Kreislaufphysiologie, Heinrich-Heine-Universität, Postfach 101007, 40001 Düsseldorf, Germany. E-mail floegel@uni-duesseldorf.de

Circulation **is available at http://circ.ahajournals.org** **DOI: 10.1161/CIRCULATIONAHA.107.737890**

present, no method is available for a true positive MRI identification of infiltrating cells into inflamed tissue.

In this study, we demonstrate the feasibility and safety of imaging inflammation in mice with a "positive" contrast at high local resolution with fluorine MRI. The naturally occurring stable fluorine isotope ^{19}F (100%) is MR active and exhibits a sensitivity close to the ^{1}H nucleus.[10,11] Because of the lack of any ^{19}F background in the body, observed signals originating from injected ^{19}F-containing compounds exhibit an excellent degree of specificity. The merging of recorded ^{19}F images with simultaneously acquired, morphologically matching ^{1}H images enables an exact anatomic localization of fluorinated substances as "hot spots."[12] In the present investigation, we used nanoparticles containing perfluorocarbons (PFCs), a family of compounds known to be biochemically inert. Some of the PFC members such as perfluorodecalin, perfluorotripropylamine, perfluorodichloroctane, and perfluorooctyl bromide (also known as perflubron) were already used in patients as artificial blood substitutes.[13] However, we used perfluoro-15-crown-5 ether, a PFC in which all 20 fluorine nuclei are chemically and magnetically equivalent and thus exhibit superior properties for ^{19}F MRI detection.[14] In contrast to previous studies using ^{19}F MRI of PFCs to track injected stem/progenitor cells after ex vivo loading,[15,16] we applied emulsified PFCs systemically, resulting in an efficient and selective enrichment in circulating cells of the monocyte/macrophage system. This approach enabled us to monitor the infiltration of immunocompetent cells into inflammatory areas in an acceptable acquisition time with a spatial resolution close to the anatomic ^{1}H image.

Methods

An expanded Methods section can be found in the online-only Data Supplement.

Preparation of the PFC Emulsion

Purified egg lecithin (E 80 S, 4% wt/wt, a generous gift from Lipoid, Ludwigshafen, Germany) was dispersed in isotonic phosphate buffer (10 mmol/L phosphate, 150 mmol/L NaCl, pH 7.4) by magnetic stirring at room temperature for 30 minutes. When lissamine rhodamine B (rhodamine dihexadecanoic phosphatidylethanolamine, Molecular Probes, Leiden, the Netherlands) was used as a fluorescent lipid marker, a lipid mixture of lecithin and rhodamine dihexadecanoic phosphatidylethanolamine (99.5/0.5 mol/mol) was dissolved in ethanol, and the solvent was subsequently removed under reduced pressure at 35°C, followed by evaporation under high vacuum. The resulting lipid film was hydrated with buffer by gentle mixing and stirring. After addition of the perfluoro-15-crown-5 ether (10% wt/wt, Fluorochem Ltd, Glossop, UK), the dispersion was pretreated with a high-performance disperser (T18 basic ULTRA TURRAX, IKA Werke GmbH & Co KG, Staufen, Germany) at 14 000 rpm for 2 minutes. The resulting crude emulsion was high-pressure homogenized (70 MPa, 10 cycles, APV Gaulin Micron Laboratory 40, APV, Unna, Germany). The formed nanoemulsion was filtered through a 0.22-μm sterile filter unit (Millex-GS, Millipore, Ireland) and stored until application at 6°C.

Animal Experiments

Animal experiments were performed in accordance with the national guidelines on animal care and were approved by the Bezirksregierung Düsseldorf. The male mice (C57BL/6; 20 to 25 g body weight; 10 to 12 weeks of age) used in this study were bred at the Tierversuchsanlage of Heinrich-Heine-Universität (Düsseldorf, Germany). They were fed a standard chow diet and received tap water ad libitum. In total, 60 mice were investigated: blood analysis and controls with PFC and saline injections, n=30 and 10, respectively; myocardial infarction, n=12; and cerebral ischemia, n=8. Myocardial infarction was provoked by ligation of the left anterior descending coronary artery (LAD). In a separate experimental series, focal cerebral ischemia was induced by photothrombosis (see the online-only Data Supplement for a complete description of both injury models). A detailed schematic of the experimental protocols applied to the different groups is shown in online-only Data Supplement Figure I.

PFC Injections

Mice were anesthetized with isoflurane (2.0%) with a home-built nose cone. A total volume of 100 μL (for fluorescence experiments) or up to 500 μL (for MRI) of the PFC emulsion was given intravenously through the tail vein at the time indicated in the different experiments.

MRI Studies

Data were recorded on a Bruker DRX 9.4-T wide-bore (89-mm) nuclear MR spectrometer (Bruker, Rheinstetten, Germany) operating at frequencies of 400.13 MHz for ^{1}H and 376.46 MHz for ^{19}F measurements. A Bruker microimaging unit (Mini 0.5) equipped with an actively shielded 57-mm gradient set was used, and images were taken from a 30-mm birdcage resonator tunable to ^{1}H and ^{19}F. After acquisition of the morphological ^{1}H images, the resonator was tuned to ^{19}F, and anatomically matching ^{19}F images were recorded. For superimposing the images of both nuclei, the "hot iron" color lookup table (ParaVision, Bruker) was applied to ^{19}F images.

Mice were anesthetized with 1.5% isoflurane and were kept at 37°C. For functional cardiac analysis, ^{1}H images of murine hearts were acquired essentially as described[17] with an ECG- and respiratory-triggered fast-gradient-echo cine sequence (field of view [FOV], 30×30 mm^2; matrix, 128×128; slice thickness, 1 mm). Corresponding ^{19}F images were recorded from the same FOV using a multislice rapid acquisition with relaxation enhancement (RARE) sequence: RARE factor, 64; matrix, 64×64; slice thickness, 2 mm; averages, 256; acquisition time, 19.12 minutes. For fusion with ^{19}F images, additional ^{1}H data sets with a slice thickness of 2 mm were recorded. Brain images were acquired using multislice RARE sequences for both nuclei from a reduced FOV of 20×20 mm^2 but otherwise unaltered geometry (see the online-only Data Supplement for a more detailed description of MRI setup, acquisition parameters, and quantification procedures).

Blood Analysis

Blood was obtained from the vena cava inferior at various times after injection of the PFC emulsion as indicated in the different experiments. Determination of serum markers of liver function was performed by the Central Laboratory of the University Hospital Düsseldorf using clinical routine protocols. In separate experiments, mononuclear cells were isolated from the blood samples by centrifugation over Histopaque density gradient (2.5-mL layers of both 1083 and 1119 [Sigma, Taufkirchen, Germany], 25 minutes, 700*g* at room temperature). Thereafter, either the tube was immediately transferred into the nuclear MR spectrometer for MRI (see the online-only Data Supplement for details) or the mononuclear cells were collected from the interface of the layers and analyzed by fluorescence-activated cell sorter (see the next section).

Flow Cytometry

In preceding experiments with the murine macrophage cell line RAW 246.7 loaded in vitro with rhodamine-labeled PFCs (online-only Data Supplement Figure II), we confirmed that fluorescence

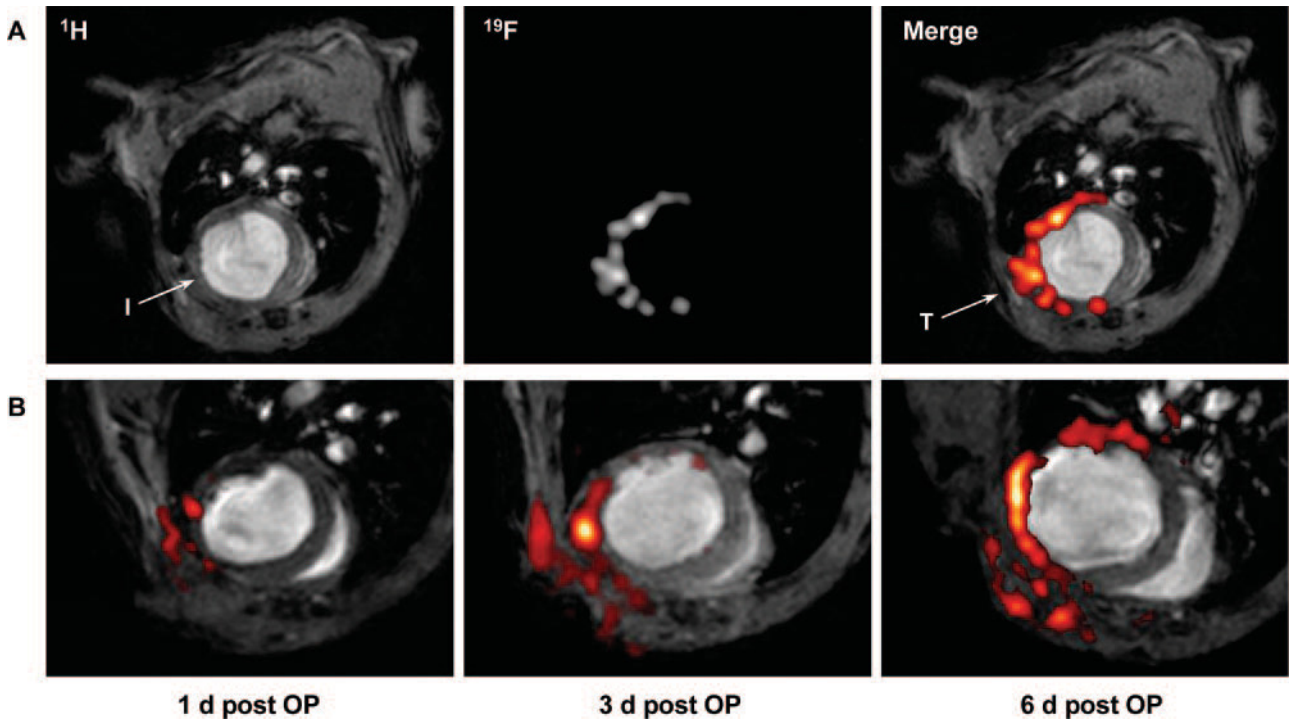

Figure 1. Infiltration of PFCs after myocardial infarction as detected by in vivo ^{19}F MRI. A, Anatomically corresponding ^{1}H and ^{19}F images from the mouse thorax recorded 4 days after ligation of the LAD showing accumulation of ^{19}F signal near the infarcted region (I) and at the location of surgery where the thorax was opened (T). PFCs were injected at day 0 (2 hours after infarction) via the tail vein. B, Sections of ^{1}H images superimposed with the matching ^{19}F images (red) acquired 1, 3, and 6 days after surgery (post OP) indicate a time-dependent infiltration of PFCs into injured areas of the heart and the adjacent region of the chest affected by thoracotomy. Note that at day 4, an additional bolus of PFCs had been injected to compensate for clearance of the particles from the bloodstream after 3 days (see text).

of rhodamine bound to the coat of the PFC particles is detectable by fluorescence-activated cell sorter analysis (data not shown). Freshly prepared peripheral blood mononuclear cells were stained for flow cytometric analysis according to standard procedures (see the online-only Data Supplement for details). Cells were analyzed on a FACScalibur flow cytometer (Becton Dickinson, Franklin Lakes, NJ), and samples were gated on live cells based on forward and side scattering and by exclusion of propidium iodide–positive cells. For each sample, at least 10 000 live events were acquired and analyzed with the CellQuestPro software (Becton Dickinson, Franklin Lakes, NJ).

Immunohistochemistry

To avoid a dissociation of rhodamine label and markers of the initial PFC carrier as a result of downstream processes after infiltration, all organs analyzed by immunohistochemistry were excised 1 day after PFC injection. Slides were air dried, and red fluorescence images were recorded without further processing because of water solubility of rhodamine-labeled PFCs and the impossibility of adequate histological fixing of the nanoparticles. The sections selected for photographs were related to anatomic landmarks to ensure retrieval of the same area after immunohistochemistry. After processing for immunofluorescence of CD11b (see the online-only Data Supplement for a detailed description of protocols applied to heart and brain slices), cardiac and cerebral sections were again microscoped, making use of the anatomic landmarks defined in the previous session. Slides were viewed with an Olympus BX50 fluorescence microscope (Olympus, Hamburg, Germany) equipped with standard filter sets and using objectives without (before immunostaining) and with (after mounting) cover glass correction. We deliberately refrained from merging images taken before and after immunostaining because an exact overlay was hampered by unavoidable minute alterations of the dried histological slices during immunohistochemical incubation steps and subsequent mounting.

The authors had full access to and take full responsibility for the integrity of the data. All authors have read and agree to the manuscript as written.

Results

PFC Infiltration Into the Heart After Infarction Assessed by In Vivo ^{19}F MRI

Cardiac infarction was induced by ligation of the LAD, a procedure well known to be associated with an acute inflammatory response. Two hours after ligation, 500 μL of 10% perfluoro-15-crown-5 ether emulsion (average size, $\approx$130 nm; ζ potential, -31.3 ± 1.5 mV) was applied via the tail vein (see the Methods section in the online-only Data Supplement for details on the PFC emulsion).

After surgery and application of the contrast agent, all animals (n=6) were imaged 5 times within 7 days. The infarcted area was localized by acquisition of fast-gradient-echo ^{1}H cine movies via akinesis of the affected region within the left ventricle. Subsequently, anatomically matching ^{19}F images were recorded for tracking of the injected PFCs. A typical example of consecutively recorded ^{1}H and ^{19}F images obtained 4 days after ligation of the LAD is illustrated in Figure 1A. The end-diastolic ^{1}H image (Figure 1A, left) clearly shows the presence of ventricular dilatation and wall thinning within the infarcted area, and in the corresponding ^{19}F image (Figure 1A, middle), a signal pattern matched the shape of the free left

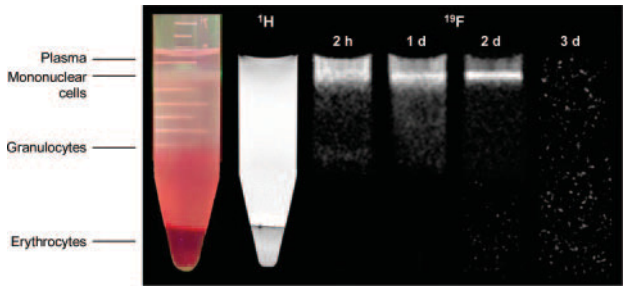

Figure 2. Uptake of PFCs by mononuclear cells. Matching ^{1}H and ^{19}F MRIs of a 15-mL Falcon tube after centrifugation of the collected mouse blood over Histopaque density gradient show a time-dependent accumulation of ^{19}F signal in mononuclear cells after tail vein injection of 500 μL PFC emulsion. Blood samples were taken 2 hours and 1, 2, and 3 days after PFC injection.

ventricular wall. Merging of these images (Figure 1A, right) confirms the localization of PFCs within the anterior, lateral, and posterior walls. In all animals studied, ^{19}F signal also was detected in the adjacent chest tissue, where thoracotomy for LAD ligation was performed. Note that no background signal from other tissue is present. Repetitive measurements from day 1 after LAD ligation revealed a time-dependent accumulation of PFCs within the infarcted region as shown in a representative example in Figure 1B. End-diastolic ^{1}H images acquired 1, 3, and 6 days after induction of myocardial infarction show the progressive left ventricular dilatation as a consequence of the insult. Merging with the matching ^{19}F images (red) demonstrates the successive infiltration of PFCs into the affected area of the heart and the region of the chest injured by surgery. Detected ^{19}F signals were restricted to the area near the infarcted region of the heart; at no time were infiltrating PFCs observed within the septum (see online-only Data Supplement Table I for individual data of all animals studied).

Although strong PFC signals were found in ex vivo ^{19}F images of blood components (see below), in vivo signals from PFCs in the circulation were not detectable at all (eg, no signal within ventricular chambers; Figure 1). Even when ^{19}F images were acquired immediately after injection, no ^{19}F signal from the streaming blood could be observed because the pulse sequence used for ^{19}F MRI (RARE) results in a signal void of flowing blood particles. Therefore, detected signals can be attributed unequivocally to accumulated PFCs in the tissue without contamination from ^{19}F signals of circulating PFCs.

Uptake and Transport of PFCs by Cells of the Monocyte/Macrophage System

To characterize the mode by which PFCs can enter the injured heart tissue, murine blood samples were investigated ex vivo by ^{19}F MRI after intravenous application of the emulsion. ^{19}F images acquired after density gradient centrifugation of blood collected at different points after injection revealed a time-dependent accumulation of the ^{19}F signal within the layer of the mononuclear cells (Figure 2). However, 3 days after injection, the PFCs were completely

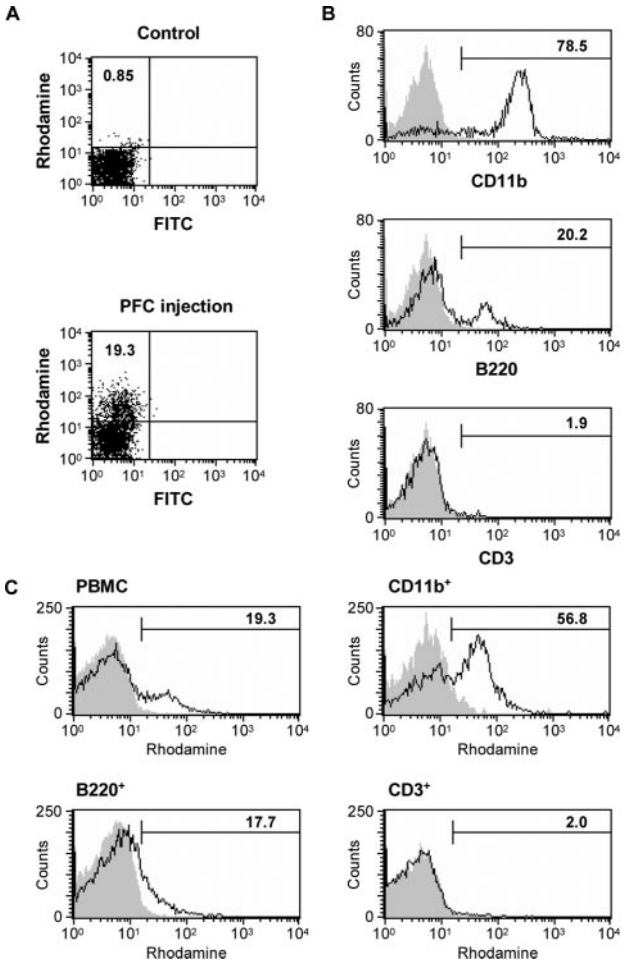

Figure 3. Flow cytometry of murine mononuclear cells 2 hours after tail vein injection of rhodamine-labeled PFCs. A, Peripheral blood mononuclear cells (PBMCs) from a control mouse (top) and a mouse treated with rhodamine-labeled PFCs (bottom) were analyzed for rhodamine fluorescence by flow cytometry. Dot blots show rhodamine vs FITC fluorescence; numbers in the top left quadrants indicate the percentage of rhodamine-positive PBMCs. B, C, PBMCs from both mice were stained with FITC-labeled anti-CD11b, anti-B220, and anti-CD3 monoclonal antibodies. B, Gated on rhodamine-positive cells, histograms display staining of specific (open) and isotype-matched (gray) control monoclonal antibodies. Numbers indicate the percentage of rhodamine-positive cells expressing the specific cell marker. C, Histograms show rhodamine fluorescence from control (gray) and treated (open) mice. Numbers indicate the percentage of rhodamine-positive cells within the cell population analyzed.

cleared from the bloodstream and were no longer detectable by ^{19}F MRI.

To further specify the cell population containing the PFCs, experiments were performed using rhodamine-labeled PFCs. These experiments enabled us to trace the fluorescence label not only within the mononuclear blood cells by flow cytometry but also within the inflamed region by means of fluorescence microscopy of tissue sections.

After tail vein injection of fluorescently labeled PFCs and subsequent collection of blood samples, we analyzed the layer of mononuclear cells containing the PFCs as assessed by ex vivo ^{19}F MRI (Figure 2). As shown in Figure 3A, 2 hours after injection of rhodamine-labeled PFCs, almost a

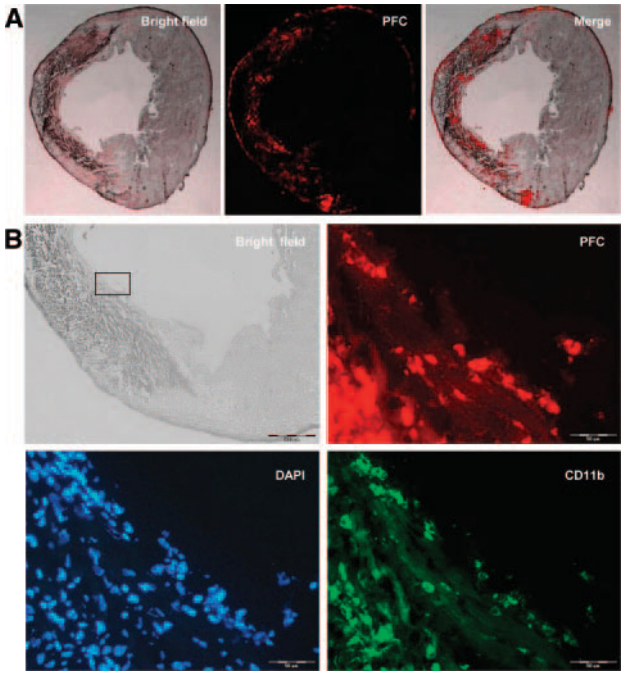

Figure 4. Colocalization of rhodamine-labeled PFCs and monocytes/macrophages in the heart 4 days after myocardial infarction. A, Overview images of the heart from frozen sections (8 μm) obtained from the same mouse shown in Figure 1A. B, Anatomically matching sections before (PFC) and after processing for immunofluorescence of CD11b (DAPI, CD11b). The black rectangle in the bright-field image (scale bar, 500 μm) represents the section displayed in the adjoining fluorescence images. Because of water solubility of the rhodamine-labeled PFCs and the impossibility of adequate histological fixing of the particles, rhodamine fluorescence images had to be recorded before immunohistochemistry. Therefore, the sections selected for photographs were carefully related to anatomic landmarks to ensure retrieval of the same area after immunohistochemistry. Rhodamine fluorescence appeared to be diffusively distributed over the cells, whereas green fluorescence patterns were restricted to surface structures of the infiltrated macrophages/monocytes. Although the PFC image is slightly shifted to the left compared with the CD11b and DAPI images, colocalization of red and green fluorescence can be unequivocally recognized. PFCs were injected at day 3 after LAD ligation via the tail vein. Scale bar=50 μm.

fifth of the mononuclear cells were found to be positive for rhodamine, with the large majority of the labeled cells (≈80%) exhibiting the monocyte/macrophage marker CD11b (Figure 3B, top). Approximately half of this cell type was detected to be loaded with PFC particles (Figure 3C). The remaining rhodamine-positive cells were observed to be B cells (B220; Figure 3B, middle), with a marginal amount of T cells (<2%; CD3; Figure 3B, bottom). Control experiments in vitro with a murine macrophage cell line confirmed that the labeled PFCs are avidly taken up by macrophages (online-only Data Supplement Figure II).

The fate of rhodamine-labeled PFCs in cardiac tissue was investigated by histology. Microscopic survey images obtained from the same mouse shown in Figure 1A are displayed in Figure 4A. Micrographs show a pattern of rhodamine fluorescence that is similar to the signal distribution in the corresponding ^{19}F MRI acquired immediately before organ excision (Figure 1A, right). The main fluorescence signals were located exclusively within the injured area. No rhodamine fluorescence was observed in the septum and necrotic areas, as confirmed by staining with triphenyltetrazolium chloride (data not shown).

Immunostaining of tissue sections for the monocyte/macrophage marker CD11b with FITC revealed some colocalization of fluorescence patterns for cells of the monocyte/macrophage system (green) and for rhodamine-labeled PFCs (red), as shown in Figure 4B. It should be noted, however, that technical reasons precluded a precise merge of the differently labeled sections. Because of the water solubility of the rhodamine-labeled PFCs, red fluorescence images had to be taken before immunohistochemistry for CD11b and required careful selection of anatomic landmarks to ensure retrieval of the same area.

PFC Infiltration Into the Brain After Focal Cerebral Ischemia

In another set of experiments, focal cerebral ischemia was chosen as an additional model of acute inflammation. After ischemia was induced by photothrombosis, all animals (n=4) were imaged at regular intervals up to 4 weeks after surgery. In RARE ^{1}H images, the ischemic region appeared initially as a bright area (Figure 5A, top left), and the corresponding ^{19}F images clearly show infiltration of PFCs into the border zone of the infarct, which was detected at the earliest at day 4 after photothrombosis. ^{19}F signal also was transiently observed supracranially at the location of skin incision (Figure 5A, bottom left). Characteristic ^{1}H and ^{19}F images (Figure 5A) acquired from an individual mouse 7, 9, 12, and 19 days after focal cerebral ischemia was induced definitely show movement of the PFCs with the rim of the shrinking infarct over time (see online-only Data Supplement Table II for individual data of all animals studied).

To support the notion that PFCs were carried into the ischemic region by monocytes/macrophages, experiments with rhodamine-labeled PFCs were again conducted (n=4). Microscopic survey images after FITC immunostaining for CD11b exhibited a pattern of green fluorescence comparable to that observed for the ^{19}F signal in the preceding MR experiment (Figure 5B). Furthermore, comparison of red and green fluorescence at large magnification indicated colocalization of PFCs and CD11b-positive cells (online-only Data Supplement Figure III).

Detection Threshold and Absolute Quantification

The sensitivity of our present approach can be estimated from Figure 2 by correlating the number of cells contained in the layer of the mononuclear cells with the signal-to-noise ratio in the corresponding areas of ^{19}F images. Two days after PFC injection, the mean signal-to-noise ratio within this layer was determined to be 24 at a voxel size of 0.44 μL (FOV, 30×30 mm^2; matrix, 64×64; slice thickness, 2 mm). The mononuclear cell layer contained 1.16×10^6 cells distributed vertically over ≈1 mm and horizontally over the inner diameter of the tube (14 mm as derived from axial ^{1}H images), which results in a cell

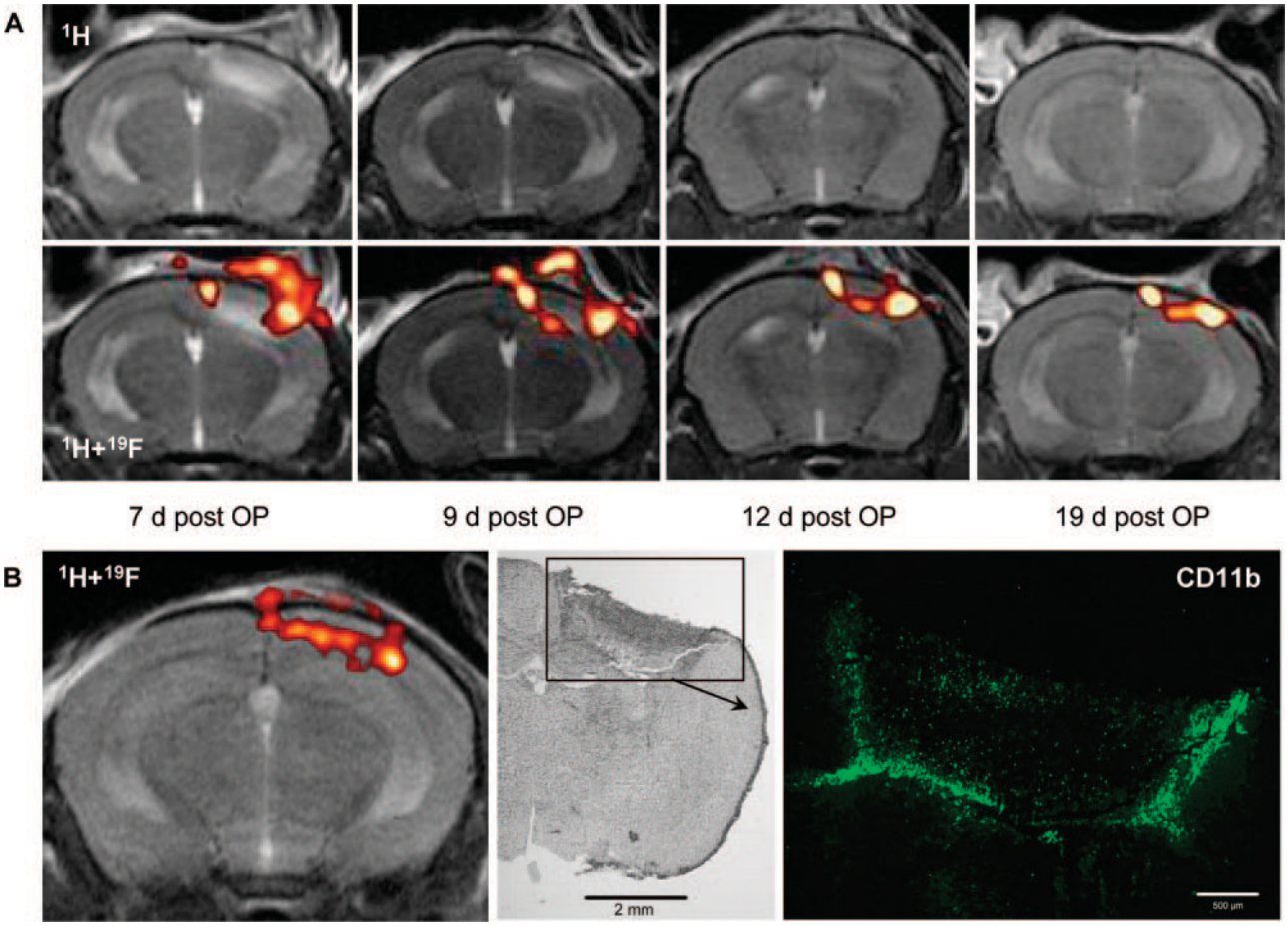

Figure 5. Infiltration of PFCs into the brain after induction of focal cerebral ischemia by photothrombosis. A, Sections of brain ^{1}H images (top) from an individual mouse superimposed with the corresponding ^{19}F images (red, bottom) showing movement of the PFCs with the rim of the infarct over time. Initially, additional signal also was observed supracranial at the location of surgery. Images were obtained 7, 9, 12, and 19 days after induction of focal cerebral ischemia (post OP). PFCs were injected at day 0 (2 hours after infarction) and day 6 via the tail vein. B, In vivo and postmortem brain images acquired 7 days after photothrombosis. Left, Section of merged ^{1}H and ^{19}F images taken immediately before organ excision. Middle, Microscopic survey of the injured hemisphere from 8-μm frozen sections (bright field; scale bar=2 mm). The black rectangle represents the section displayed in the adjoining fluorescence image. Right, Infarcted area immunostained for CD11b (scale bar=500 μm).

number of ≈3300 per ^{19}F MR voxel within this layer. Assuming a minimal signal-to-noise ratio of 3 as the detection threshold, as little as ≈400 cells are expected to be visible by MRI under these conditions. Taking into account that only a fraction of the mononuclear cells are loaded with PFCs (Figure 3), the detection limit may be even lower.

A similar conclusion was reached in a separate set of experiments in which RAW 264.7 macrophages were incubated ex vivo with PFCs under in vivo–like conditions and analyzed by ^{19}F MRI after immobilization in agarose (for details, see the Methods section of the online-only Data Supplement). Stepwise dilution of PFC-loaded macrophages revealed that <200 cells were detectable within a voxel of 0.44 μL (online-only Data Supplement Figure IV). By calibration of the absolute ^{19}F signal intensities with PFC concentration standards (R^2=0.99892; online-only Data Supplement Figure V), the average PFC loading per cell was calculated to be 0.73±0.19 pmol (n=8). Assuming a similar uptake of PFCs in vivo, the number of PFC-containing cells within ischemic areas can be quantified by interpolation from ^{19}F signal intensities of the affected regions (online-only Data Supplement Tables III and IV).

Control Experiments After PFC Injection

Without further intervention, at no time were ^{19}F signals observed within the heart or the brain. However, ^{19}F images showed a distinct signal in the spleen 1 day after injection of the PFC emulsion and a weaker signal in the liver that increased up to days 2 to 3, reaching an intensity similar to the signal from the spleen (online-only Data Supplement Figure VI). Interestingly, at the same time, additional signals regularly appeared in lymph nodes in the area of the upper thorax and the head and became clearly visible, as shown in Figure 6. The signals in the liver persisted for several months, but no adverse effects of the PFCs were observed in these animals, and serum markers of liver function were comparable to those of saline-treated animals (eg, the ratio of glutamic oxaloacetic transaminase to glutamic pyruvic transaminase was 2.53±1.01 [PFC, n=8] versus 2.26±0.57 [saline, n=7]).

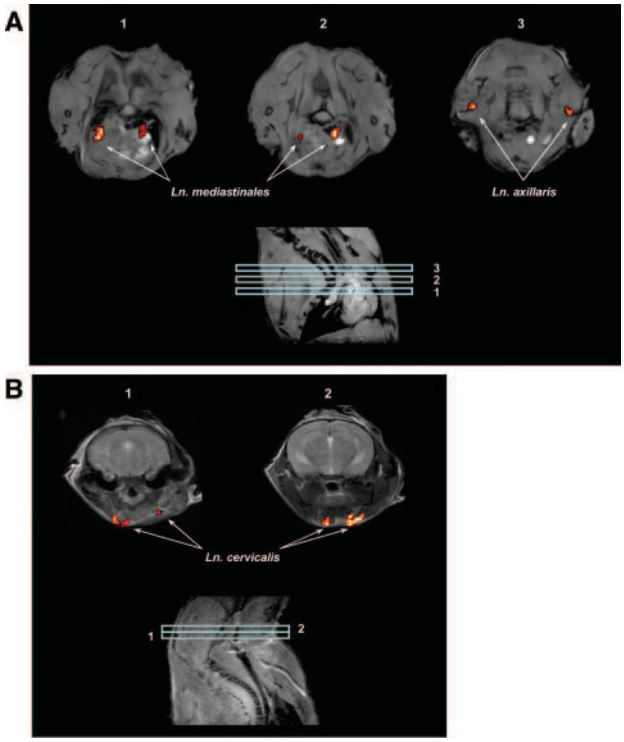

Figure 6. Accumulation of PFCs in lymph nodes (Ln) as detected by in vivo ^{19}F MRI. Axial ^{1}H MRIs (A and B, top) of a mouse superimposed with the corresponding ^{19}F MRIs (red) recorded 3 days after PFC injection via the tail vein. Orientation of axial slices is indicated in the corresponding sagittal images (A and B, bottom). A, Upper thorax (FOV, 30×30 mm^2); B, head (FOV, 20×20 mm^2).

Discussion

The present study describes a novel approach for visualizing local inflammatory processes by ^{19}F MRI using in vivo tagging of circulating monocytes/macrophages with biochemically inert PFCs. Our results show that intravenous application of emulsified PFCs after local inflammation is provoked by acute cardiac or cerebral ischemia results in the accumulation of ^{19}F-labeled cells within injured areas. Detection of infiltrating monocytes/macrophages by ^{19}F MRI at a field strength of 9.4 T is feasible in the mouse at an acceptable acquisition time (20 minutes) with a resolution close to the anatomic ^{1}H image. Therefore, PFCs can serve as a "positive" contrast agent for inflammatory processes (Figure 7), exhibiting a high degree of specificity because of the lack of any ^{19}F background.

Compared with previous ^{1}H MRI approaches for visualizing the infiltration of immunocompetent cells into inflamed areas by use of superparamagnetic iron oxide particles, the method presented here has the advantage of a direct positive detection of the tagging agent and therefore has the potential to work also in tissues that generally appear very dark in ^{1}H MRI such as the lungs. Although techniques have recently been described to image superparamagnetic iron oxide particles with a bright contrast,[18] the physical basis of detection is still the disturbance of the regional magnetic field by these particles. Therefore, it often remains difficult to unequivocally

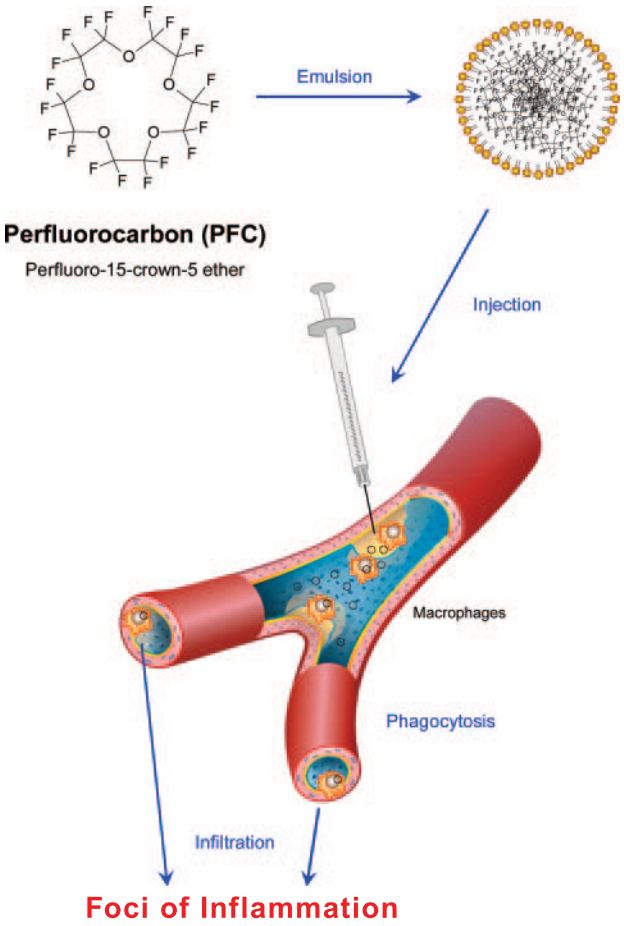

Figure 7. Schematic illustrating the use of PFCs for monitoring of inflammatory processes. After injection, emulsified particles are taken up by the monocyte/macrophage system and transported to areas of inflammation. Because of the lack of any ^{19}F background signal, the detected signals are highly specific for infiltrating immunocompetent cells loaded with PFCs. (This figure was designed with use of ScienceSlides software, VisiScience Corp, Chapel Hill, NC.)

assign alterations in local contrast to accumulating superparamagnetic iron oxide particles. Furthermore, iron-based contrast agents are readily metabolized, whereas the fluorinated crown ether used in this study is biologically inert and cannot easily be degraded. The reason is the very stable C-F bond and the dense electron cloud of the fluorine atom, which results in a protective sheath.[19] Experimentally, this provides the unique possibility for specifically and permanently labeling circulating monocytes/macrophages and following their fate within the body. It is of note that an absolute quantification of the observed signals is feasible (online-only Data Supplement Figures IV and V and Tables I through IV), which can be translated into the number of infiltrating immunocompetent cells.

Recent ^{19}F MRI tracking studies of cells loaded ex vivo with PFCs and subsequently injected into mice either required long acquisition times (up to 3 hours)[15] or were limited in spatial resolution (voxel size, 26 μL[16] compared with 0.2 to 0.4 μL in the present work). In the latter investigation, the

limit of detection was reported to be ≈6000 labeled cells. The substantial higher sensitivity observed in our study is most likely due to the fact that the monocyte/macrophage system in vivo more effectively takes up the injected PFCs compared with stem/progenitor cells incubated ex vivo. Labeling of ≈50% of the total monocyte/macrophage cell population (Figure 3C) raises a question about function and integrity of the loaded cells. Previous studies revealed that perfluoro-15-crown-5 ether labeling had no significant effect on cell proliferation, function, or maturation.[15,16] It seems likely that this also applies to the monocyte/macrophage system because both the time course of accumulation and the localization of PFC-containing monocytes/macrophages within ischemic areas are in good agreement with previous data on myocardial[20,21] and cerebral infarction,[6,9] suggesting unaltered infiltration kinetics and distribution of loaded cells. Furthermore, we did not observe any adverse effects on the animals after PFC injection, and no changes were noted in the release of liver enzymes, although this organ is a major site of PFC accumulation.

An interesting observation of this study was that lymph nodes are clearly delineated in ^{19}F images. Although the bulk of PFCs were found in CD11b-positive cells, it should be noted that ≈20% of the injected particles were taken up by B cells (Figure 3B). However, it is difficult to decide whether the labeling of lymph nodes is due to trapping of labeled B cells or to the accumulation of PFCs in resident macrophages. Therefore, we cannot exclude the possibility that local PFC deposition also may occur via an alternative pathway; nanoparticles carried by the lymphatic flow to the sites of inflammation could have been taken up by immunocompetent cells already present at the sites of injury before PFC injection.

PFCs such as perflubron have been evaluated clinically as an artificial blood substitute. In these early studies, it was observed that perflubron is phagocytized by the reticuloendothelial system.[22,23] In principle, perflubron should thus work as well as perfluoro-15-crown-5 ether, used in the present study, for ^{19}F imaging of inflammatory processes. Perflubron has the additional advantage that it is readily cleared from the body through exhalation by the lungs within 1 week.[24] Viewed from the MRI side, perflubron has a lower MRI sensitivity caused by signal splitting resulting from magnetically different ^{19}F nuclei. However, this problem can be overcome by dedicated detection methods,[25] the incorporation of gadolinium into the PFC droplets,[26] or the preparation of emulsions with a higher PFC content. Furthermore, it should be noted that the voxel size in cardiac MR diagnostics at 3 T is in the range of 2 to 30 μL, whereas it was only 0.2 to 0.4 μL in our study at 9.4 T, which translates into a substantial sensitivity increase in the clinical setting.

Acknowledgments

We thank Jutta Ziemann, Barbara Emde, and Sabine Hamm for excellent technical assistance, as well as Andreas Neub (Freiburg) for the cryoTEM studies.

Sources of Funding

This study was supported by Sonderforschungsbereich 612, subproject Z2 (Drs Flögel and Schrader), Deutsche Forschungsgemeinschaft grants SCHR154/9 (Drs Flögel, Jacoby, and Schrader) and JA690/5–2 (Dr Jander), and National Institutes of Health grant P01 HL073361 (Drs Flögel and Schrader).

Disclosures

None.

References

1. Miller JC, Thrall JH. Clinical molecular imaging. *J Am Coll Radiol*. 2004;1:4–23.
2. Tawakol A, Migrino RQ, Bashian GG, Bedri S, Vermylen D, Cury RC, Yates D, LaMuraglia GM, Furie K, Houser S, Gewirtz H, Muller JE, Brady TJ, Fischman AJ. In vivo ^{18}F-fluorodeoxyglucose positron emission tomography imaging provides a noninvasive measure of carotid plaque inflammation in patients. *J Am Coll Cardiol*. 2006;48:1818–1824.
3. Hyafil F, Cornily JC, Feig JE, Gordon R, Vucic E, Amirbekian V, Fisher EA, Fuster V, Feldman LJ, Fayad ZA. Noninvasive detection of macrophages using a nanoparticulate contrast agent for computed tomography. *Nat Med*. 2007;13:636–641.
4. Sze G, Bravo S, Baierl P, Shimkin PM. Developing spinal column: gadolinium-enhanced MR imaging. *Radiology*. 1991;180:497–502.
5. Mohs AM, Lu ZR. Gadolinium(III)-based blood-pool contrast agents for magnetic resonance imaging: status and clinical potential. *Expert Opin Drug Deliv*. 2007;4:149–164.
6. Jander S, Schroeter M, Saleh A. Imaging inflammation in acute brain ischemia. *Stroke*. 2007;38:642–645.
7. Kaufmann BA, Lindner JR. Molecular imaging with targeted contrast ultrasound. *Curr Opin Biotechnol*. 2007;18:11–16.
8. Weissleder R, Elizondo G, Wittenberg J, Rabito CA, Bengele HH, Josephson L. Ultrasmall superparamagnetic iron oxide: characterization of a new class of contrast agents for MR imaging. *Radiology*. 1990;175:489–493.
9. Kleinschnitz C, Bendszus M, Frank M, Solymosi L, Toyka KV, Stoll G. In vivo monitoring of macrophage infiltration in experimental ischemic brain lesions by magnetic resonance imaging. *J Cereb Blood Flow Metab*. 2003;23:1356–1361.
10. Holland GN, Bottomley PA, Hinshaw WS. ^{19}F magnetic resonance imaging. *J Magn Reson*. 1977;28:133–136.
11. Yu JX, Kodibagkar VD, Cui W, Mason RP. ^{19}F: a versatile reporter for non-invasive physiology and pharmacology using magnetic resonance. *Curr Med Chem*. 2005;12:819–848.
12. Bulte JW. Hot spot MRI emerges from the background. *Nat Biotechnol*. 2005;23:945–946.
13. Riess JG. Perfluorocarbon-based oxygen delivery. *Artif Cells Blood Substit Immobil Biotechnol*. 2006;34:567–580.
14. Dardzinski BJ, Sotak CH. Rapid tissue oxygen tension mapping using ^{19}F inversion-recovery echo-planar imaging of perfluoro-15-crown-5-ether. *Magn Reson Med*. 1994;32:88–97.
15. Ahrens ET, Flores R, Xu H, Morel PA. In vivo imaging platform for tracking immunotherapeutic cells. *Nat Biotechnol*. 2005;23:983–987.
16. Partlow KC, Chen J, Brant JA, Neubauer AM, Meyerrose TE, Creer MH, Nolta JA, Caruthers SD, Lanza GM, Wickline SA. ^{19}F magnetic resonance imaging for stem/progenitor cell tracking with multiple unique perfluorocarbon nanobeacons. *FASEB J*. 2007;21:1647–1654.
17. Flögel U, Jacoby C, Gödecke A, Schrader J. In vivo 2D mapping of impaired murine cardiac energetics in NO-induced heart failure. *Magn Reson Med*. 2007;57:50–58.
18. Faber C, Heil C, Zahneisen B, Balla DZ, Bowtell R. Sensitivity to local dipole fields in the CRAZED experiment: an approach to bright spot MRI. *J Magn Reson*. 2006;182:315–324.
19. Krafft MP. Fluorocarbons and fluorinated amphiphiles in drug delivery and biomedical research. *Adv Drug Deliv Rev*. 2001;47:209–228.
20. Jaffer FA, Sosnovik DE, Nahrendorf M, Weissleder R. Molecular imaging of myocardial infarction. *J Mol Cell Cardiol*. 2006;41:921–933.
21. Frangogiannis NG. Targeting the inflammatory response in healing myocardial infarcts. *Curr Med Chem*. 2006;13:1877–1893.
22. Mattrey RF, Long DM, Multer F, Mitten R, Higgins CB. Perfluoroctylbromide: a reticuloendothelial-specific and tumor-imaging agent for computed tomography. *Radiology*. 1982;145:755–758.

23. Smith DJ, Kornbrust ES, Lane TA. Phagocytosis of a fluorescently labeled perflubron emulsion by a human monocyte cell line. *Artif Cells Blood Substit Immobil Biotechnol*. 1994;22:1215–1221.
24. Spahn DR. Blood substitutes: artificial oxygen carriers: perfluorocarbon emulsions. *Crit Care*. 1999;3:R93–R97.
25. Duyn JH, Moonen CT. Fast proton spectroscopic imaging of human brain using multiple spin-echoes. *Magn Reson Med*. 1993;30:409–414.
26. Lee H, Price RR, Holburn GE, Partain CL, Adams MD, Cacheris WP. In vivo fluorine-19 MR imaging: relaxation enhancement with Gd-DTPA. *J Magn Reson Imaging*. 1994;4:609–613.

CLINICAL PERSPECTIVE

Currently, neither a clinically useful method to assess local inflammatory processes associated with the risk of plaque rupture nor a robust imaging method that provides information about local activity of inflammation (which plays a crucial role in various cardiovascular disease states such as ischemia/reperfusion, myocarditis, transplant rejection, or stroke) is available. In the present study, we demonstrate in murine models of myocardial and cerebral ischemia that nanoemulsions of perfluorocarbons can be used to precisely visualize localized inflammatory processes as hot spots by simultaneous acquisition of morphologically matching proton (^{1}H) and fluorine (^{19}F) magnetic resonance images. Injected perfluorocarbons are phagocytized primarily by monocytes/macrophages, resulting in ^{19}F magnetic resonance imaging intensity signals along the border of infarcted areas as a result of progressive infiltration of the labeled immunocompetent cells. Because of the lack of any ^{19}F background in the body, observed signals are robust and exhibit an excellent degree of specificity. Perfluorocarbons are biologically inert and have been shown to be nontoxic in humans. Thus, ^{19}F MRI has the potential to be clinically applicable as a new diagnostic modality not only for acute but also for chronic inflammatory processes such as plaques in atherosclerosis.

Disrupted fat distribution and composition due to medium-chain triglycerides in mice with a β-oxidation defect[1–4]

Sara Tucci, Ulrich Flögel, Marga Sturm, Elena Borsch, and Ute Spiekerkoetter

ABSTRACT

Background: Because of the enhanced recognition of inherited long-chain fatty acid oxidation disorders by worldwide newborn screening programs, an increasing number of asymptomatic patients receive medium-chain triglyceride (MCT) supplements to prevent the development of cardiomyopathy and myopathy.

Objective: MCT supplementation has been recognized as a safe dietary intervention, but long-term observations into later adulthood are still not available. We investigated the consequences of a prolonged MCT diet on abdominal fat distribution and composition and on liver fat.

Design: Mice with very-long-chain acyl-coenzyme A dehydrogenase deficiency (VLCAD$^{-/-}$) were supplemented for 1 y with a diet in which MCTs replaced long-chain triglycerides without increasing the total fat content. The dietary effects on abdominal fat accumulation and composition were analyzed by in vivo ^{1}H- and ^{13}C-magnetic resonance spectroscopy (9.4 Tesla).

Results: After 1 y of MCT supplementation, VLCAD$^{-/-}$ mice accumulated massive visceral fat and had a dramatic increase in the concentration of serum free fatty acids. Furthermore, we observed a profound shift in body triglyceride composition, ie, concentrations of physiologically important polyunsaturated fatty acids dramatically decreased. ^{1}H-Magnetic resonance spectroscopy analysis and histologic evaluation of the liver also showed pronounced fat accumulation and marked oxidative stress.

Conclusion: Although the MCT-supplemented diet has been reported to prevent the development of cardiomyopathy and skeletal myopathy in fatty acid oxidation disorders, our data show that long-term MCT supplementation results in a severe clinical phenotype similar to that of nonalcoholic steatohepatitis and the metabolic syndrome. *Am J Clin Nutr* 2011;94:439–49.

INTRODUCTION

The introduction of newborn screening programs for fatty acid oxidation disorders (FAOD) in many countries worldwide led to the identification of a constantly increasing number of FAOD patients who remain asymptomatic until severe catabolic situations occur (1). Typical symptoms develop during periods of prolonged fasting or because of infectious illnesses and comprise hypoketotic hypoglycemia, hepatic encephalopathy, cardiomyopathy, and skeletal myopathy (2). The most common inherited disorder of the mitochondrial β-oxidation of long-chain fatty acids (LCFAs) is considered to be very-long-chain acyl-coenzyme A dehydrogenase deficiency (VLCADD), which has a regional incidence of 1:30,000 (3–5). The clinical phenotype is very heterogeneous and involves organs and tissues that mostly rely on fatty acid β-oxidation, such as skeletal muscle and heart (4, 6, 7), but the liver may also be affected.

Therapeutic approaches to prevent metabolic derangement during situations of increased energy demand include avoidance of fasting and a fat-restricted and fat-modified diet, in which long-chain triglycerides (LCTs) are fully or in part replaced by medium-chain triglycerides (MCTs) (3, 8, 9). MCT preparations are in use for many clinical conditions and are also used for intravenous lipid solutions. The ingredients consist mainly of saturated fatty acids (SFAs; C-8 and C-10). In fact, medium-chain fatty acids (MCFAs) are able to bypass the first step of β-oxidation catalyzed by VLCAD and are supposed to supply tissues and organs with the required energy. Several reports highlight the clinical efficacy of MCTs in the prevention and treatment of cardiomyopathy and skeletal muscle symptoms (10, 11). Nevertheless, MCT supplementation as a mainstay of treatment in LCFA oxidation defects is widely debated, especially with respect to asymptomatic patients identified by newborn screening. Although an MCT diet has been considered a safe dietary intervention and largely applied in LCFA oxidation defects, recent studies in a mouse model of VLCADD showed detrimental effects on lipid homeostasis and clearance during short-term MCT use (12, 13).

Because FAOD patients routinely undergo MCT therapy in the clinical setting over a prolonged period of time, in the current study we investigated the consequences of long-term MCT supplementation in mice with VLCADD (VLCAD$^{-/-}$). These mutants have been shown to be suitable as a model for VLCADD, because symptoms and phenotypes arise by triggers very similar to those for humans, such as fasting, cold exposure, and physical exercise (8, 9, 14–16). Here, in vivo studies based on ^{1}H- and ^{13}C-magnetic resonance (MR) techniques were applied to analyze noninvasively the effects of MCTs on abdominal fat distribution

[1] From the Department of General Pediatrics, University Children's Hospital, Düsseldorf, Germany (ST, MS, and US); the Department of Cardiovascular Physiology, Heinrich-Heine-University, Düsseldorf, Germany (UF); and the Department of Gastroenterology, Hepatology and Infectiology, Heinrich-Heine-University, Düsseldorf, Germany (EB).

[2] ST and UF contributed equally to this work.

[3] Supported by grants from the Deutsche Forschungsgemeinschaft (DFG SP1125/1-1, SFB 575, and SFB 612) and the Forschungskommission of the Medical Faculty of Heinrich-Heine-University Düsseldorf.

[4] Address correspondence to S Tucci, Department of General Pediatrics, University Children´s Hospital, Moorenstrasse 5, D-40225 Düsseldorf, Germany. E-mail: sara.tucci@med.uni-duesseldorf.de.

Received January 26, 2011. Accepted for publication May 12, 2011.

First published online June 22, 2011; doi: 10.3945/ajcn.111.012948.

Supplemental Material can be found at:
http://www.ajcn.org/content/suppl/2011/07/20/ajcn.111.012948.DC1.html

and composition and on liver fat. These data were subsequently correlated with clinical standard liver and serum variables and with liver histology.

MATERIALS AND METHODS

Animals

VLCAD$^{-/-}$ mice were kindly provided by AW Strauss (currently Cincinnati Children's Hospital, Cincinnati, OH) and have been generated as described in detail previously (17). Experiments were performed on sixth- to seventh-generation intercrosses of C57BL6+129sv VLCAD genotypes. Littermates served as controls, and the mice were genotyped as described previously (17). Groups consisting of 5 to 7 mice (1-y-old) were investigated under well-fed, nonfasting conditions. All animal studies were performed with the approval of the Heinrich-Heine-University Institutional Animal Care and Use Committee and in accordance with the Committees' (LANUV) guidelines.

Diet composition and supplementation

After weaning, at ≈5–7 wk of age, mice of each genotype were divided in 2 groups and were fed with different diets for 1 y. The first group received a normal purified mouse diet containing 5% crude fat in the form of LCTs, corresponding to 12% of metabolizable energy as calculated with Atwater factors (ssniff EF R/M Control, ssniff; Spezialdiäten GmbH, Soest, Germany). The second group was fed with a diet corresponding as well to 12% of total metabolizable energy but in which 4.4% from a total of 5% fat was MCT (CeresMCT-oil, basis GmbH, Oberpfaffenhofen, Germany), whereas the remaining 0.6% was derived from soy bean oil to provide the required essential LCFAs. Both diets based on purified feed ingredients contained the same nutrient concentration as follows: 94.8% dry matter, 17.8% crude protein (N × 6.25), 5% crude fat, 5% crude fiber, 5.3% crude ash, 61.9% nitrogen free extract, 36.8% starch, 14.8% dextrin, and 11% sugar. Detailed fatty acid composition of the diets is reported in the supplementary material. In both diets the carbohydrate and protein contents corresponded to 69% and 19% of metabolizable energy, respectively. All mice groups received water ad libitum.

Magnetic resonance imaging and spectroscopy analysis

General

Data were recorded on a Bruker DRX 9.4 Tesla Wide Bore (89 mm) nuclear magnetic resonance spectrometer operating at frequencies of 400.13 MHz for ^{1}H and 100.62 MHz for ^{13}C measurements. Experiments were carried out by using a Bruker microimaging unit (Micro 2.5) equipped with an actively shielded 40-mm gradient set (capable of 1 T/m maximum gradient strength and 150 μs rise time at 100% gradient switching) and Paravision 4 as operating software. ^{1}H-MR images and spectra were taken from a 30-mm saw resonator, and proton-decoupled ^{13}C-MR spectra were acquired with a 12 × 8 mm transmit/receive ^{13}C surface coil (Bruker) inserted into the resonator and fixed over the mice's abdomen.

The mice were anesthetized with 1.5% isoflurane in a water-saturated gas mixture of 20% oxygen in nitrogen applied at a rate of 75 mL/min by manually restraining the animal and placing its head in an in-house-built nose cone. Respiration was monitored with a pneumatic pillow positioned at the animal's back. Vital function was acquired by using an M1025 system (SA Instruments, Stony Brook, NY) to synchronize data acquisition with respiratory motion. Throughout the experiments mice were breathing spontaneously at a rate of ≈100 min^{-1} and were kept at 37°C. Animals were placed within the resonator so that in z-direction (30 mm) the field of view (FOV) covered the abdomen from just below the diaphragm down to the pelvis. The entire protocol—including animal preparation, fat MRI and ^{1}H, and ^{13}C-MRS—lasted ≈1 h and was well tolerated by all mice, which recovered from anesthesia within 1–2 min after removal of the nose cone.

Abdominal fat content and distribution by ^{1}H-MRI

Abdominal fat content was determined by acquisition of images with a 2D ^{1}H multislice turbo spin echo sequences with and without fat suppression. Data were taken from a FOV of 30 × 30 mm^2 with a matrix of 256 × 192, which resulted in a spatial resolution of 117 × 117 μm^2 after zero filling (RARE factor, 8; TE, 10.8 ms; TR, 3.5 s; slices, 30; slice thickness, 1 mm; averages, 2, acquisition time, ≈3 min). With the use of the same receiver gain, 2 image sets were recorded with and without chemical shift selective fat suppression. To produce essentially fat-only images, fat-suppressed data were substracted in absolute intensity mode from nonsuppressed data sets by using an in-house-developed software module based on the LabVIEW package (National Instruments, Austin, TX). For further analysis, all data sets (suppressed, nonsuppressed, and fat only) were imported into the 3D visualization software Amira (Mercury Computer Systems, Mérignac, France). With reference to the corresponding fat-suppressed anatomic images, signals in fat-only images were associated with visceral or subcutaneous (subdivided into deep and superficial) areas by using the Segmentation Editor of Amira. For quantification of the fat content, the integral was calculated over the segmented areas and was related to the total volume analyzed as determined from the anatomic reference images.

Liver fat by ^{1}H-MRS

For the analysis of liver fat, localized respiratory-triggered ^{1}H-MR spectra were acquired from a 3 × 3 × 3 mm^3 voxel placed in the middle of the right liver lobe. After manual shimming, the spectra were recorded by using a PRESS sequence with outer volume suppression (TE, 20 ms; TR, 600 ms; spectral width, 6 kHz; data size, 2 k; average, 16; acquisition time, ≈10 s). Exponential weighting resulting in a 10-Hz line broadening was applied before Fourier transformation. Chemical shifts were referenced to the water signal at 4.8 ppm. After the manual phase and baseline correction, signals arising from water and lipid protons were integrated for quantification of the liver fat content. The results are given as a percentage of the total ^{1}H signal.

Abdominal fat composition by ^{13}C-MRS

After global shimming of the whole FOV, nonvolume selective proton-decoupled ^{13}C-MR spectra were recorded over the entire abdominal region for determination of fat composition (rectangular pulse, ≈60° at coil center; TR, 2 s; spectral width, 2 kHz; data size, 4 k; composite pulse decoupling with WALTZ-16;

The American Journal of Clinical Nutrition

average, 560; acquisition time, ≈18 min). Exponential weighting resulting in a 10-Hz line broadening was applied before Fourier transformation, and chemical shifts were referenced to the methylene resonance of fatty acids at 29 ppm. After the manual phase and baseline correction, individual contributions of the signals from carboxylic, olephinic, methylene, and methyl moieties were quantified by integration. Signal assignments and calculation of the amount of SFAs, MUFAs, and polyunsaturated fatty acids (PUFAs) and the average chain length was carried out according to data in the literature (18, 19).

Twenty-four hours after nuclear magnetic resonance spectroscopy, the mice were starved for 60 min and then killed by carbon dioxide asphyxiation. Blood samples were collected by heart puncture, and the serum was obtained by centrifugation at 16,000 × *g* for 10 min and was stored at −80°C for further analysis. The liver was rapidly removed and either immediately frozen in liquid nitrogen or transferred in 10% formaldehyde for histology.

Histologic evaluation

Liver tissue was excised from the eviscerated animals and fixed in 10% formalin. For light microscopy examination, the tissues were embedded in paraffin and sectioned at 5 μm. Liver slices were stained with hematoxylin and eosin (H&E) for assessment of steatosis, inflammation, and necrosis or with Sirius red for assessment of fibrosis. To determine lipid content, 10-μm thick cryostat sections were collected on Superfrost slides and stained with Sudan III. Steatosis was rated by a blinded investigator according to the percentage of hepatocytes containing macrovesicular fat: 0 is none, 1 is up to 33%, 2 is 33–66%, and 3 is >66% (20). The degree of inflammation was graded to none, mild, moderate, and severe. The histopathologic scoring of fibrosis stage was as follows (20):

1) Stage 1: zone 3 perisinusoidal/pericellular fibrosis, focally or extensively present
2) Stage 2: zone 3 perisinusoidal/pericellular fibrosis with focal or extensive periportal fibrosis
3) Stage 3: zone 3 perisinusoidal/pericellular fibrosis and portal fibrosis with focal or extensive bridging fibrosis
4) Stage 4: cirrhosis

Liver homogenates, enzyme activity, and lipid content

Liver was homogenized in ice-cold phosphate-buffered saline (pH 7.3) and centrifuged at 4°C and 16,000 × *g* for 15 min to pelletize any cell debris. The clear supernatant fluid was immediately used for the enzyme assays or stored at – 80°C. Protein concentrations in tissue homogenates were measured by using the bovine serum albumin method as described previously (21).

Reduced glutathione (GSH) was measured in liver homogenates by using an enzymatic kit (Glutathione Assay Kit; Bio Trend, Cologne, Germany). Glutathione peroxidase (GPX) activity was determined by calculating the oxidation rate of NADPH to $NADP^+$ spectrophotometrically at 340 nm for 4 min as previously described (22, 23). The concentration of thiobarbituric acid–reactive substances (TBARS) resulting from the decomposition of lipid peroxide products was determined fluorimetrically as previously described (24). Triglyceride concentrations were measured in liver as duplicates by using enzymatic kits (EnzyChrom Triglyceride Assay Kit; Bio Trend, Cologne, Germany) following the manufacturer's instructions.

Analysis of serum lipids and transaminases

Free fatty acid (FFA) and lipoprotein concentrations were measured as duplicates in serum samples as described previously (13). Aspartate aminotransferase (AST) and alanine aminotransferase (ALT) were measured at 37°C accordingly to the International Federation of Clinical Chemistry and Laboratory Medicine procedures (25, 26).

Real-time polymerase chain reaction analysis

Total liver RNA was isolated with the RNeasy mini kit (Qiagen, Hilden, Germany). Forward and reverse primers for β-actin (BC138614), fatty acid synthase (*FASN*; NM_007988.3), sterol regulatory element binding transcription factor 1 (*SREBP-1c*; BC056922.1), and stearoyl-coenzyme A desaturase (*SCD1*; NM_009127.4), annotated in **Table 1**, were designed with the FastPCR program (R Kalendar; Institute of Biotechnology, Helsinki). Real-time polymerase chain reaction (PCR) was performed in a single-step procedure with the QuantiTect SYBR Green RT-PCR (Qiagen) on an Applied Biosystems 7500 Sequence Detection System in Micro Amp 96-well optical reaction plates capped with MicroAmp optical caps (Applied Biosystems, Foster City, CA) as previously described (27). The values in all samples were normalized to the expression level of the internal standard.

Statistical analysis

MR data are presented as means ± SDs. All other reported data are presented as means ± SEMs. The *n* value denotes the number of animals tested. The significance of differences was analyzed by using Student's *t* tests for paired and unpaired data. The effect of the 2 variables, diet and genotype, was analyzed by using 2-factor analysis of variance with a Bonferroni post hoc test. (GraphPad Prism 5; GraphPad Software, San Diego CA). Differences were considered significant if $P < 0.05$.

TABLE 1
Primer used for real-time polymerase chain reaction analysis[1]

Gene	Forward 5′ →3′	Reverse 5′ →3′
SREBP-1c	CAGCTCAGAGCCGTGGTGA	TTGATAGAAGACCGGTAGCGC
FASN	TCTGGAATCCGCACCGGCTACC	TTCCCGGGTTGCCCTGTCAAGG
SCD-1	AGATCTCCAGTTCTTACACGACCAC	GACGGATGTCTTCTTCCAGGTG
β-actin	TAGGCACCAGGGTGTGATGG	CTCCATGTCGTCCCAGTTGG

[1] *SREBP-1c*, sterol regulatory element binding protein; *FASN*, fatty acid synthase; *SCD1*, stearoyl-coenzyme A desaturase.

RESULTS

Animal weights and dietary intake

To study the long-term effect of the MCT diet, the mice were fed for 1 y with either an LCT diet containing 5% fat or with a diet in which 4.4% fat was replaced with MCT, whereas the remaining 0.6% contained the essential LCT in the form of soybean oil. The daily dietary intake did not differ between the groups, independent of the diet received. Over a period of 3 wk, the WT and VLCAD$^{-/-}$mice consumed 3.36 ± 0.13 and 3.38 ± 0.38 g of the LCT diet, whereas the intake from the MCT diet was 3.14 ± 0.36 compared with 3.18 ± 0.26 g, respectively. With the normal LCT diet, no significant differences were observed in mean body weights between the WT and VLCAD$^{-/-}$ groups, although the VLCAD$^{-/-}$ mice had higher weights (32.17 ± 2.61 compared with 28.94 ± 2.25 g). After 1 y of the MCT diet, the VLCAD$^{-/-}$ mice had a slight but significantly higher mean body weight (32.49 ± 0.75 g) than did the WT mice (28.73 ± 1.23 g) with the same dietary regimen ($P < 0.05$).

MCT diet alters abdominal fat distribution and composition

To gain more detailed insight into the effect of a prolonged MCT diet on lipid homeostasis, we analyzed the abdominal fat distribution using ^{1}H-MR imaging (MRI). The analysis of fat-only images showed that the VLCAD$^{-/-}$ mice fed the MCT diet had a significantly higher overall fat content per measured body volume than did the WT mice fed the same dietary regimen (**Figure 1**A, left; $P < 0.05$). The classification of abdominal fat

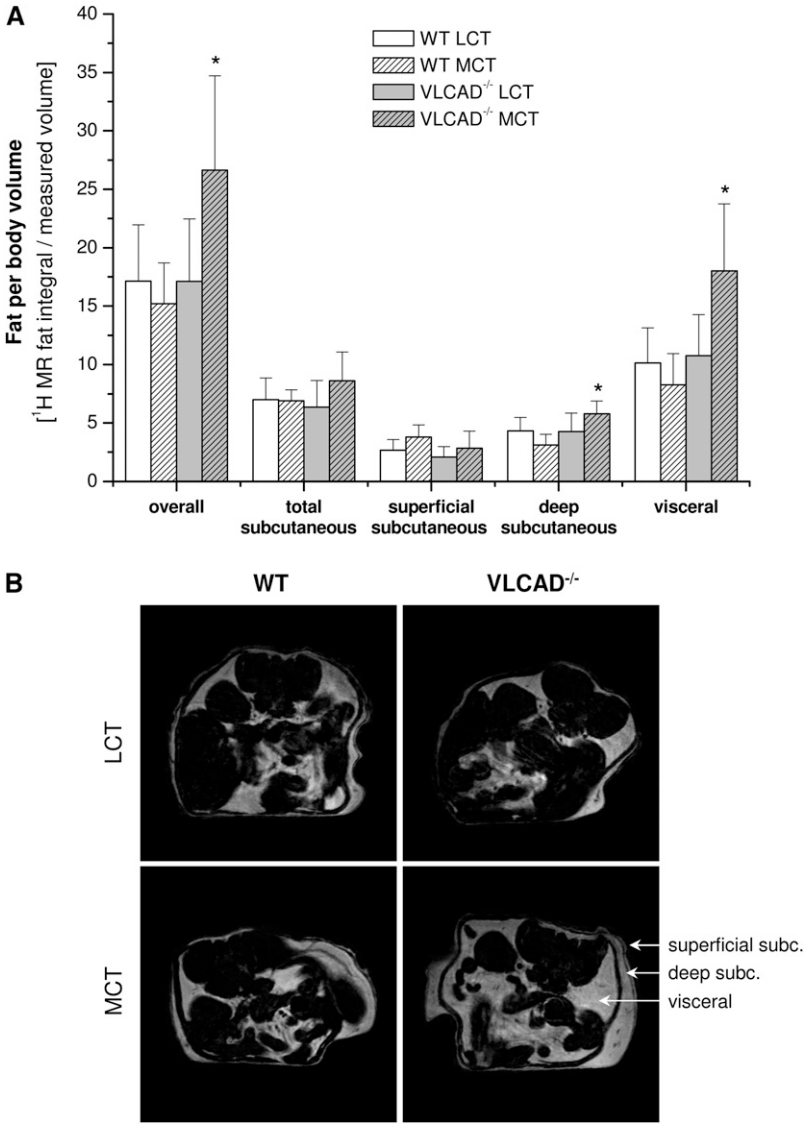

FIGURE 1. Quantification of abdominal fat distribution by ^{1}H-magnetic resonance (^{1}H-MR). Signals in fat-only images were associated with visceral or subcutaneous (subc.) areas, subdivided into deep and superficial, with reference to corresponding fat-suppressed anatomic images. A: Quantitative analysis showed an ≈2-fold increase in abdominal fat in mice with very-long-chain acyl-coenzyme A dehydrogenase deficiency (VLCAD$^{-/-}$) after long-term supplementation with medium-chain triglycerides (MCT), which was predominantly caused by an increase in visceral fat. Values are expressed as means ± SDs (n = 5–7). B: Representative ^{1}H-MR fat-only images of wild-type (WT) and VLCAD$^{-/-}$ mice after 1 y of long-chain triglyceride (LCT) and MCT supplementation. *Significantly different from WT mice within the same diet group, $P < 0.05$ (2-factor ANOVA and Student's t test).

The American Journal of Clinical Nutrition

in visceral and deep/superficial subcutaneous fat showed that this was predominantly caused by an increase in visceral fat (Figure 1A, right) and only to a minor extent by alterations in subcutaneous fat, as also evident in Figure 1B.

In the same experimental setting, natural abundance ^{13}C-MR spectra were acquired for the parallel analysis of abdominal fat composition. Characteristic ^{13}C-MR spectra for the VLCAD$^{-/-}$ mice after 1 y of the LCT and MCT diets are shown in **Figure 2**A. The most striking difference was the dramatic drop in signal intensity for polyunsaturated carbons [Δ_p, $(\Delta - 1)_p$]. Quantification of the spectra showed a PUFA content of only 13 ± 5% with the MCT diet and 49 ± 6% with the control diet ($P < 0.05$). Concomitantly, we found a massive increase in MUFAs ($P < 0.05$) and a moderate up-regulation of SFA levels (Figure 2B; $P < 0.05$). However, these effects were not specific for VLCAD$^{-/-}$ mice, but were similarly found in WT mice (Figure 2B). Surprisingly, in both groups, MCT supplementation had only a minor effect on the average FA chain length in abdominal fat (Figure 2C) as calculated from the ratio of signal intensities for terminal and nonterminal carbons (18). Although the MCT diet comprised mainly C-8 and C-10 triglycerides, the average FA chain length in triglycerides incorporated into abdominal tissue was still found to be in the range of 16 to 17 carbons—even after an intake of this diet for 1 y. Of note, the average FA length was slightly but significantly shorter in MCT-fed VLCAD$^{-/-}$ mice than in all others mouse groups, as shown in Figure 2C ($P < 0.05$).

Increased liver fat in VLCAD-deficient mice after MCT therapy

To determine intrahepatic lipid accumulation, in a last step of the MR session localized in vivo, ^{1}H-MRS were acquired from the middle of the right liver lobe. Under control conditions (LCT

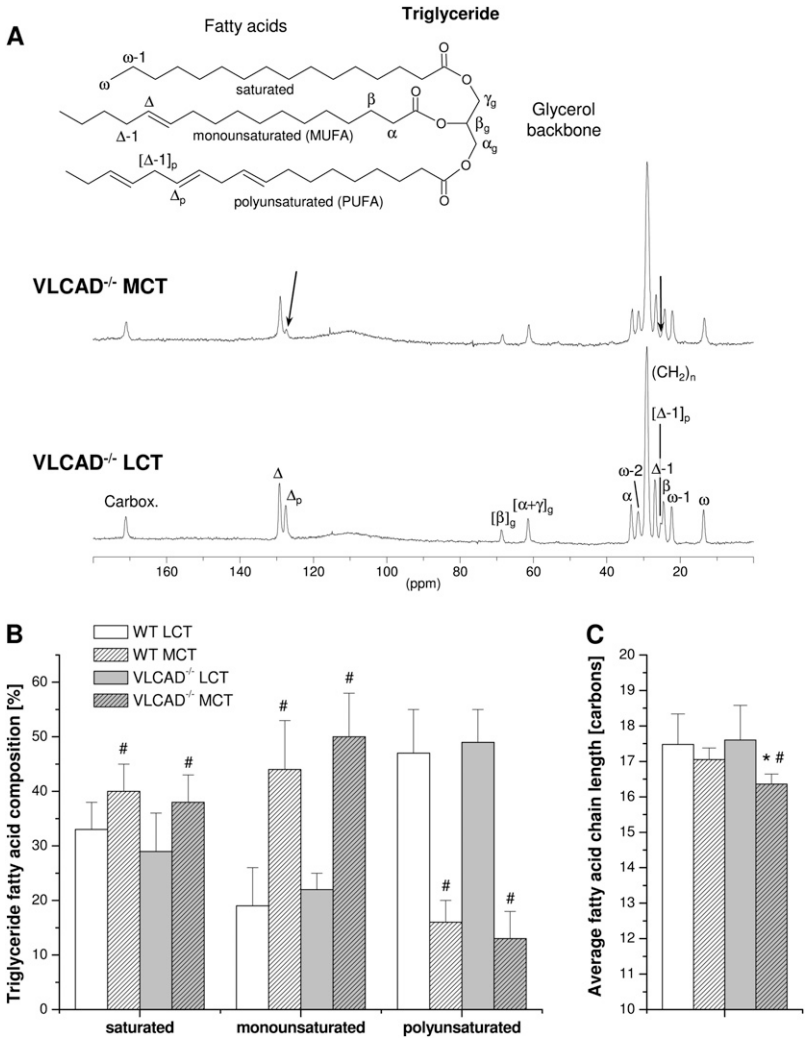

FIGURE 2. Analysis of triglyceride composition in abdominal fat. A: In vivo ^{13}C-magnetic resonance (MR) spectra acquired over the abdomen of mice with very-long-chain acyl-coenzyme A dehydrogenase deficiency (VLCAD$^{-/-}$) after long-term supplementation with medium-chain triglycerides (MCT) and long-chain triglycerides (LCT). Arrows indicate the dramatic decrease in signals for polyunsaturated fatty acids (PUFAs) [Δ_p, $(\Delta - 1)_p$] on MCT therapy. For signal assignments, refer to the structure and nomenclature of the triglycerides given at the top. Relative contribution of saturated fatty acids, monounsaturated fatty acids (MUFAs), and PUFAs to the overall triglyceride content (B) and average fatty acid chain length (C) in wild-type (WT) and VLCAD$^{-/-}$ mice after 1 y of LCT and MCT supplementation. The data were calculated from ^{13}C-MR spectra after signal integration by using established relations (18, 19) and are expressed as means ± SDs (n = 5–7). *Significantly different from WT mice within the same diet group, $P < 0.05$ (2-factor ANOVA and Student's t test). #Significant differences between mice within the same genotype under different dietary conditions, $P < 0.05$ (2-factor ANOVA and Student's t test). Carbox., carboxylic.

The American Journal of Clinical Nutrition

diet), the WT and VLCAD$^{-/-}$ mice did not show substantial differences in intrahepatic lipid concentrations (**Figure 3**A). However, as can be seen from representative spectra shown in Figure 3B, ^{1}H-MRS showed pronounced alterations in both liver fat content and composition in VLCAD$^{-/-}$ mice fed the MCT diet. The ratio of water to fat signals indicated a massive increase in liver fat, whereas the loss of the signal for the double allylic protons $[\Delta - 1]_p$ reflected the dramatic decrease in PUFA content, which was also observed at the entire abdominal level (*see* above). Quantification of the spectra showed almost twice as much liver fat in the VLCAD$^{-/-}$ mice fed the MCT diet than in those fed the LCT diet ($P < 0.05$); however, only a tendency toward an increase in liver fat was observed in the WT mice fed the MCT diet, which was not significant (Figure 3A).

Severe structural and functional impairment in liver of VLCAD$^{-/-}$ mice fed the MCT diet

To substantiate the in vivo MR findings, mice livers were processed for histologic evaluation and enzymatic analysis. WT and VLCAD$^{-/-}$ mice had higher mean liver weights with the MCT diet than with the LCT diet, but significant differences were detected only in WT mice (**Table 2**; $P < 0.05$). In contrast, histologic analysis showed that an MCT diet resulted in cloudy swelling of hepatocytes with or without microvesicular, and rarely macrovesicular vacuolization, in ≈50% of the WT mice (**Figure 4**, C and D). However, nearly all VLCAD$^{-/-}$ mice developed severe and diffuse macrovesicular steatosis (grade 3) in the liver, with accumulation of large lipid droplets that displaced and condensed the nuclei of hepatocytes (Figure 4, G–I). Other features were observed with variable frequency and included mild lobular inflammation consisting of lymphocytes and other mononuclear cells and an occasional small collection of polymorphonuclear leukocytes (Figure 4, K and L). Furthermore, moderate ballooning of hepatocytes, stage 1 pericellular/perisinusoidal fibrosis in particular around cells with large fat vacuoles and single acidophil bodies, were also detected (Figure 4J). A significant increase in the triglyceride content was observed in both groups fed with MCT ($P < 0.05$), but the VLCAD$^{-/-}$ mice had a much more pronounced accumulation of triglycerides than did the WT mice with the same treatment (346 ± 31.8 compared with 253.8 ± 25.7 nmol/mg; $P < 0.05$; n = 5–7). In addition, we analyzed serum markers of liver function and found the activity of both serum transaminases—AST and ALT—in VLCAD$^{-/-}$ mice fed the MCT diet to be significantly enhanced compared with the activity in WT and VLCAD$^{-/-}$ mice fed the control diet (Table 2; $P < 0.05$).

MCT diet increases circulating FFA concentrations

Blood lipid analysis indicated no differences in the lipoprotein content between genotypes or diets. However, pronounced differences were found in the amount of FFAs between the individual groups. Although the FFA content was already substantially higher in the VLCAD$^{-/-}$ mice than in the WT mice fed the LCT diet (1.85 ± 0.4 compared with 0.22 ± 0.05 mmol/L), the MCT diet led to an additional increase in FFAs, with concentrations up to 1.20 ± 0.3 and 3.64 ± 0.4 mmol/L in the WT and VLCAD$^{-/-}$ mice, respectively ($P < 0.05$; n = 5–7). Furthermore, total cholesterol concentrations were significantly higher in the VLCAD$^{-/-}$ mice than in the WT mice under both dietary regimens (Table 2; $P < 0.05$). However, the long-term MCT diet also

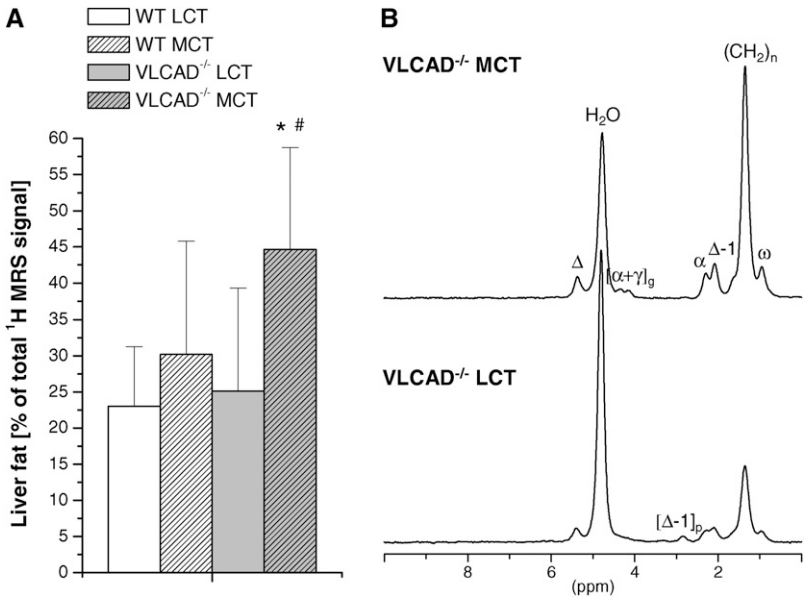

FIGURE 3. Quantification of intrahepatic lipid content. A: Relative contribution of lipid signals to the total magnetic resonance (MR) signal from non–water-suppressed ^{1}H-MR spectra (^{1}H-MRS) of the liver. Values are expressed as means ± SDs (n = 5–7). *Significantly different from wild-type (WT) mice within the same diet group, $P < 0.05$ (2-factor ANOVA and Student's t test). #Significant differences between mice within the same genotype under different dietary conditions, $P < 0.05$ (2-factor ANOVA and Student's t test). B: Localized in vivo ^{1}H-MRS acquired from the middle of the right liver lobe (voxel size: $3 \times 3 \times 3$ mm^3) showing the massive increase in liver fat and an almost complete disappearance of polyunsaturated fatty acid signals $(\Delta - 1)_p$ in mice with very-long-chain acyl-coenzyme A dehydrogenase deficiency (VLCAD$^{-/-}$) after prolonged supplementation with medium-chain triglycerides (MCT) as compared with long-chain triglycerides (LCT; control). For signal assignments, refer to the structure and nomenclature of the triglycerides given in Figure 2A (top).

TABLE 2
Liver variables, serum lipids, and serum transaminases in wild-type (WT) and very-long-chain acyl-coenzyme A dehydrogenase deficient (VLCAD$^{-/-}$) mice fed a diet supplemented with either long-chain triglycerides (LCTs) or medium-chain triglycerides (MCTs)[1]

	LCTs		MCTs	
	WT	VLCAD$^{-/-}$	WT	VLCAD$^{-/-}$
Liver weights and liver TGs				
Liver weight (g)	1.20 ± 0.06	1.48 ± 0.14	1.40 ± 0.06$^{\#}$	1.60 ± 0.08
Liver TGs (nmol/mg)	181.1 ± 18.2	204.7 ± 11.1*	253.8 ± 25.7$^{\#}$	346 ± 31.8$^{\#}$
Serum transaminases				
AST (U/L)	107.8 ± 18	167.8 ± 26	122 ± 22.8	245.3 ± 19.9*,$^{\#}$
ALT (U/L)	26.4 ± 1.3	47.6 ± 9	25.5 ± 4.5	76.9 ± 15*
Serum lipids				
FFA (mmol/L)	0.22 ± 0.05	1.85 ± 0.4*	1.20 ± 0.3$^{\#}$	3.65 ± 0.4*
Total cholesterol (mg/dL)	90.6 ± 7.5	120 ± 12.1*	119.9 ± 12.4$^{\#}$	166.4 ± 12*,$^{\#}$
HDL (mg/dL)	63.6 ± 11.6	46.1 ± 10.7	48.3 ± 10.6	63.5 ± 4.9
VLDL/LDL (mg/dL)	22.1 ± 3.3	23.4 ± 3.7	20.5 ± 2.9	21.5 ± 2.8

[1] All values are means ± SEMs; n = 5–7. TGs, triglycerides; FFA, free fatty acid; AST, aspartate aminotransferase; ALT, alanine aminotransferase. $^{\#}$Significantly different from WT or VLCAD$^{-/-}$ mice under different dietary conditions, $P < 0.05$ (2-factor ANOVA and Student's t test). *Significantly different from WT mice under the same dietary conditions, $P < 0.05$ (2-factor ANOVA and Student's t test).

led to a further increase in total serum cholesterol concentrations in both genotypes.

MCT-induced lipid deposition is associated with oxidative stress in the liver

Because intrahepatic lipid accumulation is known to be accompanied by the enhanced formation of reactive oxygen species (ROS), which may further amplify hepatic damage (28), we verified in the next step the presence of established markers of oxidative stress (**Figure 5**). The MCT diet led to a massive increase in GPX activity in VLCAD$^{-/-}$ mice ($P < 0.05$). In contrast, the WT mice had a less pronounced but also significantly higher GPX activity with the MCT diet than with the control diet ($P < 0.05$). As shown in Figure 5A, the VLCAD$^{-/-}$ mice had a 2-fold higher GPX activity (117.1 ± 9.1 U/mg) than

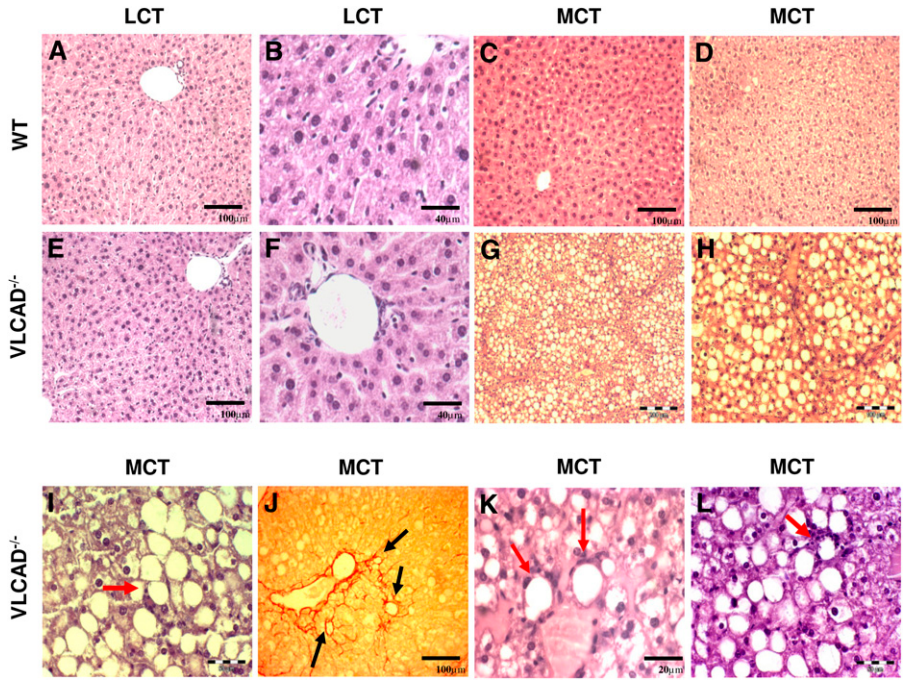

FIGURE 4. Histologic evaluation of liver tissue. Representative liver slices from wild-type (WT) mice and mice with very-long-chain acyl-coenzyme A dehydrogenase deficiency (VLCAD$^{-/-}$) supplemented with either long-chain triglycerides (LCT) or medium-chain triglycerides (MCT). Liver slices were stained with hematoxylin and eosin for assessment of steatosis and inflammation (A–I, K, L) and with Sirius red for assessment of fibrosis (J). To determine the degree of steatosis, the liver slices were additionally stained with Sudan III (C, D, G, H). In LCT-fed WT and VLCAD$^{-/-}$ mice, no abnormalities were detected (A, B, E, F). With the MCT diet, the WT mice had no clinical findings (E) or microvesicular lipid droplets (F). With the same dietary regimen in the liver tissue of VLCAD$^{-/-}$ mice, prominent steatosis (G, H) with nuclei degeneration (I), stage 1 pericellular/perisinusoidal fibrosis (J), and inflammatory cell infiltration (K, L) were detected.

The American Journal of Clinical Nutrition

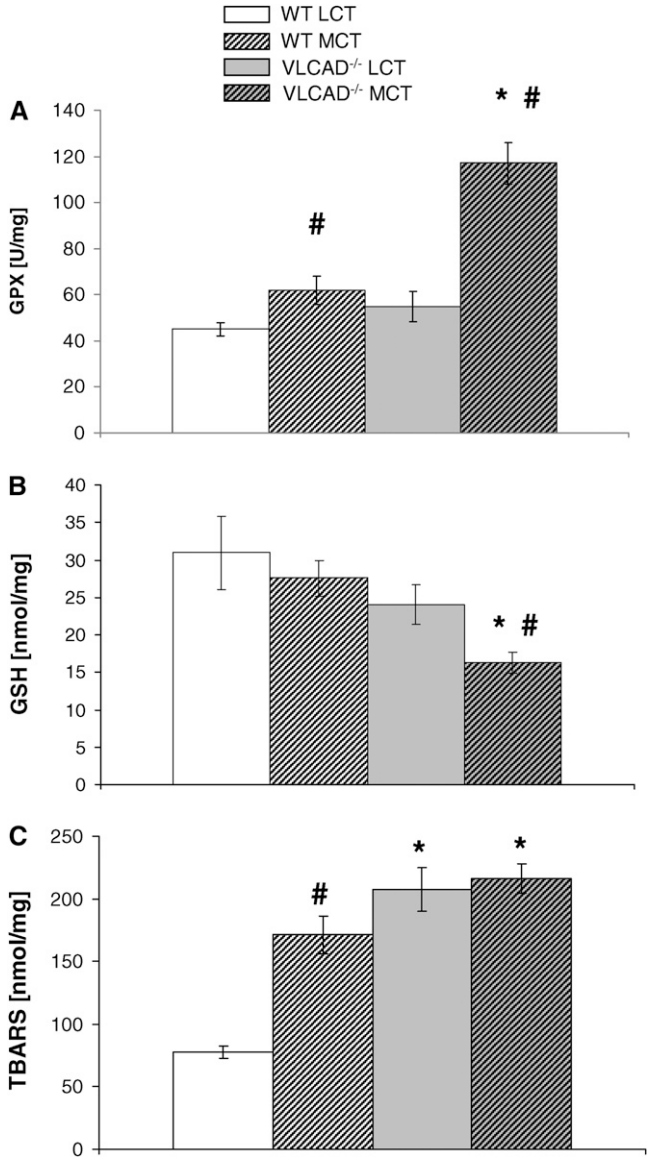

FIGURE 5. Liver oxidative stress in wild-type (WT) mice and mice with very-long-chain acyl-coenzyme A dehydrogenase deficiency (VLCAD$^{-/-}$) supplemented with either long-chain triglycerides (LCT) or medium-chain triglycerides (MCT). A: Glutathione peroxidase (GPX) activity. B: reduced glutathione (GSH). C: Thiobarbituric acid–reactive substances (TBARS). The values are expressed as means ± SEMs (n = 5–7). *Significantly different from WT mice within the same diet group, $P < 0.05$ (2-factor ANOVA and Student's t test). #Significant differences between mice within the same genotype under different dietary conditions, $P < 0.05$ (2-factor ANOVA and Student's t test).

did the MCT-fed WT mice (61.8 ± 6.2 U/mg; $P < 0.05$; n = 5–7). Quantification of GSH as substrate for GPX showed a direct correlation between increased GPX activity and reduced GSH content in mice fed the MCT diet (Figure 5B). In fact, the MCT diet induced a significant decrease in GSH concentrations to a value of 16.3 ± 1.4 nmol/mg in the VLCAD$^{-/-}$ mice compared with LCT-fed VLCAD$^{-/-}$ mice (24 ± 2.6 nmol/mg; $P <$ 0.05). Furthermore, in both genotype groups, the MCT diet resulted in increased hepatic concentrations of TBARS (171 ± 15.1 nmol/mg in WT mice compared with 215.9 ± 11.7 nmol/mg in VLCAD$^{-/-}$ mice; $P < 0.05$; n = 5–7), although the livers of VLCAD$^{-/-}$ mice fed the LCT diet had a TBARS concentration >2-fold that of WT mice (207.5 ± 17.7 compared with 77.6 ± 4.9 nmol/mg; $P < 0.05$; Figure 5C).

Effect of MCT diet on genes regulating lipid metabolism

In a final step, we investigated whether MCT supplementation resulted in an up-regulation of lipogenesis at the mRNA level. We therefore, analyzed the expression of *SREBP-1c*, which directly activates *FASN*, which is involved in the biosynthesis and elongation of short- and MCFAs, respectively. In addition, we also verified the expression of *SCD1*, which is responsible for the biosynthesis of unsaturated fatty acids (29). As shown in **Figure 6**, RT-PCR showed that the expression of *SREBP-1c* and *FASN,* but not of *SCD-1*, was strongly up-regulated in WT mice fed the MCT diet. In contrast, all of the lipogenic genes analyzed in VLCAD$^{-/-}$ mice—*SREBP-1c, FASN*, and *SCD1*—were already up-regulated under control conditions. Surprisingly, the long-term MCT diet resulted in a down-regulation of these genes comparable with levels in the WT mice fed the normal LCT diet.

DISCUSSION

A diet based on MCTs is a recommended treatment in symptomatic VLCAD deficiency. Whereas an MCT-modified diet is currently considered extremely safe, in the current study we showed that the replacement of LCTs by MCTs resulted in a dramatic accumulation of visceral fat and liver lipids in VLCAD$^{-/-}$ mice when applied over 1 y. Furthermore, not only did the abdominal lipid content increase, but the tissue fat composition changed significantly. The contents of SFAs and MUFAs were elevated, whereas the content of physiologically important PUFAs decreased by >60% with MCT therapy as compared with the normal diet. Concomitantly, the long-term MCT diet induced severe liver damage in VLCAD$^{-/-}$ mice and substantial signs of oxidative stress and steatohepatitis. These findings are of significant clinical relevance, because both symptomatic and many asymptomatic patients with LCFA oxidation

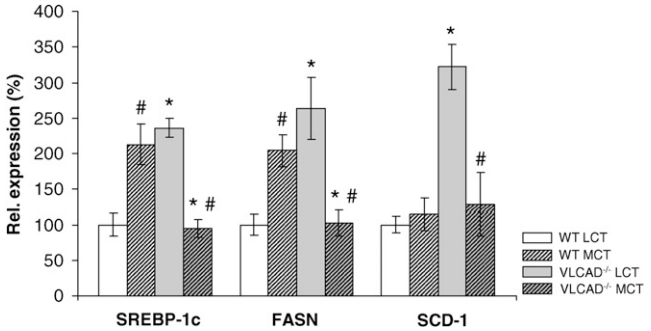

FIGURE 6. Hepatic relative messenger RNA expression of genes involved in fatty acid biosynthesis in wild-type (WT) mice and mice with very-long-chain acyl-coenzyme A dehydrogenase deficiency (VLCAD$^{-/-}$) supplemented with either long-chain triglycerides (LCT) or medium-chain triglycerides (MCT). *SREBP-1c*, sterol regulatory element binding protein 1c; *FASN*, fatty acid synthase; *SCD1*, stearoyl-coenzyme A desaturase 1. Values are expressed as means ± SEMs (n = 5–7). *Significantly different from WT mice within the same diet group, $P < 0.05$ (2-factor ANOVA and Student's t test). #Significant differences between mice within the same genotype under different dietary conditions, $P < 0.05$ (2-factor ANOVA and Student's t test).

The American Journal of Clinical Nutrition

defects are supplemented, beginning in the neonatal period, with a long-term MCT diet.

The detrimental effects induced by the altered triglyceride composition of the diet are particularly striking because the total fat content of the MCT preparation was equal to that of the LCT diet. However, the metabolism of MCTs differs in many aspects from that of normal LCTs. In fact, MCTs are rapidly hydrolyzed to FFAs and quickly absorbed by the gastrointestinal tract. In contrast with LCFAs, only a minor amount of MCFAs are incorporated into chylomicrons (30) but exit the enterocyte via the portal circulation as nonesterified FAs and thus may be easily accessed by cardiac and skeletal muscle. Of note, spillover MCFAs are not stored as MCTs in adipocytes, as shown by ^{13}C-MRS analysis of the average fatty acid chain length in abdominal tissue, which—even after 1 y of the MCT diet—showed only a slight shortening of the carbon chain as compared with the LCT diet. This finding agrees with previous findings of an impaired uptake of MCFAs into adipocytes (31). As a consequence, excess MCFAs are primarily transported to the liver (32), where they can be converted via β-oxidation into C2-fragments and ketone bodies, respectively, or elongated to LCFAs and subsequently esterified to LCTs (13, 33). As evidenced by the ^{13}C-MRS data, the latter pathway clearly dominates under well-fed conditions in both WT and VLCAD$^{-/-}$ mice. Because elongated FAs cannot be used for energy production in VLCAD-deficient mice, this results in a massive lipid accumulation in the mutant as shown by localized ^{1}H-MRS of the liver and, in the long run, constitutes a vicious cycle because of the continuously enhanced enrichment and turnover of MCFAs in the liver.

Elevated lipid concentrations in the liver are known to be associated with elevated lipid peroxidation and oxidative stress (34). In line with this, we found GPX—a major player in detoxification of mitochondrial ROS (35)—to be up-regulated in MCT-treated VLCAD$^{-/-}$ mice. Interestingly, in both MCT-supplemented and -nonsupplemented VLCAD$^{-/-}$ mice, decomposition products of lipid peroxides were increased, which suggests that, independent of the degree of steatosis, VLCAD-deficient livers are exposed to enhanced oxidative stress. Elevated hepatic lipid concentrations in MCT-fed VLCAD$^{-/-}$ mice were accompanied by a pronounced increase in both serum FFAs and visceral fat deposition. These data emphasize the adverse effects of long-term MCT supplementation because high serum FFAs and visceral fat are strongly related with the development of cardiovascular disease, insulin resistance, and the metabolic syndrome (36–38). On the other hand, the content of physiologic important PUFAs was massively reduced in mice fed with MCTs. PUFAs have cardioprotective properties through several mechanisms (39–42), whereas elevated SFAs have been reported to activate a signal cascade leading to apoptosis (43). PUFAs, but not MUFAs or SFAs, down-regulate the expression of *SREBP-1c*—a key regulator of lipogenesis (44). Therefore, the initial up-regulation of liver lipogenesis in WT and VLCAD$^{-/-}$ mice fed the MCT diet for 5 wk, as observed previously (13, 33), was not surprising. Of note, these alterations persisted only in WT mice after 1 y of the MCT diet, whereas in VLCAD$^{-/-}$ mice the lipogenic transcription was no longer up-regulated. This was most likely associated with the severe pathologic liver phenotype in the mutant with macrovesicular lobular steatosis accompanied by fibrosis and inflammation as consequence of prolonged MCT therapy.

Despite the finding that all MCT-induced effects were exceptionally pronounced in VLCAD$^{-/-}$ mice, WT mice also showed a trend to a "fatty" phenotype similar to that of VLCAD-deficient mice. After 1 y of the MCT diet, a tendency to enhanced lipid deposition in the liver (in both ^{1}H MRS and histology data) and elevated AST and ALT concentrations in the blood were observed. These effects were accompanied by enhanced oxidative stress (elevated TBARS levels and GPX activity), increased concentrations of circulating FFAs, and up-regulation of genes involved in lipogenesis, although alterations in visceral fat content were not observed. Furthermore, the alterations induced by the MCT diet on body fat composition were as striking as in VLCAD$^{-/-}$ mice. The development of this tendency to a fatty liver into a serious pathological phenotype in VLCAD$^{-/-}$ mice, similar to the clinical characteristics of nonalcoholic steatohepatitis (NASH), might be favored by *1*) the presence of enhanced oxidative stress as described above and *2*) the significantly shorter chain size ($\approx$16 carbons) of stored triglyceride fatty acids, because palmitic acid is considered to be one of the key factors in promoting insulin resistance and the metabolic syndrome (45–48).

From a clinical point of view, supplementation with MCTs has been proven to be effective in preventing the development of cardiomyopathy and skeletal myopathy in VLCADD in that they bypass the metabolic bottlenecks and provide organs relying on fatty acids as a major energy source with the required substrates (12, 13). Furthermore, several short-term studies in both animals und humans suggest that an MCT diet might also be beneficial in the treatment of obesity because of the limited deposition of MCFAs in adipocytes (31, 49). The enhanced energy requirement for MCFA elongation indeed may contribute to weight loss in the short term (50); however, in the long term, the permanently enhanced fat supply to the liver obviously increases the risk of the development of steatosis, as was also observed in the current study for healthy WT animals. Thus, it was not surprising that there are reports about the occurrence of fatty liver on a ketogenic MCT diet during untreatable epilepsy (51). Importantly, the development of significant fatty liver was also observed in a patient with an LCFA oxidation defect after the start of continuous MCT supplementation for muscular pain (U Spiekerkoetter, unpublished observations, 2010), which in the long run is associated with the risk of steatosis and with the clinical characteristics of NASH, as shown for our murine model of FAOD.

In summary, this study showed in a murine model of VLCADD that a long-term MCT-based diet (1 y) results in severe deterioration of whole-body lipid homeostasis, with strongly elevated serum FFA concentrations, massive visceral fat infiltration, impaired body fat composition with decreased PUFAs, and the development of steatohepatitis. All of these changes are comparable with those reported for NASH and the metabolic syndrome (52, 53). Although the recommended dietary treatment in asymptomatic newborns with VLCADD is less MCTs, as used in this study (3, 8), patients with a disorder of the mitochondrial trifunctional protein should receive a strictly MCT-modified diet, as used in this study. Similar, but milder, effects may be expected by a lower MCT content and need to be carefully investigated and monitored. As a noninvasive strategy for surveillance of changes in body fat distribution and composition in treated patients, we argue for the use of the MR techniques used in this study which could be readily transferred to clinical scanners. According to the data

The American Journal of Clinical Nutrition

presented here, the use and dose of MCT supplementation has to be reevaluated not only for the treatment of VLCADD but also for all other applications.

The authors' responsibilities were as follows—ST, UF, and US: designed the research; ST: conducted the research and drafted the manuscript; UF: performed the MR analysis and drafted the manuscript; MS: contributed to the data collection and analysis; EB: performed the histological evaluation; and US: had primary responsibility for the final content. All authors read and approved the final manuscript. The authors had no conflicts of interest to disclose.

REFERENCES

1. Wilcken B, Wiley V, Hammond J, Carpenter K. Screening newborns for inborn errors of metabolism by tandem mass spectrometry. N Engl J Med 2003;348:2304–12.
2. Spiekerkoetter U, Tokunaga C, Wendel U, et al. Changes in blood carnitine and acylcarnitine profiles of very long-chain acyl-CoA dehydrogenase-deficient mice subjected to stress. Eur J Clin Invest 2004; 34:191–6.
3. Arnold GL, Van HJ, Freedenberg D, et al. A Delphi clinical practice protocol for the management of very long chain acyl-CoA dehydrogenase deficiency. Mol Genet Metab 2009;96:85–90.
4. Gregersen N, Andresen BS, Corydon MJ, et al. Mutation analysis in mitochondrial fatty acid oxidation defects: exemplified by acyl-CoA dehydrogenase deficiencies, with special focus on genotype-phenotype relationship. Hum Mutat 2001;18:169–89.
5. Spiekerkoetter U. Mitochondrial fatty acid oxidation disorders: clinical presentation of long-chain fatty acid oxidation defects before and after newborn screening. J Inherit Metab Dis 2010;33:527–32.
6. Kompare M, Rizzo WB. Mitochondrial fatty-acid oxidation disorders. Semin Pediatr Neurol 2008;15:140–9.
7. Orngreen MC, Norgaard MG, Sacchetti M, van Engelen BG, Vissing J. Fuel utilization in patients with very long-chain acyl-CoA dehydrogenase deficiency. Ann Neurol 2004;56:279–83.
8. Spiekerkoetter U, Lindner M, Santer R et al. Treatment recommendations in long-chain fatty acid oxidation defects: consensus from a workshop. J Inherit Metab Dis 2009 ;32 :498–505.
9. Spiekerkoetter U, Lindner M, Santer R, et al. Management and outcome in 75 individuals with long-chain fatty acid oxidation defects: results from a workshop. J Inherit Metab Dis 2009;32:488–97.
10. Gillingham MB, Scott B, Elliott D, Harding CO. Metabolic control during exercise with and without medium-chain triglycerides (MCT) in children with long-chain 3-hydroxy acyl-CoA dehydrogenase (LCHAD) or trifunctional protein (TFP) deficiency. Mol Genet Metab 2006;89:58–63.
11. Roe CR, Sweetman L, Roe DS, David F, Brunengraber H. Treatment of cardiomyopathy and rhabdomyolysis in long-chain fat oxidation disorders using an anaplerotic odd-chain triglyceride. J Clin Invest 2002; 110:259–69.
12. Primassin S, Tucci S, Herebian D, et al. Pre-exercise medium-chain triglyceride application prevents acylcarnitine accumulation in skeletal muscle from very-long-chain acyl-CoA-dehydrogenase-deficient mice. J Inherit Metab Dis 2010;33:237–46.
13. Tucci S, Primassin S, Ter VF, Spiekerkoetter U. Medium-chain triglycerides impair lipid metabolism and induce hepatic steatosis in very long-chain acyl-CoA dehydrogenase (VLCAD)-deficient mice. Mol Genet Metab 2010;101:40–7.
14. Spiekerkoetter U, Sun B, Zytkovicz T, Wanders R, Strauss AW, Wendel U. MS/MS-based newborn and family screening detects asymptomatic patients with very-long-chain acyl-CoA dehydrogenase deficiency. J Pediatr 2003;143:335–42.
15. Spiekerkoetter U, Tokunaga C, Wendel U, et al. Tissue carnitine homeostasis in very-long-chain acyl-CoA dehydrogenase-deficient mice. Pediatr Res 2005;57:760–4.
16. Spiekerkoetter U, Ruiter J, Tokunaga C, et al. Evidence for impaired gluconeogenesis in very long-chain acyl-CoA dehydrogenase-deficient mice. Horm Metab Res 2006;38:625–30.
17. Exil VJ, Roberts RL, Sims H, et al. Very-long-chain acyl-coenzyme a dehydrogenase deficiency in mice. Circ Res 2003;93:448–55.
18. Kunnecke B, Verry P, Bénardeau A, von Kienlin M. Quantitative body composition analysis in awake mice and rats by magnetic resonance relaxometry. Obes Res 2004;12:1604–15.
19. Moonen CT, Dimand RJ, Cox KL. The noninvasive determination of linoleic acid content of human adipose tissue by natural abundance carbon-13 nuclear magnetic resonance. Magn Reson Med 1988;6: 140–57.
20. Brunt EM, Janney CG, Di Bisceglie AM, Neuschwander-Tetri BA, Bacon BR. Nonalcoholic steatohepatitis: a proposal for grading and staging the histological lesions. Am J Gastroenterol 1999;94:2467–74.
21. Bradford MM. A rapid and sensitive method for the quantitation of microgram quantities of protein utilizing the principle of protein-dye binding. Anal Biochem 1976;72:248–54.
22. Lawrence RA, Burk RF. Glutathione peroxidase activity in selenium-deficient rat liver. Biochem Biophys Res Commun 1976;71:952–8.
23. Mantha SV, Prasad M, Kalra J, Prasad K. Antioxidant enzymes in hypercholesterolemia and effects of vitamin E in rabbits. Atherosclerosis 1993;101:135–44.
24. Yagi K. A simple fluorometric assay for lipoperoxide in blood plasma. Biochem Med 1976;15:212–6.
25. Schumann G, Bonora R, Ceriotti F, et al. IFCC primary reference procedures for the measurement of catalytic activity concentrations of enzymes at 37 degrees C. International Federation of Clinical Chemistry and Laboratory Medicine. Part 4. Reference procedure for the measurement of catalytic concentration of alanine aminotransferase. Clin Chem Lab Med 2002;40:718–24.
26. Schumann G, Bonora R, Ceriotti F, et al. IFCC primary reference procedures for the measurement of catalytic activity concentrations of enzymes at 37 degrees C. International Federation of Clinical Chemistry and Laboratory Medicine. Part 5. Reference procedure for the measurement of catalytic concentration of aspartate aminotransferase. Clin Chem Lab Med 2002;40:725–33.
27. Schafer C, Hoffmann L, Heldt K, et al. Osmotic regulation of betaine homocysteine-S-methyltransferase expression in H4IIE rat hepatoma cells. Am J Physiol Gastrointest Liver Physiol 2007;292:G1089–98.
28. Jaeschke H, Gores GJ, Cederbaum AI, Hinson JA, Pessayre D, Lemasters JJ. Mechanisms of hepatotoxicity. Toxicol Sci 2002;65:166–76.
29. Ntambi JM. The regulation of stearoyl-CoA desaturase (SCD). Prog Lipid Res 1995;34:139–50.
30. Swift LL, Hill JO, Peters JC, Greene HL. Medium-chain fatty acids: evidence for incorporation into chylomicron triglycerides in humans. Am J Clin Nutr 1990;52:834–6.
31. Guo W, Xie W, Han J. Modulation of adipocyte lipogenesis by octanoate: involvement of reactive oxygen species. Nutr Metab (Lond) 2006;3:30.
32. Guillot E, Vaugelade P, Lemarchal P, Rerat A. Intestinal absorption and liver uptake of medium-chain fatty acids in non-anaesthetized pigs. Br J Nutr 1993;69:431–42.
33. Turner N, Hariharan K, TidAng J, et al. Enhancement of muscle mitochondrial oxidative capacity and alterations in insulin action are lipid species dependent: potent tissue-specific effects of medium-chain fatty acids. Diabetes 2009;58:2547–54.
34. Letteron P, Fromenty B, Terris B, Degott C, Pessayre D. Acute and chronic hepatic steatosis lead to in vivo lipid peroxidation in mice. J Hepatol 1996;24:200–8.
35. Pessayre D, Mansouri A, Fromenty B. Nonalcoholic steatosis and steatohepatitis. V. Mitochondrial dysfunction in steatohepatitis. Am J Physiol Gastrointest Liver Physiol 2002;282:G193–9.
36. Bergman RN, Kim SP, Catalano KJ, et al. Why visceral fat is bad: mechanisms of the metabolic syndrome. Obesity (Silver Spring) 2006; 14(suppl 1):16S–9S.
37. Mathew M, Tay E, Cusi K. Elevated plasma free fatty acids increase cardiovascular risk by inducing plasma biomarkers of endothelial activation, myeloperoxidase and PAI-1 in healthy subjects. Cardiovasc Diabetol 2010;9:9.
38. Phillips LK, Prins JB. The link between abdominal obesity and the metabolic syndrome. Curr Hypertens Rep 2008;10:156–64.
39. Calder PC. n−3 polyunsaturated fatty acids, inflammation, and inflammatory diseases. Am J Clin Nutr 2006;83(suppl):1505S–19S.
40. Harris WS, Miller M, Tighe AP, Davidson MH, Schaefer EJ. Omega-3 fatty acids and coronary heart disease risk: clinical and mechanistic perspectives. Atherosclerosis 2008;197:12–24.
41. Massaro M, Scoditti E, Carluccio MA, De CR. Basic mechanisms behind the effects of n−3 fatty acids on cardiovascular disease. Prostaglandins Leukot Essent Fatty Acids 2008;79:109–15.
42. Mori TA, Beilin LJ. Omega-3 fatty acids and inflammation. Curr Atheroscler Rep 2004;6:461–7.

The American Journal of Clinical Nutrition

43. Fessler MB, Rudel LL, Brown JM. Toll-like receptor signaling links dietary fatty acids to the metabolic syndrome. Curr Opin Lipidol 2009; 20:379–85.
44. Nakamura MT, Cheon Y, Li Y, Nara TY. Mechanisms of regulation of gene expression by fatty acids. Lipids 2004;39:1077–83.
45. Alkhateeb H, Chabowski A, Glatz JF, Luiken JF, Bonen A. Two phases of palmitate-induced insulin resistance in skeletal muscle: impaired GLUT4 translocation is followed by a reduced GLUT4 intrinsic activity. Am J Physiol Endocrinol Metab 2007;293:E783–93.
46. Reynoso R, Salgado LM, Calderon V. High levels of palmitic acid lead to insulin resistance due to changes in the level of phosphorylation of the insulin receptor and insulin receptor substrate-1. Mol Cell Biochem 2003;246:155–62.
47. Riserus U. Fatty acids and insulin sensitivity. Curr Opin Clin Nutr Metab Care 2008;11:100–5.
48. Vessby B, Gustafsson IB, Tengblad S, Boberg M, Andersson A. Desaturation and elongation of fatty acids and insulin action. Ann N Y Acad Sci 2002;967:183–95.
49. Nagao K, Yanagita T. Medium-chain fatty acids: functional lipids for the prevention and treatment of the metabolic syndrome. Pharmacol Res 2010;61:208–12.
50. Hill JO, Peters JC, Swift LL, et al. Changes in blood lipids during six days of overfeeding with medium or long chain triglycerides. J Lipid Res 1990;31:407–16.
51. Beverley D, Arthur R. Fatty liver and medium chain triglyceride (MCT) diet. Arch Dis Child 1988;63:840–2.
52. Neuschwander-Tetri BA. Hepatic lipotoxicity and the pathogenesis of nonalcoholic steatohepatitis: the central role of nontriglyceride fatty acid metabolites. Hepatology 2010;52:774–88.
53. Schattenberg JM, Galle PR. Animal models of non-alcoholic steatohepatitis: of mice and man. Dig Dis 2010;28:247–54.

The American Journal of Clinical Nutrition

American Journal of Transplantation 2011; 11: 235–244
Wiley Periodicals Inc.

doi: 10.1111/j.1600-6143.2010.03372.x

Noninvasive Detection of Graft Rejection by *In Vivo* ^{19}F MRI in the Early Stage

U. Flögel[a,*], S. Su[b], I. Kreideweiß[a], Z. Ding[a], L. Galbarz[a], J. Fu[b], C. Jacoby[a], O. Witzke[b] and J. Schrader[a]

[a] *Cardiovascular Physiology, Heinrich Heine University Düsseldorf, Germany*
[b] *Department of Nephrology, University Hospital Essen, Germany*
* *Corresponding author: Ulrich Flögel, floegel@uni-duesseldorf.de*

Diagnosis of transplant rejection requires tissue biopsy and entails risks. Here, we describe a new ^{19}F MRI approach for noninvasive visualization of organ rejection via the macrophage host response. For this, we employed biochemically inert emulsified perfluorocarbons (PFCs), known to be preferentially phagocytized by monocytes and macrophages. Isografts from C57BL/6 or allografts from C57B10.A mice were heterotopically transplanted into C57BL/6 recipients. PFCs were applied intravenously followed by ^{1}H/^{19}F MRI at 9.4 T 24 h after injection. ^{1}H images showed a similar position and anatomy of the graft in the abdomen for both cases. However, corresponding ^{19}F signals were only observed in allogenic tissue. ^{1}H/^{19}F MRI enabled us to detect the initial immune response not later than 3 days after surgery, when conventional parameters did not reveal any signs of rejection. In allografts, the observed ^{19}F signal strongly increased with time and correlated with the extent of rejection. In separate experiments, rapamycin was used to demonstrate the ability of ^{19}F MRI to monitor immunosuppressive therapy. Thus, PFCs can serve as positive contrast agent for the early detection of transplant rejection by ^{19}F MRI with high spatial resolution and an excellent degree of specificity due to lack of any ^{19}F background.

Key words: Graft rejection, ^{19}F MRI, heart transplantation, perfluorocarbons, monocytes

Abbreviations: MRI, magnetic resonance imaging; MIOs, micrometer-sized paramagnetic iron oxide; PFC, perfluorcarbons; SPIOs, superparamagnetic iron oxide; USPIOs, ultrasmall superparamagnetic iron oxide.

Received 12 July 2010, revised 18 October 2010 and accepted for publication 09 November 2010

Introduction

Within the last decades transplantation has become an established treatment for end-stage organ disease. The survival rate has considerably improved due to advances in organ preservation and immunosuppressive treatments. However, allograft rejection still remains a major complication after transplantation. For surveillance of transplant rejection tissue biopsy is traditionally used (1,2), which yet is the 'gold standard' for determining organ rejection. However, due to its invasive nature biopsy carries finite risks of complication and is also prone to sampling error because of the limited tissue size available. Since rejection sites are highly heterogeneous, false-negative results can easily be obtained due to spot sampling from the tissue. In addition, discrepancies have been found between biopsy-based diagnosis and actual rejection (3,4). Therefore, many attempts have been made to uncouple the threshold for antirejection therapy from histological biopsy grading and to link it more closely to graft dysfunction by noninvasive analysis of physiological parameters (5–8) and serum proteins (9,10). However, none of these approaches have yet gained widespread clinical use, since functional changes resulting from acute rejection are barely detectable by conventional imaging modalities until later rejection stages (11,12), when it may be too late for therapeutic intervention, and standard laboratory parameters lack the sensitivity and specificity for detection of graft rejection.

All organs undergoing acute rejection are infiltrated by immune cells in the early stage of the rejection process. Activated macrophages make up a large part of the cellular invasion during this period and are increasingly recognized as key inflammatory amplifiers in organ rejection (13,14). Since they have been found to appear in the early cellular infiltrate of rejecting grafts, a specific tracking of these cells would be an ideal target for a molecular imaging approach to visualize graft rejection in the initial stage. Magnetic resonance imaging (MRI) is an established technique for noninvasive detection of cells *in vivo* by use of contrast agents incorporated within target cells. Most cellular MRI studies rely on the use of (ultrasmall) superparamagnetic iron oxide particles (USPIOs, SPIOs or MPIOs) as contrast agent, which are readily phagocytized by the monocyte-macrophage system (15,16). Subsequently, loaded cells give rise to hypointense spots on T2*-weighted MR images (15). Thus, areas with decreased MR signal

intensity may then be associated with sites of immune cell infiltration—an approach which has recently also applied for detection of cardiac graft rejection (17–20). However, it is not always clear whether signal depletion in anatomic proton (^{1}H) MR images are caused by these nanoparticles or by other reasons, which makes it often difficult to interpret the images and hampers an appropriate diagnosis.

In the present study, we validated a fluorine (^{19}F) MRI approach for the early and specific detection of organ rejection via an increase in MR signal intensity related to the macrophage host response using a murine abdominal heart transplantation model. We employed biochemically inert emulsified perfluorocarbons (PFCs), which are preferentially phagocytized by monocytes and macrophages similar to SPIOs (21,22), and which we have recently shown to be suitable for visualizing the infiltration of immunocompetent cells during pneumonia as well as cardiac and cerebral ischemia (22,23). Because of the lack of any ^{19}F background in the body, observed signals originating from injected ^{19}F-containing compounds are highly specific and hold the potential for absolute quantification.

Materials and Methods

Preparation of the PFC emulsion

The PFC emulsion containing 10% wt/wt perfluoro-15-crown-5 ether (Chempur, Karlsruhe, Germany) and 4% wt/wt purified egg lecithin E 80 S (Lipoid, Ludwigshafen, Germany) in isotonic buffer (10 mM HEPES, 2.5% glycerol, pH 7.4) was prepared essentially as previously reported (22). High pressure homogenization (75 MPa, 10 cycles) with an Emulsiflex C5 homogenizer (Avestin, Mannheim, Germany) resulted in a particle size of ≈130 nm as determined by dynamic light scattering using a ZetatracTM (Particle Metrix, Meerbusch, Germany) which was also used to measure the ζ potential of the particles (–31.3 ± 1.5 mV) as the average of at least 10 runs at the stationary level. The resulting nanoemulsion was sterilized by autoclaving and stored until administration at 6°C.

Animals

Animal experiments were performed in accordance with the national guidelines on animal care and were approved by the 'Landesamt für Natur, Umwelt und Verbraucherschutz Nordrhein-Westfalen'. The male mice (20–25 g body weight; 10–12 weeks of age) used in this study were bred at the Tierversuchsanlage of Heinrich-Heine-Universität (Düsseldorf, Germany). They were fed a standard chow diet and received tap water *ad libitum*. To study acute rejection, allomismatched murine heterotopic cardiac transplantation was performed using hearts from C57B10.A (H-2^a) mice as donor and C57BL/6 (H-2^b) mice as recipient. Isografts (C57BL/6–C57BL/6) served as controls.

Heart transplantation

Abdominal heart transplantation was carried out as previously described (24). In brief, for preparation of the donor heart, mice were deeply anesthetized by a mixed solution of 2% xylazine and 10% ketamine, and a U-shaped anterior thoracotomy was made to arrest the heartbeat by using cardioplegic solution. The ascending aorta and the vena cava inferior were freed from the surrounding tissues while the right and left superior vena cava, the pulmonary artery and veins were ligated *en bloc*. For recipient operation, a median transverse abdominal incision bilaterally to the border between the abdomen and the dorsum was performed, and a vessel length of about 3 mm below the renal vessels was prepared for anastomosis. After temporally occluding the abdominal aorta and vena cava, longitudinal venotomy and aortotomy were carried out. The end-to-side anastomosis between graft aorta and recipient aorta was performed with single-knot running suture (10–0) and the donor vena cava was joined end-to-side to the recipient vena cava. In this model, blood flow to the coronary arteries of the graft occurs via retrograde perfusion from the abdominal aorta of the recipient. After completion of anastomosis the graft readily takes a normal heartbeat within the physiological range characteristic for mice (500–600 bpm), but without vital function to the recipient. The abdomen was then closed and 1 mL of saline was administered subcutaneously to the back of the animal for hydration. The animal was placed under a heating lamp and monitored visually until it was fully awake. The heartbeat was palpated through the abdominal wall by a blinded investigator once a day and was scored from 0 to 3, where 3 indicates a strong contraction, 2 indicates a mild contraction, 1 indicates a weak contraction and 0 indicates no contraction (25).

For MRI investigations, 500 μL of the PFC emulsion was injected into the tail vein of the mice 24 h prior to scanning of the animals. For experiments with immunosuppressive therapy, mice received 0.4 mg/kg body weight rapamycin (Pfizer, Berlin, Germany) intraperitoneally. Treatment was started 48 h pretransplantation and was repeated every 2 days. PFC injections were carried out 6 and 10 days after surgery followed by MRI investigations at day 7 and 11, respectively.

MRI studies

Experiments were performed at a vertical 9.4 T Bruker DRX Wide Bore NMR spectrometer (Bruker, Rheinstetten, Germany) operating at frequencies of 400.13 MHz for ^{1}H and 376.46 MHz for ^{19}F measurements using a Bruker Microimaging unit (Mini 0.5) equipped with an actively shielded 57-mm gradient set (200 mT/m maximum gradient strength, 110 μs rise time at 100% gradient switching) and a ^{1}H/^{19}F 30-mm birdcage resonator. After acquisition of anatomical ^{1}H images, the resonator was tuned to ^{19}F, and morphologically matching ^{19}F images were recorded. For superimposing the images of both nuclei, the 'hot iron' color lookup table (ParaVision, Bruker) was applied to ^{19}F images.

Mice were anesthetized with 1.5% isoflurane and were kept at 37°C. Anatomical ^{1}H images were acquired with an ECG- and respiratory-triggered fast gradient echo cine sequence [field of view (FOV), 30 × 30 mm^2; matrix, 256 × 256; slice thickness (ST), 1 mm]. The ECG of the donor heart was obtained by attaching the ECG leads to the hind paws of the recipient animal and exhibited no 'contaminations' from signals of the recipient heart. Corresponding ^{19}F images were recorded from the same FOV using a multislice rapid acquisition with relaxation enhancement (RARE) sequence: RARE factor, 64; matrix, 128 × 128; ST, 2 mm; averages, 256; acquisition time, 19.12 minutes. For fusion with ^{19}F images, additional ^{1}H data sets with a ST of 2 mm were recorded. For a more detailed description of MRI setup, acquisition parameters and quantification procedures please refer to the expanded Materials and Methods section in the Online Data Supplement.

Histology

After MRI analysis, grafts were excised and processed for hematoxylin and eosin (H&E) or immunohistochemical staining according to standard procedures. For a detailed description please refer to the expanded Materials and Methods section in the Online Data Supplement. Slides were viewed with an Olympus BX50 fluorescence microscope and images were captured with a 12-bit CCD monochrome camera driven by Cell^P software. For quantification of CD11b-positive cells nine randomized sections equally selected from epi-, mid- and endocardium were counted for each graft.

Statistical analysis

All results are expressed as the means ± SD. Data were compared by Student's unpaired t-test, and a value of $p < 0.05$ was considered to be significant.

Results

PFC infiltration into allografts as assessed by ^{19}F MRI

Allografts from C57B10.A mice were transplanted into C57BL/6 recipients to undergo predictable progressive rejection, leading to graft failure within 2 weeks (26,27). To visualize this rejection by ^{1}H/^{19}F MRI, 500 μL of 10% perfluoro-15-crown-5 ether emulsion was injected via the tail vein at various times after surgery. Mice were imaged not until 24 h after application of the contrast agent to ensure efficient PFC loading of circulating monocytes and macrophages (22,23).

To locate the grafted heart within the abdomen of the recipient ^{1}H fast gradient echo MR images were acquired. Axial, coronal and sagittal example images are shown in Figure 1 to illustrate the position of the grafted heart and the sites of anastomosis to the recipient (see also Online Data Supplement movies 1–3). Subsequently, anatomically matching ^{19}F images were recorded for localizing the injected PFCs. A representative of consecutively acquired ^{1}H and ^{19}F images obtained 6 days after allotransplantation is depicted in the upper panel of Figure 2. The reference ^{1}H image (left) shows a short axis view of the grafted heart, and the corresponding ^{19}F image (middle) matched a signal pattern in shape of the ventricular walls. Merging of these images (right) confirms the deposition of PFCs within the myocardium of left and right ventricle. Since the pulse sequence used for ^{19}F MRI (RARE) results in a signal void of flowing blood particles, signals from circulating fluorine are suppressed, and the ^{19}F signals detected by this method can therefore be attributed unequivocally to accumulated PFCs in the tissue. To demonstrate that the acquired ^{19}F signals relate to immune cell invasion into the graft, tissue sections were processed for histology. As expected conventional H&E staining showed a substantial cell infiltration into allografts and immunohistochemistry for CD11b as a global marker for most cells of the innate immune system proved the invasion of cells with high phagocytosis capacity (Figure S1, top and middle panels). Costaining for

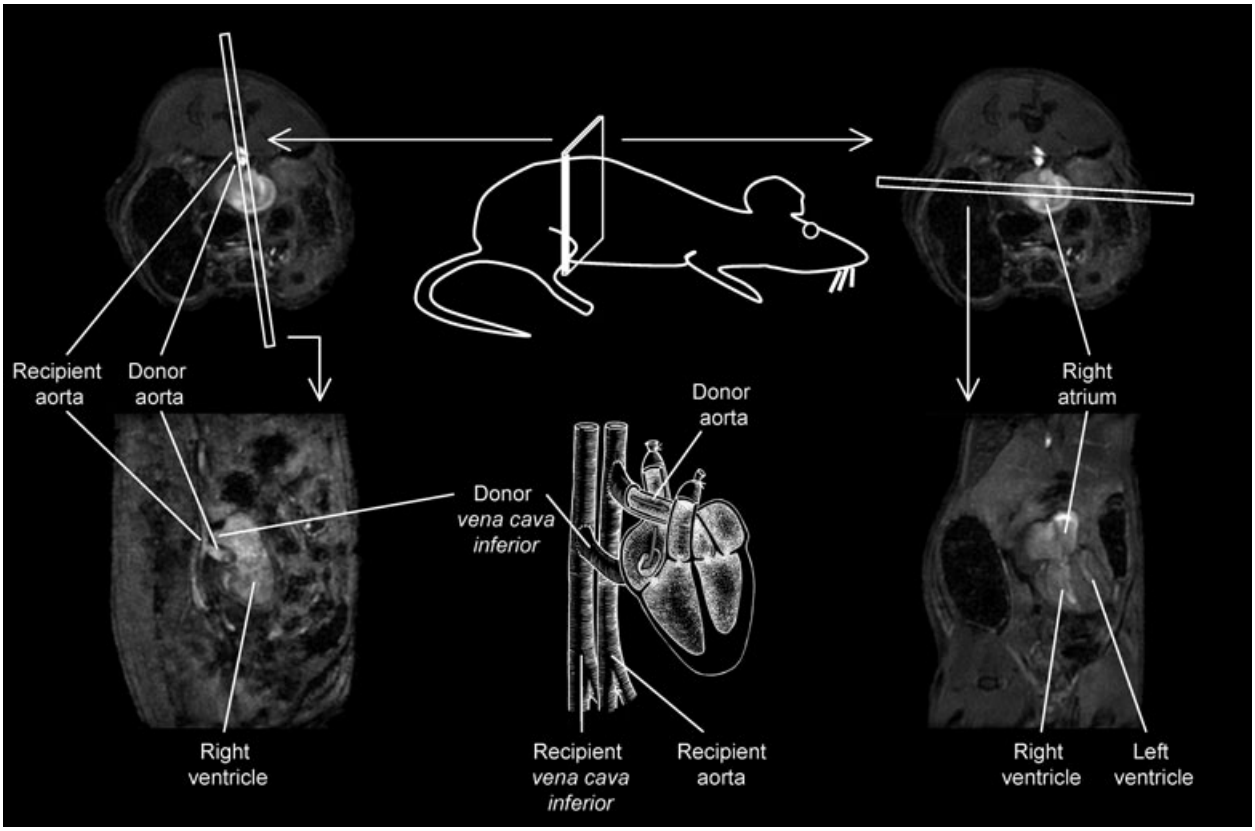

Figure 1: Mouse abdominal heart transplantation model. Schematic drawing of the heterotopic heart transplantation model and ^{1}H MR gradient echo images in different orientations. Axial (top), coronal (bottom right) and sagittal slices (bottom left) show the localization of the graft within the recipient and the sites of anastomosis (see also Online Data Supplement movies 1–3).

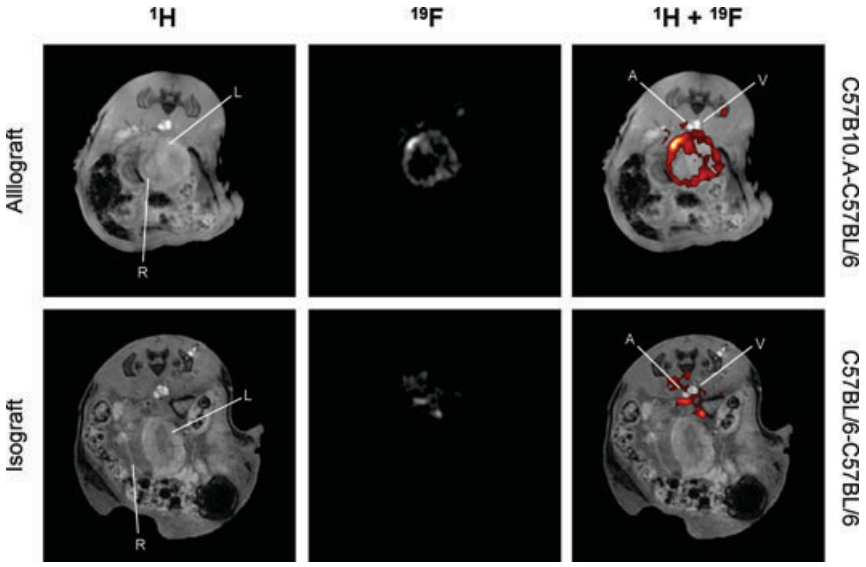

Figure 2: Infiltration of PFCs after transplantation as detected by *in vivo* ^{19}F MRI. ^{1}H (left) and ^{19}F (middle) images of the recipient mouse abdomen recorded from the same field of view (30 × 30 mm^2) 6 days after heterotopic transplantation of allo- (top) and isografts (bottom), respectively. Merging of the anatomically corresponding images (right) reveals intense ^{19}F signals (red) in left (L) and right (R) ventricular walls of the allograft (C57B10.A-C57BL/6) while for isografts (C57BL/6-C57BL/6) strong signals were mainly observed near the sites of vessel anastomosis (A, abdominal aorta of the recipient; V, vena cava inferior of the recipient). PFCs were injected via the tail vein 24 h prior to the MRI investigation.

CD68 and CD3 as specific markers for macrophages and T cells revealed both cell populations to be present in similar amounts in allogenic tissue confirming that macrophages make up a large part of the cellular infiltrate during the early process of rejection (Figure S1, bottom panel).

In control experiments, we analyzed genetically identical isografts at the same time after surgery, to exclude that inflammatory processes induced by the surgical intervention itself may interfere with the immune reaction associated with rejection. ^{1}H images indicate a similar location and morphology of the donor heart in the abdomen for both iso- and allograft 6 days posttransplantation (Figure 2, left-hand side). However, anatomical matching ^{19}F images of the isograft showed ^{19}F signals only at surgery sites of anastomosis (Figure 2, bottom panels) and a minimal deposition of PFCs within the myocardium. Histology confirmed the rather low cell infiltration into the cardiac tissue of iso- as compared to allografts (Figure S1).

Rejection is reflected by increasing ^{19}F signal intensity

In order to monitor the time course of rejection, animals were scanned from day 3 to 11 after transplantation. Day 3 was chosen for the first investigation, because the animals had to recover from the severe surgical intervention before applying the next general anesthesia for MRI. As can be seen from Figure 3, ^{1}H/^{19}F MRI enabled us to detect immune cell infiltration into allogenic tissue already at the earliest point in time, at day 3 after surgery. At this time anatomical ^{1}H images, functional cine movies or conventional parameters like the palpation score did not reveal any signs of rejection or cardiac dysfunction (Figure 4B). Detected ^{19}F signals were again restricted to the ventricular walls and the sites of anastomosis. In the myocardium of allografts, the observed ^{19}F signal strongly increased with time correlating with the extent of rejection (Figures 3 and 4). In the course of organ rejection PFC deposition appears to proceed from the epi- and endocardial borders toward the midwall of the myocardium (Figure 3, bottom). In isografts, cold ischemia resulted only in moderate deposition of PFCs with almost unchanged signal intensity over the period of time investigated (Figure 4A). Already at the very first MRI examination 3 days after surgery, ^{19}F content of allografts was significantly higher than in isografts (10.30 ± 2.67 vs. 4.56 ± 2.37 arbitrary units; $n = 5$, $p < 0.05$).

In the final set of experiments, we investigated whether this imaging approach could also be used to assess the efficacy of immunosuppressive therapy. Toward this end, animals were treated 48 h before allotransplantation by intraperitoneal injection with rapamycin (0.4 mg/kg body weight, every 2 days). Intravenous application of the PFC emulsion was carried out 5 and 10 days after surgery followed by MRI at days 6 and 11, respectively. As can be seen from the representative ^{1}H/^{19}F images displayed in Figure 5, rapamycin treatment substantially retarded the onset of the hosts immune response. After 6 days of immunosuppressive therapy an almost 'isograft phenotype' was observed (Figure 5, top right), again the ^{19}F signals being particularly visible at the site of vessel anastomosis. On the other hand, in untreated animals once more the characteristic pattern of PFC distribution within the grafted heart incipient from the epi- and endocardial borders was detected (Figure 5, top left). Quantification of ^{19}F signals 6 days after transplantation revealed that rapamycin significantly inhibited PFC accumulation by ~70% (Figure 6A; $n = 4$–5, $p < 0.05$). Continuing immunosuppressive therapy resulted in still strongly depressed ^{19}F signals in the treated as compared to the control group after 11 days (Figures 5 and 6). To relate the results obtained by *in vivo* ^{19}F MRI to pathological markers of rejection, grafts were excised and processed for immunohistochemistry.

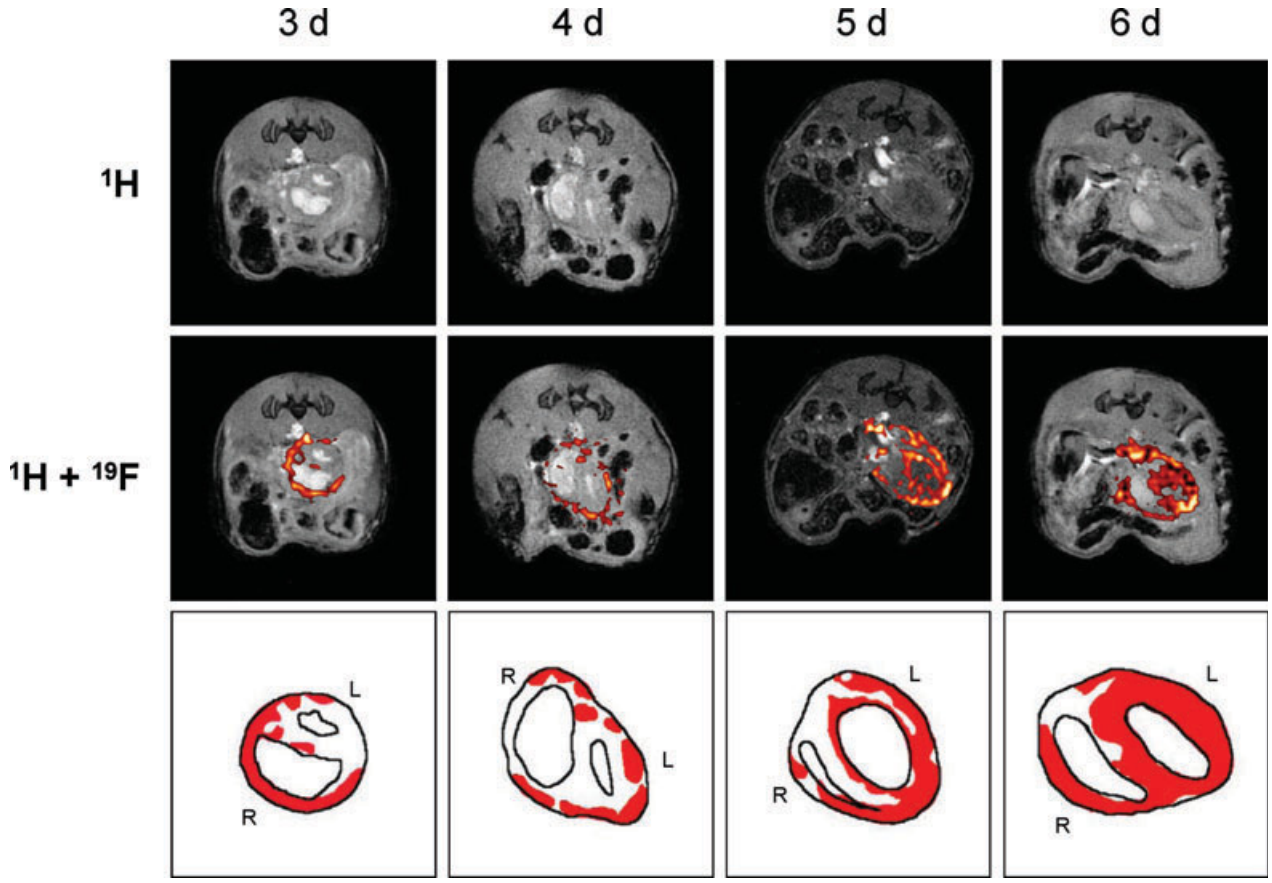

Figure 3: Increase of ^{19}F signals during progressive rejection. ^{1}H images (top) from different recipients superimposed with the matching ^{19}F images (middle) acquired 3, 4, 5 and 6 days after allotransplantation. The schematic drawings at the bottom indicate the main sites of PFC deposition within the grafted heart (L, R: left and right ventricle). For the sake of clarity, ^{19}F signals from sites of anastomosis have been omitted in the schemes. The time-dependent infiltration of PFC-loaded immune cells into the allograft seems to proceed from epi- and endocardial borders to the midwall of the myocardium. PFCs were injected intravenously 24 h before the respective MRI investigation.

Stainings for CD3, CD11b and CD68 indicated that immune cell infiltration into allogenic myocardium was strongly reduced by rapamycin treatment (Figure S2). Quantitative analysis showed CD11b-positive cells to be significantly diminished in the grafts during immunosuppressive therapy (day 6: 15 ± 10 vs. 53 ± 17 cells per mm^2; day 11: 64 ± 22 vs. 212 ± 50 cells per mm^2; $n = 4–5$, $p < 0.05$). As shown in Figure 6, the *in vivo* measurements (^{19}F) agreed well with the *in vitro* data (histology).

Discussion

In the present study, we demonstrate in a murine abdominal heart transplantation model that intravenously applied nanoemulsions of PFCs can be used as 'positive' contrast agent to sensitively visualize graft rejection in the initial stage via the hosts innate immune response. PFCs are preferentially phagocytized by monocytes/macrophages and are readily detected within the myocardium of allografts by simultaneous acquisition of morphologically matching ^{1}H and ^{19}F MR images. Because of the lack of any ^{19}F background in the body, observed signals are robust and exhibit an excellent degree of specificity. Histologic analysis confirmed that ^{19}F signals correlate with the quantity of infiltrating monocytes. Thus, ^{19}F MRI is suitable to monitor progressive organ rejection and to determine the effectiveness of therapeutic interventions.

The early assessment of organ rejection by ^{19}F MRI—when functional parameters did not reveal any signs of rejection—is based on the *in vivo* detection of PFC-loaded monocytes, which are quickly recruited to the grafted heart during the allogenic response (13). Currently, the gold standard for the detection of organ rejection is the histologic analysis of the immune response in biopsied tissue (28). However, the invasive nature of the biopsy is associated with risks and results are subject to possible false-negative results. This is underlined by the heterogenous ^{19}F pattern noted in the present study together

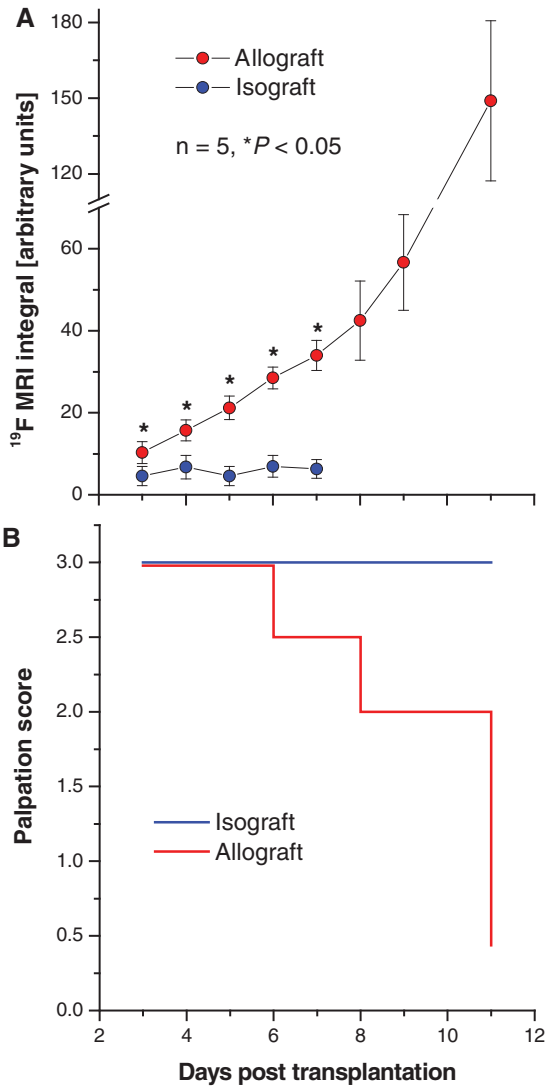

Figure 4: PFC detection precedes conventional parameters. (A) Quantification of ^{19}F MR signals and (B) palpation score in allo- (red) and isografts (blue) over time. Values are means ± SD, n = 5. ^{19}F signals were significantly different between allo- and isografts already at the first MRI examination after surgery (*p < 0.05). Due to methodological reasons no measurements were carried prior to day 3, because animals had to recover from the severe surgical intervention before applying the next general anesthesia for MRI.

with a progressive PFC deposition from epicardial and endocardial borders to the midwall. The observed heterogeneity is in line with previous observations (18) and strongly emphasizes the difficulties related with the withdrawal of small tissue samples by biopsy and its susceptibility to sampling errors. On the other hand, direct imaging of monocyte/macrophage infiltration with ^{19}F MRI not only is noninvasive, but also provides a whole organ visualization circumventing the problems associated with small sample biopsies.

Compared with previous ^{1}H MRI approaches for monitoring the infiltration of immunocompetent cells into sites of rejection via signal-depleting iron oxide-based contrast agents, the method presented here has the advantage of positive signal detection of the tagging agent. This enabled the recognition of PFC deposition within allografts already at the earliest time of investigation (3 days postsurgery). In contrast, the use of iron oxide nanoparticles in a very similar acute murine rejection model [Balb/c (h-2^{d}) to C57BL/6 (h-2^{b}) mice] revealed significant differences between allo- and isografts not until day 7, although in histologic sections already at day 3 posttransplantation an enhanced macrophage infiltration into allografts was observed in this study (20). Similarly, previous work on comparable rat allotransplantation models (BN to DA rats) with USPIOs and MSPIOs showed the potential of this approach to visualize organ rejection, but again at later points in time as with the present technique (17,18,29). Furthermore, background-free ^{19}F images can be conveniently quantified, which is much more challenging for the signal-depleting iron oxide agents. Additionally, it is not always clear whether dark areas are caused by these nanoparticles or result from other sources of susceptibility artifacts, such as hemorrhaging or tissue interfaces. Thus, the current study is the first to show a clear quantitative relationship between MR signal intensity and the degree of organ rejection (Figure 4).

The sensitivity of the current approach is additionally demonstrated by detection of ^{19}F signals at sites of vessel anastomosis as well as by observation of a minor PFC deposition in the myocardium of isografts. In the unaffected, nontransplanted heart *in vivo* we observed at no time any ^{19}F signals within the myocardium or in adjacent vessels (22). Therefore, the ^{19}F signal at the site of anastomosis and within the heart most likely reflects direct surgery-induced tissue trauma and ischemia/reperfusion injury occurring during transplantation, respectively. Because allo- and isografts are similarly affected by the cold ischemia, the 'true' ^{19}F signal caused by the gradually increasing immune response in the allograft can be calculated by substraction of the values for the syngeneic controls.

Intravenous injection of PFC emulsions results in an efficient labeling (≈50%) of the monocyte/macrophage cell population as previously shown by us and others (21–23,30). In recent experiments on blood and tissue samples combining blood density gradient centrifugation, FACS analysis and ^{1}H/^{19}F MRI, we found only a minor uptake of PFC nanoparticles by other circulating cells like neutrophils, B or T cells. This is in line with previous reports where the use of transfection agents like lipofectamine was required to achieve an efficient PFC labeling of weakly phagocytic cell types (31). Thus, a specific *in situ* labeling of other immune cells seems to be difficult under these conditions, but modifications of size and surface properties of the nanoparticles may be a promising future option to direct PFCs also into different

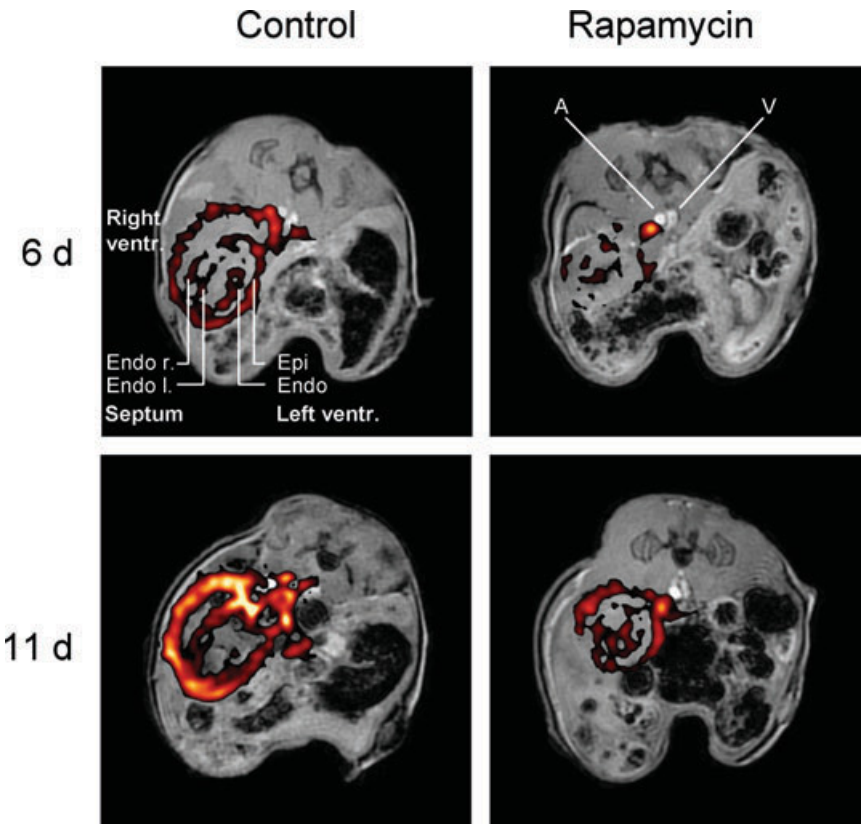

Figure 5: Monitoring immunosuppressive therapy. ^{1}H/^{19}F MRI of rapamycin (0.4 mg/kg body weight, i.p.) and saline-treated recipients 6 and 11 days after allotransplantation. Rapamycin treatment was started 48 h prior to transplantation and repeated every 2 days. PFC injections were carried out 1 day before MRI at day 5 and 10 after surgery, respectively (A, abdominal aorta recipient; Endo, endocardium donor; Epi, epicardium donor; l, left ventricle donor; r, right ventricle donor, V, vena cava inferior recipient).

cell populations. Since our approach presently is limited to the tracking of PFC-loaded monocytes/macrophages, it does not allow the detection of T and B cells which are known to orchestrate the allogenic response (13,32). However, monocytes/macrophages have been shown to comprise a substantial part of the early cellular infiltrate into allogenic cardiac tissue (17,33), and their large number as well as the key role of their effector functions during rejection render them as useful index for acute rejection as demonstrated not only for cardiac but also for renal and corneal allografts (13,34–36).

The PFC load does not seem to alter the functional properties of monocytes, since the infiltration kinetics of labeled cells into allografts observed in this study is in good agreement with literature data (13,18,20). The physiological inertness of PFCs is further supported by our previous study showing that PFC-loaded leukocytes properly responded to threshold stimuli in the case of LPS-induced pneumonia (23). The underlying reasons for this inert behavior are related to the strength of the C–F bond resistant to any cleavage by endogenous enzymes, and the dense and repellent electron sheath coating the C–F-chains, which results in extremely weak intermolecular interactions (37). Thus, others and we have not yet observed any adverse side effects after PFC administration, neither on animals nor on proliferation or maturation of cultured cells (22,23,31,38). Since some of the PFC members such as perfluorodecalin and perfluorooctyl bromide (also known as oxygent®) were already used in patients as artificial blood substitutes (39), ^{19}F MRI may be applicable for clinical diagnosis of organ rejection. Up to now there are no clinical routine applications of ^{19}F MRI, but fluorine coils can readily be interfaced with clinical scanners. Since the ^{19}F nucleus exhibits a sensitivity close to the ^{1}H nucleus (40), clinical 3 T scanners should operate at least with similar sensitivity at human voxel sizes in the range of 2–20 μL as compared to only 0.4 μL in the present study at 9.4 T. Furthermore, in the clinical setting ^{19}F MRI can be combined with advanced ^{1}H MRI techniques such as tagging to correlate the inflammatory state with subtle alterations in cardiac wall motion and circumferential strain (29).

Successful organ transplantation requires effective immunosuppression. Most of the advances in tissue transplantation have resulted from our understanding of the immune mechanisms involved in tissue rejection. Rapamycin is a potent immunosuppressant that induces long-term allograft survival in rodent models. In the present study rapamycin reduced the inflammatory response within the transplanted heart as measured by ^{19}F MRI by about 70%. These *in vivo* data were in good agreement with data from histochemistry, suggesting that ^{19}F MRI is suitable not only for the early detection of rejection but equally well to assess the efficacy of immunosuppressive therapy.

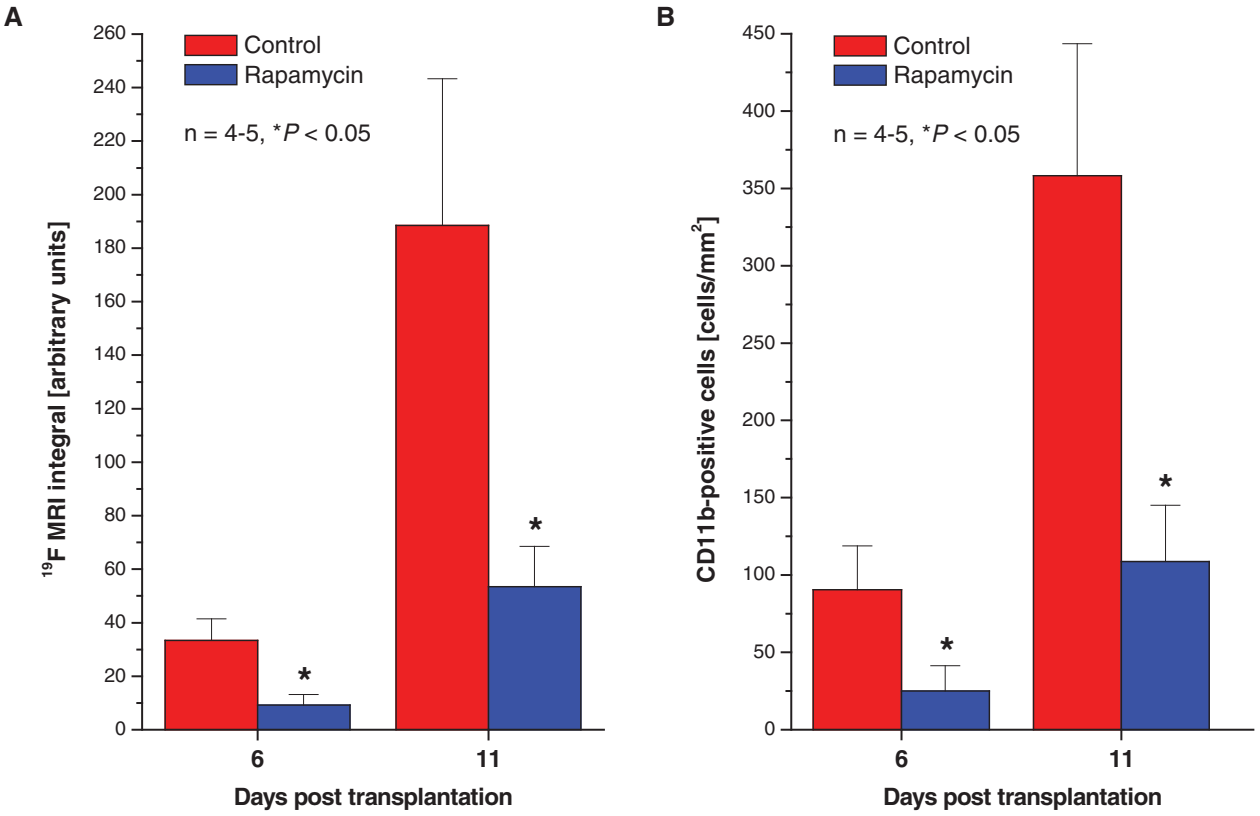

Figure 6: ^{19}F signals correlate with quantity of infiltrating immune cells. Quantification of ^{19}F MR signals (A) and number of CD11b-positive cells (B) found in the myocardium of allografts with and without rapamycin treatment (0.4 mg/kg body weight, i.p.) 6 and 11 days after transplantation, respectively (n = 4–5; *p < 0.05 vs. control at the same point in time).

Acknowledgments

The authors thank Christine Opfermann-Rüngeler for help in illustration and Jutta Ziemann as well as Barbara Emde for excellent technical assistance.

Funding source: This study was supported by the Deutsche Forschungsgemeinschaft (DFG), Subproject Z2 of the Sonderforschungsbereich 612 (to U.F. and J.S.).

Disclosure

The authors of this manuscript have no conflicts of interest to disclose as described by the *American Journal of Transplantation*.

References

1. Billingham ME. Endomyocardial biopsy diagnosis of acute rejection in cardiac allografts. Prog Cardiovasc Dis 1990; 33: 11–18.
2. Yoshizato T, Edwards WD, Alboliras ET, Hagler DJ, Driscoll DJ. Safety and utility of endomyocardial biopsy in infants, children and adolescents: A review of 66 procedures in 53 patients. J Am Coll Cardiol 1990; 15: 436–442.
3. Yang HM, Lai CK, Gjertson DW et al. Has the 2004 revision of the International Society of Heart and Lung Transplantation grading system improved the reproducibility of the diagnosis and grading of cardiac transplant rejection? Cardiovasc Pathol 2009; 18: 198–204.
4. Hummel M, Muller J, Dandel M, Hetzer R. Surveillance biopsies in heart and lung transplantation. Transplant Proc 2002; 34: 1860–1863.
5. Izrailtyan I, Kresh JY, Morris RJ, Brozena SC, Kutalek SP, Wechsler AS. Early detection of acute allograft rejection by linear and nonlinear analysis of heart rate variability. J Thorac Cardiovasc Surg 2000; 120: 737–745.
6. Bourge R, Eisen H, Hershberger R et al. Noninvasive rejection monitoring of cardiac transplants using high resolution intramyocardial electrograms: Initial US multicenter experience. Pacing Clin Electrophysiol 1998; 21: 2338–2344.
7. Fabregas RI, Crespo-Leiro MG, Muniz J et al. Usefulness of pulsed Doppler tissue imaging for noninvasive detection of cardiac rejection after heart transplantation. Transplant Proc 1999; 31: 2545–2547.
8. Moidl R, Chevtchik O, Simon P et al. Noninvasive monitoring of peak filling rate with acoustic quantification echocardiography accurately detects acute cardiac allograft rejection. J Heart Lung Transplant 1999; 18: 194–201.
9. Dengler TJ, Zimmermann R, Braun K et al. Elevated serum concentrations of cardiac troponin T in acute allograft rejection after human heart transplantation. J Am Coll Cardiol 1998; 32: 405–412.
10. Müller TF, Vogl M, Neumann MC, Lange H, Grimm M, Müller MM. Noninvasive monitoring using serum amyloid A and serum

neopterin in cardiac transplantation. Clin Chim Acta 1998; 276: 63–74.
11. Yeoh TK, Frist WH, Eastburn TE, Atkinson J. Clinical significance of mild rejection of the cardiac allograft. Circulation 1992; 86: II267–II271.
12. Valantine HA, Yeoh TK, Gibbons R et al. Sensitivity and specificity of diastolic indexes for rejection surveillance: Temporal correlation with endomyocardial biopsy. J Heart Lung Transplant 1991; 10: 757–765.
13. Wyburn KR, Jose MD, Wu H, Atkins RC, Chadban SJ. The role of macrophages in allograft rejection. Transplantation 2005; 80: 1641–1647.
14. Russell ME, Hancock WW, Wallace AF, Wyner LR, Karnovsky MJ. Modulation of inflammatory activation pathways in the Lewis-to-F-344 rat chronic cardiac rejection model. Transplant Proc 1995; 27: 2100–2104.
15. Weissleder R, Elizondo G, Wittenberg J, Rabito CA, Bengele HH, Josephson L. Ultrasmall superparamagnetic iron oxide: Characterization of a new class of contrast agents for MR imaging. Radiology 1990; 175: 489–493.
16. Kleinschnitz C, Bendszus M, Frank M, Solymosi L, Toyka KV, Stoll G. In vivo monitoring of macrophage infiltration in experimental ischemic brain lesions by magnetic resonance imaging. J Cereb Blood Flow Metab 2003; 23: 1356–1361.
17. Kanno S, Wu YJ, Lee PC et al. Macrophage accumulation associated with rat cardiac allograft rejection detected by magnetic resonance imaging with ultrasmall superparamagnetic iron oxide particles. Circulation 2001; 104: 934–938.
18. Wu YL, Ye Q, Foley LM et al. In situ labeling of immune cells with iron oxide particles: An approach to detect organ rejection by cellular MRI. Proc Natl Acad Sci USA 2006; 103: 1852–1857.
19. Ye Q, Wu YL, Foley LM et al. Longitudinal tracking of recipient macrophages in a rat chronic cardiac allograft rejection model with noninvasive magnetic resonance imaging using micrometer-sized paramagnetic iron oxide particles. Circulation 2008; 118: 149–156.
20. Christen T, Nahrendorf M, Wildgruber M et al. Molecular imaging of innate immune cell function in transplant rejection. Circulation 2009; 119: 1925–1932.
21. Mattrey RF, Long DM, Multer F, Mitten R, Higgins CB. Perfluoroctylbromide: A reticuloendothelial-specific and tumor-imaging agent for computed tomography. Radiology 1982; 145: 755–758.
22. Flögel U, Ding Z, Hardung H et al. In vivo monitoring of inflammation after cardiac and cerebral ischemia by fluorine magnetic resonance imaging. Circulation 2008; 118: 140–148.
23. Ebner B, Behm P, Jacoby C et al. Early assessment of pulmonary inflammation by ^{19}F MRI in vivo. Circ Cardiovasc Imaging 2010; 3: 202–210.
24. Wu K, Zhang J, Fu J et al. Novel technique for blood circuit reconstruction in mouse heart transplantation model. Microsurgery 2006; 26: 594–598.
25. Hasegawa T, Visovatti SH, Hyman MC, Hayasaki T, Pinsky DJ. Heterotopic vascularized murine cardiac transplantation to study graft arteriopathy. Nat Protoc 2007; 2: 471–480.
26. Wasowska BA, Qian Z, Cangello DL et al. Passive transfer of alloantibodies restores acute cardiac rejection in IgKO mice. Transplantation 2001; 71: 727–736.
27. Hasegawa T, Bouis D, Liao H, Visovatti SH, Pinsky DJ. Ecto-5′ nucleotidase (CD73)-mediated adenosine generation and signaling in murine cardiac allograft vasculopathy. Circ Res 2008; 103: 1410–1421.
28. Caves PK, Stinson EB, Billingham M, Shumway NE. Percutaneous transvenous endomyocardial biopsy in human heart recipients. Experience with a new technique. Ann Thorac Surg 1973; 16: 325–336.
29. Wu YL, Ye Q, Sato K, Foley LM, Hitchens TK, Ho C. Noninvasive evaluation of cardiac allograft rejection by cellular and functional cardiac magnetic resonance. JACC Cardiovasc Imaging 2009; 2: 731–741.
30. Smith DJ, Kornbrust ES, Lane TA. Phagocytosis of a fluorescently labeled perflubron emulsion by a human monocyte cell line. Artif Cells Blood Substit Immobil Biotechnol 1994; 22: 1215–1221.
31. Ahrens ET, Flores R, Xu H, Morel PA. In vivo imaging platform for tracking immunotherapeutic cells. Nat Biotechnol 2005; 23: 983–987.
32. Shimizu K, Libby P, Shubiki R et al. Leukocyte integrin Mac-1 promotes acute cardiac allograft rejection. Circulation 2008; 117: 1997–2008.
33. Dreßke B, Zhu X, Herwartz C, Brotzmann K, Fandrich F. The time pattern of organ infiltration and distribution of natural killer cells and macrophages in the course of acute graft rejection after allogeneic heart transplantation in the rat. Transplant Proc 1997; 29: 1715–1716.
34. Jose MD, Ikezumi Y, van RN, Atkins RC, Chadban SJ. Macrophages act as effectors of tissue damage in acute renal allograft rejection. Transplantation 2003; 76: 1015–1022.
35. Slegers TP, Broersma L, van RN, Hooymans JM, van RG, Van Der Gaag R. Macrophages play a role in the early phase of corneal allograft rejection in rats. Transplantation 2004; 77: 1641–1646.
36. Magil AB. Monocytes/macrophages in renal allograft rejection. Transplant Rev 2009; 23: 199–208.
37. Krafft MP, Riess JG. Chemistry, physical chemistry, and uses of molecular fluorocarbon–hydrocarbon diblocks, triblocks, and related compounds–unique "apolar" components for self-assembled colloid and interface engineering. Chem Rev 2009; 109: 1714–1792.
38. Partlow KC, Chen J, Brant JA, Neubauer AM, Meyerrose TE, Creer MH, et al. ^{19}F magnetic resonance imaging for stem/progenitor cell tracking with multiple unique perfluorocarbon nanobeacons. FASEB J 2007; 21: 1647–1654.
39. Riess JG. Perfluorocarbon-based oxygen delivery. Artif Cells Blood Substit Immobil Biotechnol 2006; 34: 567–580.
40. Holland GN, Bottomley PA, Hinshaw WS. ^{19}F magnetic resonance imaging. J Magn Reson 1977; 28: 133–136.

Supporting Information

Additional Supporting Information may be found in the online version of this article:

Movies 1 and 2: Coronal (1) and sagittal (2) ^{1}H fast gradient echo cine movies showing the beating heart within the abdomen of the recipient. ECG triggering was carried out via leads attached to the hind paws. Heart rate of the graft was ∼500 bpm.

Movie 3: 3D interpolation of a multislice 2D time-of-flight MR angiography (MRA) dataset merged with three fast gradient echo cine movies in different orientation to give a more spatial impression of graft localization and sites of anastomosis to the recipient.

Figure S1: Histologic sections from grafted hearts excised 6 days after transplantation showing an enhanced cell infiltration into allograft (left) as compared to isograft tissue (right). Top: Conventional H&E slices, overview images of the septal wall (scale bar = 100 μm). Middle and bottom: Higher magnification of immunostainings for CD11b [green (DAPI, blue), scale bar = 50 μm] as global marker of most innate immune cells (middle), and for CD68/CD3 [green/red (DAPI, blue), scale bar = 50 μm] as specific markers for macrophages and T cells, respectively (bottom).

Figure S2: Immunohistochemical slices from allografts excised 6 days after transplantation treated with rapamycin (0.4 mg/kg body weight, i.p.: right) or saline (left). Top: Overview images of epicardial sections show a strongly reduced infiltration of CD11b-positive cells [green (DAPI, blue), scale bar = 100 μm] under immunosuppressive therapy. Bottom: Higher magnification of coimmunostainings for CD68/CD3 [green/red (DAPI, blue), scale bar = 50 μm] confirmed the suppression of both macrophage and T cell invasion by rapamycin treatment.

http://www.nmr.uni-duesseldorf.de/suppl/transpl

Please note: Wiley-Blackwell are not responsible for the content or functionality of any supporting materials supplied by the authors. Any queries (other than missing material) should be directed to the corresponding author for the article.